Charge Dynamics in Femtosecond Laser Filaments

by

Alexander C. Englesbe

A dissertation submitted in partial fulfillment
of the requirements for the degree of
Doctor of Philosophy
(Nuclear Engineering and Radiological Sciences)
in The University of Michigan
2019

Doctoral Committee:

Professor Karl Krushelnick, Co-Chair
Dr. Andreas Schmitt-Sody, Co-Chair, Air Force Research Laboratory
Professor Ronald Gilgenbach
Research Scientist John Nees
Professor Theodore Norris

Alexander C. Englesbe

aengles@umich.edu

ORCID iD: 0000-0003-4535-6142

Make it so.

–*Jean-Luc Picard*

ACKNOWLEDGEMENTS

This document is the capstone of a journey I started a decade ago in the basement of the physics building at Johns Hopkins University. I thank Michael Finkenthal and Deepak Kumar-Batheja for being there at the beginning and investing their time in me when I was in college.

Since starting graduate school I have had the privilege of working with and learning from many kind and very talented people. I am most grateful for my advisors, Andreas Schmitt-Sody and Karl Krushelnick. Andreas gave me an interesting problem to work on, allowed me the freedom and resources to investigate in the way I wanted, has been a steadfast mentor for the past five years. Andreas and Will White also gave me the opportunity to start my scientific career at the Air Force Research Laboratory, and I look forward to its continuation. In my time as a student at Michigan, Karl has been nothing but supportive, patient, and insightful. This is remarkable given my rather circuitous and unusual path through graduate school.

There was a time in my first year or so when I was deathly afraid of turning on a 30 milliwatt diode laser. With a great deal of patience, and a commendable amount of handholding, John Nees taught me how to run a much more impressive terawatt-class laser system. I thank Jennifer Elle and Remington Reid for always listening, always giving encouragement, and for their eagerness to help me so many times.

Most importantly I thank my parents Laurie and Andy for their boundless support in every moment of the my time in school.

TABLE OF CONTENTS

LIST OF FIGURES

Figure

LIST OF TABLES

Table

LIST OF APPENDICES

Appendix

ABSTRACT

The balance of self-focusing and ionization-induced de-focusing of a nonlinearly propagating laser pulse leads to a transversely confined, high intensity structure called a filament that can persist for long distances. The plasma channel left in the wake of the laser pulse has many interesting properties. One of these is the ability to generate short pulses of microwaves, which oscillate at gigahertz (GHz) frequencies.

The thesis presents an experimental investigation of the microwave radiation. While terahertz radiation from plasmas generated by laser filamentation in air is well known, there are very few studies of the radiation in the microwave regime. The experiments measure several characteristics of the microwave emission in order to understand the source of the current formation in the plasma. These include the angular emission pattern of the radiation, its electric field polarization, the qualitative features of the time domain microwave waveforms, and their absolutely calibrated frequency spectrum up to a maximum frequency of 70 GHz.

The dependence of the radiation on the electron-neutral collision rate is investigated by changing the air pressure in the filamentation region. The microwave measurements indicate that competition occurs between the nonlinear susceptibility of the air, and the conductivity of the plasma. As the pressure decreases, the microwave field increases by an order of magnitude. However it diminishes as the electron-neutral collision rate approaches the frequency of the microwave measurements.

The dependence of the microwave radiation on the laser wavelength is studied by using two different laser systems to generate plasmas from pulses in the mid-infrared at 3900 nm, and the near-infrared at 800 nm, respectively. The microwave

field strength due to the mid-infrared laser pulses is an order of magnitude larger than that due the near-infrared pulses. The relative increase may indicate that the microwave radiation is initiated by transfer of laser energy to the electrons via the ponderomotive force. Comparison of images of the plasma length to the microwave frequency spectrum shows that the generation mechanism involves changes in the current density over spatial scales of the plasma equal to its longitudinal extent. The mid-infrared laser is also used to demonstrate the dependence of the microwave radiation on the relative phase of the laser harmonics in a two color laser pulse.

A third laser system uses a deformable mirror that is run by a genetic algorithm to shape the laser wavefront. The algorithm takes in the microwave amplitude as feedback and configures the wavefront to optimize the microwave emission from the plasma. The optimization leads to an increase in the length, width, and brightness of the plasma, which accompanies a doubling of the microwave field amplitude relative to the unoptimized case. Finally, the deformable mirror can also be used to arbitrarily configure the filaments in a multi-filamenting laser pulse simultaneously, enabling general studies of the mutual interactions of many co-propagating filaments.

Together, the experiments imply that the energy transferred to the plasma by the ponderomotive force over subpicosecond timescales results in a long-lived, nanosecond plasma current with a phase velocity that approaches the group velocity of the laser. It evolves longitudinally along the length of the laser plasma, producing a forward-directed cone of radiation.

CHAPTER I

Introduction

1.1 Microwave Radiation and Ultrashort Laser Pulse Filamentation

One outcome of the study of ultrashort light pulses is the frequent need to reconcile physical phenomena which occur over a range of timescales that is difficult to intuitively grasp. At present, laser systems producing pulses of tens of femtoseconds in duration are commonplace in laboratories around the world. The central challenge of the work presented in this dissertation is the measurement and explanation of an effect initiated by a femtosecond laser pulse that has a characteristic period on the nanosecond scale. While this is not a long time, for perspective, the relative difference between the laser pulse duration and a nanosecond is the same as the difference between an hour and about 14 months. The disparity arises from the generation of plasma by the laser pulse, and the effect of interest is a previously unexplored consequence of its evolution.

The experiments described in the dissertation constitute a detailed investigation of the radiation of microwaves from ultrashort pulse laser-produced plasmas, which are generated during the nonlinear propagation of the laser in air. When a high intensity laser pulse propagates in the atmosphere, it drives competing intensity-dependent

effects that simultaneously try to collapse and defocus the beam [1]. The balance of these nonlinear effects leads to a transversely confined, high intensity structure called a filament that can persist for long distances. The self-focusing is counterbalanced by ionization of the air, and the resulting plasma channel has many interesting and poorly understood properties. One of these is the ability of the plasma to generate and radiate short pulses of microwaves. These are electromagnetic fields that oscillate with frequencies from 1-300 GHz, or equivalently have oscillation periods of 1 nanosecond down to 3 picoseconds (1 ns = 10^{-9} s, and 1 ps = 10^{-12} s).

The radiation results from a time varying current density, but the nanosecond timescale of the current variation is slow relative to that of known charged particle motions in the plasma. The precise radiation mechanism that is the source of the microwaves is unknown, but the experiments make substantial progress toward its identification. Prior research in microwave generation from filament plasmas is extremely limited, and several of the experiments presented in the dissertation are the first of their kind. Since this situation has not been closely looked at before, one basic purpose of the experiments is to establish the nature of the microwave radiation. However the more vital reason for the research is to explore if the radiation can be used as a means for understanding the evolution of the filament plasma. In this regard, the primary aim is to add to the physical picture of charge dynamics in the plasma subject to the laser conditions of filamentation.

The fact that microwave generation from laser plasmas in gases has been generally overlooked is not surprising. There are many mature sources of microwaves that can achieve high power at frequencies from about 1 GHz, such as a magnetron [2], to well in excess of 100 GHz, such as a backward wave oscillator [3] or a gyrotron [4]. The microwaves radiated from the filament plasma are not meant to be competitive with existing sources as their characteristics are different. A microwave vacuum device is usually considered to operate in a narrow frequency band (although harmonics can

be included in the output) [2]. If configured to be pulsed, the radiation often consists of many periods of the electromagnetic field.

The microwaves radiated from the filament plasma are extremely broadband because the pulses contain only a few cycles. That is, the period of the field oscillation is comparable to the total pulse duration. The experiments show that the microwaves from filament plasmas that extend for several centimeters span a frequency range of about 1-20 GHz. However, if the plasma is only a few millimeters long, then the spectrum of the microwave radiation can have a continuous range from less than 5 GHz to over 70 GHz, which makes it the largest bandwidth microwave source in existence aside from a blackbody radiator. The broad frequency range and short pulse duration present significant challenges for making spectral measurements. In fact, no existing test instrument, such as a spectrum analyzer, can measure their spectrum correctly.

A significant portion of the research is devoted to the development of a technique that can accomplish the spectral measurements. The technique is then applied to several experiments that attempt to elucidate the microwave generation mechanism. The first experiment explores the role of electron-neutral collisions in the formation of the currents that lead to microwave emission. The second experiment compares the radiation from the air plasma that results from two different laser systems that generate pulses at different wavelengths. The energy imparted to the electrons in the plasma increases with the wavelength of the laser light. The comparison is accomplished by repeating the same experiment on the two lasers whose wavelengths lie in the mid-infrared and near-infrared ranges, respectively. The results of these experiments point to longitudinal variations in the plasma current as the radiation source.

An additional experiment demonstrates that manipulation of the laser wavefront, which determines the laser intensity profile in its focal region, is able to optimize the generation of the longitudinal plasma current and increase the field strength of the

radiated microwaves. Feedback provided to a genetic algorithm controls the shape of a deformable mirror, which reshapes the wavefront when the laser pulse reflects from its surface. Lastly, a proof-of-concept experiment is described that demonstrates a new capability for controlling laser propagation in the multi-filamentation regime. The same genetic algorithm can be configured to arbitrarily set the transverse locations of several filaments simultaneously within the laser beam.

Multi-filamentation results at very high peak powers when the laser wavefront becomes unstable to small perturbations, causing the beam to break up into co-propagating filaments whose number is constrained by the available energy contained in the pulse. Using the deformable mirror to cause the filaments to form at user-defined locations within the beam profile constitutes a novel method that could be used to study the mutual interactions of arbitrary numbers of filaments. The majority of filament interaction studies to date have only involved two filaments [5, 6].

The dissertation describes research efforts regarding the physics of the microwave radiation that identify a phenomenon that has not been investigated in any significant depth, create an approach for gathering useful measurements of its attributes, and present detailed experimental results that demonstrate its physically rich nature. Previous observations of the microwave radiation are described in Section 1.4. There are only a few studies, and they do not explore the possibility that the microwaves arise from a generation mechanism that is distinct from other more closely examined sources of secondary radiation caused by filamentation, such as terahertz (THz) waves [7]. Furthermore, the research provides the groundwork for two possible pathways for its own continuation. The first follows from proving the utility of adaptive wavefront shaping for controlling the random nature of filamentation. The second is the proposal of a novel plasma diagnostic based on the microwave radiation that may allow for direct determination of the electron temperature of the filament plasma, which if successful would represent a significant advancement for filamentation science.

The remaining sections in this Chapter explain how high peak power, ultrashort laser pulses are generated, and how filamentation can occur as they propagate. The Chapter also discusses the limited existing research on the microwave generation, and concludes by enumerating the subjects of the subsequent Chapters.

1.2 Ultrashort Laser Pulses

The process for generating a high intensity ultrashort laser pulse is called chirped pulse amplification (CPA) [8]. Its inventors, Donna Strickland and Gérard Mourou, were awarded the 2018 Nobel Prize in Physics for its discovery [9]. CPA was originally proposed to amplify microwaves [10]. The adaptation of the idea for optical light required significant insight into solid state physics and nonlinear optics, and is the enabling technology that allows for the study of laser filamentation in gases.

The difficulty in creating high-power ultrashort laser pulses is that only solid state materials have sufficient absorption and emission bandwidths to be employed as amplifier gain media. However, they are easily damaged by intense light pulses. The predecessors to solid state ultrashort pulse lasers were dye lasers [11]. They too can produce ultrashort pulses [12] but the dye is poisonous, carcinogenic and must be replaced often due to photochemical degradation [13]. Before CPA, the only way to reduce the intensity enough to avoid damage in a solid state laser would be to transmit very large diameter pulses through the amplifiers. A gain crystal of sufficient size would be either prohibitively expensive, or beyond the abilities of crystal growth techniques. Intensity is defined as the flow of energy per unit time and area. Instead of expanding the beam in space to decrease the intensity, CPA stretches the pulse in time.

The steps involved in CPA are depicted in Figure 1.1. It begins with a source of low energy, low peak power ultrashort pulses that contain the total frequency bandwidth needed to achieve the ultrashort pulse duration. Fourier analysis shows

that there is a fundamental limit on the temporal duration of a pulse that is inversely related to the 'number' of frequency components that the pulse contains. The span of the frequency components is called the bandwidth. The Fourier limit (also called the transform limit) depends on the pulse shape, and is expressed as a product of the pulse duration and bandwidth. For a Gaussian pulse, it is given by

$$\Delta\nu\Delta t \geq 0.441, \tag{1.1}$$

where $\Delta\nu$ is the bandwidth, and Δt is the pulse duration [14]. In practice, the short pulses are generated in an oscillator cavity that often employs passive mode-locking [15]. A standard passive mode-locking technique used with titanium-doped sapphire (Ti:sapphire) based lasers is called Kerr lens mode-locking, and the reader is referred to References [16] and [17] for details. The pulses coupled out of the oscillator cavity seed the CPA process.

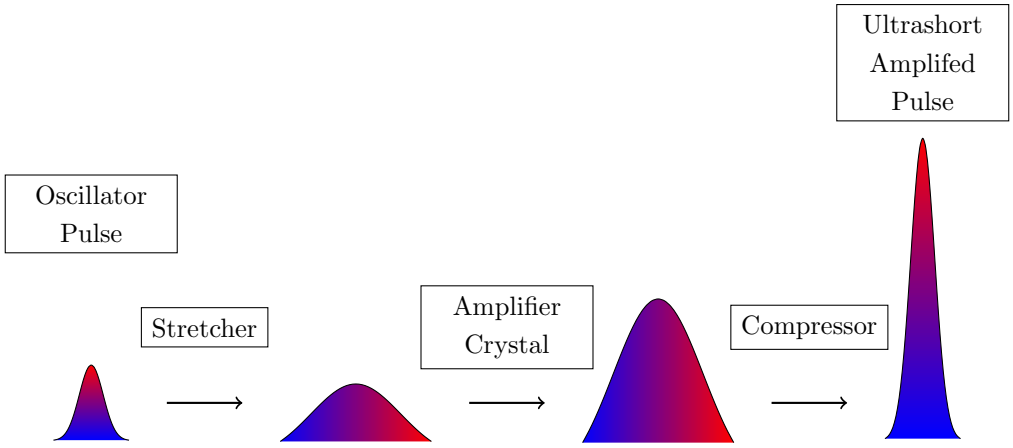

Figure 1.1: The process of chirped pulse amplification. A stretcher uses group velocity dispersion to apply chirp to a low power ultrashort seed pulse. The pulse maintains low peak power through the main amplifier to prevent damage. After amplification, a compressor reverses the applied chirp, producing a high power ultrashort pulse.

The peak power of the pulse is decreased during amplification by elongating it in time. CPA accomplishes stretching in time by imposing a relative delay on the pulse's frequency components. The ordering in time of the different frequencies within the

pulse is called the spectral phase or chirp, and the next step in CPA is to use group velocity dispersion (GVD) that is provided by a diffraction grating or transmission through a material to create chirp. The stretcher in a CPA architecture may take an oscillator pulse that had a duration of 30 fs and extend it to 100-200 ps without changing its frequency content. This decreases the pulse intensity by a factor of nearly 10^4. Figure 1.1 uses red and blue shading to demonstrate the spectral phase. The temporal pulse envelopes are shown at each step. Vertical shading indicates that the pulse is transform limited and the spectral phase is minimized. Horizontal shading corresponds to the applied chirp. The chirped, low energy pulse is amplified in the third step so that it attains low peak power, but high energy. The final step is to reverse the applied chirp, usually implemented with another diffraction grating having the opposite sign GVD, which is called compression. This gives a high power, high energy ultrashort pulse. It is common to achieve terawatt (TW) power levels in compressed pulses, although petawatt peak power is the current state-of-the-art [18, 19].

1.3 Filamentation and Multi-Filamentation

Filamentation in a gas was first experimentally demonstrated and explained at the University of Michigan in 1995 by Gérard Mourou's group in the Center for Ultrafast Optical Science (CUOS) [1]. Before the advent of ultrashort pulse lasers, it had been observed in solids [20] and liquids [21] with long pulse lasers. While the term 'filament' or 'filamentation' is used in several contexts throughout the field of plasma physics such as in high voltage discharges [22], astrophysics [23], and even other types of laser-plasma interactions [24], it has a specific definition within nonlinear optics, and does not exclusively refer to the plasma left in the wake of the laser pulse. Figure 1.2 illustrates how laser filamentation occurs.

The response of the medium, which is air for all the experiments in the dissertation,

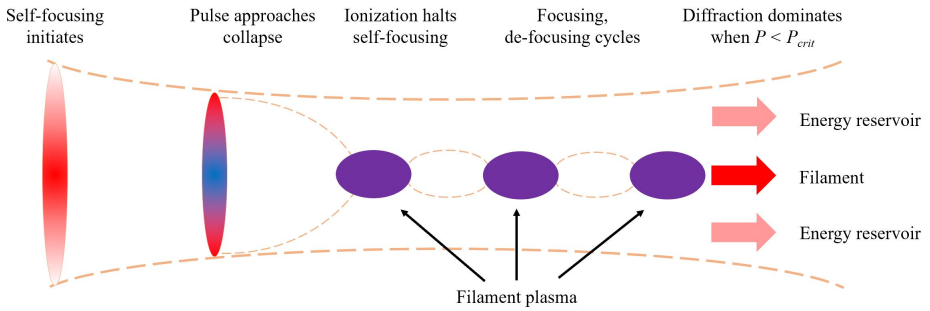

Figure 1.2: The process of laser filamentation. When the laser power is above the critical threshold for self-focusing, it tends toward collapse. The intensity becomes high enough to ionize the medium, and the resulting plasma de-focuses the laser field. The balance of self-focusing and de-focusing persists as long as sufficient energy remains in the laser field. Once its energy is depleted such that it falls below the self-focusing critical power, the field diffracts out of the filamentation region.

depends on the local intensity of the laser field. The contribution of the intensity dependent response is third order in the laser electric field, so it does not become dominant unless the field strength is very high. This is achievable with ultrashort pulses whose peak power exceeds the critical power for self-focusing in air, that is the laser power necessary for the nonlinear response of the air molecules to exceed natural diffraction of the laser field. It is given by

$$P_{crit} > \frac{\lambda^2}{8\pi n_0 n_2}, \tag{1.2}$$

where λ is the laser wavelength, and n_0 and n_2 are the linear and nonlinear indices of refraction, respectively. Equation 1.2 can be applied to filamentation in solids, liquids, and gases. The indices of refraction account for the macroscopic material response. Section 2.1.1 gives derivation of P_{crit}. It is introduced here simply to explain the concept of filamentation.

When $P > P_{crit}$, the nonlinear response is greater near the center of the laser pulse where the intensity is highest, than at its periphery. This causes a relative phase delay between the edge of the laser field and the center in the same manner as if it had passed through a positive lens. The phase delay results in self-focusing,

and is the effect that initiates filamentation, as shown on the left side of Figure 1.2. Section 2.1.2 states the mathematical form of the wave equation that can be used to describe filament propagation. Once self-focusing starts, it experiences positive feedback as the laser becomes more intense. The laser field tends toward collapse, but the field strength becomes so large that ionization of the air de-focuses the pulse and arrests the collapse.

The phase between the center and edge of the field experiences the opposite relative delay when the laser propagates in ionized air. The free electrons and ions in the ionized air can be treated as a plasma. The phase velocity, v_{phase}, of an electromagnetic wave in an unmagnetized plasma is

$$v_{phase} = \frac{c}{n_{plasma}} = \frac{c}{\sqrt{1 - \frac{N_e(\mathbf{r},t)}{N_{crit}}}}, \tag{1.3}$$

where c is the speed of light, n_{plasma} is the plasma refractive index, $N_e(\mathbf{r}, t)$ is the local electron density, and N_{crit} is the critical density at which the electromagnetic wave becomes evanescent in the plasma [25]. The plasma generation is also intensity dependent, so its density is greater on axis than at the edges. This means that v_{phase} in the plasma is greater on axis, which causes the beam to de-focus. However once the de-focusing occurs, the plasma generation diminishes, and self-focusing takes over again. The self-focusing and de-focusing are balanced and cyclical in filamentation, and the laser pulse remains transversely confined without diffracting as long as there is sufficient power to support the self-focusing and plasma generation. The pulse leaves in its wake a longitudinally extended plasma column, an example of which is shown in Figure 1.3. This plasma is the source of the microwave radiation.

Surrounding the intense filament at the core of the laser pulse is an energy reservoir of non-filamenting laser light [26]. The laser intensity profile must continuously vary from its peak to zero both longitudinally and transversely, and it is the parts

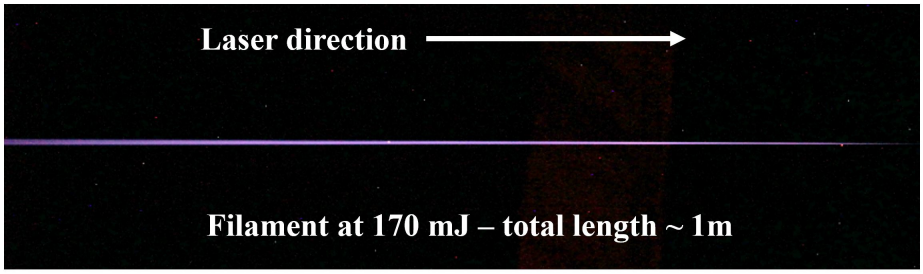

Figure 1.3: Side view of the plasma fluorescence due to laser filamentation in air. The peak power of the input pulse is ~ 3.4 TW or $\sim 680 P_{crit}$ at $\lambda = 800$ nm.

of the pulse at the periphery that do not exceed P_{crit} which constitute the energy reservoir. It plays an important role in filament propagation, because as its name implies, it serves as a source of energy that maintains the filament [27, 28]. There is a complicated interplay between the energy reservoir and the filament that is not completely understood [29, 30].

The relationship between the filament and the energy reservoir becomes even more complex at peak powers well in excess of P_{crit} [31, 32, 33]. Chapter VI indirectly explores this relationship. Because of the balance of self-focusing and de-focusing, the intensity of a filamenting laser pulse cannot be significantly increased above a particular value that depends on n_0, n_2, and λ regardless of the power, beam mode, and to a degree external focusing applied by a lens [34, 35, 36, 37]. This is called intensity clamping, and for $\lambda = 800$ nm in air, the clamped intensity is on the order of 10^{14} W/cm^2 [38, 39]. Now consider the case where $P \gg P_{crit}$, which is easily achieved with the laser systems used in the experiments. If the intensity is clamped, but there is an excess of energy in the pulse for the generation of a single filament, the diameter of the filament and the plasma must increase. An intuitive explanation is that the propagation of higher power pulses will sooner generate plasma having sufficient density to force the laser to de-focus.

A large diameter single filament at $P \gg P_{crit}$ is theoretically possible for a perfect beam mode that consists of plane waves when the beam is neither focusing or

de-focusing. However real laser pulses have imperfect transverse profiles. The modulational instability [40] amplifies the imperfections and causes the beam profile to evolve chaotically and break up into localized hot spots that seed co-propagating filaments in the pulse [31, 41, 42]. This is called multi-filamentation, and the experiments in the dissertation are performed in the single and multi-filamentation regimes. Figure 1.4 shows examples of beam profiles that result from multi-filamentation. The

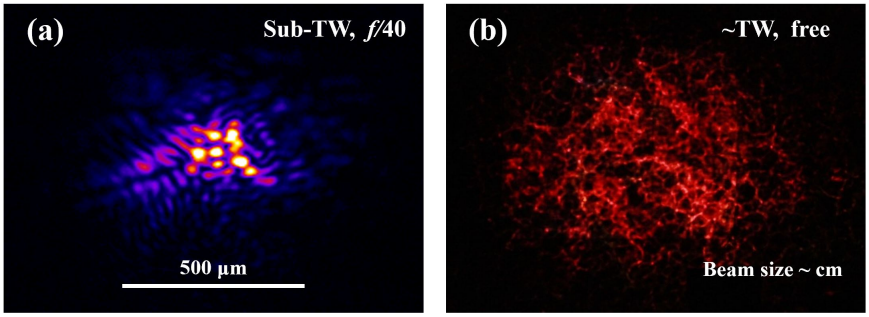

Figure 1.4: (a) Multi-filamentation of a sub-TW, 800 nm laser pulse that is also externally focused at $f/40$. The image is taken at the exit plane of the filamentation region. (b) Multi-filamentation of a TW-class, 800 nm laser pulse that does not include strong external focusing. The image of the beam profile is taken far beyond the exit plane of the filamentation region. The images use different color maps, but illustrate the very different behaviors that are possible in different situations of multi-filamentation.

images are taken at different longitudinal positions relative to the region where filamentation occurs, and come from different laser systems. However, they illustrate the fact that differences in the pulse peak power and focusing geometry can cause the laser pulse evolution to unfold in completely different manners. The sub-TW laser pulse in Figure 1.4(a) is externally focused at $f/40$, and contains fewer than 10 hot spots, which correspond to the filaments. A pulse such as this, while well into the multi-filamentation regime, will not produce the extremely scintillated beam profile shown in Figure 1.4(b) that results when there is no external focusing, and a much larger number of filaments which form when $P > 100P_{crit}$. Another significant difference between externally focused and freely propagating single, or multiple filaments is that the electron density of the filament plasma is much greater if external focusing

is imposed on the laser beam [36].

It is important to acknowledge the complex nature of multi-filamentation and its acute sensitivity to the conditions of the input laser pulses [43, 44, 45]. However, from the perspective of the microwave radiation measurements, these fine details can largely be neglected because the distance between the filaments is much smaller than the microwave wavelengths. The experiments are all performed under conditions that more closely resemble the situation in Figure 1.4(a), than Figure 1.4(b). When a filamenting laser pulse is externally focused, the filamentation region and the plasma extend beyond the Rayleigh range of the focusing optic. However, the external focusing serves to fix the longitudinal location of the filaments in the vicinity of the geometric focal plane with high repeatability between each shot of the laser. This is necessary in order to perform experiments in a laboratory of practical size, as the self focusing distance without significant external focusing can be tens of meters or greater [46, 47, 48].

Under the conditions of external focusing, the filaments are longitudinally confined, and transversely packed with spacing on the order of tens to hundreds of microns [49, 50]. The microwave wavelength at 70 GHz is about 4.3 mm, which is the highest frequency that the microwave receiver can measure. This is much larger than any transverse spatial nonuniformities in the plasma that might result from multi-filamentation. Therefore, it is possible to treat the filament plasma as one continuous radiating body, whether the laser pulse is in the single or multi-filamentation regime. It is not necessary to consider the randomly shaped, sub-wavelength features of the filament plasma that may result from multi-filamentation. It is possible that variations in the longitudinal start and end points of the filaments in the multi-filament regime could result in interference of the microwave fields, which would could appear as amplitude modulations of the microwaves in both the time and frequency domains. These modulations, if present do not dominate the observed frequency spectra of the

microwave radiation.

1.4 Prior Observations of Microwave Radiation from Filament Plasmas

Microwave radiation from filament plasmas has been observed before, but it has not been investigated in any significant depth. There are three experiments that the author is aware of where fields oscillating in the microwave frequency range have been measured without any external stimulation of the emission, such as an applied DC electric field. The first is a near field measurement performed by Proulx *et al.* [51], where an unterminated coaxial cable connector was positioned a distance from the plasma that was much less than the wavelength of the observed fields. The end of the cable was translated longitudinally along the plasma over many laser shots to try to infer the presence of any net charge imbalances. They found a longitudinal variation in the signal, which the authors attributed to ponderomotive acceleration of the plasma electrons.

The second study that is also closely related to the work presented in the dissertation used a narrow bandwidth heterodyne receiver operating at center frequencies 94 and 118 GHz each with 2 GHz bandwidth [52]. A heterodyne receiver is a common detector type used in microwave instrumentation [53], and is described in detail in Appendix B. The angular emission pattern of the radiation at those frequencies is reported. The paper is presented as a preliminary observation that such radiation exists, and does not attempt to explain its source in detail.

The third experiment uses the same heterodyne receiver centered at similar frequencies. It reports an additional measurement of the radiation at 11 GHz (also with 2 GHz bandwidth) in the near field, with the antenna aperture 1 cm from the filament plasma. The measurement appears in the doctoral dissertation of Grégoire

Méchain [54], and is meant to demonstrate that the polarization of the emission is similar to that of dipole radiation over a large frequency range. To the best of the author's knowledge, the measurement at 11 GHz was not developed into a study that was published in peer reviewed literature.

Other experiments report the generation of microwave and radiofrequency ($\leq$ 1 GHz) fields radiated from filament plasmas when the filamentation occurs in a region of an externally applied electric field in air. An experiment that examined the radiation over a frequency range of 150 MHz to 6 GHz claimed that in a field of a few hundred V/cm, ion motion in the plasma is responsible for the low frequency radiation [55]. Consideration of collisional timescales typical of filament plasmas in atmosphere makes this conclusion dubious. If the filament propagates between two electrodes so that the filament axis coincides with the direction of the applied electric field, the spectrum of the microwave emission is greatest at a wavelength corresponding to the spacing between the electrodes [56]. The resonance shows that the microwave radiation is more dependent on the presence of the external field than on charge motion in the filament plasma driven by the laser pulse. Therefore existing experiments of this nature cannot be used to make a useful comparison to those described in the dissertation.

There is not a wealth of literature on microwave generation from filament plasmas. The experiments that have been reported are fairly preliminary in scope. Therefore, the investigations that the dissertation documents represent the most in depth examination of the effect to date. The most likely reason the microwave radiation has garnered such little attention is that filamentation and filament plasmas are promising sources of THz radiation. In contrast to microwaves, THz generation has been closely studied for nearly two decades [57]. The dissertation makes comparison to the body of research on filament-produced THz where necessary since it is the most thoroughly investigated phenomenon that may have some relationship to the microwave

radiation.

1.5 Organization of the Dissertation

The dissertation contains the detailed progress made during the research efforts to measure and understand the microwave radiation from the plasma. After providing theoretical foundations for the general physical concepts needed to understand the research, it describes the progression of the experiments. This begins with the development of a technique to make the measurements. The dissertation then demonstrates its repeated use in several experiments that probe the nature of the generation mechanism, and culminates in an explanation of how the microwave radiation could be used to provide new understanding of laser filamentation and filament produced plasmas.

- Chapter II presents the theoretical basis for the physics examined in the experimental chapters. Nonlinear propagation and filamenation are described mathematically, and the ionization mechanisms in intense optical fields are noted. Preliminary measurements are used to place constraints on the possible microwave generation mechanism.

- Chapter III details the method that was created to perform the microwave measurements, including calculation of the absolute electric field spectrum over nearly two decades of bandwidth. Since the method is new, the design considerations that enable it to work are discussed in depth. The calibration procedure is described, and the calibration data sets are presented.

- Chapter IV describes experiments performed at the Air Force Research Laboratory (AFRL) using a 10 TW-class near-infrared (NIR) laser. The experiments examine the dependence of microwave emission from the filament plasma on electron-neutral collisions by changing the air pressure where the filaments

propagate. It explains the experiments' unexpected result, which is that the microwave yield increases by over an order of magnitude as the pressure decreases.

- Chapter V describes experiments accomplished in collaboration with the University of Maryland that test the laser wavelength dependence of the microwave radiation. The laser system at Maryland uses several stages of nonlinear frequency differencing to generate pulses whose center wavelength is in the mid-infrared (MIR) at 3.9 μm. The microwave yield and frequency spectrum from 2-70 GHz is compared in the MIR for single and two color laser plasmas. The single and two color experiments are repeated at AFRL using the NIR laser from Chapter IV. The measurements show that the microwaves fields radiated from the MIR produced plasma are an order of magnitude larger than than from the NIR produced plasma. The dependence of the broadband microwave spectrum from single color laser pulses indicates that the microwave frequency content is determined by longitudinal variations in the filament plasma along its entire extent.

- Chapter VI combines two experiments performed on the λ^3 laser at the University of Michigan. λ^3 is a high repetition rate NIR system that is capable of advanced optimization testing. A deformable mirror at its output shapes the transverse spatial phase of the laser pulses using a closed feedback loop to run a genetic algorithm. In the first experiment, the microwave yield from the filament plasma is optimized as a function of air pressure, building upon the results of Chapter IV. The second experiment presents a proof of concept method to control multiple filamentation that might be useful in other aspects of filamentation research, and is not specialized for microwave generation.

- Chapter VII concludes the dissertation by summarizing its findings and con-

tributions. It proposes how the microwave radiation might be employed as a diagnostic of the filament plasma electron temperature. It also suggests several possibilities for additional investigations regarding secondary radiation from laser plasmas in air.

Role of the Author

The author played the primary role in designing and executing the experiments described in the dissertation, and processed all of the data collected during the experimental measurements. The only exception is the measurement of the microwave dependence on air pressure that shows a clear maximum in Figure 4.9. Those data were taken by Dr. Jennifer Elle. Running the experiments and constructing the experimental apparatus were collaborative efforts. The microwave antenna calibrations were accomplished with help from Hugh Pohle. Dr. Elle and Dr. Ryan Phillips helped to record the microwave data pertaining to air pressure dependence (Chapter IV), laser wavelength dependence, and the comparison of single and two color laser pulses (Chapter V). Robert Schwartz, Anastasia Korolov, and Daniel Woodbury maintained and ran the MIR laser used in the laser wavelength comparison experiments. Dr. Dogeun Jang and Prof. Ki-Yong Kim set up the optical path for the two color experiment performed in the MIR, and provided images of the plasma fluorescence generated by the MIR pulses (Chapter V). Jinpu Lin, John Nees, Dr. Milos Burger, and Patrick Skrodzki ran the λ^3 laser and assisted taking data during the microwave emission optimization experiments (Chapter VI). The interface for the genetic algorithm used in the optimization experiments was written by Dr. Zhaohan He. Finally, many of the experimental structures, such as the gas cell used in Chapters IV and VI, and the rotating antenna mounts, were designed and built by Adrian Lucero.

CHAPTER II

Physical Concepts

This Chapter gives theoretical descriptions of physical phenomena relevant to microwave radiation from plasmas generated by nonlinear laser filamentation. This includes nonlinear propagation of high intensity laser pulses in gases, non-relativistic electron motion in a laser field, and strong field ionization. The dissertation does not attempt to formulate an analytical theory of the microwave radiation generation. Instead, it uses several examples of experimental data to define constraints on the nature of current source that causes the radiation.

2.1 Filamentation of Nonlinear Laser Pulses

2.1.1 Derivation of the Critical Power

While there are many unusual aspects of nonlinearly propagating laser pulses, the work presented here results from the ability of such pulses to focus on their own. This is known as self-action, or more specifically self-focusing, because the pulse can reshape itself to become more spatially confined and more intense without passing through any lenses. Askaryan showed the index of refraction of a liquid or gas must be described with an additional contribution that is proportional to the local field

intensity $I(\mathbf{r}, t)$ when the intensity is large [58]

$$n(\mathbf{r}, t) = n_0 + n_2 I(\mathbf{r}, t). \tag{2.1}$$

For an initially Gaussian laser pulse, Equation 2.1 shows that the index of refraction is greater in the center of the pulse than at its periphery. The center of the pulse propagates more slowly than the edges as if the pulse had passed through a positive lens. Diffraction, that is the natural transverse spreading of waves in a finite aperture beam, competes with the nonlinearity. If the intensity is high enough that the nonlinearity overcomes diffraction, then the pulse initiates self-focusing. The critical power at which self-focusing and diffraction balance can be found by equating the phase contribution due to the nonlinearity with that of diffraction.

Before proceeding with the derivation, it is useful to mathematically define a few relevant concepts of laser beam propagation. For a linearly polarized CW beam far below the critical power, it is permissible to assume that the longitudinal variation in the laser electric field amplitude occurs over distances much larger than a wavelength, so that it can be separated into a quickly varying time component $E(t)e^{-i(\omega t - kz)}$ multiplied by a slowly varying spatial component $\psi(\mathbf{x})$

$$\mathbf{E}(\mathbf{x}, t) = \psi(\mathbf{x}) E(t) e^{-i(\omega t - kz)} \hat{\mathbf{x}}, \tag{2.2}$$

where the we consider only the forward going wave propagating in the z direction, and the field has frequency ω and wavenumber $k = 2\pi/\lambda$. The wavelength of the laser field is λ. The spatial component obeys the Helmholtz equation

$$\nabla^2 \psi + k^2 \psi = 0, \tag{2.3}$$

which is simplified under the paraxial approximation to neglect the $\partial^2/\partial z^2$ term in

Equation 2.3

$$\nabla_{\perp}^2 \psi + 2ik\frac{\partial \psi}{\partial z} + 2k^2\psi = 0, \tag{2.4}$$

where $\nabla_{\perp}^2 = \partial^2/\partial x^2 + \partial^2/\partial y^2$. The Gaussian beam is a solution to Equation 2.4 and is given by [14],

$$\psi(\mathbf{x}) = \psi(x,y,z) = \frac{\psi_0}{\sqrt{1+\frac{z^2}{z_R^2}}} \exp\left(\frac{-(x^2+y^2)}{w^2(z)}\right) \exp\left[\frac{-ik(x^2+y^2)}{2R(z)} - i\Theta(z)\right], \tag{2.5}$$

where the leading factor and exponential term in parenthesis describe the spatial amplitude, and the exponential term in brackets describes the spatial phase. The transverse surfaces where the spatial phase is constant are called wavefronts. The longitudinally varying functions within Equation 2.5 are the beam waist, the wavefront curvature, and the Gouy phase, respectively. These and the Rayleigh range, z_R are defined to be

$$z_R = \frac{n_0 \pi w_0^2}{\lambda} \tag{2.6}$$

$$w(z) = w_0\sqrt{1+\frac{z^2}{z_R^2}} \tag{2.7}$$

$$R(z) = z + \frac{z_R^2}{z} \tag{2.8}$$

$$\Theta(z) = \tan^{-1}\left(\frac{z}{z_R}\right). \tag{2.9}$$

Equation 2.5 is a solution to Equation 2.4, and is stated to establish that it is possible to mathematically describe the laser spatial phase. In filamentation, the transverse part of the spatial phase is a useful concept for providing an intuitive picture for self-focusing. However Equations 2.5-2.9 only apply to Gaussian beams in the linear regime. In the nonlinear regime, the spatial phase cannot be described analytically for general situations.

We can now find the critical power for self-focusing by using the transverse vari-

ation in the spatial phase due to diffraction, which is given in the first term inside the brackets in Equation 2.5. The wavefront curvature over a small propagation distance of L_z can be approximated as $R(L_z) \approx z_R^2/L_z$, so that the spatial phase due to diffraction becomes

$$\phi_{\text{diffraction}}(r, L_z) = -\frac{kL_z}{2z_R^2}r^2, \tag{2.10}$$

where $r^2 = x^2 + y^2$. The transverse intensity profile of a Gaussian beam is $I(r) = I_0 \exp(-2r^2/w_0^2)$, where the factor of 2 accounts for the fact that I is proportional to the square of the field, which goes like $\exp(-r^2/w_0^2)$. As Equation 2.1 states, the nonlinear contribution to the total index of refraction is $+n_2 I$. Therefore the spatial phase due to self-focusing over a distance L_z is

$$\phi_{\text{self-focus}}(r, L_z) = \frac{2\pi}{\lambda}L_z n_2 I = \frac{2\pi}{\lambda}L_z n_2 I_0 \exp(-2r^2/w_0^2). \tag{2.11}$$

Near $r = 0$, we can Taylor expand the exponential ($e^x \approx 1 + x$) to give

$$\phi_{\text{self-focus}}(r, L_z) \approx \frac{2\pi}{\lambda}L_z n_2 I_0 \left(1 - \frac{2r^2}{w_0^2}\right). \tag{2.12}$$

The criterion for self-focusing is that $\phi_{\text{self-focus}} \geq \phi_{\text{diffraction}}$, which follows from Equations 2.10 and 2.12,

$$\frac{2\pi}{\lambda}L_z n_2 I_0 \frac{-2r^2}{w_0^2} \geq -\frac{2\pi n_0}{\lambda}\frac{L_z}{2z_R^2}r^2, \tag{2.13}$$

where the first term in Equation 2.12 is neglected because there is no spatial variation. Equation 2.13 simplifies to [14]

$$\frac{\pi}{4}w_0^2 I_0 = P_{crit} \geq \frac{\lambda^2}{8\pi n_0 n_2}. \tag{2.14}$$

where P_{crit} is the critical power that was stated in Equation 1.2. For a Ti:sapphire

laser pulse at $\lambda = 800$ nm propagating in standard air, $P_{crit} \sim 5$ GW [39]. Equation 2.14 follows from a simplified derivation of the critical power that is meant to illustrate the balance of nonlinear self-focusing and diffraction. A more general form is given by

$$P_{crit} \geq \frac{\alpha\lambda^2}{8\pi n_0 n_2}, \tag{2.15}$$

where the constant α is determined by the spatial and temporal pulse shape[14]. Even though the critical power can change depending on the pulse shape [46, 59] and frequency chirp [60, 61, 62], the fundamental scaling, that is λ^2/n_2, remains the same.

2.1.2 Nonlinear Wave Equation and Filament Formation

A fairly general wave equation that describes the nonlinear propagation of the laser pulse is given by

$$\nabla^2\mathbf{E} - \frac{n_0^2}{c^2}\frac{\partial^2\mathbf{E}}{\partial t^2} = \mu_0\left(\frac{\partial^2\mathbf{P}^{\mathrm{NL}}}{\partial t^2} + \frac{\partial\mathbf{J}}{\partial t}\right), \tag{2.16}$$

where $\mathbf{P}^{\mathrm{NL}}$ is the nonlinear polarization vector field induced in the medium by the electric field, and $\mathbf{J}$ is the current density in the plasma. The material polarization describes the averaged, macroscopic bound electron response of the material per unit volume. Equation 2.16 neglects delayed material responses due to molecular rotation [63] or periodic alignment [64, 65], and allows for net current to flow, but not the accumulation of net charge distributions.

Filamentation is due to the dominant contributions to $\mathbf{P}^{\mathrm{NL}}$. In linear optics, the material polarization is proportional to the applied field $\mathbf{P}^{\mathrm{L}} = \epsilon_0\chi^{(1)}\mathbf{E}$, while in nonlinear optics, it is described in a Taylor series expansion

$$\mathbf{P} = \mathbf{P}^{\mathrm{L}} + \mathbf{P}^{\mathrm{NL}} = \epsilon_0\left(\chi^{(1)}\mathbf{E} + \chi^{(2)}\mathbf{E}^2 + \chi^{(3)}\mathbf{E}^3 + \ldots\right), \tag{2.17}$$

where $\chi^{(n)}$ is the nth order material susceptibility. The bound electron response of a gas does not have macroscopic anisotropy, so only the odd terms in Equation 2.17 are nonvanishing. This is different in a crystalline material, for example, where the dipole moments of its microscopic constituents are aligned to give it a macroscopic anisotropic susceptibility. In a gas, the leading term of $\mathbf{P}^{\mathrm{NL}}$ is associated with $\chi^{(3)}$, although anisotropy can be induced by the pulse itself in molecular gases [65]. The third term of Equation 2.17 can be written as

$$\mathbf{P}^{(3)} = \epsilon_0 \chi^{(3)} \mathbf{E}^3 \approx \epsilon_0 \chi^{(3)} |E|^2 \mathbf{E}, \tag{2.18}$$

to give the wave equation that describes filamentation

$$\nabla^2 \mathbf{E} - \frac{n_0^2}{c^2} \frac{\partial^2 \mathbf{E}}{\partial t^2} = \mu_0 \left(\epsilon_0 \frac{\partial^2}{\partial t^2} \chi^{(3)} |E|^2 \mathbf{E} + \frac{\partial \mathbf{J}}{\partial t} \right). \tag{2.19}$$

The connection of Equation 2.18 to the intensity dependent contribution to the refractive index is clear, since $I = \frac{1}{2} c \epsilon_0 |E|^2$. The third order nonlinear susceptibility is related to the nonlinear index of refraction by [66]

$$n_2 = \frac{3}{2 n_0^2 \epsilon_0 c} \chi^{(3)}. \tag{2.20}$$

It is possible to approximate the total index of refraction during filamentation as

$$n(\mathbf{r}, t) \simeq n_0 + n_2 I(\mathbf{r}, t) - \frac{e^2 N_e(\mathbf{r}, t)}{2 \epsilon_0 m_e \omega_L^2}, \tag{2.21}$$

where ω_L is the laser frequency [67]. From Equation 2.21 and the argument of Section 2.1.1, it is clear that the plasma formed by the laser pulse has a defocusing effect. The creation of the electron-ion pairs that make the filament plasma is described in the next Section.

2.2 Single Electron Motion in a Non-Relativistic Laser Field

The equation of motion of a single electron in an electromagnetic field is given by the Lorentz force

$$\frac{d\mathbf{p}}{dt} = -e\left(\mathbf{E} + \mathbf{v} \times \mathbf{B}\right), \tag{2.22}$$

where the electron momentum $\mathbf{p}$ depends on its velocity $\mathbf{v}$ and the $\mathbf{E}$ and $\mathbf{B}$ fields of the laser. We can compare the relative magnitudes of the electric and magnetic components of the Lorentz force by considering Faraday's law for time harmonic electromagnetic plane waves ($\mathbf{E}, \mathbf{B} \sim \exp[-i\omega + kt]$) in the frequency domain

$$\mathbf{k} \times \mathbf{E} = i\omega\mathbf{B}. \tag{2.23}$$

Neglecting the complex and vector nature of Equation 2.23 and considering magnitudes only gives

$$\frac{\omega}{k} = \frac{E}{B} \rightarrow E = cB. \tag{2.24}$$

Equation 2.24 implies that in order for the electric and magnetic forces to have the similar numerical values, the magnitude of the electron velocity in Equation 2.22 must approach the speed of light. If the electron velocity in the laser field is non-relativistic ($v \ll c$) then the magnetic component can be neglected in a first order approximation.

In this case, the equation of motion for the electron in the laser field and the amplitude of its velocity as it oscillates reduces to

$$m_e \frac{d\mathbf{v}}{dt} = -e\mathbf{E} \rightarrow |\mathbf{v}| = v_{osc} = \frac{eE}{m_e\omega_L}. \tag{2.25}$$

Equation 2.25 leads to a dimensionless parameter that determines whether or not the electron motion is relativistic by comparing v_{osc} with c. It is called the normalized

vector potential [68], or laser strength parameter, and is defined as

$$a_0 \equiv \frac{v_{osc}}{c} = \frac{eE}{m_e \omega_L c}. \tag{2.26}$$

A convenient numerical formula for estimating a_0 is given by [69]

$$a_0 = 0.85 \left(\frac{I\lambda^2[\mu\mathrm{m}^2]}{10^{18}[\mathrm{W\ cm}^{-2}]} \right)^{1/2}. \tag{2.27}$$

For the typical conditions of laser filamentation in air with a Ti:sapphire laser ($\lambda = 0.8\ \mu$m) and the clamped intensity of approximately 10^{14}W/cm^2, $a_0 \simeq 0.007$. The electron motion in the laser field during filamentation of near-infrared laser pulses in air is not relativistic.

While the magnetic field of the laser pulse does not contribute to the electron motion to first order, that does not mean it is entirely negligible. By its nature, the laser pulse has intensity gradients, and the variation means that the motion of the electron does not average to zero over multiple cycles of the field. The magnetic component of the Lorentz force while small, pushes the electron slightly along the direction of laser propagation within a single cycle of the field. Since the amplitude of the next laser cycle is different, the longitudinal motion does not average to zero. This second order drift motion is called the ponderomotive force, and it results in the expulsion of electrons from high intensity regions of the laser pulse. For non-relativistic electron motion, the ponderomotive force is equal to

$$\mathbf{F}_p = -\frac{e^2}{4m_e\omega_L^2} \nabla \langle E^2 \rangle, \tag{2.28}$$

where the angle brackets indicate time averaging over the laser field cycle [70]. Because $\mathbf{F}_p$ has the form of a conservative force: $\mathbf{F}_p = -\nabla U_p$ it is also often discussed

in terms of the ponderomotive potential,

$$U_p = \frac{e^2\langle E^2\rangle}{4m_e\omega_L^2}. \tag{2.29}$$

An electron in a pre-formed collisionless plasma cannot gain energy from the electric component of the laser field [71] because its transverse displacement during the positive and negative half-cycles cancels. However, if the electron is ionized from an air molecule in the peak of the pulse, it will retain residual kinetic energy after the pulse is gone [72], and the energy in principle can be transferred to the plasma through collisions. This interaction precipitates the formation of currents in the filament plasma [73]. However whether or not it is directly responsible for the microwave radiation is unknown. The possibility must be considered that additional interactions occur later in the filament plasma lifetime that drive the microwave emission.

2.3 Ionization of Gases in Strong Optical Fields

The primary ionization mechanism that causes plasmas to form in intense ultrashort laser fields results from its distortion of the atomic potential that holds electrons in bound states [74]. The laser pulse durations are generally too short for collisional ionization to occur in the laser field. The photon energies of the lasers used in the dissertation ($\hbar\omega_L = 1.55$ eV for $\lambda = 800$ nm, and $\hbar\omega_L = 0.32$ eV for $\lambda = 3.9$ μm) are far too low for ionization of gas atoms to occur by the photoelectric effect, that is ionization due to absorption of a single photon. For example, the ionization potential of nitrogen is 14.53 eV, and for oxygen it is 13.61 eV [75]. The energy equal to that of several laser photons must be absorbed in order to get an ionization event. The cross section for the simultaneous absorption of multiple photons is small, but it is the dominant ionization mechanism in intense laser fields [76].

The rate at which ionization occurs depends upon whether or not the distortion of the atomic potential can be considered constant or time varying when the ionization event takes place. This results in two limits for strong field ionization. When the distortion may be considered constant, the electron wavefunction can be treated as tunneling through the diminished potential barrier into a free state. On the other hand, when the distortion is time varying, the electron is treated as though it is excited through multiple virtual transitions spaced by the laser photon energy until its energy exceeds that of the binding potential. The theoretical description of the two limits of multiphoton ionization was first given by Keldysh [77], who defined the parameter, γ, which determines which picture is appropriate for determining the ionization rate. The Keldysh parameter is defined as

$$\gamma \equiv \sqrt{\frac{U_{iz}}{2U_p}}, \tag{2.30}$$

where U_{iz} is the ionization potential, and U_p is the ponderomotive potential. The limit $\gamma < 1$ corresponds to tunneling ionization, while $\gamma > 1$ means that the non-adiabatic multiphoton absorption picture must be used. In both cases, the ionization rate increases with ω_L [74] for fixed laser intensity. For the laser filaments in air at $\lambda = 800$ nm, $\gamma \sim 1$ so neither limit is dominant. Recently, a theory was developed that in principle bridges the two limits to give ionization rates even if $\gamma \sim 1$ [78].

2.4 Constraints on the Microwave Generation Mechanism in the Filament Plasma

Two basic measurements of the microwaves can be used to place some constraints on the nature of the current source in the filament plasma that causes the radiation. The first is a relative angular emission pattern, shown in Figure 2.1. The data points correspond to the peak-to-peak voltage of the microwave waveform recorded with an

antenna whose frequency range is 2-18 GHz. The voltage is measured as the antenna translates around the plasma at a constant radial distance. Pulses from a Ti:sapphire laser having a peak power on the order of 1 TW are focused at $f/60$ with a 3 meter focal length concave mirror to generate the filaments.

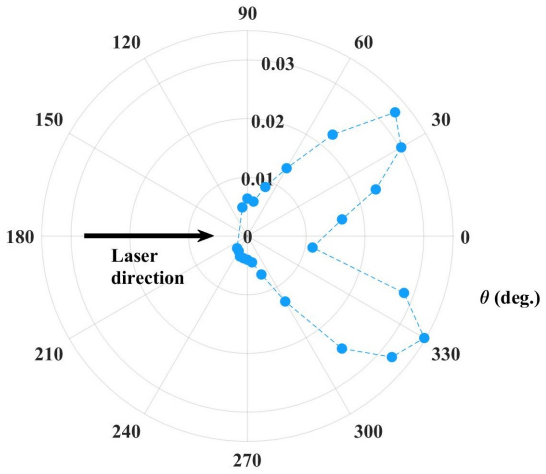

Figure 2.1: Typical microwave angular emission pattern from the filament plasma.

The microwaves radiate in a forward directed cone. This emission pattern is qualitatively similar to that of Cherenkov radiation [79], however Section 2.2 shows that the laser is not intense enough to generate highly relativistic electrons. It therefore must be an impulsive, longitudinally varying current due to a wave whose phase velocity is close to that of the laser pulse's group velocity as it traverses the plasma. This emission pattern is also qualitatively similar to that predicted by D'Amico *et al.* for THz radiation from filament plasmas [80]. In their paper, the model for the THz emission is compared to narrowband measurements centered at a frequency of about 100 GHz, which technically is in the microwave regime. The model is based on the apparent motion at the speed of light of unscreened space charge that forms in response to the ponderomotive force at the back of the filamenting laser pulse, even though there are no electrons in longitudinal relativistic motion. The experiments of Chapter IV show that the mechanism given by D'Amico *et al.* is likely not the source

of the microwaves, in spite of the similar predicted and measured emission patterns.

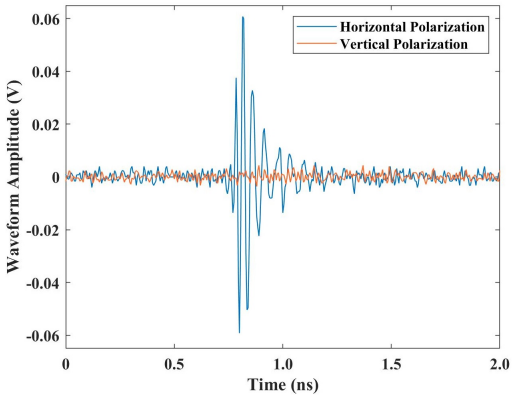

Figure 2.2: Microwave signal recorded when the antenna polarization axis is aligned to the polarization of the incident microwave electric field (blue curve) compared with when it is rotated 90° to the microwave electric field (orange curve).

The second measurement is of the polarization state of the microwave electric field. Figure 2.2 shows that the microwave radiation is linearly polarized in the plane formed by the laser propagation vector and its electric field polarization direction. The antennas that receive the microwaves are linearly polarized, and produced maximum signal when the polarization of the incident electric field aligns with the polarization axis defined by its structure. Rotating this polarization axis by 90° results in zero measured signal. However, if the measurement is repeated in the plane perpendicular to the laser electric field polarization, the horizontal polarization of the microwave field is now vertical. In this antenna position, the horizontal orientation of the antenna polarization axis produces no signal. This means that the microwave field is radially polarized. In a cylindrical coordinate system, the radial polarization of the radiated microwave electric field corresponds to an azimuthal magnetic field. The polarization of the radiated fields requires that the current flows longitudinally along the filament plasma.

Figures 2.1 and 2.2 show that any mechanism proposed to explain the microwave radiation must:

- Arise from the generation of a current in the plasma along the filament axis.
- Cause radiation because the current varies parallel to the direction in which it flows.

CHAPTER III

Measurement Methods

3.1 Introduction

This Chapter explains the principles and details of the measurements of the radiated microwave field, especially its absolutely calibrated frequency spectrum. Measuring the radiated field is desirable for diagnostic purposes because the technique causes no perturbation to the plasma. Calibrating the frequency spectrum is not simple, but it enables a practical and powerful tool for improving the understanding of filament plasmas, and possibly other types of laser-produced plasmas as well. To see why, consider the inhomogeneous wave equation for the electric field,

$$\nabla^2 \mathbf{E} - \frac{1}{c^2}\frac{\partial^2 \mathbf{E}}{\partial t^2} = \mu_0 \frac{\partial \mathbf{J}}{\partial t}, \tag{3.1}$$

and suppose that the electric field and current density have the Fourier integral representations

$$\left.\begin{aligned} \mathbf{E}(\mathbf{x},t) &= \frac{1}{2\pi}\int_{-\infty}^{\infty} \mathbf{E}(\mathbf{x},\omega)e^{-i\omega t}d\omega \\ \mathbf{J}(\mathbf{x},t) &= \frac{1}{2\pi}\int_{-\infty}^{\infty} \mathbf{J}(\mathbf{x},\omega)e^{-i\omega t}d\omega \end{aligned}\right\}. \tag{3.2}$$

Using Equation 3.2 to rewrite Eq. 3.1 as the inhomogeneous Helmholtz equation gives

$$\left(\nabla^2 + \frac{\omega^2}{c^2}\right)\mathbf{E}(\mathbf{x},\omega) = -i\omega\mu_0 \mathbf{J}(\mathbf{x},\omega), \tag{3.3}$$

which has the following solution for the field outgoing from the current source assuming that it must decay to zero at infinity,

$$\mathbf{E}(\mathbf{x},\omega) = \frac{i\omega\mu_0}{4\pi}\int_V \mathbf{J}(\mathbf{x}_0,\omega)\frac{e^{i\frac{\omega}{c}|\mathbf{x}-\mathbf{x}_0|}}{|\mathbf{x}-\mathbf{x}_0|}d^3x_0. \tag{3.4}$$

In Equation 3.4, $\mathbf{x}$ is understood to be the location where the field is measured, $\mathbf{x}_0$ is the location where the field originated, and $|\mathbf{x}-\mathbf{x}_0|$ is the distance between them.

Equation 3.4 is a statement of the principle that underlies the experimental measurements presented in the rest of the dissertation. The frequency content of the radiated fields, that is the actual function of ω that gives $\mathbf{E}(\mathbf{x},\omega)$, is determined by the frequency content of the current in the plasma, $\mathbf{J}(\mathbf{x}_0,\omega)$. If the dominant contributions to $\mathbf{J}(\mathbf{x}_0,\omega)$ can be predicted from an equation of motion for the plasma written in the frequency domain, then they can be experimentally tested by measuring the spectrum of the field that the plasma radiates. The microwave measurements are primarily a spectroscopic diagnostic of the plasma currents.

There is not an accepted experimental technique for spectroscopy of nanosecond duration broadband microwave pulses with nearly two decade bandwidth, so a method was developed in order to accomplish it. The method is to directly digitize the waveform of the fields incident at the aperture of an antenna that is connected by high-frequency coaxial cable to a fast oscilloscope, and to absolutely calibrate the components so that it can be compared directly to spectra acquired with other antennas operating in adjacent frequency ranges. Because this is an unusual diagnostic in the field of laser plasma physics, the details needed to replicate the measurements are presented in this Chapter. The components that make up the microwave receivers (antenna, cable, and oscilloscope) each have finite operating frequency ranges. However, achieving the largest possible bandwidth (range of ω) in the microwave measurements is important for 3 reasons:

- The currents driven in the plasma are impulsive in nature, therefore the bandwidth of the radiation is large.

- The center frequency of the spectrum depends at least in part on the plasma length and the angle of emission relative to the laser axis, so it is necessary to be able to measure at frequencies as low and as high as possible.

- In order to make preliminary, non-rigorous comparisons to THz measurements, the maximum frequency of the measurement should approach the THz range as much as possible, as it is usually difficult to make accurate direct comparisons between different techniques for measuring fields in disparate frequency regimes (e.g. a microwave receiver versus a THz Fourier transform spectrometer).

The total frequency range of the measurements is 70 GHz, which is extremely large for this technique. For comparison, the operating bandwidth of common oscilloscopes is presently around 500 MHz. Microwave antennas operate in frequency bands of usually 10-20 GHz centered at a wavelength that is determined by the antenna's physical dimensions. Coverage of the whole 70 GHz frequency range is provided by four antennas that operate in adjacent frequency ranges. The response of each antenna, cable, and the oscilloscope itself are compensated to permit direct comparison of the microwaves measured over the entire frequency range. The method is described conceptually in Section 3.2, with emphasis on the reasoning for proceeding with this particular approach as opposed to other possibilities. The details of the antennas used in the measurements are in Section 3.3, while use of the reference sources for calibrating the receivers is described in Section 3.4. The antenna response is measured separately from the cable and oscilloscope response, so the receiver calibration consists of these two components. The procedure for using the measured waveforms to calculate the electric field frequency spectrum at the antenna aperture is presented in Section 3.5. It is important to delve deeply into the details of the measurement

method because it is absolutely calibrated, and because this particular technique is not a well established plasma diagnostic.

3.2 Microwave Signal Acquisition

3.2.1 Microwave Time Domain Spectroscopy

There are many methods and types of measurements for characterizing electromagnetic waves that are guided or propagating in free space. Figure 3.1 describes the general classes of these measurements. It is possible to make measurements directly in the time or frequency domains, and the method in either case can further be categorized as coherent or incoherent in nature. Coherent detection means that the signal produced by the detector depends on the phase of the incident waves in some way. An incoherent method is indifferent to the phase of the incident waves. For example, the detector in a grating spectrometer is usually a spatially segmented energy sensor, whose response to electromagnetic waves destroys the information about their phase. These categories are not rigid, and many techniques can combine aspects from multiple areas. All four classes of measurements can be practically implemented in the microwave frequency regime.

The method developed to accomplish the experiments results from considering the frequency range of interest, the short duration of the microwave pulses, and the time jitter inherent to signal acquisition. The setup used to detect and digitize the microwaves is shown in Figure 3.2. It is a coherent detector because the signal depends on both the amplitude and phase of the incident waves. For a continuous, real-valued signal $v(t)$, the Fourier transform may be written

$$v(t) = \int_0^\infty 2V(f)e^{-i[2\pi ft+\phi(f)]}\, df, \tag{3.5}$$

where the frequency in Hz is $f = \omega/2\pi$. $V(f)$ is the positive, real-valued amplitude of

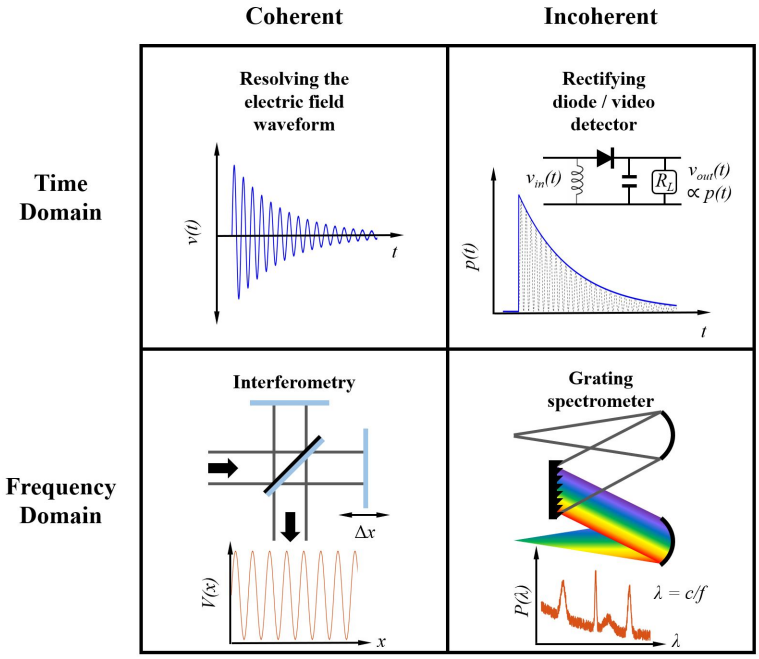

Figure 3.1: Each of the four panels in the figure gives an example of a general method or specific technique for each type of measurement. The method employed in the thesis is a type of coherent, time domain detection.

the Fourier transform, while $\phi(f)$ is its phase. An important property of Equation 3.5 is that $V(f)$ and $\phi(f)$ are independent, but together they uniquely determine $v(t)$. The oscilloscope measures a voltage $v_m(t)$ that depends on the distance between the

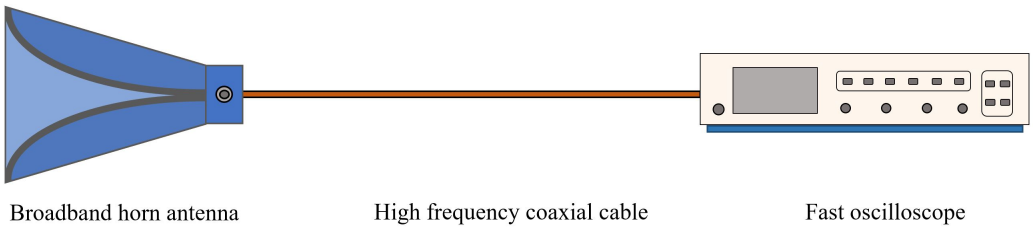

Figure 3.2: Microwave receiver used to record time domain waveforms of the radiated microwave fields.

plasma and antenna aperture, the antenna gain and dispersion, the cable losses and dispersion, and the oscilloscope frequency response. The frequency response is essentially frequency-dependent loss, but better reflects the fact that the oscilloscope has a small nonuniform response (including small amounts of gain) to signals at different

frequencies up to its operating bandwidth. The frequencies are high enough that details that would be trivial under other circumstances become critical to successful implementation of the receiver. The losses due to any microwave adapters and connectors in line with the cable or antenna are assumed to be negligible, although they are often included in the calibration measurements. The spectrum of $v_m(t)$ is calculated using a discrete Fourier transform (DFT) to approximate $V_m(f)$, but the phase of $v_m(t)$ is neglected. This is time domain spectroscopy, which is a type of Fourier transform spectroscopy. The interferometer in Figure 3.1 represents the other type of Fourier transform spectroscopy.

The decision to neglect the phase is significant, because $\phi(f)$ contains useful information about the source of the microwaves in the plasma. For example, the magnitude of the phase delay between frequency components would in part depend on dispersion in the plasma. If the plasma dispersion could be discriminated from other sources of dispersion in the signal, then it could be directly compared to a dispersion relation for possible normal modes of the plasma that would definitively determine the source of the microwaves. Unfortunately, extracting the plasma contribution from the total signal dispersion with sufficient accuracy is difficult in practice for a single receiver. Absolute dispersion compensation of multiple receivers is even more exacting. At the frequencies of interest, the acceptable uncertainty for such a dispersion measurement would be on the order of 10 ps (or $\sim \pi/5$ at 10 GHz), which corresponds to a free space propagation distance of 3 mm. Among other difficulties, this would require the distance between the plasma and the antenna aperture to be always known within a few millimeter tolerance in order for a multi-receiver dispersion measurement to be reliable. It is much more simple to instead neglect $\phi(f)$, measure and compensate the frequency response of different antennas and cables, then measure $V_m(f)$ and calculate the electric field amplitude incident on the antenna aperture.

There are important reasons to measure $v_m(t)$ in this situation instead of directly

measuring $V_m(f)$. The initial approach for the microwave spectral measurements up to 40 GHz resulted in the construction of a heterodyne receiver, but it was abandoned in favor of direct digitization of the microwave waveform. Heterodyning is one of the few methods available to make measurements in the 100-500 GHz frequency range, which is why it was pursued earlier during the dissertation research. It uses a microwave mixer that multiplies the input signal with that from a tunable oscillator. The power of the resulting beat wave is measured after a final bandpass filter. The idea is to generate the beat wave in a frequency band where microwave circuit components are very mature, robust, and low-cost even if the frequency of the microwaves being measured is much higher. This avoids having to construct the receiver entirely from components that would be expensive and have high loss, which can become prohibitive once the microwave frequency exceeds 40 GHz.

Heterodyne receivers do not tolerate time jitter in the signal well because the output amplitude depends on the instantaneous relative phase of the input and the oscillator. Pulsed signals always experience jitter due to multiple sources (such as random electronic jitter in the oscilloscope or laser oscillator clock, or deterministic jitter due to timing mismatch between the heterodyne receiver and the laser trigger) so one must consider the acceptable amount of jitter when using a heterodyne receiver in this manner. A further complication arises if the oscillator is not phase locked to the generation of the laser pulses. The plasma might be generated at any phase of the oscillator cycle. Using a fast oscilloscope to resolve the electric field waveform avoids these difficulties, which is why it is the preferred approach for the experiments. Appendix B is dedicated to describing the principles and details of heterodyne receivers, as they remain potentially important for future experiments in the submillimeter frequency range.

There are other potentially less costly ways to achieve similar results as the receiver of Figure 3.2. For example, one could use a series of bandpass filters set before

the input of a broadband rectifying diode detector (i.e. upper right panel of Figure 3.1) to measure power in a narrow spectrum as a function of time, and build up a spectrum by using many bandpass filters of similar bandwidth centered at adjacent frequencies. The issue with such a receiver is that its frequency resolution is inversely proportional to its throughput. Heterodyne receivers also have this problem, but it can be ameliorated by increasing the oscillator power. Narrowly filtering the microwaves results in a poor signal to noise ratio (SNR). This is why Fourier transform spectroscopy is used with pulsed signals: it can decouple resolution and throughput.

The direct digitization method was chosen and developed into an absolutely calibrated diagnostic with an awareness of the breadth of microwave measurement techniques. Our implementation of time domain spectroscopy in which the each receiver is absolutely calibrated is unusual for microwave detection in part because it is applied to short microwave pulses, where the pulse duration and the period of the carrier frequencies become comparable. Calibrating the frequency response of a single receiver with a reference standard is a common practice in microwave detection, although it is usually performed in the context of purely frequency domain techniques and CW signals. Calibrating across multiple receivers and concatenating the individual signals into a single spectrum is not common, and assumes a highly repeatable waveform. As Chapters IV to VI show, this assumption is permissible for these experiments. Together, the receiver and its calibration procedure are a novel contribution to experimental physics in general, and laser plasma physics in particular.

3.2.2 Existence of Microwave Emission

Having considered the best way to measure the microwaves in this context, it is important to establish that the observed signal is real, and not an artifact caused by another electromagnetic transient associated with the filament plasma. Specifically, we want to be sure that the signal we measure is not actually the THz emission. In

principle it is possible for the microwave receiver to register a signal due to aliasing by the oscilloscope (see Section 3.2.3), or resonance of the antenna or coaxial cable.

Section 3.2.4 describes the capabilities of modern high performance oscilloscopes, one of which is near immunity to aliasing. Digital filtering provides a sharp cutoff of its frequency response. Forcing the scope to respond at frequencies above the cutoff would require such a large signal amplitude that it would damage the acquisition circuit board before any significant aliasing could occur.

The coaxial cables strongly attenuate high frequency components due to ohmic and dielectric losses before they reach the oscilloscope. In this sense they effectively act as low pass filters to frequency components above their rated maximum frequency. Even if in principle the cable could transport a THz pulse, it would excite higher order modes of the coaxial geometry that would constructively and destructively interfere along the cable length, producing noise at its output. If the pulse caused the cable to resonate, it would not appear within the frequency range of interest. The resonant frequency of the cable is determined by the LC time constant even with significant losses. The capacitance and inductance per unit length for the coaxial geometry are given by

$$\begin{aligned} C &= \frac{2\pi\epsilon}{\log\frac{D}{d}}, \\ L &= \frac{\mu}{2\pi}\log\frac{D}{d}, \end{aligned} \tag{3.6}$$

where $\epsilon = \epsilon_0\epsilon_R$ and $\mu = \mu_0\mu_R$ are the permittivity and permeability of the dielectric between the center and outer conductors, respectively. D is the inner diameter of the outer conductor, d is the outer diameter of the inner conductor, and $\log(x)$ is the natural logarithm. PTFE (the plastic commonly known as Teflon) is usually the dielectric that separates the inner and outer conductors inside the cable. It has $\epsilon_R = 2.1$ and $\mu_R = 1$. A section of coax with length l will have the resonant frequency

$$f_{coax} = \frac{1}{2\pi l\sqrt{LC}} = \frac{1}{2\pi l\sqrt{\mu\epsilon}} \sim \frac{33\text{ MHz}}{l\text{ [meters]}}. \tag{3.7}$$

Any practical length of cable would resonate at a frequency far below the microwave regime, and therefore is not of concern. The spectra in the 2-70 GHz frequency range presented in the experimental results therefore cannot be mistaken for cable resonance. Equations 3.6 and 3.7 show that an ideal coaxial cable is dispersionless as there is no explicit frequency dependence. At the frequencies of interest, the loss in the cables cannot be neglected, and therefore dispersion is significant. The lossy nature of the cable does not strongly affect its resonant frequency, however it is necessary to compensate the cable losses in the analysis of the microwave spectra. Section 3.4.2 presents the theory of lossy coaxial transmission lines alongside simulation data that demonstrate frequency dependent signal attenuation in the cables.

While a coaxial cable operates from DC to a maximum frequency, horn antennas have a lower cutoff that is determined by their physical dimensions, and theoretically no upper frequency limit, overmoded response notwithstanding. In reality ohmic losses will attenuate high frequency currents induced in the antenna structure. While some types of antennas rely on resonance with the driving voltage source (e.g. dipoles) wide band horn antennas are not resonant over their operating frequency band, and therefore have a complicated phase response to incident radiation. They are linear however, and cannot generate frequency content that is not present in the electric field that they receive. Section 3.3 describes their properties in greater detail.

3.2.3 Digitizing Analog Signals

The microwave waveforms are recorded as digital signals, and are processed using discretized versions of the continuous operations, namely a fast Fourier transform (FFT) algorithm. It is a computationally efficient technique for calculating a DFT, although FFT and DFT are often used as interchangeable terms because of how common FFTs are in data analysis. A DFT is meant to be applied to a digital signal of finite length that is sampled uniformly in time. Discretizing continuous time into a

sequence of N uniformly spaced samples such that $t \rightarrow t_n = n\Delta\tau$ and $v(t) \rightarrow v_n(t_n)$ for $n = 0, 1, ..., N-1$, where $\Delta\tau$ is the sampling interval, allows the digital signal v_n to be constructed

$$v_n = \frac{1}{N} \sum_{k=0}^{N-1} V_k e^{-i[2\pi kn/N + \phi_k]}. \tag{3.8}$$

Equation 3.8 is the inverse DFT of the sequence V_k, and it is stated this way in order to make a direct comparison to Equation 3.5. If the DFT takes in a sequence of N real values for v_n, then it returns a sequence of N complex numbers $V_k e^{-i\phi_k}$, just like the continuous Fourier transform. However, there is an important difference between $V(f)$ and V_k that is often overlooked in discussions of digital signal processing: *they have different units*. $V(f)$ has units of [signal/time] and therefore is a distribution in the mathematical sense, whereas V_k have the same units as the signal $v(t)$, and are related to the coefficients in a Fourier series. Throughout the dissertation, the term 'spectrum' has often been applied to both continuous and discrete cases, although the technically accurate term for the former is 'spectral density'. The distinction is neglected within the text because the discrete case is much more significant.

Usually in experimental spectroscopy, this subtlety is unimportant. The relative amplitudes within the spectrum will be the same whether or not it is accounted for. However, since we are reporting results in terms of an absolute quantity, specifically V/m – the electric field incident at the antenna aperture – not accounting for this difference can result in a multiplicative error equal to $\sqrt{N\Delta\tau}$. This is one of a few nuances of the calibrations that are described in Sections 3.4-3.5. Otherwise, the rigorous discrete mathematics of digital signal processing is taken for granted as its details are beyond the scope of the data analysis in the dissertation.

Since one of the goals of the experiments is to measure the microwave spectrum up to the highest frequency possible, a requirement of the oscilloscopes is that they sample the microwave waveform at extreme rates. The fundamental limitation of approximating an analog signal with a digital one is the rate at which samples are

recorded in time. The Nyquist theorem sets a threshold for the highest frequency of an analog signal that can be resolved in a digitized approximation. For a given sampling rate $f_s = 1/\Delta\tau$, the maximum, or Nyquist frequency is

$$f_{max} = \frac{f_s}{2}. \tag{3.9}$$

Signal content at the Nyquist frequency is said to be critically sampled. If one were to plot a time trace of a digital signal that is critically sampled, it will not look smooth and continuous, but it at least would appear at the correct frequency after a DFT operation. It is best practice to oversample a signal - sampling faster than necessary to correctly measure the frequency content of a signal. Trouble comes from undersampling a signal. If the frequency content of a signal oscillates faster than $f_s/2$, then the digitizer will capture instances of its phase from distinct (and possibly distantly spaced) half-cycles. The spectrum of an undersampled signal will have a non-zero amplitude, but it will not correspond to the frequency content of the analog input. Undersampled frequency content at $f_{us} > f_s/2$ is aliased to a frequency equal to $f_{alias} = |f_{us} - Mf_s|$, (where M is an integer that gives a value of $f_{alias} < f_s/2$) and is indistinguishable from real content at f_{alias}.

Aliasing is avoided either by knowing beforehand that all the frequency content in a signal is less than $f_s/2$, or by using a low pass filter to block anything above the Nyquist frequency. In the context of the filament plasma radiation, we do not know the upper limit of the microwave frequency content, and it is entirely possible if not likely that it extends continuously through the THz regime. This means that the microwave receiver must impose a low pass filter on the radiation to avoid aliasing. While the antennas and cables tend to attenuate signal at frequencies that could cause aliasing on the oscilloscopes, the oscilloscopes themselves are engineered to prevent it.

3.2.4 High Performance Oscilloscopes

The experiments rely on two high performance oscilloscopes to digitize microwave waveforms: an Agilent DSOX91304A, and a Tektronix DPO77002SX. The analog-to-digital converters (ADCs) in both scopes have 8-bit resolution. The Agilent scope has a maximum sampling rate of 80 GS/s, and real time bandwidth of 13 GHz, while the Tektronix scope can sample at up to 200 GS/s with a real time bandwidth of 70 GHz. This is required to digitize the frequency content of a pulse in a single shot. They are real time oscilloscopes and not sampling oscilloscopes which require many cycles of a repetitive signal in order to resolve a waveform in equivalent time.

Even a fast flash ADC cannot acquire samples every 12.5 ps or 5 ps. What makes these oscilloscopes 'high performance' is that they use many ADCs that work in concert to achieve very high sampling rates. The technique for using many ADCs together for this purpose is called interleaving, and it requires different hardware and software than what might be seen in a conventional oscilloscope. Figure 3.3 illustrates an example how the staggered timing of four ADCs can be used to sample an input analog signal. After each of the ADC channels samples and converts a different

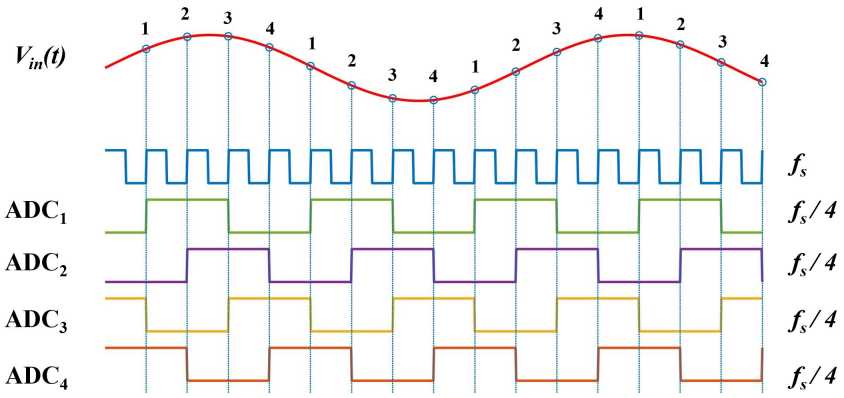

Figure 3.3: Conceptual timing diagram for the sampling behavior of four time interleaved ADCs. It is common for each ADC to sample on the rising edge of its clock as in the figure, but other schemes are possible. The net sampling rate is f_s even though the sampling rate of each individual ADC channel is $f_s/4$.

instant of the input, a de-multiplexer reconstructs the digitized signal by sequencing the samples in the correct order.

In order for the interleaved ADCs produce a high fidelity digitization of the input, it is critical for all of the individual ADC channels to behave exactly the same. Any differences, for example, gain mismatch or relative timing errors, will produce amplitude and phase distortions of the input that appear in the spectrum of the digitized output as artifacts called interleaving spurs whose amplitude is proportional to that of the input signal and the magnitude of the mismatch. Figure 3.4 shows examples of the interleaving spurs in the spectra generated by the oscilloscopes used in the experiments. These are acquired simply by digitizing the noise internal to the scopes. They are compared to a conventional scope that has 500 MHz bandwidth at 2.5 GS/s and does not use a highly interleaved ADC architecture. In reality, small

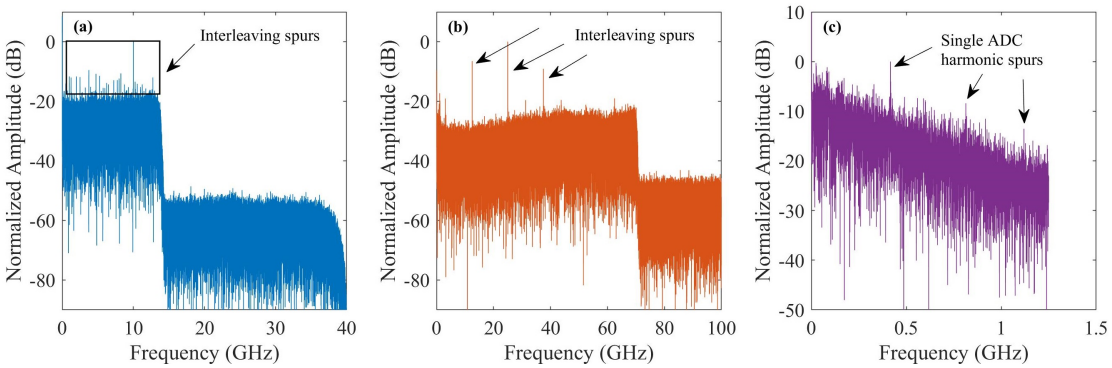

Figure 3.4: Internal noise spectrum of the (a) Agilent DSOX91304A, (b) Tektronix DPO77002SX, and (c) Tektronix DPO3054. The high performance oscilloscopes have several interleaving spurs, while the conventional scope has a few small spurs that are harmonics caused by the small nonlinearity inherent to any ADC. The high performance scopes also exhibit brick wall filtering at their respective maximum rated frequencies.

differences between channels are unavoidable, but there are strategies for mitigating them (interested readers are referred to [81, 82]). Although the designs used in the Agilent and Tektronix scopes are not publicly available, the distortion that would have the greatest effect on the measurements is the total system phase noise, which increases with frequency. Phase noise is the frequency domain manifestation of time

jitter. For the Agilent scope at its frequency limit of 13 GHz, the integrated phase noise [83] is about -29 dB, or 0.13%. Similarly, the Tektronix scope at its frequency limit of 70 GHz has an integrated phase noise is about -23 dB, or 0.50%. All other sources of distortion are smaller, or are compensated by the calibration procedure described in Sections 3.4 and 3.5.

Managing signal distortions due to interleaving in state-of-the-art systems relies heavily on digital post processing of the signal after the de-multiplexing step. Some refer to this as calibration and compensation of the ADC channel mismatching. These routines, which include digital filtering, are the enabling technology that permits oscilloscopes such as those used in the experiments to have such high net sampling rates while producing useful digitizations of high frequency analog signals. The specific capabilities of post processing algorithms are typically proprietary to each oscilloscope manufacturer. In order to maintain signal fidelity, the post processing degrades the real time bandwidth of the oscilloscope to some value near, but below the Nyquist frequency that corresponds to the sampling rate. This is why, for example, the Tektronix DPO77002SX is rated for 70 GHz instead of 100 GHz.

This filtering is clearly demonstrated in Figures 3.4(a)-(b) in contrast to the behavior exhibited in Figure 3.4(c). The slow roll off of the conventional oscilloscope's noise spectrum implies that its response above its Nyquist frequency (1.25 GHz) is only about -10 dB down from its response below 500 MHz, and therefore may exhibit significant aliasing. The high performance scopes have sharp cutoffs in their frequency responses which occur at 13 GHz and 70 GHz, respectively. The imposed cutoff is called a brick wall filter. It is an approximation of a sinc filter, which is the ideal low pass filter (i.e. perfect transmission below the cutoff, and perfect rejection above) [84]. The filtering implemented in the high performance oscilloscopes ensures that any frequency content that they register is always oversampled. They are functionally immune to aliasing.

High performance oscilloscopes are not ideal instruments since they can produce small artifacts due to interleaving, and do not have perfectly flat frequency response. However, the technology behind them has advanced enough to be able to directly digitize the microwave signals of interest with sufficiently high fidelity so that the amplitude and phase errors due to the scopes are negligible compared to other sources of uncertainty, and that the frequency content they record actually exists in the input signal.

3.3 Antenna Fundamentals

Antennas are used to convert between radiation propagating in free space, and guided waves transported in waveguide or transmission line. The filament plasma radiates microwaves into free space, and an antenna ensures predictable collection of the microwaves for the purposes of the measurements. This means that the antenna has known gain and polarization over a well defined range of frequencies. This is critical to correctly calculating the electric field amplitude based on the voltage transient digitized by the oscilloscope. This calculation, as shown in Equation 3.48 of Section 3.5 requires three measured quantities: the antenna gain, the combined cable and oscilloscope response, and the microwave voltage spectrum. The gain of each antenna and each combined cable and scope response are what make up the calibration, and need only be measured once. Then they can be used to compensate the microwave voltage spectra for the corresponding configuration of antenna, cable, and oscilloscope. This Section is dedicated to the first element – the essential properties of the antennas that must be understood in order to correctly find and use the antenna gain to calculate the incident microwave electric fields.

The detailed properties of antennas can be very complicated, and the use of horn antennas in the experiments is partially motivated by a desire to avoid placing undue focus on the antenna behavior, even though types of antennas exist that could cover

wider frequency bands than the four horn antennas used in the experiments [85]. Relative to other antenna types [86], horn antennas have well behaved gain, polarization, and directivity over a wide bandwidth. The significance of these properties, and the simplifying assumptions they enable are described in the subsequent sections.

3.3.1 Radiation Field Regions

An important assumption made in the calibration procedure is that the antenna is located in the far field of the microwave radiation. Under this approximation, the microwave fields can be considered to propagate as plane waves whose amplitude decays with $1/r$ (power like $1/r^2$), where r is the distance from their source. The complete picture of the fields generated by a radiation source is much more complex, but it can be demarcated into three regimes that depend on the distance from the source and the size of the source and receiver relative to the wavelength of radiation: the near field, a transition region (or Fresnel region), and the far field (or Fraunhofer region).

The fields produced by the motion of charges consist of a radiating term and a non-radiating one [87]. In the near field close to the element, the non-radiating part of the fields dominates. Because they do not propagate, the near fields are sometimes also called static fields. If they are measured experimentally, the radiating part cannot be distinguished from the non-radiating part. However the non-radiating fields decay with $1/r^3$, so if the fields are measured a bit farther away in the transition region, one can expect the non-radiating component to be insignificant. In the transition region the static fields might be gone, but the radiating waves still have significant curvature to their wavefronts. Techniques have been developed for microwaves to interpret radiation received in the Fresnel region [88], but they are inconvenient to use. One has to account for the difference in phase of the incident radiation between the part of a wave entering at the center and the edge of an antenna aperture [89].

This statement is equivalent to saying that the radiation cannot be approximated as TEM propagation. The longitudinal component of the electric field cannot be neglected in the transition region. If the signal is strong enough, it is ideal to work in the far field.

The problem at hand is essentially stated in Equation 3.4, except that it is more general to express the solution of the wave equation in terms of the vector potential

$$\mathbf{A}(\mathbf{x},\omega) = \frac{\mu_0}{4\pi}\int_V \mathbf{J}(\mathbf{x_0},\omega)\frac{e^{i\frac{\omega}{c}|\mathbf{x}-\mathbf{x_0}|}}{|\mathbf{x}-\mathbf{x_0}|}\,d^3x_0, \tag{3.10}$$

where $\mathbf{J}(\mathbf{x_0},\omega)$ is the current flowing in the antenna structure. The integral in x_0 is carried out over the dimensions of the source. Outside the radiation source,

$$\mathbf{B} = \nabla \times \mathbf{A} \tag{3.11}$$

$$\mathbf{E} = ic^2/\omega\ \nabla \times \mathbf{B}. \tag{3.12}$$

The difficulty of completely describing the fields created by the source arises from evaluating the integral in Equation 3.10 including the $|\mathbf{x}-\mathbf{x_0}|$ terms. An exact expression for the distance between the source and observation points is

$$|\mathbf{x}-\mathbf{x_0}| = \left[(r\sin\theta\cos\phi - x_0)^2 + (r\sin\theta\sin\phi - y_0)^2 + (r\cos\theta - z_0)^2\right]^{1/2}, \tag{3.13}$$

where spherical coordinates have been used to describe the observation point $\mathbf{x} = (x,y,z)$ and r is the distance from the origin to $\mathbf{x}$. Equation 3.13 shows that using the full expression for the distance makes Equation 3.10 inconvenient to solve analytically. The near, transition, and far field regions arise from different approximations for $|\mathbf{x}-\mathbf{x_0}|$ that simplify the solution. In free space, $k = 2\pi/\lambda = \omega/c$. Assuming a source size that is close to or more than λ, the near field condition is valid when $r \ll \lambda$, and the exponential in Equation 3.10 can be approximated as unity.

Table 3.1: Radiation Field Regions

Region	Field Dependence	Distance Condition
Near Field	$1/r^3$	$0 < r < 0.62\sqrt{\frac{D^3}{\lambda}}$
Transition (Fresnel)	$E_\perp \sim 1/r$, $E_\parallel \sim 1/r^2$	$0.62\sqrt{\frac{D^3}{\lambda}} < r < \frac{2D^2}{\lambda}$
Far Field (Fraunhofer)	$1/r$	$r > \frac{2D^2}{\lambda}$

The far field approximation is to take $r \gg \lambda$ so that the phase term in Equation 3.10 is

$$\exp\left(ik|\mathbf{x} - \mathbf{x_0}|\right) \approx \exp\left[ik(r - \hat{\mathbf{n}} \cdot \mathbf{x_0})\right], \tag{3.14}$$

where $\hat{\mathbf{n}} = \mathbf{x}/||\mathbf{x}||$ is a unit vector along $\mathbf{x}$. Further, the inverse distance dependence is approximated as $|\mathbf{x} - \mathbf{x_0}| \approx r$. This gives the vector potential under the far field approximation

$$\mathbf{A}(\mathbf{x}, \omega) = \frac{\mu_0}{4\pi} \frac{e^{ikr}}{r} \int_V \mathbf{J}(\mathbf{x_0}, \omega) e^{-ik\hat{\mathbf{n}} \cdot \mathbf{x_0}} \, d^3x_0. \tag{3.15}$$

Equation 3.15 is much easier to evaluate than Equation 3.10. In Equation 3.15, the vector potential consists of spherical waves that decrease in amplitude like $1/r$ away from the source.

It is generally permissible to approximate the near, transition, and far field regions occurring at $r \ll \lambda$, $r \sim \lambda$, and $r \gg \lambda$, respectively. Practitioners of antenna theory have determined the boundaries of the three field regions more rigorously based on the acceptable phase error incurred by the approximation in Equation 3.14. Nearly a century of designing and fielding antennas has led to an empirical value of phase error that is $\pi/8$ [90] that is sufficient for most applications. Table 3.1 lists the locations of the field regions based on wavelength, and the largest source dimension D assuming a maximum phase error of $\pi/8$. When considering a source (transmitter) and receiver, the appropriate value for the D is $D_{total} = D_{Tx} + D_{Rx}$. For the filament radiation, $D \sim L_{filament} + D_{horn}$.

For a few reasons, the experimental measurements did not strictly adhere to the requirements of the field region separation given in Table 3.1. Instead we tried to at all times follow a separation distance of $r > 10\lambda_{max}$ and $r > 10D_{horn}$. This is primarily because the length of the filament is variable between experiments, and difficult to measure accurately since the plasma extends beyond the region of visible fluorescence. Sometimes the limiting factor was available laboratory space, as in Chapters V and VI. However, a small deviation from the requirements of the far field will primarily affect the measured phases of the microwaves, which our results ultimately neglect. There is some flexibility with measuring in the far field because the microwaves are broadband, and the locations of the field regions will change significantly over the frequency range of interest.

The variability of the field regions with frequency is also the primary reason why the proper approach is to make far field measurements with a high-directivity antenna. Previous investigations have used a small wire near [51], electrodes placed around the filament [91, 92, 93], or propagated the filament through a waveguide [94, 95] to measure plasma conductivity and microwave emission. An assumption of these experiments is that the measurements are in the near field regime, and therefore that electrostatics and magnetostatics can be applied in analysis of the data. It is not true to say that this is universally a bad approximation for filaments. However, it has been common practice within the community to neglect the possibility that the measured signal might consist of components due to both the static and radiating fields, as the high frequency emission will transition to radiation about an order of magnitude closer to the filament than the low frequencies. This is a real concern in light of the aliasing issues described in Section 3.2.3. A diagnostic of the currents in the filament plasma using non-perturbative free space techniques is most accurately realized through far field measurements, not near field ones.

3.3.2 Horn Antennas

Horn antennas are one of the most simple and commonly used antenna types. The experiments make use of two sub-types of horn antennas. Figure 3.5 shows each of the horns used to make the measurements. In the U-band and V-band, pyramidal horns are used. They consist of flared waveguide, and are designed to operate within a single waveguide frequency band. Below 40 GHz, pyramidal horns are also used, however

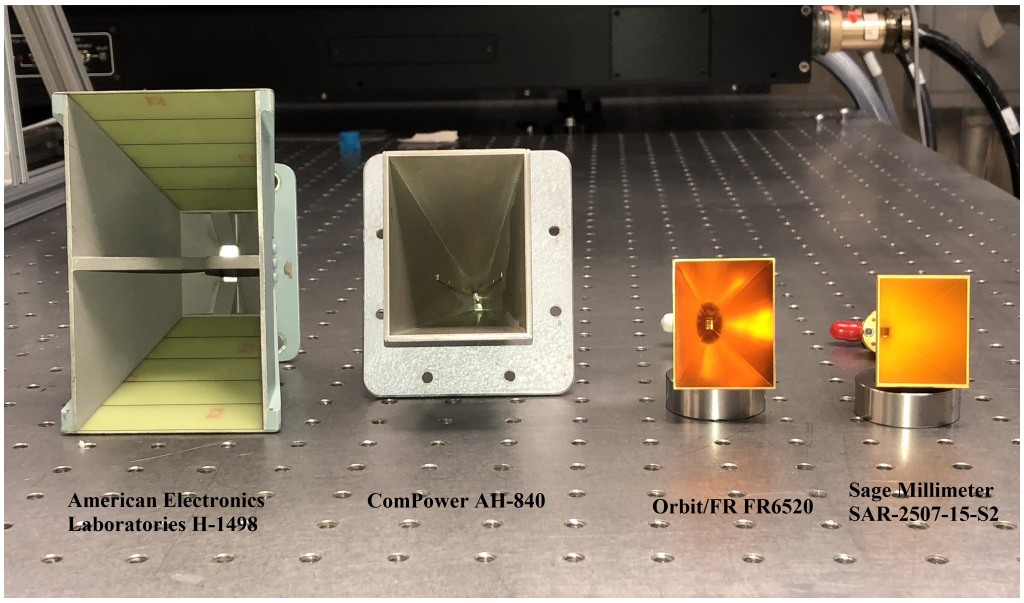

Figure 3.5: Antennas used in the experiments. From left to right: AEL H-1498 double ridge horn (2-18 GHz), ComPower double ridge horn (18-40 GHz), Orbit/FR FR6520 U-band pyramidal horn (40-60 GHz), and Sage Millimeter SAR-2507-15-S2 V-band pyramidal horn (50-70 GHz).

their structure is slightly more complicated than the flared rectangular waveguide. Their apertures contain a pair of fins that are exponentially tapered. Because of the additional structure, they are called double ridge horn antennas. The flat surfaces receive lower frequencies, while the higher frequencies interact with the exponential taper. Double ridge horns do not necessarily perform as well in many respects as other horn antennas [96], and are instead optimized to have a broadband frequency response, which is the goal in this context. The double ridge horns achieve nearly 40% bandwidth.

To better understand why horns were chosen, and also some of the assumptions involved in the calibrations it is important to define a few relevant antenna metrics. The fundamental property of all antennas is gain. While this is often stated in an antenna specification as a single number, it varies with angle of incidence and frequency. For a transmitter (and equivalently a receiver, due to reciprocity) it is the ratio of the intensity of radiated power per unit solid angle I_{rad} relative to that which would be obtained if the power input to the antenna were radiated isotropically. The latter is simply the input uniformly distributed over 4π steradians: $P_{input}/4\pi$. The gain then is given by

$$G(\theta, \phi, f) = 4\pi \frac{r^2 I_{rad}(\theta, \phi, f)}{P_{input}}. \tag{3.16}$$

Because it accounts for the relative difference between input and output power, the gain includes losses the antenna incurs in generating radiation, excluding impedance mismatch between the source and antenna. This is to say that the antenna radiation efficiency is part of the definition of gain. The variation of gain with angle is called an antenna pattern. In the context of the dissertation, the function $U(\theta, \phi, f) = r^2 I_{rad}(\theta, \phi, f)$ is the absolute antenna pattern, while a relative antenna pattern can be expressed by the ratio of the gain in a given direction to the maximum gain $g(\theta, \phi, f) = G(\theta, \phi, f)/G(f)_{max}$. U has units of W/sr, and is related to a quantity called directivity, which can be understood as how confined the antenna pattern is in a particular direction. Mathematically, it is just the gain less the radiation efficiency $D = G/\eta_{rad}$.

A high directivity antenna will radiate or receive along a narrow beam, while a low directivity antenna will approach an isotropic source. Figure 3.6 gives an example of a pattern for a pyramidal horn. It has high directivity because its gain is primarily along a single direction, which is called the main beam or main lobe. In practice, one can achieve a useful approximation of the horn pattern by setting $g(\theta) \sim (1 + \cos\theta)^2$. The pattern in Figure 3.6 shows that horns have side lobes. However, the they can be

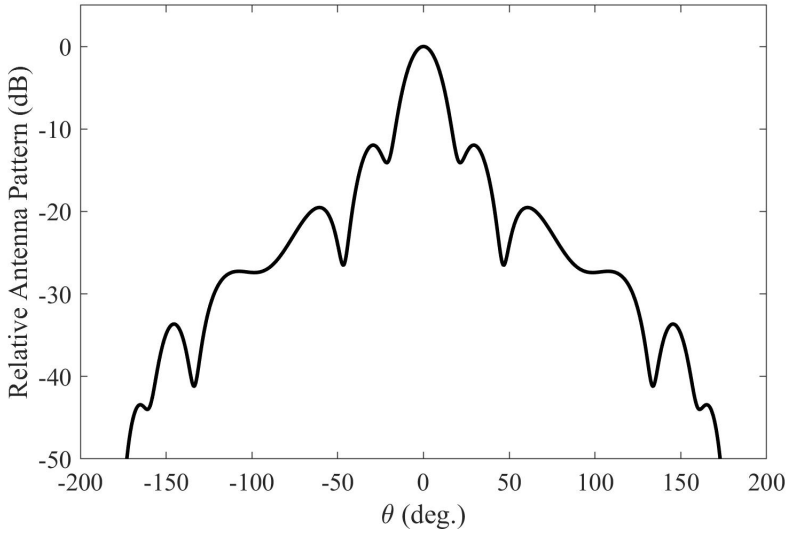

Figure 3.6: Analytical solution for the relative antenna pattern of a typical pyramidal horn antenna at a single frequency. It is valid for an azimuthal angle of $\phi = \pi/2$.

at least an order of magnitude less sensitive to microwaves incident along a side lobe relative to the main lobe, and therefore their contribution to measured signals can be neglected. This is an important characteristic of horns that greatly simplifies the calibration, and allows resolution of the radiation pattern due to the filament plasma. The directivity of a horn degrades as its bandwidth increases, meaning that the width of the main lobe grows. This issue does not seem to significantly affect our results, although it presents an opportunity for improvement of the measurements. A low directivity receiver will cause significant spatial smearing of a transmitter's measured radiation pattern. Strictly speaking, to measure an antenna pattern it is necessary to de-convolve the receiver's pattern from that of the transmitter. Experiments in which such calculations might be necessary are left as future work.

Another important antenna property is polarization, or the spatial orientation of the field vectors transmitted by an antenna. Horn antennas are linearly polarized, and have orthogonal E- and H-planes. The E-plane is defined by a vector normal to the antenna aperture, and the orientation of the electric field vector in the TE_{01}

mode at the aperture. Similarly, the H-plane contains the magnetic field vector and the direction of the antenna pattern maximum. In Figure 3.5, the E-plane is along the horizontal direction of the antennas. If the electric field of incoming microwaves is not aligned to the E-plane, then the amplitude of the signal will be reduced by $|\hat{\mathbf{e}}_{E-plane} \cdot \hat{\mathbf{e}}_{inc}|$, which is equal to the cosine is of the angle between the E-plane and the incident electric field vector. Horn antennas are their own linear polarizers. We have taken advantage of this property in Figure 2.2 to verify that the radiation from the filaments is radially polarized.

3.3.3 Friis Transmission Equation

The preceding subsections largely defined concepts that inform how and why horn antennas are used in the microwave measurements. We now apply the concepts to the analysis used to calibrate the receivers. To measure antenna gain, it is necessary to know how to relate the power transmitted from one antenna to the portion of the power that another antenna receives. Figure 3.7 shows the general case for the transmitter and receiver arrangement. The receiver must be in the far field region. The Friis Transmission Equation allows the ratio of transmitted and received power

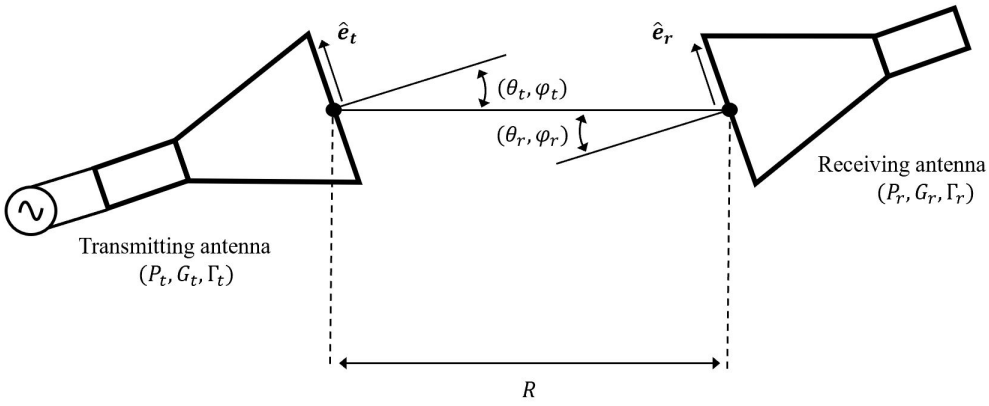

Figure 3.7: Diagram of the general orientation of horn antennas in a transmitter-receiver configuration. The microwave source feeds the transmitter. The angles $\theta_{r,t}$ and $\phi_{r,t}$ account for the degree to which they are aimed at each other. The unit vectors $\hat{\mathbf{e}}_{r,t}$ indicate the direction of each horn's E-plane.

to be calculated as a function of frequency according to

$$\frac{P_r}{P_t} = \left(1 - |\Gamma_r(f)|^2\right)\left(1 - |\Gamma_t(f)|^2\right)\left(\frac{c}{4\pi f R}\right)^2 G_r(\theta_r, \phi_r, f) G_t(\theta_t, \phi_t, f) |\hat{\mathbf{e}}_r \cdot \hat{\mathbf{e}}_t|^2, \quad (3.17)$$

where Γ_r and Γ_t are the voltage reflection coefficients due to impedance mismatch between the receiver and its load, and the transmitter and the microwave source. The transmitter and receiver apertures are separated by a distance $R \gg \lambda, > 2D^2/\lambda$. Loss due to antenna polarization mismatch is quantified by $|\hat{\mathbf{e}}_r \cdot \hat{\mathbf{e}}_t|^2$.

In our measurements of the antenna gain, the horns are mounted so that their E-planes are aligned, and the microwave source and the receiver load are matched to both antenna terminals with 50 Ω impedance over the measured frequency range. The antennas are oriented so that the main lobes are directed at each other for maximum reception. This reduces Equation 3.17 to

$$\frac{P_r}{P_t} = \left(\frac{c}{4\pi f R}\right)^2 G_r(f) G_t(f). \quad (3.18)$$

Equation 3.18 is the basis for calculating antenna gain using the two-antenna technique.

3.3.4 Horn Antenna Gain Curves Using the Two-Antenna Technique

A common method for measuring the gain of an antenna is the two-antenna technique [90]. It consists of directing the main lobes of the antennas at normal incidence to each other in the far field with matched polarization, and transmitting a signal of known frequency and power from one antenna, while receiving it at the other. The setup for the measurement is shown in Figure 3.8. In order to measure the absolute gain of an unknown antenna using Equation 3.18, either the transmitter or receiver must be a reference antenna with known gain. If there is no reference antenna, then the solution is to use two of the same antenna (manufacturer, model, and age) to es-

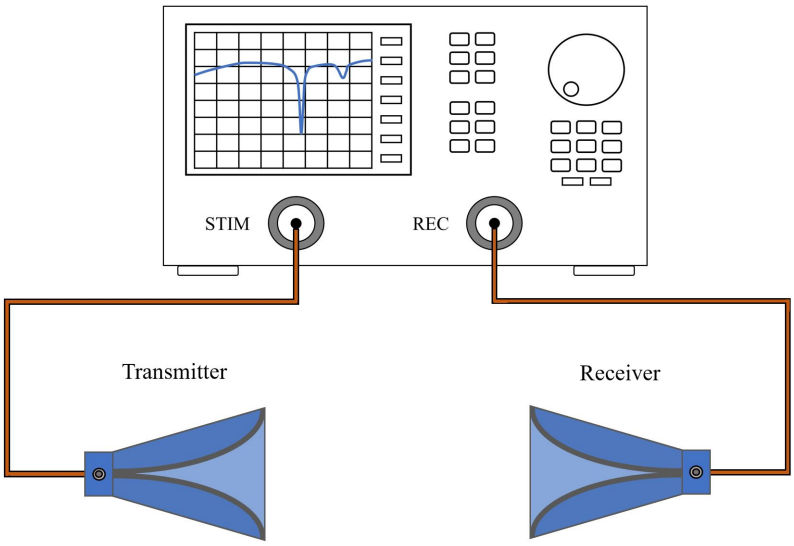

Figure 3.8: Setup for measuring antenna gain with the two-antenna technique. A VNA is used to measure the two-port scattering parameter S_{21} from which the gain is calculated.

tablish the reference, because $G_r = G_t$. For this reason, it is good practice to acquire antennas in pairs. For such a matched pair, Equation 3.18 becomes

$$\frac{P_r}{P_t} = \left(\frac{c}{4\pi f R}\right)^2 G^2(f). \tag{3.19}$$

A vector network analyzer (VNA) is used to accomplish the measurement. For gain measurements up to 40 GHz, a Rohde & Schwarz ZVA40 is used, while for the millimeter wave antennas in the U-band and V-band, an Agilent E8361A can measure up to 67 GHz. The VNA stimulate port produces microwaves at a known frequency, power, and phase. They are a high quality reference signal. The receive port is tuned to the frequency of the stimulate port. The power and phase of microwaves entering the receive port are compared to the reference, which allows the calculation of microwave network scattering parameters [97], which are complex numbers relating the amplitude and phase of forward and backward voltage waves in the network as seen at its ports. The antenna gain is related to the quantity S_{21} whose physical interpretation for a two-port network (single input, single output) is the transmission

coefficient of the voltage wave.

$$S_{21}[\text{linear}] \equiv \frac{V_{out}^{forward}}{V_{input}^{forward}} \tag{3.20}$$

$$S_{21}[\text{dB}] = 20\log_{10}\left(S_{21}[\text{linear}]\right) \tag{3.21}$$

It is common practice in microwave engineering to define quantities on a voltage basis with linear units, but report data on a power basis with a decibel scale. The VNA reports S_{21} as the ratio of power output by the stimulate port to that measured at the receive port on a decibel scale as in Equation 3.21, so it is related to P_r/P_t by

$$\frac{P_r}{P_t} = 10^{S_{21}[\text{dB}]/10}. \tag{3.22}$$

For passive, linear devices like antennas, measuring S_{21} at a single power level from the stimulate port is sufficient, as their scattering parameters are independent of power to a good approximation. This is not the case for other types of devices, such as amplifiers, whose scattering parameters will start to show signs of compression with sufficiently large signals. The VNA is also able to account for cable losses, so the absolute gain can be found for a matched pair using Equations 3.19 and 3.22 where

$$G(f)[\text{dB}] = 10\log_{10}\left[\left(\frac{4\pi Rf}{c}\right) \times 10^{S_{21}(f)[\text{dB}]/20}\right]. \tag{3.23}$$

For two different antennas operating in the same frequency range where the receiver gain is unknown, Equation 3.18 gives

$$G_r(f)[\text{dB}] = 10\log_{10}\left[\left(\frac{4\pi Rf}{c}\right)^2 \times 10^{(S_{21}(f)[\text{dB}]-G_t(f)[\text{dB}])/10}\right], \tag{3.24}$$

where the transmitter G_t is the reference. Figure 3.9 shows a comparison of the gain measured using the two antenna technique (Equation 3.19) to one of the reference

antennas used to make other gain measurements. The experimental measurement

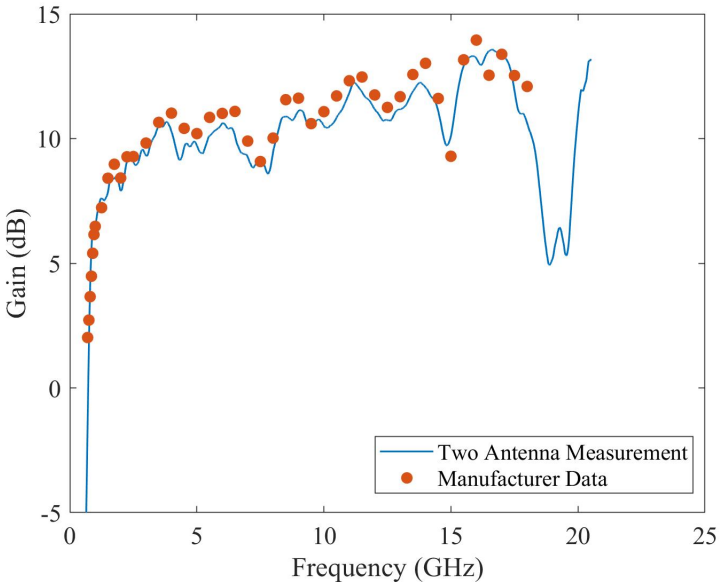

Figure 3.9: Comparison of the gain measurement performed with the two antenna technique (solid blue curve) for a reference antenna (ComPower AH-118) with the initial calibration gain data provided by the manufacturer for that particular antenna unit (orange dots). Its rated frequency range is 0.7-18 GHz, and the separation distance used in the measurement is $R = 1.6$ m.

matches the manufacturer data over its rated frequency range, so use of the two antenna technique is a valid and accurate procedure. The dip in gain near 20 GHz is indicative of overmoding, which is expected above an antenna's maximum frequency as the short wavelengths resonate with higher order modes of the antenna structure. This particular model of antenna was used to calibrate the AEL H-1498 antenna whose operating frequency range is 2-18 GHz.

Figure 3.10 shows the gain measured for the four antennas used in the experiments. The VNA frequency was swept below and above the rated ranges of the antennas where possible to show their limitations out of band. Figure 3.10(a),(b), and (d) show that the gain drops dramatically for low frequencies. If the free space microwave wavelength is large compared to the effective area of the antenna, it will behave as if the antenna is not present. Figure 3.10(c) shows that the U-band antenna starts

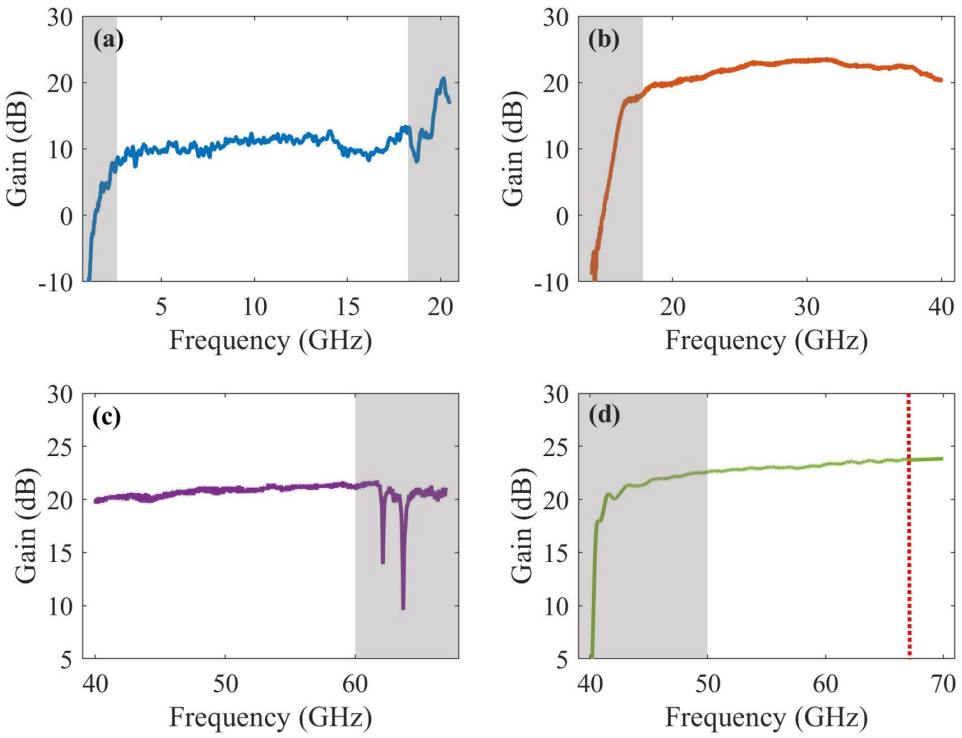

Figure 3.10: Gain curves measured by the two antenna technique for (a) AEL H-1498 (rated 2-18 GHz), (b) ComPower AH-840 (rated 18-40 GHz), (c) Orbit/FR FR6520 (rated for 40-60 GHz), and (d) Sage Millimeter SAR-2507-15-S2 (rated for 50-70 GHz with waveguide-to-coax adapter). Data falling within the shaded regions is not used in the calibration calculations. The red dotted vertical line at 67 GHz indicates the maximum frequency at which the Agilent VNA can measure. The gain from 67-70 GHz is a linear extrapolation.

to overmode just above its rated maximum frequency of 60 GHz. Only the in-band part of the antenna gain is used in the calibration calculations. Each antenna gain curve is truncated at the rated frequency limits, as indicated by the shaded regions in Figure 3.10.

The Agilent E8361A can only measure up to 67 GHz, so the highest 3 GHz of the V-band antenna gain are extrapolated from the measured data. The extrapolation is performed with the gain in linear, not decibel units using the data in the frequency range of 62-66 GHz. The extrapolated data have been converted back to a decibel

scale in Figure 3.10(d). In the range of 67-70 GHz, it is given by

$$G[\text{dB}](67\text{ GHz} < f \leq 70\text{ GHz}) = 10\log_{10}\left(\frac{2.21}{\text{GHz}} f[\text{GHz}] + 86.7\right). \tag{3.25}$$

For all of the antennas, what has been referred to as the 'antenna' thus far is actually an assembly of two components: the antenna structure itself, and a waveguide-to-coax adapter. For the three horns that function at or below 60 GHz, the adapter bandwidth matches or exceeds that of the antenna. In the V-band, the antenna is rated for 50-75 GHz, while the manufacturer only certifies the adapter to 70 GHz. This is a limitation of the coaxial connector assembly on the adapter output, which by design need only conform to the industry standard of 67 GHz for fundamental mode operation [98]. It is possible to slightly exceed the rated frequency, since it is common practice for manufacturers to include a small safety factor. Overmoding the coaxial assemblies above 67 GHz is discussed in Section 3.4.2, and the frequency limits of microwave design specifications are described in Appendix A. If the V-band waveguide-to-coax adapter were to overmode above 67 GHz, it would be obvious from the experimental data, as there would be significant narrowband dips or spikes of the voltage spectrum at the adapter's resonances due to interference with the fundamental mode. That is, the spectrum would contain features like those in Figure 3.10(c). Since the features do not appear in the experimental measurements of the filament radiation, we can be confident that the antenna adapter does not overmode between 67 GHz $< f \leq$ 70 GHz. Since the V-band antenna does not overmode, its apparent gain will not rapidly change from 67-70 GHz relative to the gain below 67 GHz. Consequently, the extrapolation should be a good approximation of the actual gain.

The uncertainty in the antenna gain is assumed to be 0.5 dB, which is a reasonable estimate based on the comparison of manufacturer and laboratory gain data given in Figure 3.9. The total uncertainty in the field, including contributions from the

two calibration components is quantified in Section 3.5. The data in Figure 3.10 are the first component of the calibration. The other part is presented in Section 3.4. It accounts for the frequency response of the other parts of the receiver due to cable losses and the slight non-uniformity of the oscilloscope.

3.4 Frequency Domain Calibration of Microwave Receivers

3.4.1 Definition of Instrument Response

The total receiver calibration is composed of two parts: the antenna gain, which was defined and quantified in Section 3.3, and the combined frequency response of the cable, oscilloscope, and any in-line adapters. The frequency response is defined as the relative measure of how much signal a detector registers as the frequency of the input signal changes. In the context of the dissertation instrument response and frequency response are used somewhat interchangeably. The latter has a specific mathematical definition in the context of linear systems theory, which is addressed in this Section. For a uniform power spectral density of radiation, an ideal detector will produce a signal whose amplitude is also spectrally uniform. The response of a real detector departs significantly from the ideal, and it will be more sensitive at certain frequencies and less so at others.

Many spectroscopic diagnostics in plasma physics that infer plasma properties from atomic or molecular line emission in the visible, ultraviolet, and x-ray regimes require a well-characterized instrument response to correctly measure the relative amplitudes of spectral features [99], or to perform lineshape analysis on individual features [100, 101]. In that context it is often called the instrument function because it is fit with a continuous function which is then de-convolved from the measured spectrum. The sources of non-uniform instrument response are different in time domain spectroscopy from the latter case, but the procedure for correcting them is

essentially the same.

Compensating for the instrument response is accomplished by using a reference signal source to compare a measured spectrum to the known spectrum of the reference. We use calibrated microwave noise sources that produce broadband noise at a known power spectral density that are traceable to a NIST primary calibration standard specification [102]. Section 3.4.3 describes the reference sources used to measure the instrument responses.

The noise source calibration of the instrument response is a relative calibration. The total receiver calibration is made absolute (i.e. the spectrum can be stated correctly in units of electric field or intensity, instead of arbitrary units) by combining with the antenna gain. Splitting the calibration procedure into two parts is the most practical approach that achieves a high accuracy result. Transmitting the noise source spectrum through free space as the reference for calibrating the whole receiver at once is possible, but one would still have to know the gain of the transmitting antenna. Furthermore, the noise source signal is fairly weak, and even with a low noise amplifier (LNA) boosting the transmitted signal, the receiver would not achieve a large SNR. In the present case, there is no advantage to trying to calibrate the receiver as a whole over calibrating its components individually.

While the antenna gain measurement is a well-defined and accepted practice, the instrument response measurement is less so. One circumstance to consider is that the experiments measure short microwave pulses, while the calibration applied to those measurements is made under CW conditions. This would be a problem if the receiver were a nonlinear system or a linear time varying (LTV) system. There may be some situations in which the oscilloscope could exhibit LTV behavior since it contains active components, however such behavior is not evident in the measurements. As long as it is externally triggered it should always achieve a non-LTV state before starting to record the microwave pulses. The receiver as a whole can be regarded as a linear

time-invariant (LTI) system, and therefore has a well-defined impulse response and frequency response that do not change with the nature of the input signals.

The oscilloscope and the cable connected to it have a transfer function $X(s)$ that can be defined as the complex ratio the voltage present at the input of the cable to the voltage measured on the oscilloscope. This assumes that the signal levels are low enough to drive only a linear response, which is always the case in the experiments. The variable $s = \sigma + i\omega$ is a complex number that is the conjugate to time in a Laplace transform

$$X(s) = \mathcal{L}\{x(t)\} = \int_0^\infty x(t)e^{-st}dt = \frac{V_m(s)}{V_{in}(s)}, \tag{3.26}$$

where $x(t)$ is the time response of the cable and scope. They can be modeled as an RLC circuit, meaning $x(t)$ is the solution to the characteristic equation of a damped harmonic oscillator that is forced by a voltage at the frequency components of the input pulse. In this case, the important feature of $x(t)$ without presenting the mathematical details is that the scope and cable have a short-lived transient response that is convolved with the input voltage transient to give the measured voltage. For long pules or constant input, $x(t)$ achieves a steady state. If the voltage transient approaches a delta function, then it excites the system's impulse response. For an LTI system, $x(t)$ is the impulse response, and it is related to the transfer function by Equation 3.26. The frequency response is a special case of the transfer function in which we take the limit $\sigma \to 0$. If $s = i\omega$ then the definition of the transfer function reduces to the single-sided Fourier transform of $x(t)$, and $X(s) \to X(\omega)$. This approximation ignores the time domain transient response of the system. In the frequency domain this is equivalent to neglecting high frequency components of the frequency response magnitude that are filtered out by the scope. The approximation also imposes a phase distortion, but the measurements neglect the phase. Section 3.4.4 presents the instru-

ment response, $X(\omega)$, for the combinations of oscilloscopes, cables, and attenuators used in the experiments.

The horn antenna also has a transfer function and impulse response. In the time domain, the relationship between a voltage pulse transmitted by an arbitrary antenna and received by another polarization-matched antenna can be described by

$$\frac{E_r(t,R)}{\sqrt{\eta_0}} = \frac{1}{2\pi Rc}\delta\left(t-\frac{R}{c}\right) \circ x_t(t) \circ \left(\frac{\partial}{\partial t}\frac{v_t(t)}{\sqrt{Z_{L,t}}}\right) \tag{3.27}$$

$$\frac{v_r(t,R)}{\sqrt{Z_{L,r}}} = x_r(t) \circ \frac{E_r(t,R)}{\sqrt{\eta_0}}, \tag{3.28}$$

where the subscripts r and t correspond to receiver and transmitter respectively, E_r is the received electric field, η_0 is the impedance of free space, $x(t)$ is the impulse response, Z_L is the load impedance of the transmitter or receiver [103, 104, 105]. The factor $\delta(t - R/c)$ is a delta function propagating at the retarded time. The open circles denote convolution. Equations 3.27 and 3.28 would be one way to relate the current pulse in the filament to the voltage waveform recorded on the oscilloscope. For the plasma $v_t(t)$ would come from solving Ohm's law, although without a definite generating mechanism it is unclear which terms in Ohm's law must be retained. A further difficulty is finding the impulse responses of the filament plasma and antenna, but it is possible they could be estimated from a sophisticated finite difference time domain simulation solving Maxwell's equations.

3.4.2 Coaxial Transmission Line Behavior at High Frequencies

The variation of the instrument response with frequency is dominated by losses in the coaxial cables. The oscilloscopes and attenuators have small non-uniformities, but are relatively flat over their rated frequency range. Typically for frequencies below 1 GHz, coaxial transmission lines can be assumed to be dispersionless, and their circuit properties are accurately described by Equations 3.6-3.7. At microwave

and millimeter wave frequencies, losses in coax cables become strong functions of frequency, and therefore dispersive per the Kramers-Kronig relations. Transporting microwave signals by waveguide becomes favorable at high frequencies because the losses are much lower. Still, we have avoided waveguide for three reasons: it must have a lower cutoff frequency unlike a coax cable, it operates in frequency bands that are more narrow than what the experiments require, and it is physically rigid, which would make spatial mapping of the filament radiation prohibitively cumbersome.

A more accurate circuit model of a coaxial cable accounts for resistance, R, and imperfect capacitance, which is called shunt conductance, G [97]. We have recycled the notation for G and R from Sections 3.3.2 and 3.3.3. The dispersion relation for a lossy coaxial cable is

$$\gamma(\omega) = \sqrt{(R + i\omega L)(G + i\omega C)} = i\omega\sqrt{LC}\sqrt{1 - i\left(\frac{R}{\omega L} + \frac{G}{\omega C}\right) - \frac{RG}{\omega^2 LC}}. \quad (3.29)$$

If the cable losses are approximated to be small, then $R < \omega L$, $G < \omega C$, and $RG \ll \omega^2 LC$, and γ becomes

$$\gamma(\omega) \approx i\omega\sqrt{LC}\left[1 - \frac{i}{2}\left(\frac{R}{\omega L} + \frac{G}{\omega C}\right)\right], \quad (3.30)$$

where the Taylor expansion $\sqrt{1+x} \approx 1 + x/2$ has been used. Separating γ from Equation 3.30 into real and imaginary parts $\gamma = \alpha + i\beta$ gives the attenuation and phase constants, respectively

$$\alpha = \frac{1}{2}\left(R\sqrt{\frac{C}{L}} + G\sqrt{\frac{L}{C}}\right) \quad (3.31)$$

$$\beta = \omega\sqrt{LC}, \quad (3.32)$$

where the phase velocity is given by ω/β. Equations 3.31 and 3.32 show that the low loss limit does not capture the strong frequency dependence of the attenuation that is

measured for the calibration procedure. It proves the point that coaxial transmission lines are robust to dispersion in typical situations. The manner in which we use coax then tends toward an atypical case.

In order to capture the frequency dependent loss, the frequency dependence of its dielectric and conductive properties have to be accounted for. Figure 3.11 shows the result of a simulation performed in Keysight ADS of a coaxial cable whose dimensions are based off the SR-085 cable specification [106], but that has the composition of the 70 GHz coaxial cable used in the experiments. The voltage transmission coefficient through a 3 foot length of cable is plotted as a function of frequency. It shows that

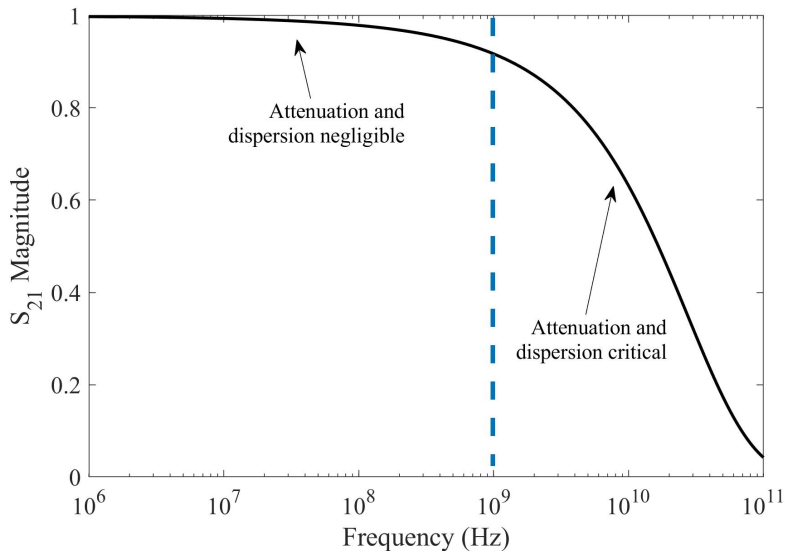

Figure 3.11: Simulated S_{21} for a realistic coaxial cable that is 3 feet long as a function of frequency. In linear units, it represents the transmission coefficient of the voltage wave measured at the output connector of the cable.

losses become significant above about 1 GHz, and dramatically increase above 10 GHz. While the simulation result is close to our observations, it will not match the calibration measurements exactly because the actual dimensions of the cables are proprietary, and can only be measured by destroying them.

The simulation used to create Figure 3.11 assumes that only the fundamental TEM mode propagates in the coax cable. In reality, it is possible to overmode the

cables, and the TE_{11} mode is the first higher order mode that will be excited if the frequency is too high. The frequency at which the TE_{11} mode is no longer evanescent and starts propagating with the fundamental TEM mode defines the cutoff frequency for a coax cable. Its exact value for a given geometry can be found from the solution of the Helmholtz equation in cylindrical coordinates, but a useful heuristic is given by

$$f_{TE11} = \frac{2c}{\pi(D+d)\sqrt{\epsilon_R}}, \tag{3.33}$$

where D is the inner diameter of the outer conductor, d is the diameter of the center conductor, and ϵ_R is the relative permeability of the dielectric separating them. Equation 3.33 in essence says that the TE_{11} mode propagates when the microwave wavelength in the coaxial geometry approaches the average diameter of the coaxial region, $(D+d)/2$. Table 3.2 lists the cutoff frequencies for the cables in the experiments based on Equation 3.33, and the maximum frequency which the cable was used to measure. Because the actual dimensions of the cables are unknown, Table 3.2 uses the dimensions and permeability of the connectors at each cable's ends [107]. The

Table 3.2: Cutoff Frequencies for Coaxial Cables

Cable Model	Connector Type	Dielectric	f_{TE11} (GHz)	f_{max} (GHz)
PE304-120	N and SMA	PTFE (SMA)	25.2	18
KBL-2M-LOW+	2.92 mm	Air	49.6	40
GE08	1.85 mm	Air	80.9	70

dimensions of connectors and cables produced by different manufacturers vary within a small tolerance, so slightly different values for f_{TE11} will exist depending on the exact cable assembly. However, Table 3.2 shows that it is unlikely that the cables are at risk of overmoding in the experiments as there is a $\sim 10\% - 30\%$ margin between the f_{TE11} and f_{max}.

3.4.3 Calibrated Microwave Noise Sources

The reference sources that are used to measure the instrument response consist of a diode array that is packaged with a coaxial connector. The outputs of the noise sources are calibrated against a primary blackbody standard [102] so that they produce a known power spectral density of microwaves over a large bandwidth. Alternate calibration sources exist for this type of measurement. The simplest is a resistor that is carefully held at a constant temperature. The easiest way to do this is to immerse the resistor in boiling liquid nitrogen which at standard conditions is a steady 77 K. Unfortunately, the noise power produced under these circumstances is very small, and is better measured using a device which has a greater sensitivity than the oscilloscopes. Another more practical alternative is to use a tunable frequency synthesizer, which can produce known power at a single frequency. The advantage of a synthesizer over the diode noise source is that usually the synthesizer power is adjustable, while calibration of the diode source only holds at a single power. However, finely measuring a spectrum can be time consuming even if the synthesizer frequency is swept in time. Another difficulty is that its internal calibration does not account for the output connector, which can cause significant and unknown losses if it is not in good condition. The advantages of diode noise sources are a broad spectrum, and the reliability of the calibration.

Three noise sources are used to calibrate the total receiver bandwidths up to 70 GHz: NW346KA (0.1-40 GHz), NW40G60-W-ISO (40-60 GHz), and NW50G75-W-ISO (50-75 GHz). They are manufactured and initially calibrated by the Noisewave Corporation. The noise sources are shown in Figure 3.12, and they are actually an assembly of a few components. The 40 GHz noise source connects to an LNA (B&Z Technologies BZR-00104000-500828-252525) directly by coaxial connector. The U-band and V-band noise sources are also amplified by LNAs (Millitech LNA-19V-180255 and Sage Millimeter SBL-5037031850-15VF-E1, respectively), however there

is a Faraday isolator between the output of the noise source itself, and the LNA. The

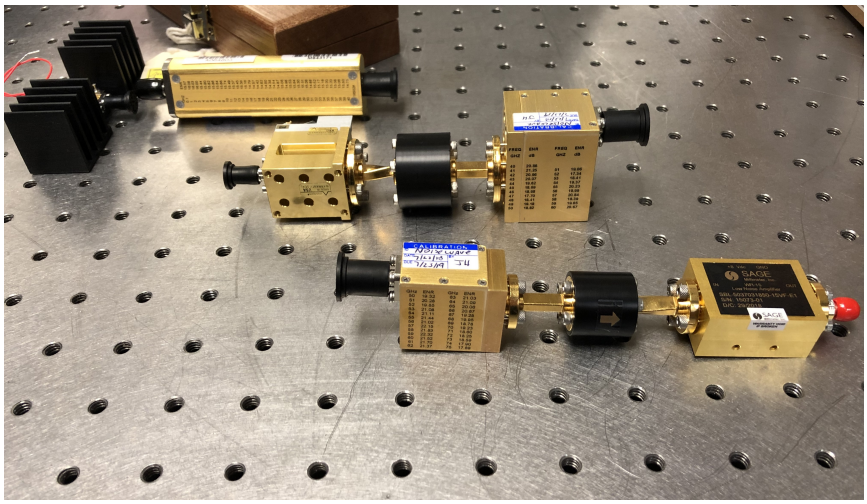

Figure 3.12: The calibrated noise sources collectively span 100 MHz to 75 GHz. From top to bottom they are Noisewave's NW346KA (0.1-40 GHz), NW40G60-W-ISO (40-60 GHz), and NW50G75-W-ISO (50-75 GHz). All noise sources are pictured with the LNAs that are used to amplify their outputs. The U-band and V-band noise sources also have Faraday isolators in-line with the LNAs. A table of each noise source's initial ENR versus frequency is printed on the side of its casing.

isolator is meant to diminish frequency pulling due to reflected signal that would result from connecting the noise source to an element that is not well impedance matched to the noise source. The noise power of the U-band and V-band noise sources is measured after the isolators. In truth, as long as the noise sources are connected to the LNAs, the isolator is a bit of overkill, as amplifiers inherently have large return isolation.

The signal in a noise source comes from reverse biasing a diode. The small amount of current that flows consists of shot noise, which is described statistically by a Poisson distribution. In the limit of a large number of charge carriers that are allowed to interact integrated over the total sampling time, the Poisson distribution is well approximated by a Gaussian distribution. The thermal equilibrium that it defines means that a temperature can be assigned to the charge carriers, where the bias voltage on the diodes is the dominant heat source. It is called the noise temperature, even though shot noise is not thermal noise (that is, Johnson noise), and does not

reflect the physical temperature of the diodes or any resistive load connected to them. To establish that the approximation is permissible, Figure 3.13 shows a typical time domain waveform measured for the 40 GHz noise source and its corresponding LNA, and a histogram of the measured voltage samples fit with a Gaussian distribution.

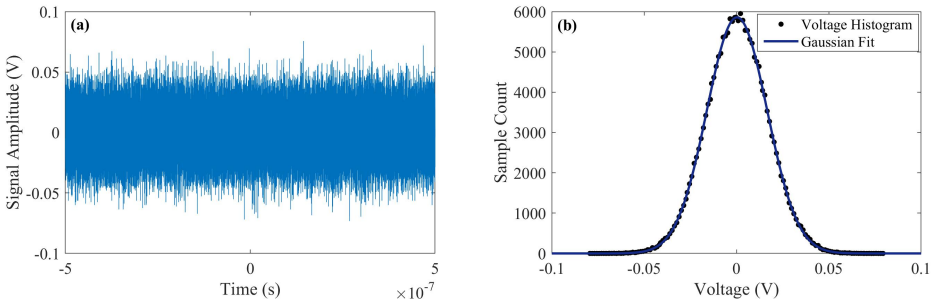

Figure 3.13: (a) Waveform of the 40 GHz noise source recorded on the Tektronix 70 GHz oscilloscope. (b) Histogram of the voltage samples in the waveform (black dots) fit with a Gaussian distribution (dark blue solid curve).

Nyquist showed that the fluctuating charges in a matched resistive load in thermal equilibrium generate a root-mean-square (RMS) voltage whose frequency dependence is given by the square root of a Planck distribution

$$\langle V_N \rangle = \sqrt{\frac{4hfBR}{e^{hf/k_B T_N} - 1}} \tag{3.34}$$

where R is the resistance, h is Planck's constant, k_B is Boltzmann's constant, and T_N is the noise temperature. B is the bandwidth over which the voltage spectrum is measured [108]. Because the frequencies of interest are low, the Rayleigh-Jeans law is used to approximate the Planck distribution. In the limit $hf \ll k_B T_N$, Equation 3.34 becomes

$$\langle V_N \rangle = \sqrt{4k_B T_N BR}. \tag{3.35}$$

The RMS power dissipated in the resistor due to thermal fluctuations of the charge carriers is

$$P_N = \frac{\langle V_N \rangle^2}{4R} = k_B T_N B. \tag{3.36}$$

The power generated by a noise source is specified in terms of excess noise ratio (ENR) which is the noise power spectral density above that which exists at 290 K, which is -174 dBm/Hz. For example an ENR of 15 dB means that the noise power density is $-174+15 = -159$ dBm/Hz. While decibels are usually a relative quantity, dBm is an absolute measure of power, and is defined as power relative to 1 milliwatt, or 0 dBm = 1 mW. The specified ENR gives the reference voltage for the calibration per Equation 3.35. T_N and ENR are related by

$$\mathrm{ENR} = 10\log_{10}\left(\frac{T_N - T_0}{T_0}\right), \tag{3.37}$$

where $T_0 = 290$ K. Figure 3.14 shows the ENRs for each of the noise sources as a function of frequency. The voltage produced by a noise source with a 20 dB ENR can

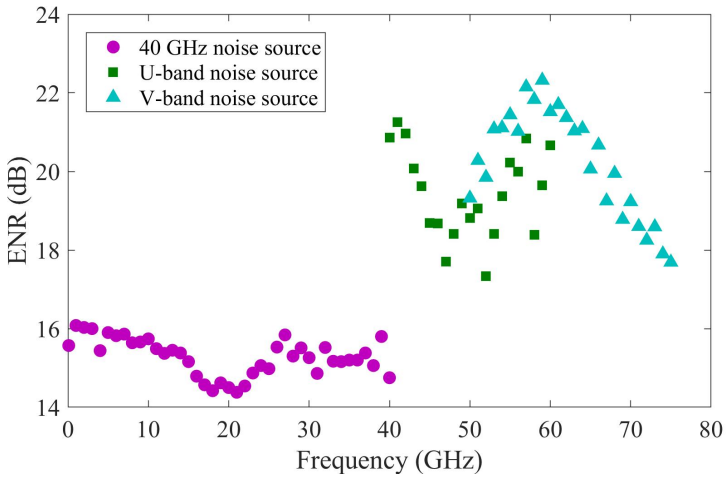

Figure 3.14: The calibration data for each of the noise sources given as ENR versus frequency.

predicted using Equations 3.35 and 3.36. Assuming a 100 MHz bandwidth, the power is -174 dBm/Hz + 20 dB + 80 dB-Hz = -74 dBm. On a 50 Ω load, this corresponds to about 126 μV peak-to-peak. This is well below the noise floor of the oscilloscopes used to measure the calibration data. The voltage can be increased by increasing the bandwidth, but that sacrifices spectral resolution. This is why the LNAs are

incorporated with the noise sources: adding their gain makes the noise spectrum measurable. This means that the amplifier gain must be accurately known in order to make the calibrations. Figure 3.15 shows the manufacturer specified gain versus frequency for each amplifier. The data in Figures 3.14 and 3.15 together constitute

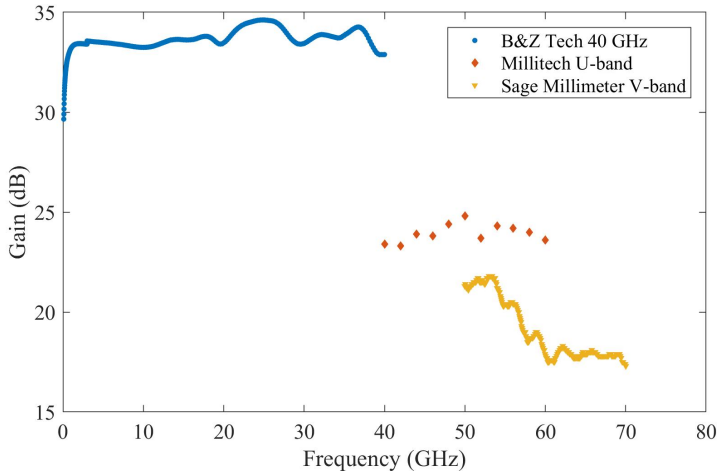

Figure 3.15: The gain of each LNA used with the noise sources as a function of frequency. While the B&Z Tech and Sage Millimeter amplifiers came with finely measured gain, the frequency interval for the Millitech U-band amplifier is 2 GHz.

the reference spectra that are used to calculate the instrument response.

3.4.4 Instrument Response Calculation

The instrument response is given by the steady state limit of the transfer function in Equation 3.26 of the cable and scope, which is the ratio of the Fourier transform of the measured voltage waveform to the reference voltage produced by the noise sources

$$V_{NS}(f) = X(f)V_{ref}(f). \tag{3.38}$$

Since the LNAs are needed to amplify the noise source signals, $V_{ref}(f)$ must also account for their gain

$$V_{ref}(f) = \sqrt{4G_{LNA}(f)k_B T_N(f)BR}, \tag{3.39}$$

where G_{LNA} is converted to linear units ($G(f) = 10^{G[\mathrm{dB}]/10}$) from the appropriate dataset in Figure 3.15, and $T_N(f)$ is found using Equation 3.37 using the calibration data from Figure 3.14. The load resistance is $R = 50\ \Omega$. The correct value of B is the resolution bandwidth (RBW, Δf_{RBW}) of the digitized waveform. For a waveform that has a record length of N samples that are collected at a rate of f_s, the RBW is

$$\Delta f_{RBW} = \frac{f_s}{N} = B. \tag{3.40}$$

Equation 3.40 is only to be used if the waveform is not windowed in the time domain. In digital signal processing it is common to multiply a waveform by an apodization function that is symmetric about the middle sample of the time record that smoothly brings its beginning and end down to zero. This minimizes the introduction of spurious high frequency content in the DFT that results from the truncating the signal at the boundaries of the time record. Common window types are the Hanning, Hamming, and Welch functions [84]. If a windowing function is used, then in Equation 3.39, $B = \alpha f_s$, where α is determined by the windowing function [109]. For the CW calibration measurements, any spurious high frequencies introduced into the Fourier transform of the noise waveform will contribute frequency content that is integrated over 10's of ps out of a total about 1 μs. The microwave pulses in the experiments start and stop far from the beginning of the end of the time record. In both cases no windowing function is necessary.

Having addressed the procedure for calculating the reference voltage spectrum, the next step is to measure the spectrum with an oscilloscope. Figure 3.16 shows the setup for the calibration measurements. The calibration plane is the input connector of the cable. While the LNAs are so named because they have relatively small noise figures, they still make enough noise that it needs to be subtracted before calculating the instrument response. Furthermore, there is thermal noise associated with the physical

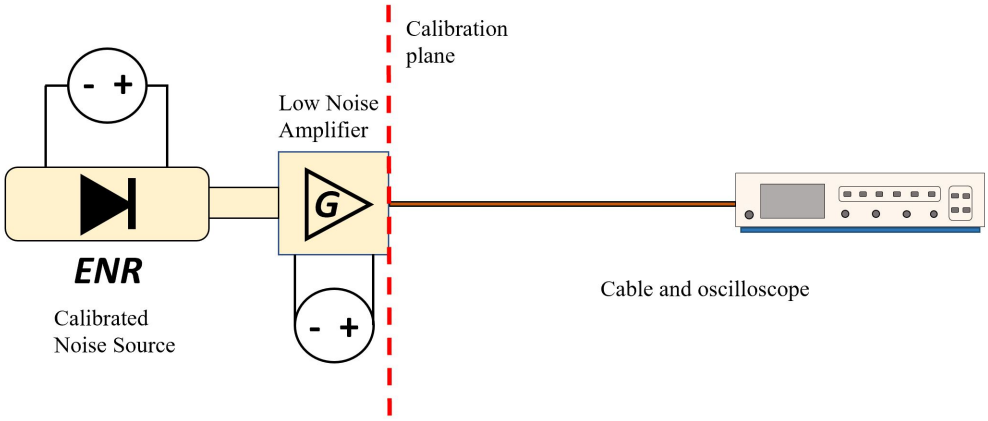

Figure 3.16: Diagram of the setup for measuring the cable and oscilloscope response. The gain of the amplifier is great enough that attenuators in line with the cable can also included in the instrument response measurement if necessary.

temperature of the noise source and amplifier. A simple background subtraction with the noise source powered off, but the amplifier on is sufficient to account for the difference. Because these are incoherent signals, only their power can be added and subtracted.

Noise inherently has a large variance, as shown in Figure 3.13, so long integration times, or many repetitive samples are needed to resolve the RMS signal. We typically record 400 noise waveforms with the noise source on, and an additional 400 background waveforms in which the amplifier is powered, but the noise source is not. The sampling rate is set to maximum, and the total record length is noted so that the RBW is known while making the measurement. Averaging noise in the time domain results in zero signal, of course, so the calculations must be performed in the frequency domain. The voltage spectrum of each noise and background record is calculated using an FFT. Either the power spectrum, or power spectral density (PSD) is then calculated for each voltage spectrum. The power spectra samples of the noise source are averaged, and their variance is calculated as a function of frequency. This is repeated for the background power spectra. The average background power spectrum is subtracted from the average noise source spectrum. The final noise source

voltage spectrum is the square root of the net power spectrum, and its uncertainty is propagated from the variance of each group of samples to contribute to the estimation of the uncertainty in the instrument response. For reference purposes, the procedure is given below. In converting from voltage to power the factor of $4R$ in Equation 3.36 is neglected because the result needs to be converted back to voltage, so it cancels.

Frequency Domain Background Compensation Procedure

Record M waveforms $v(t)_{on,i}$ and $v(t)_{off,i}$ of record length N at sample rate f_s

$$V_{on,i}(f) = \mathrm{FFT}\{v(t)_{on,i}\} \qquad V_{off,i}(f) = \mathrm{FFT}\{v(t)_{off,i}\}$$

$$P_{on,i} = 2|V_{on,i}|^2 \qquad P_{off,i} = 2|V_{off,i}|^2$$

OR

$$\mathrm{PSD}_{on,i} = \tfrac{2N}{f_s}|V_{on,i}|^2 \qquad \mathrm{PSD}_{off,i} = \tfrac{2N}{f_s}|V_{off,i}|^2$$

$$P_{NS} = \left(\tfrac{1}{M}\textstyle\sum_{i=1}^{M} P_{on,i}\right) - \left(\tfrac{1}{M}\textstyle\sum_{i=1}^{M} P_{off,i}\right)$$

OR

$$P_{NS} = \left(\tfrac{1}{M}\textstyle\sum_{i=1}^{M} \int_{\Delta f} \mathrm{PSD}_{on,i}(f')df'\right) - \left(\tfrac{1}{M}\textstyle\sum_{i=1}^{M} \int_{\Delta f} \mathrm{PSD}_{off,i}(f')df'\right)$$

$$V_{NS} = \sqrt{P_{NS}} \qquad \delta V_{NS}^2 = \mathrm{var}(V_{NS}) = \tfrac{\delta V_{on}^2 + \delta V_{off}^2}{4P_{NS}}$$

If one wants to know the total power contained in a bandwidth other than the RBW, then it is necessary to estimate the PSD. For example, this step should be performed with a heterodyne receiver. Since we do not window the voltage waveforms, the power spectrum and PSD approximation differ by a factor of N/f_s. If the PSD

is calculated, then it should be integrated over the desired frequency interval Δf before computing V_{NS}. The factor of 2 in the calculation of the power spectrum and PSD arises from an implied change from a double-sided spectrum ($f \in [-f_s/2, f_s/2]$) to a single-sided one ($f \in [0, f_s/2]$). Results are always reported with single-sided spectra. However, most DFT algorithms return a double-sided spectrum, which for a real-valued input like $v(t)$ is symmetric about $f = 0$. The factor of 2 follows from Parseval's theorem, or conservation of energy in the spectrum of a time domain waveform. This is an important but often neglected detail that is critical to getting the calibration correct. The best practice is to test the DFT algorithm with a known waveform and make sure that the analysis routine conserves its energy.

The variance in V_{NS} is composed of that due to the spectra with the noise source on and off

$$\delta V_{on}^2 = \mathrm{var}(V_{on}) = \frac{1}{4\bar{P}_{on}} \frac{1}{M^2} \sum_{i}^{M} \sum_{j>i} \left(P_{on,i} - P_{on,j}\right)^2, \tag{3.41}$$

where $\bar{P}_{on}$ is the average power. δV_{off}^2 is calculated the same way with the background noise power spectra. However in propagating the uncertainty, $1/4P_{NS}$ is the correct divisor to use instead of $1/4\bar{P}_{on}$.

The background compensation procedure is the most likely place to make mistakes in the calibration. The way it has been presented here is determined by how Matlab calculates FFTs, so it may need to be adapted to the analysis tool in use. Because small differences in the calculation may be necessary, the value of validating an analysis routine against a known or analytical result cannot be overstated.

The instrument response follows from Equation 3.38 as $X(f) = V_{NS}/V_{ref}$. Its uncertainty is given by

$$\begin{aligned} \delta X(f) &= \sqrt{\left(\frac{\partial X}{\partial V_{NS}}\right)^2 \delta V_{NS}^2 + \left(\frac{\partial X}{\partial V_{ref}}\right)^2 \delta V_{ref}^2} \\ &= X\sqrt{\left(\frac{\delta V_{NS}}{V_{NS}}\right)^2 + \left(\frac{\delta V_{ref}}{V_{ref}}\right)^2}, \end{aligned} \tag{3.42}$$

where $\delta X = \sqrt{\mathrm{var}(X)}$. The variance in the reference voltage is given by

$$\delta V_{ref}^2 = \frac{V_{ref}^2}{4}\left[\left(\frac{\delta G_{LNA}}{G_{LNA}}\right)^2 + \left(\frac{\delta T_N}{T_N}\right)^2\right], \tag{3.43}$$

where the uncertainties in the amplifier gain data and ENR are both assumed to be $\delta G_{LNA} = \delta\mathrm{ENR} = 0.5$ dB.

Figure 3.17 shows $X(f)$ for most of the cable and oscilloscope combinations used in the measurements in order of increasing maximum frequency. Interleaving artifacts have been removed from the traces where necessary. They have been plotted with linear units so that they read like measurements of the voltage transmission coefficient. A traditional presentation of this information is a Bode magnitude plot, which uses a decibel scale to highlight resonances and cutoffs in the instrument transfer function. However, we are not interested in the critical points of the transfer function. The estimate of the uncertainty in the instrument responses is calculated using Equation 3.42, and has been propagated from the calibration measurements along with Equation 3.43. The shaded regions in Figures 3.17(a)-(d) bound δX, which is typically about 30%. Consistency of the instrument response calculation is established in Figures 3.17(d) and (f), where the response of the same receiver configuration is calibrated with two different noise sources that operate in overlapping frequency bands.

In Figures 3.17(e) and (f), the indication of the uncertainty is omitted for clarity. These plots compare the instrument response when high flatness, broadband attenuators are added to the receiver. It is easy to apply too large a voltage to the fast oscilloscopes, especially to the 70 GHz channel of the Tektronix scope which can only handle 300 mV. The attenuators are added to protect the scopes from large signals, and it is simple to account for their contribution to the instrument response. As the Figures 3.17(c)-(f) show, the attenuators have no resonances, and provide uniform

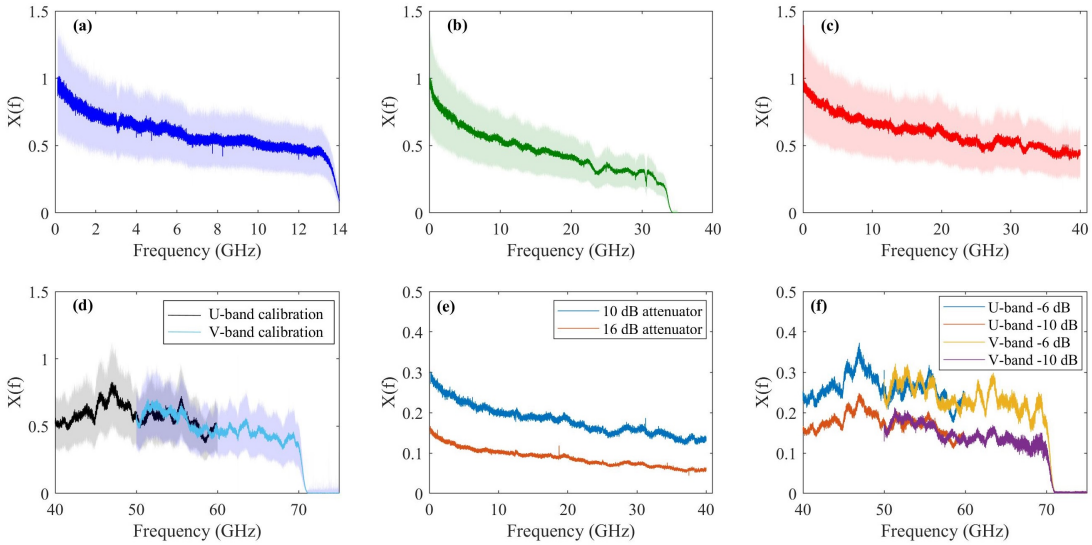

Figure 3.17: Instrument response functions measured with the 40 GHz noise source for (a) Agilent 13 GHz scope with 18 GHz cable, (b) the 33 GHz bandwidth channel on the Tektronix scope with 18 GHz cable, and (c) Tektronix 70 GHz channel with 40 GHz cable. (d) Comparison of response functions for the 70 GHz channel and 70 GHz cable measured with the U-band and V-band noise sources. In (a)-(d) the estimated uncertainty in $X(f)$ is bounded by the shaded regions. (e) Response function for the same scope and cable configuration as in (c), but additional attenuators are in line with the cable. (f) Attenuators in line with the 70 GHz cable measured in the U-band and V-band.

attenuation up to 70 GHz.

The instrument responses show that there is nearly perfect transmission of low frequencies at a few GHz, while signals at 10's of GHz are reduced in amplitude by about 1/2 up to the brick wall filter of the oscilloscopes. The high frequency losses are due to the cables. While manufacturers generally do not provide continuously measured data that for example could be compared to the simulation in Figure 3.11, the cable specification will often state attenuation per unit length in coarse frequency ranges [110]. Those specifications are consistent with the instrument response measurements. Measuring the flatness of the oscilloscope would require compensation of the cable losses. This is possible and interesting from the standpoint of better understanding their performance, but it is unnecessary for the experiments performed in the dissertation.

3.5 Measurement of the Absolute Free Space Electric Field Amplitude

3.5.1 Total Receiver Calibration and the Antenna Factor

Sections 3.3 and 3.4 developed the components needed for the calibrations. This Section shows how they are applied to the experiments. The experimental data are presented in terms of electric field amplitude defined to be that incident at the aperture of the antenna. The aperture fields can be related to the field amplitude at the plasma if the filament radiation pattern and finite solid angle of the antenna main beam are accounted for. That calculation is not necessary to reach the conclusions of the dissertation, but is a potential direction for future work.

The electric field amplitude at the aperture of an antenna is related to the voltage it induces across the antenna terminals V_{term} by a quantity called the antenna factor (AF), which is derived as follows. The RMS power received by an antenna is equal to the Poynting flux of the incident radiation S_i multiplied by the active area of the antenna that is responsible for converting that field into a current flowing in the antenna structure

$$P_{rec} = \frac{V_{term}^2}{2Z_L} = S_i A_e = \frac{E_i^2}{2\eta_0} A_e, \tag{3.44}$$

where $\eta_0 = \sqrt{\mu_0/\epsilon_0}$ is the impedance of free space, and E_i is the amplitude of the incident electric field, and Z_L is the output impedance ($50\,\Omega$) at the antenna terminals. The active area A_e, called the effective aperture is related to the antenna's gain by

$$A_e = \frac{c^2 G}{4\pi f^2}. \tag{3.45}$$

The antenna factor is defined as the ratio E_i/V_{term}, which can be found from Equations 3.44 and 3.45

$$\mathrm{AF} \equiv \frac{E_i}{V_{term}} = \sqrt{\frac{4\pi\eta_0 f^2}{c^2 Z_L G}}. \tag{3.46}$$

Equation 3.46 shows that antennas can also be thought of impedance matching elements between free space and the antenna load. There are a few assumptions implicit in using the antenna factor to calculate the aperture field. The antenna must be polarization matched to the incident radiation, and the antenna aperture must be uniformly illuminated by the incident electric field. Equation 3.46 does not account for the angular and frequency dependence of the antenna pattern. The directivity and polarization properties of horn antennas described in Section 3.3.2 means that the error incurred by assuming all of the incident radiation enters the antenna with matched polarization through the main beam is at most about 10% based on the relative amplitude of the main lobe and nearest side lobe in the calculation shown in Figure 3.6.

The instrument response found in Section 3.4 relates the measured voltage V_m to the antenna terminal voltage

$$V_{term} = \frac{V_m}{X}. \tag{3.47}$$

The calibration plane for the instrument response is the input connector of the cable, or equivalently, the antenna terminals. Therefore, the aperture field can be expressed

$$E_i(f) = \frac{V_m(f)}{X(f)} \sqrt{\frac{4\pi\eta_0}{\lambda^2 Z_L G(f)}}, \tag{3.48}$$

where λ is the free space microwave wavelength. Equation 3.48 combines the two elements of the calibration that were found in Sections 3.3.4, and 3.4.4. E_i is an absolutely calibrated quantity. It is independent of the antenna-cable-oscilloscope combination that is used to make the measurement. Therefore, we can measure E_i with different receiver configurations across their combined frequency range, and compare the results as if they came from a single instrument. The uncertainty in E_i is

$$\delta E_i = E_i \sqrt{\left(\frac{\delta V_m}{V_m}\right)^2 + \left(\frac{\delta X}{X}\right)^2 + \left(\frac{\delta G}{2G}\right)^2}. \tag{3.49}$$

The measured voltage spectra in Equations 3.48 and 3.49 are compensated for background microwave noise by subtraction in the frequency domain, which will include environmental or internal receiver noise. The background subtraction on the measured signal spectra is performed according the procedure in Section 3.4.4. While it is technically correct to add and subtract waveforms because they are coherent signals, we do not do this because of time jitter in the signals. Averaging in the time domain results in huge signal distortions because the waveform, while stable, shifts in time from shot-to-shot. Once the DFT is performed and the phase information is neglected, the signal is incoherent and must be treated the same way as the noise waveforms measured for the calibrations.

Figure 3.18 shows the total receiver calibration factor for the configurations used in the experiments without microwave attenuators. The calibration factor is equal to $1/X \times \mathrm{AF}$, or equivalently E_i/V_m. It is stated in terms of the aperture electric field amplitude that corresponds to 1 V of measured signal as a function of frequency. The uncertainty is given by Equation 3.49 with $\delta V_m = 0$, and $V_m = 1$ over the appropriate frequency span. Each calibration factor is for a particular combination of horn antenna, cable, and oscilloscope. The calibration factor in Figure 3.18(a) is used to interpret the deformable mirror optimization measurements in Chapter VI. The gas pressure dependence measurements of Chapter IV rely on the calibration factors in Figures 3.18(b) and (c). Calibrating the spectra presented in Chapter V requires the data of Figures 3.18(b)-(d).

While the experimental data are absolutely calibrated, there are possible systematic biases in the measurements that arise from the assumptions made in the calibration calculations that are not included in the uncertainty estimations. These assumptions have been introduced in prior Sections of this Chapter. The most consequential are quickly restated for convenience. The antenna polarization must be matched to that of the incident microwave electric field. The output impedance of

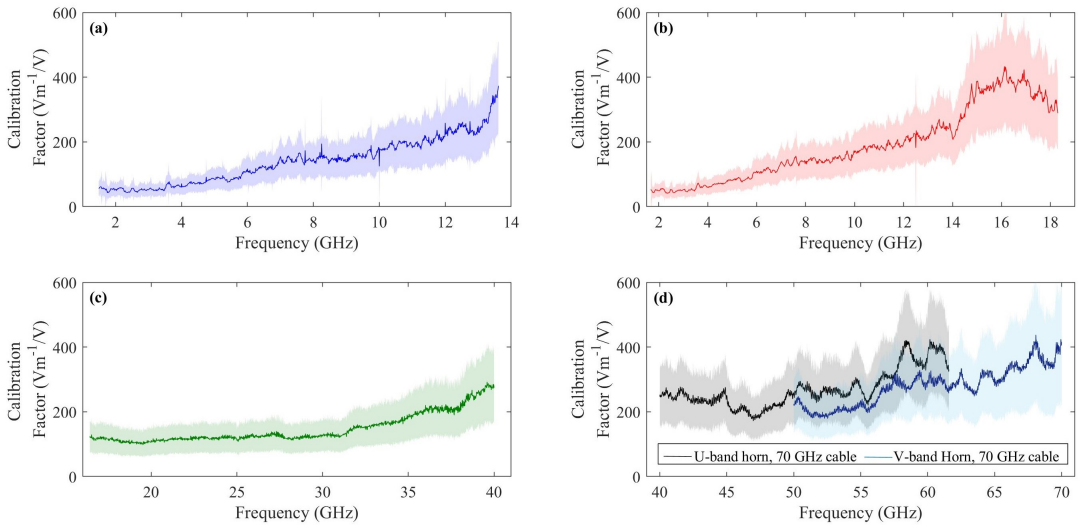

Figure 3.18: Receiver calibration factors for the aperture electric field amplitude that generate a unit measured voltage (V/m per V). (a) AEL H-1498 horn with Pasternack PE304-120 cable and Agilent DSOX91304A 13 GHz oscilloscope. (b) AEL H-1498 and PE304-120 on the 33 GHz channel of the Tektronix DPO77002SX oscilloscope. (c) ComPower AH-840 horn with Minicircuits KBL-2M-LOW+ cable and the 70 GHz channel on the Tektronix scope. (d) Orbit/FR FR6520 (black) and Sage Millimeter SAR-2507-15-S2 (blue) with MegaPhase GE08 cable on the 70 GHz channel of the Tektronix scope. The uncertainty associated with each calibration factor is bounded by the shaded region.

the antenna must be matched to the rest of the receiver at 50 Ω. All of the measured microwave radiation is assumed to enter through the main lobe of each antenna. Smearing of the filament's radiation pattern due to the finite main lobe solid angle is not accounted for because it is frequency dependent. The steady state limit of the transfer function of the cables, scopes, and antennas has been assumed in the calibrations. This does not mean that the approximation introduces error in the measured frequency responses. Further, all receiver components are linear and will not generate in-band frequency content that is not already present in the incident microwave field. The estimated measurement errors associated with these assumptions are left out of the uncertainty propagation calculations either because their contribution to the total uncertainty is dominated by other causes, or because they are too difficult to quantify properly. However, if such errors were significant it would likely not be possible to get good agreement between the electric field spectra measured with different receiver

configurations.

3.5.2 Spatially Resolved Electric Field Spectra

This Chapter describes the procedure for analyzing the microwave data, but there are a few considerations to be made when performing the measurements. Capturing the angular variation of the microwave spectrum is an important part of understanding how the plasma generates radiation. Mapping the spectra as a function of emission angle is performed over many laser shots. A single configuration of the receiver in a fixed position can acquire a complete waveform in a single shot, but the FFT of one waveform tends to be very noisy unless the RBW is large. Good statistics and angular maps are constructed from thousands of laser shots. The fundamental assumption is that the microwave waveform is highly repeatable shot-to-shot. Signals in general that repeat well from shot-to-shot are unusual in plasma physics experiments. Laser plasma experiments are especially fraught in this regard because of their transient nature, and sensitivity to initial conditions. However, as the data in Chapters IV to VI show, the microwave waveforms usually exhibit a high degree of shot-to-shot stability. There are limitations, namely the slow drift of laser power with time. High repetition rate lasers can also cause the gas to retain enough heat and possibly long-lived gas species from previous shots to cause a memory effect [111]. There is sufficient time for the gas to recover at standard laser repetition rates of 10-20 Hz. These limitations are highlighted where necessary in the discussion of the experiments.

The standard protocol employed in collecting the data is to measure waveforms at angular intervals of $5^\circ - 10^\circ$, and to collect 100 waveforms at each angular position. Even though the beamwidth of the horns is significantly larger than the angular increment, the radiation pattern from the plasma has a strong enough angular dependence that the small increments are needed to better resolve the emission. Increments of 5° is close to the smallest angular displacement that can be achieved without the

horn apertures overlapping adjacent angular positions of the horn. The background microwave environment is usually loud enough to require subtraction per the procedure given in Section 3.4.4. This is especially an issue at X-band frequencies and below ($\leq$ 12.4 GHz) where current communications technologies operate. Further, the background noise levels can change with the angular position of the antenna at low frequencies. For example, the pulsers used to switch the Pockels cells in a regenerative amplifier produce fairly broadband noise between 3-5 GHz, but this is only apparent if the horn is pointed at the front end of the laser. For this reason it is necessary to also acquire 100 waveforms of background with each set of signal waveforms. Background noise is less pronounced at the millimeter wave frequencies ($>$ 40 GHz). However, it is usually good practice to acquire background waveforms for each set of signal waveforms because the noise level of the oscilloscope changes depending on its sensitivity setting (the setting of the V/div knob). Changing the sensitivity changes the pre-amplifier stage that the oscilloscope uses to process the waveform, and therefore its noise level. One can often recognize this as an audible click the oscilloscope makes when changing the sensitivity as it switches pre-amplifiers. For signals with small SNR, keeping track of the sensitivity setting can be significant.

Finally, the apparatus used to mount the antenna has two requirements: the radial distance between the horn aperture and the plasma must be constant, and it must allow the horn to be positioned so that reflections of the microwaves from nearby surfaces can be managed. It is standard practice to make free space microwave measurements in an anechoic chamber to minimize reflections, but such facilities are highly specialized and usually are not combined with a laser facility. The sensitivity of the receiver is not great enough to need an anechoic chamber. Our measurements are in a single plane for simplicity, but it can be helpful to have the ability to make out-of-plane measurements as well. One good option for meeting the requirements was originally fielded at the Naval Research Laboratory (NRL) and is called an NRL

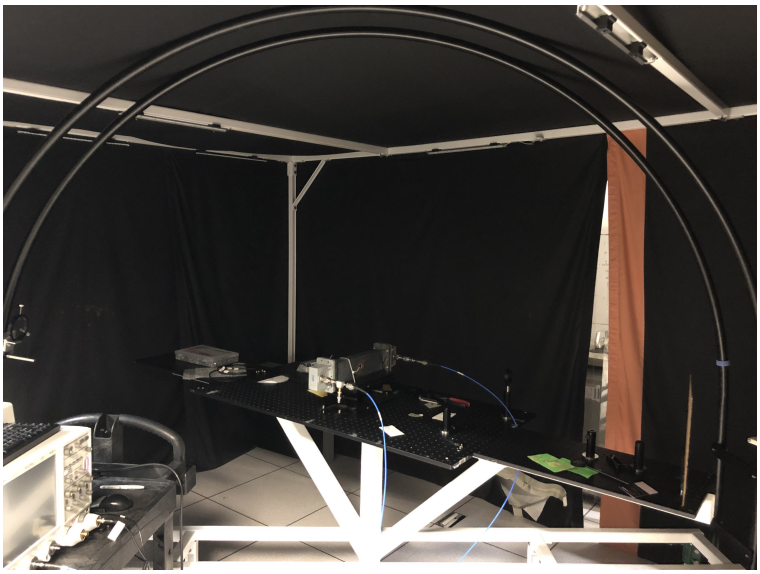

Figure 3.19: Rotating NRL arch for mounting antennas. The arch rotates to enable angular resolution of the filament radiation in the coronal plane.

arch, shown in Figure 3.19. One was constructed for the measurements performed at AFRL in addition to similar setups for the other experiments. The arch sits on a rotating bearing, so it is possible in principle to measure radiation over an entire half-sphere.

The data presented in Chapters IV to VI result from applying the measurement and analysis procedures described here to different experiments with laser plasmas generated in air. The receiver and the calibration procedure enable new measurements of broadband microwave radiation that have not been employed before, and may find use as a non-perturbing plasma diagnostic. While further development of the receiver and calibration procedure would enhance its capabilities, it enables a useful spectroscopic technique in its current form.

CHAPTER IV

Gas Pressure Dependence of Microwave Generation from Filamentation

4.1 Introduction

Filamentation gives rise to a number of counterintuitive results such as pulse self-compression [112, 113, 114] or secondary lasing on oxygen bands in filament plasmas in air [115, 116, 117]. We have discovered another unexpected behavior with the microwave generation from filaments that supports the notion that the plasma currents the laser pulse drives during filamentation are more complex than previously thought. The experimental results presented in this Chapter are reported in a recent publication [118]. Decades of previous work measuring THz from filament plasmas has built a consensus that the plasma currents in single-color filaments are excited by the laser pulse's ponderomotive force. Or for a two-color pulse, that the aperiodic laser field of the combined harmonics causes a net transverse motion of the plasma electrons, which becomes a significant macroscopic current when integrated over the laser pulse duration. This Chapter shows experimentally that the current responsible for the microwaves is likely distinct from those which radiate THz waves.

For fixed laser pulse energy, duration, and focal geometry we find that the microwave yield increases dramatically as the air pressure decreases. Section 4.4.1 argues

that this is due to an increase in the plasma's conductance at microwave frequencies. The ability of the plasma to radiate is quantified by its conductance, that is the conductivity integrated over the dimensions of the plasma. The inverse dependence of the conductance and microwave yield on pressure is an odd result because low pressure air contains a smaller density of electrons that, upon ionization by the laser can carry the current in the plasma responsible for the microwave emission. One would normally expect that the radiation yield scales with the gas density. While this is true in other laser plasma interactions [119], the experiments show that the opposite holds for microwaves due to laser filamentation. Our measurements are the first observation of this behavior in the microwave frequency range. The pressure dependence of the microwave yield may also enable a novel diagnostic for the electron temperature in the filament plasma. The diagnostic is proposed at the conclusion of the dissertation in Chapter VII.

Filamentation depends sensitively on the properties of the medium in which the laser pulse propagates. Changing the gas pressure, in this case air, alters the magnitude of the nonlinearity that the pulse experiences, which affects the critical power for Kerr self-focusing. The features of filamentation in low pressure gas have been explored before. Simulations [120] and experiments [121, 122] show that the filament length and diameter change with the gas pressure. Comparison of the microwave pressure dependence to previous work is discussed further in Section 4.4.2.

We generated filaments in a gas cell where the air pressure was varied from atmosphere (630 Torr at altitude in Albuquerque, New Mexico) to 0.5 Torr – a range of a little more than three orders of magnitude. The peak-to-peak voltage of the measured microwave waveforms increased monotonically over that pressure range by a factor of about 40. The calibration procedure described in Chapter III was used to measure the spectrum of the electric field as a function of pressure and emission angle from 2-40 GHz. The amplitude of the electric field increases across the whole band-

width of the measurement, meaning that the conversion efficiency of the microwave generation increases. However, the amplitude increase is not uniform in frequency, and the low frequency components (< 10 GHz) see a much greater increase than the high frequency components (> 20 GHz) with decreasing air pressure.

4.2 Experimental Methods

4.2.1 Description of the Experimental Setup

The laser used in the experiments is a terawatt-class Ti:sapphire CPA system with a central wavelength of 800 nm. The front end consists of a Coherent Mantis oscillator and Legend Elite regenerative amplifier. The $\sim$ 1 mJ output of the regenerative amplifier enters a multi-pass power amplifier that can increase the pulse energy to a maximum of about 600 mJ before compression. The peak power is low enough that the grating compressor need not be enclosed in a vacuum chamber.

The optimized pulse duration is approximately 50 fs at a repetition rate of 10 Hz. The experiments use a constant pulse energy of 40 ± 2 mJ. The pulses are focused at $f/60$ with a concave mirror that has a 3 meter focal length. The filaments, which form near the geometric focus of the concave mirror, exist in a transitional propagation regime between pure nonlinear self-focusing and geometric focusing. The external focusing strongly influences the the filament propagation in terms of location and extent [123], but because it is relatively gentle it does not dominate the balance of nonlinear self-focusing and plasma defocusing. Even though externally focused filamentation is a different propagation regime and can dramatically increase the plasma density relative to pure self-focusing [36], it is necessary for practical experiments in limited laboratory space.

Figure 4.1 shows the experimental setup for the gas pressure dependence measurements. The filamentation region is contained inside a 2 meter long gas cell. It

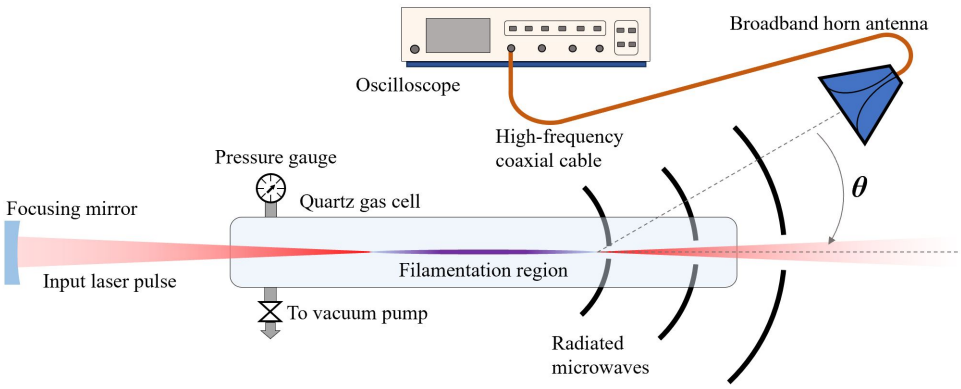

Figure 4.1: Diagram of the experimental setup.

consists of a quartz tube 3.8 cm in diameter whose entrance is capped with a 2 mm thick fused silica window that is anti-reflection coated for 800 nm light. A scroll pump connected to the cell allows it to reach a base pressure of about 0.3 Torr. The microwave radiation is measured with two horn antennas that cover 2-18 GHz (AEL H-1498) and 18-40 GHz (ComPower AH-840) respectively. They are mounted to the rotating gantry that is described in Section 3.5.2 so that the distance between the antenna aperture and the plasma is 1.2 meters. The microwaves are measured as a function of emission angle, labeled θ in Figure 4.1 in 5° increments from $\theta = 5° - 90°$ where $\theta = 0°$ is parallel to the laser propagation. In the plane formed by the laser propagation vector and the angular translation of the horn, the microwave electric field polarization aligns with the E-plane of each horn antenna.

The voltage waveforms from the antennas are directly digitized using a Tektronix DPO77002SX that has a maximum sampling rate of 200 GS/s, and 70 GHz real time bandwidth. Microwave frequency spectra are calculated from the Fourier transform of the voltage waveforms, which are absolutely calibrated using reference sources according to the procedure in Sections 3.3-3.5. The uncertainty associated with a single frequency component is dominated by that of the calibration factor and the statistical spread in the measured frequency spectra of microwaves. For a single

frequency component, it ranges from about 40% (4 dB) to 100% (10 dB). While the uncertainty for a single component is large, microwave spectral data are in general not useful if there is only one component. Typically several components are averaged within a suitable bandwidth, significantly reducing the uncertainty.

The calibration allows calculation of the electric field amplitude incident at the antenna apertures, which means that the spectrum from 2-40 GHz can be presented as if it were acquired with a single receiver. The environmental microwave background is significant, especially in the 2-18 GHz frequency range, so background waveforms are recorded with each set of signal samples. The background compensation is performed in the frequency domain according to the procedure stated in Section 3.4.4.

The supports for the gas cell are mounted on an optical breadboard so that the filamentation region occurs about 15 centimeters above its surface. This and other solid structures near to the experiment present a risk of reflecting the microwaves emitted by the plasma back into the horns. However, the microwave pulses are short enough, and the reflecting surfaces are far enough away from the plasma that there is sufficient path length difference to allow for time discrimination of any reflections. Depending on the orientation of the surface relative to the horn aperture, it is sometimes possible to place a baffle over the surface (this can be as simple as a sheet of aluminum foil) that re-directs microwave reflections away from the horn.

4.2.2 Microwave Losses During Propagation

Microwaves can propagate through a variety of materials with negligible absorption. This is one advantage of using microwaves over THz waves as a diagnostic for the filament plasma. THz waves are absorbed strongly by water vapor in air [124, 125]. While there is a band of rotational transitions of molecular oxygen at 60 GHz [126], its attenuation per unit length of propagation peaks at about 11 dB/km [127]. Below 40 GHz, the attenuation of microwaves in air is less than 0.1 dB/km. The attenuation

of the microwaves over the 1.2 meter distance between the plasma and the antennas is negligible. Further, the changing air density inside the gas cell has no effect on the microwave radiation.

Quartz is chosen as the gas cell material because it has very low absorption at microwave frequencies. Microwave absorption is characterized by the loss tangent as opposed to an absorption coefficient. While the latter corresponds to the 1/e folding of a wave's amplitude due to absorption losses, the loss tangent is directly calculated from the material permittivity and conductivity. The permittivity of a dielectric is complex, and can be expressed in terms of relative permittivity as $\epsilon_R = \epsilon'_R - i\epsilon''_R$, where ϵ''_R corresponds to absorption. The loss tangent δ_L is defined as

$$\tan \delta_L = \frac{\sigma + \omega \epsilon''_R}{\omega \epsilon'_R}. \tag{4.1}$$

Equation 4.1 accounts for ohmic and dielectric losses because the two are difficult to discriminate experimentally. The dielectric constant of quartz is a constant $\epsilon_R = 3.8$ for the frequencies of interest [128, 129], while the loss tangent is $\tan \delta_L = 0.00006$ [130] at 10 GHz, and $\tan \delta_L = 0.0002$ at 1 GHz [131]. The thickness of the quartz tube is smaller than the shortest microwave wavelength (at 40 GHz $\lambda = 0.75$ cm) so it is not necessary to account for reflections at the air-quartz interface.

4.3 Results

4.3.1 Time Domain Analysis

Even though we are most interested in the spectrum of the microwaves, there is useful information about the behavior of the radiation that can be gleaned from time domain measurements. Figure 4.2 shows several measurements of the waveform peak-to-peak voltage using the 70 GHz Tektronix oscilloscope. Figure 4.2(a) shows that the microwave waveforms increase in amplitude from atmosphere to 0.5 Torr with both

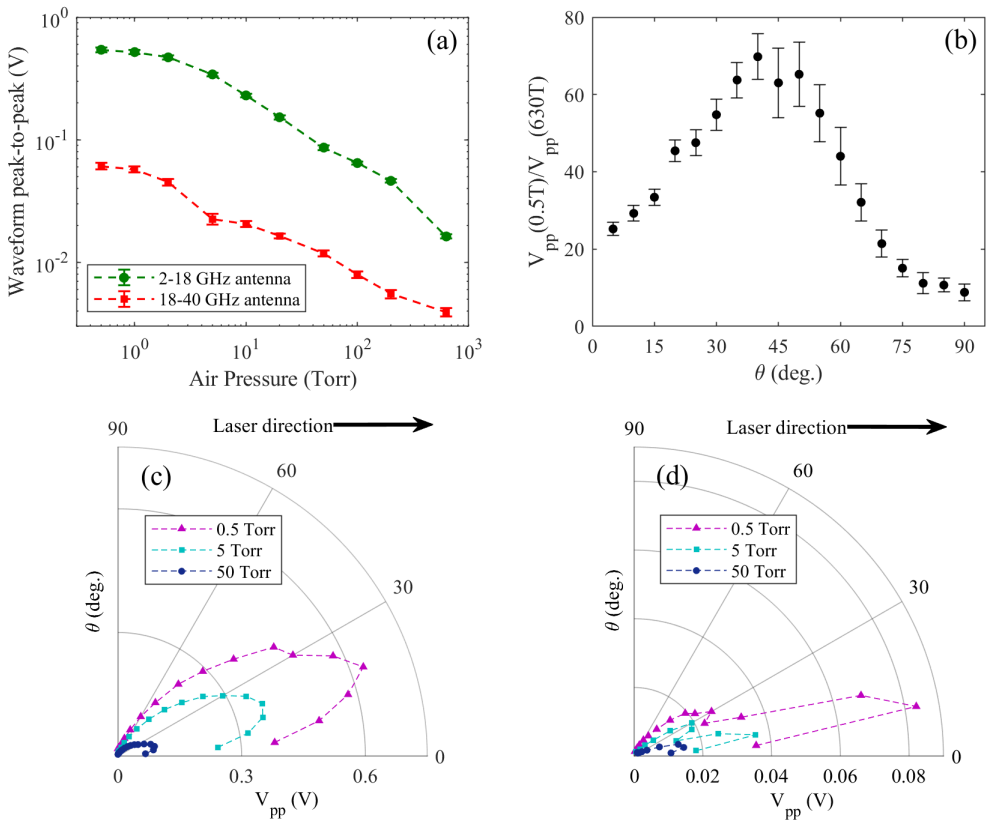

Figure 4.2: Time domain measurements of the peak-to-peak voltage V_{pp} using the 70 GHz Tektronix scope. (a) Dependence of V_{pp} on air pressure at $\theta = 15°$ (b) The ratio of V_{pp} at 0.5 Torr to 630 Torr measured with the 2-18 GHz antenna as a function of emission angle. The angular emission pattern of V_{pp} for the (c) 2-18 GHz and (d) 18-40 GHz horns. The emission patterns are symmetric about the 0 degree axis. The arrows above (c) and (d) indicate the direction of laser propagation.

of the horns that are used to measure calibrated spectra. The microwave amplitude does eventually diminish at pressures below 0.5 Torr, and this is demonstrated and discussed in Section 4.4. The amount by which the waveform increases between atmosphere and 0.5 Torr is shown in Figure 4.2(b) as a function of angle. The increase is a minimum of a factor of 10, while at $\theta \sim 45°$ it is close to a factor of 70. That means the maximum increase in the microwave power is a factor of almost 4.9×10^3.

The angular radiation pattern of the microwaves is shown in Figures 4.2(c) and (d). The shape of the emission pattern is roughly constant with air pressure, although

the magnitude increases significantly as the pressure decreases. In the lab frame, the plasma radiates microwaves in a forward-directed cone with a null along the propagation direction of the laser. This is indicative of an abrupt change in the current density directed parallel to the laser propagation direction. The measurements with the 18-40 GHz horn are more forward-directed than those from the 2-18 GHz horn.

Aside from the peak-to-peak amplitude, the changes in the microwave emission with pressure can be ambiguous in the time domain. Waveforms are the raw measurement, and are shown in order to demonstrate the qualitative behavior of the radiation. Detailed analysis and calibration must be done in the frequency domain. However data in the frequency domain can come across as abstractions since the spectra cannot indicate whether the radiation is continuous or pulsed. Nor can they give a sense the polarity of the current flow induced in the receiver. The purpose in including the waveforms is to supplement the quantitative spectral data with information that may be understood more intuitively.

The microwave pulses from the plasma have a measured duration on the order of a nanosecond at atmospheric pressure. Figure 4.3 shows the microwave waveforms at various values of air pressure with the 2-18 GHz and 18-40 GHz horn antennas at $\theta = 15°$. The waveforms are normalized to their peak-to-peak amplitude to highlight how their shapes change with air pressure. The pulse duration measured with the 2-18 GHz horn increases to several nanoseconds at low pressure. There is a difference between the microwave pulse duration measured with a single horn antenna and the actual pulse duration of the microwave radiation. Estimating the latter based on the duration of the waveforms is not reliable because of instrument dispersion. Also the measurements do not capture the total bandwidth of the radiation, which is needed for an accurate determination of the pulse length. However, it is possible to make qualitative statements about the relative behavior of the waveforms from a single receiver configuration because the instrument bandwidth and dispersion are

constant. In Figure 4.3(a) it is clear that the features of the waveform stretch in time as the pressure decreases. Additional cycles of the pulse rise above the noise at low pressure and look like long-lived relaxation of the waveform. These changes appear in the spectra as a large increase in the low-frequency components of the microwave electric field.

The recombination time of the filament plasma in atmosphere is several nanoseconds [91], which is on the order of the observed microwave pulse duration. The recombination time will increase as collisions between electrons and ions (or electron attachment to oxygen) become less frequent at lower pressure. This may allow the plasma current to exist for longer periods of time, which might explain the apparent increase in the microwave pulse duration. However, if the recombination time increases as pressure decreases, then the relative change in the pulse duration should be close to the relative change in the air pressure, which is a factor of about 10^3. Clearly, Figure 4.3(a) does not show such a dramatic increase in the duration of the microwave waveforms.

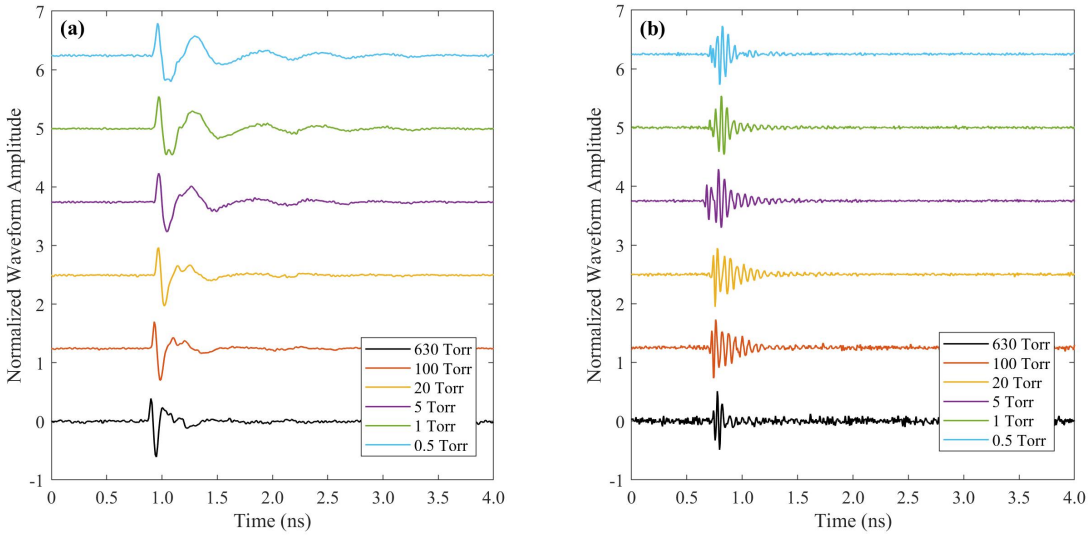

Figure 4.3: Microwave waveforms normalized to their peak-to-peak voltage at different pressures recorded using the (a) 2-18 GHz and (b) 18-40 GHz antennas positioned at $\theta = 15°$. The waveforms have been vertically displaced for clarity.

Figure 4.3(b) makes a similar comparison of normalized waveforms measured with the 18-40 GHz antenna. The blue trace on top corresponds to the minimum air pressure at 0.5 Torr, while the black trace on the bottom corresponds to atmosphere at 630 Torr. As the pressure increases it seems that the features of the waveforms do not demonstrate a clear trend with pressure. The duration of the waveform envelopes appears to increase and then decrease, with the longest pulse occurring at 5 Torr. In addition to the lack of a trend in the pulse duration, there is not an obvious change in the frequency content in the 18-40 GHz range unlike in Figure 4.3(a).

Figure 4.4 is meant to convey similar information to Figure 4.3, but as a function of emission angle at fixed pressure. The waveforms at 0.5 Torr are used because they have the greatest SNR. The changes in the shapes of the waveforms are similar to Figure 4.3. However, the waveforms from the 2-18 GHz waveforms in Figure 4.3(a) contain additional cycles at low pressure. In Figure 4.4(a) it looks like the same waveform repeats at the different emission angles, but with longer periods as the emission angle increases. This implies that the microwaves are Doppler shifting to higher frequencies closer to the laser propagation axis. The frequency component analysis in Section 4.3.2 supports this observation. It should be possible to also see Doppler shifting of the microwaves in Figure 4.4(b) as well, but this does not seem to be the case. The pulse duration does not clearly increase with emission angle, much like the non-monotonic pressure dependence shown in Figure 4.3(b). It is possible that as the emission angle decreases, the content of the pulse is shifting to higher frequencies where the 18-40 GHz antenna may have less gain.

4.3.2 Frequency Domain Analysis

In the frequency domain, changes in the underlying time scales of the microwave generation by the plasma are reflected in the spectral content of the radiated fields. The microwave waveforms that are recorded as a function of emission angle and air

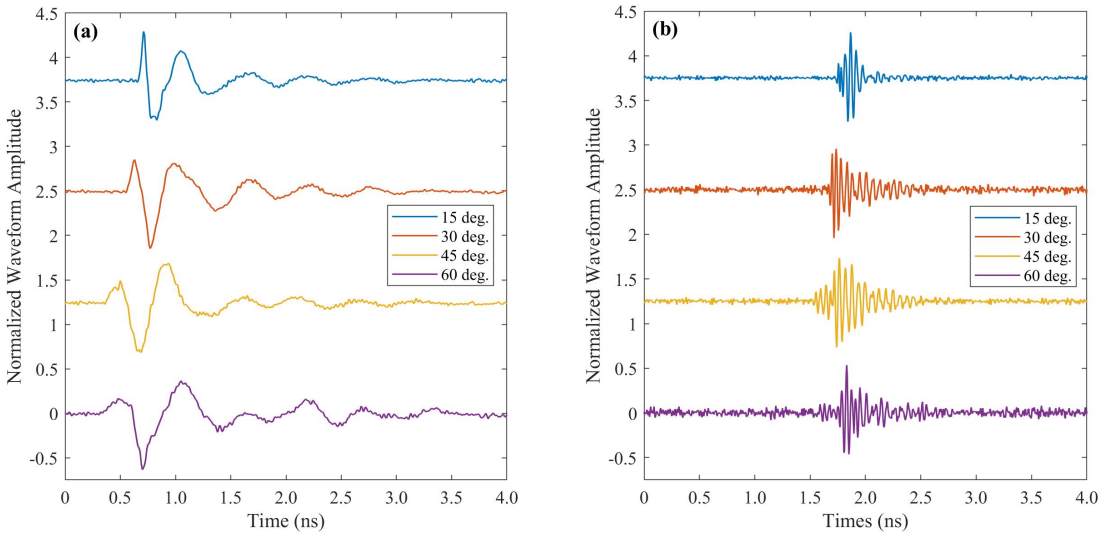

Figure 4.4: Microwave waveforms normalized to their peak-to-peak voltage at a pressure of 0.5 Torr recorded at different emission angles using the (a) 2-18 GHz and (b) 18-40 GHz antennas, respectively. The waveforms have been vertically displaced for clarity.

pressure are analyzed according to the procedure described in Section 3.5. The result is a spectral-angular map of the absolute electric field amplitude at each value of air pressure. Figure 4.5 shows several of the maps from the complete pressure range of the measurements. The maps prove that the microwave emission increases over both the spectral and angular ranges as the pressure decreases. This means that the total conversion efficiency of the laser energy to microwave radiation depends inversely on the air pressure. The angular distribution of the microwave spectrum does not appear to change significantly with pressure, aside from the global amplitude increase. However there are subtle changes, such as a large increase in low frequency components at about 3 GHz and $\theta \sim 15^{\circ}$ relative to high frequency components.

Figure 4.5 gives a quantitative but high level demonstration of the microwave emission. Down-sampling the complete dataset to show dependence of the microwaves on fewer variables clarifies the details of the radiation, and is more accessible to comparison with theoretical predictions of possible radiation mechanisms.

In order to show the large amplitude increase of the low frequencies relative to the

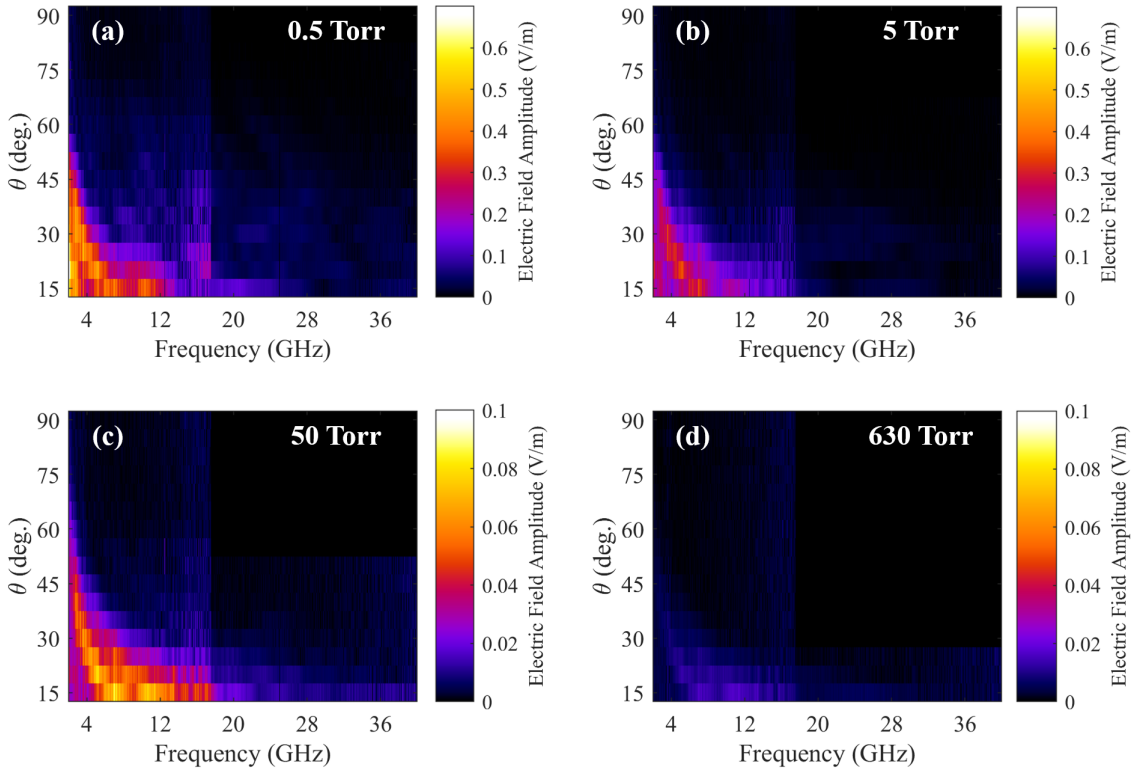

Figure 4.5: Spectrally resolved electric field amplitude of the microwave pulses generated by the plasma as a function of the emission angle and air pressure. The air pressure varies by three orders of magnitude: (a) 0.5 Torr, (b) 5 Torr, (c) 50 Torr, and (d) 630 Torr. The color bars correspond to a maximum field amplitude of 0.7 V/m at 0.5 and 5 Torr, while the maximum is 0.1 V/m for 50 and 630 Torr.

high ones, Figure 4.6 compares lineouts taken at $\theta = 15°$ from the spectral-angular maps at several different values of air pressure. The calibrated spectra quantify the pressure dependence of the waveforms observed at low pressure in Figure 4.3. The low frequency cycles of the waveform contribute to the spectrum as an extreme increase in the amplitude of the low-frequency components of the microwave pulses. This is a circumstantial indication that there is another mechanism in the filament plasma that generates the microwaves that is distinct from that which drives THz radiation. If the THz and microwaves were due to the same current flowing in the plasma, then one would expect that the microwaves are simply the low frequency tail of the THz spectrum. In this case, the frequency components near 40 GHz should have larger amplitude than those near 2 GHz. Furthermore, one would expect the high frequency

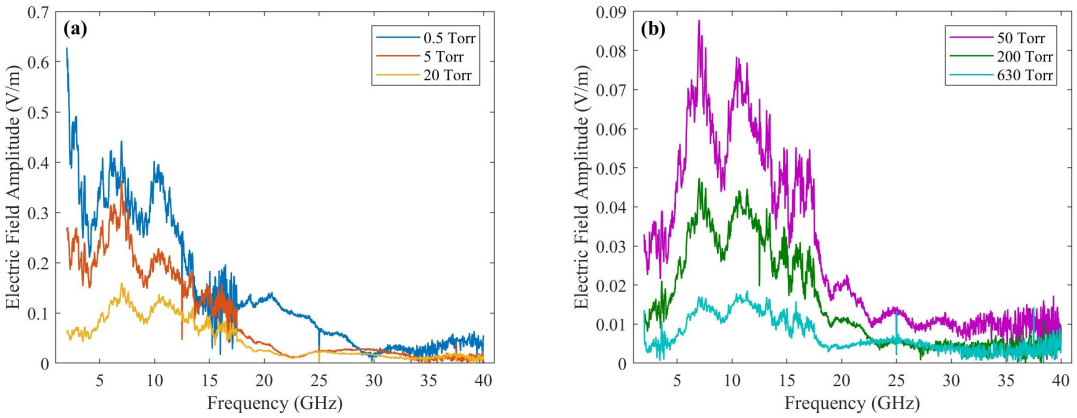

Figure 4.6: Electric field frequency spectra at $\theta = 15°$ at increasing values of air pressure. Note that the maximum value of the ordinate is 0.7 V/m in (a), while it is 0.09 V/m in (b).

components of the radiation to be more sensitive to changes in the plasma current and therefore exhibit larger changes in amplitude with air pressure. We observe the opposite trend over the frequency range achieved in the experiments. This alone is not proof that the microwaves and THz arise from difference sources. However, the unusual pressure dependence of the microwave generation means that the fundamental physics of secondary radiation from the filament plasma warrants further scrutiny.

Figure 4.7 shows the angular dependence of the electric field spectrum at 10 Torr. It is representative of the angular dependence at other values of air pressure, as indicated by Figure 4.5. The stretching in time of the waveform with increasing emission angle observed in Figure 4.4 corresponds to a downward shift of the frequency content. Not only are the higher frequencies of the emission more forward-directed, Figure 4.7 shows that emission at all frequencies is usually greater closer to the laser propagation axis. The maximum spectral amplitude is ~ 0.2 V/m up to $\theta = 30°$, but it quickly drops to ~ 0.1 V/m at $\theta = 45°$. These observations agree with the time domain measurements of the waveform peak-to-peak voltage as a function of emission angle in Figures 4.2(c) and (d), and the spectral-angular maps in Figure 4.5.

While the spectral amplitude generally increases as θ decreases, some frequencies

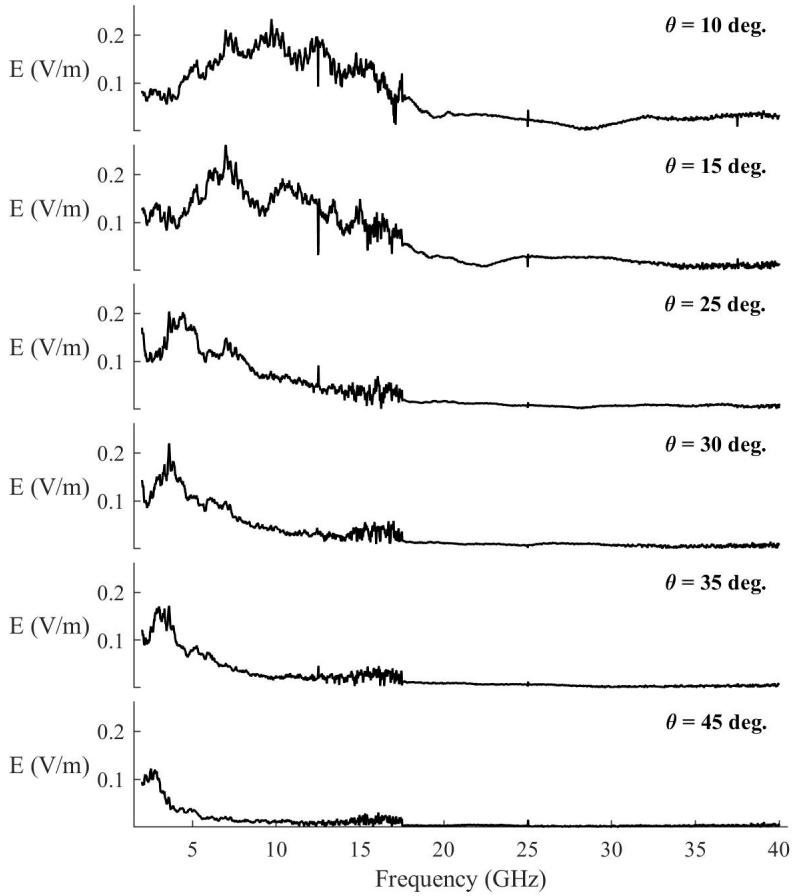

Figure 4.7: Angular dependence of the electric field spectrum at a fixed pressure of 10 Torr.

increase, peak, and diminish within the angular range of the measurements. This can be shown by sampling the spectral-angular maps over a small frequency bandwidth. Figure 4.8 demonstrates the angular dependence of fixed frequency components that are the average of a spectrum over a 1 GHz bandwidth. The frequencies in the plots are the center of each of the 1 GHz frequency windows. Figure 4.8 quantifies the nonuniformity in the amplitude changes of individual frequency components. The 3 GHz component sees the largest amplitude difference, with higher frequency components changing less, but still increasing as the pressure decreases. The 24 GHz and 36 GHz frequency components change in amplitude by a factor of approximately 5

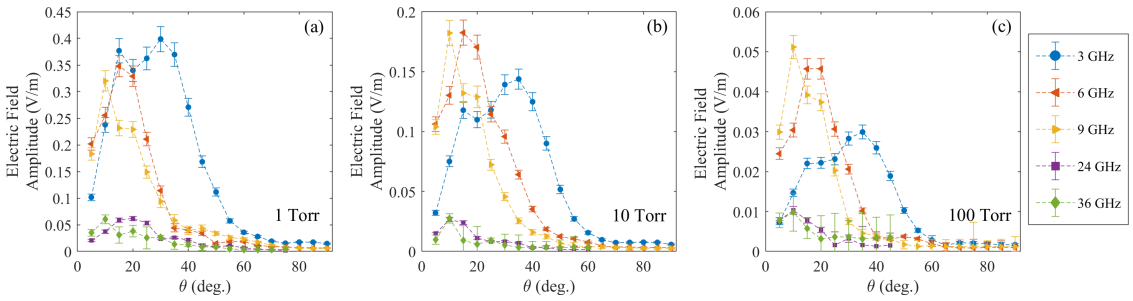

Figure 4.8: Electric field amplitude as a function of emission angle for individual frequency components. These are compared at pressures of (a) 1 Torr, (b) 10 Torr, and (c) 100 Torr. Each data point is an average of many adjacent frequency components out to ±500 MHz, which are centered at each of the frequencies in the plots.

between 1 Torr and 100 Torr, while for the 3-9 GHz components, the change is closer to a factor of 8. The clear angular stratification of the frequency components is further demonstration of the Doppler effect. The emission patterns are consistent with a radiation source in longitudinal relativistic motion.

4.4 Discussion

4.4.1 Gas Pressure Dependence of the Filament Plasma Conductance

The inverse dependence of the microwave yield on air pressure cannot persist in high vacuum. If there is no gas then there is nothing to ionize, and no Kerr nonlinearity to initiate self-focusing and filamentation. The waveform peak-to-peak voltage measurements in Figure 4.9 show that the microwave yield does eventually diminish as expected. The setup used to measure the microwave yield is slightly different than that given in Figure 4.1. A 13 GHz Agilent oscilloscope is used instead of the 70 GHz oscilloscope, and a turbomolecular pump is added to the vacuum line in order to reach pressures below 0.3 Torr. The are two important observations to make in Figure 4.9. The first is that the waveform amplitude increases monotonically over an enormous pressure range. Many laser plasma experiments are performed at base pressures that are not much less than the minimum of Figure 4.9. Even at less

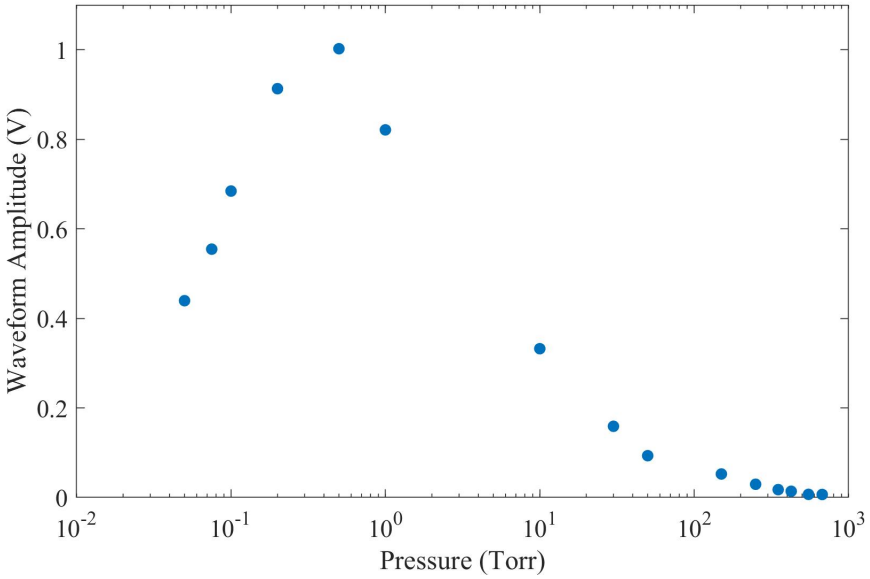

Figure 4.9: Peak-to-peak of voltage waveform measured at $\theta \sim 25°$ with an 18 GHz horn antenna (ComPower AH-118) connected to a 13 GHz oscilloscope (Agilent DSOX91304A).

than 0.1 Torr there is still enough air for the laser to generate plasma. The other important observation is that there is a distinct pressure for maximum microwave emission at 0.5 Torr. This coincides with the lowest pressure measurements reported in Section 4.3.

The behavior of the microwave yield in Section 4.3 and Figure 4.9 can be explained by deriving the conductance of the filament plasma. Conductance is simply the inverse of resistance, and has units of siemens ($\mathrm{S} = 1/\Omega$). Assuming a cylindrically symmetric volume of plasma that has uniform conductivity, σ_p, the conductance of the filament plasma can be estimated

$$G = \sigma_p \frac{A}{L}, \tag{4.2}$$

where A is the cross sectional area, L is the plasma length, and the plasma conductivity is

$$\sigma_p = \frac{\epsilon_0 \omega_{pe}^2}{\nu_m + i\omega}. \tag{4.3}$$

Separating σ_p into real and imaginary parts gives

$$\sigma_p = \mathcal{R}[\sigma_p] + i\mathcal{I}[\sigma_p] = \frac{\epsilon_0 \omega_{pe}^2}{\nu_m^2 + \omega^2} (\nu_m - i\omega) . \tag{4.4}$$

The total electron momentum transfer rate is $\nu_m = \nu_{en} + \nu_{ei}$, where ν_{en} is the electron-neutral collision rate, and ν_{ei} is the electron-ion collision rate

$$\nu_{en} = N\sigma_N \sqrt{\frac{k_B T_e}{m_e}}, \tag{4.5}$$

$$\nu_{ei} = \frac{N_e e^4}{4\pi\epsilon_0^2} \frac{\log\Lambda}{m_e^2 (k_B T_e/m_e)^{3/2}}. \tag{4.6}$$

In the filament plasma neutral collisions dominate the momentum transfer collision rate. The neutral collision cross section is approximately $\sigma_N \sim 5 \times 10^{-15}$ cm^2 [132], and N is the neutral gas density. The electron velocity is taken to be the thermal speed $v_{the} = \sqrt{k_B T_e/m_e}$. The Coulomb logarithm is assumed to be $\log\Lambda \approx 10$. Singly charged ions are assumed in Equation 4.6 so that $N_i = N_e$. At atmospheric pressure, the typical electron density for the plasma generated by a single color filament with an 800 nm laser pulse is on the order of $N_e \sim 10^{16}$ cm^{-3}[133, 134, 135]. The electron density due to multiphoton ionization of the gas depends linearly on the neutral density assuming no depletion of neutrals

$$\frac{dN_e}{dt} = \sigma_K I^K (N - N_e) \rightarrow N_e \sim \sigma_K I^K N \tau_p \tag{4.7}$$

where σ_K is the multiphoton ionization cross section, I is the laser intensity, K is the number of laser photons required to singly ionize an oxygen molecule ($K = 8$ at 800 nm) [136], and τ_p is the laser pulse duration.

Figure 4.10 shows the pressure dependence of ν_{en} and ν_{ei} assuming that $N_e \propto N$ based on Equation 4.7, and that $T_e = 1$ eV is constant with pressure for a given laser pulse energy and duration. Figure 4.10 shows that $\nu_{en} > \nu_{ei}$ by a constant factor

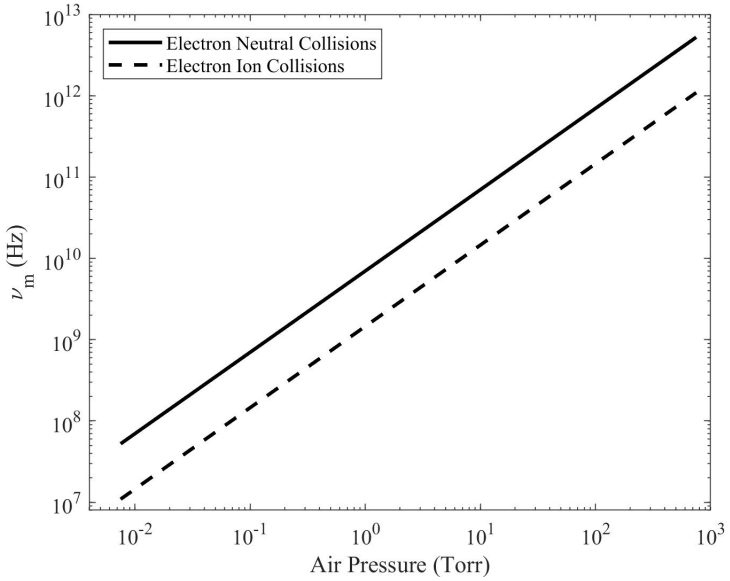

Figure 4.10: The electron neutral and electron ion collision rates from 7.5 mTorr to 750 Torr assuming typical values for the filament plasma of $N_e \sim 10^{16} = \text{cm}^{-3}$ at atmosphere and is proportional to N, and $T_e = 1$ eV but does not change with pressure.

of about 5 given the assumptions above. Therefore the calculation of the plasma conductivity in Equation 4.3 neglects ν_{ei}.

The cross sectional area of the plasma is approximately that of the filamenting laser pulse, so

$$A = \frac{P_{cr}}{I}. \tag{4.8}$$

Equation 4.8 assumes single filament propagation. While at atmospheric pressure the pulse is well into the multifilamentation regime, P_{cr} varies inversely with pressure, so single filamentation is achieved at reduced pressure. An assumption implicit in this analysis is that the plasma behaves as a single contiguous volume regardless of the pressure even though the number of filaments changes. This is reasonable because individual filaments have a diameter of tens to hundreds of microns, which is much smaller than the shortest wavelength of the microwave radiation. It is also possible that the plasma actually is contiguous, and can be considered a 'superfilament' [50]. Regardless, the radiation should not be sensitive to subwavelength spatial features

of the source. The pressure dependence of the transverse packing fraction of the filaments is an interesting question, but any changes still would only result in sub-wavelength modification of the plasma size as far as the microwaves are concerned. I is the clamped intensity [136] in Equation 4.8,

$$I \simeq \left(\frac{2n_2 N_c}{\sigma_K \tau_p N} \right)^{\frac{1}{K-1}}, \tag{4.9}$$

where N_c is the critical plasma density

$$N_c = \epsilon_0 m_e \left(\frac{2\pi c}{e\lambda} \right)^2. \tag{4.10}$$

An estimate of the filament length with external focusing calculated by Geints *et al.* [137] is given by

$$L_{fil} \simeq \frac{f^2}{2z_R} \sqrt{\frac{P_L}{P_{cr}} - 1} \sim \frac{f^2}{2z_R} \sqrt{\frac{P_L}{P_{cr}}}, \tag{4.11}$$

where f is the focal length of the focusing optic, z_R is its Rayleigh length, and P_L is the laser power.

Equations 4.3, 4.8, and 4.11 each depend on the air pressure. While Torr is the preferred unit of pressure throughout the dissertation, the following calculations use atmospheres (0 atm = vacuum, 1 atm = 760 Torr) for the purposes of finding the pressure dependence of G. The following quantities are proportional to pressure, and can be written in terms of a constant that is known at atmospheric pressure, denoted

with the subscript 0, multiplied by the pressure p in atm

$$n_0 = n_{0,0} \times p \simeq 1 \tag{4.12}$$

$$n_2 = n_{2,0} \times p \tag{4.13}$$

$$N = N_0 \times p \tag{4.14}$$

$$\nu_{en} = \nu_{en,0} \times p \tag{4.15}$$

$$\omega_{pe}^2 = \omega_{pe,0}^2 \times p, \tag{4.16}$$

which allows the expression of G as a function solely of p

$$G = \underbrace{\left(\frac{\epsilon_0 \nu_{en,0} \omega_{pe,0}^2 p^2}{\nu_{en,0}^2 p^2 + \omega^2}\right)}_{\sigma_p} \underbrace{\left[\frac{\lambda^2}{4\pi n_0 n_{2,0} p}\left(\frac{2 n_{2,0} p N_c}{\sigma_K \tau_p N_0 p}\right)^{\frac{-1}{K-1}}\right]}_{A} \underbrace{\left(\frac{2 z_R}{f^2 \sqrt{4\pi n_0 n_{2,0} p P_L \lambda^{-2}}}\right)}_{L^{-1}} \tag{4.17}$$

$$= \frac{A\sqrt{p}}{(Bp^2 + \omega^2)}, \tag{4.18}$$

where

$$A = \frac{\epsilon_0 \nu_{en,0} \omega_{pe,0}^2 \lambda^3 z_R}{4(\pi n_0 n_{2,0})^{3/2} f^2 \sqrt{P_L}} \left(\frac{2 n_{2,0} N_c}{\sigma_K \tau_p N_0}\right)^{\frac{-1}{K-1}} \tag{4.19}$$

$$B = \nu_{en,0}^2 \tag{4.20}$$

Equation 4.17 uses the real part of the plasma conductivity from Equation 4.4. The linear index of refraction $n_0 \simeq 1$ does depend on air pressure, but it can only more closely approach unity at low pressure.

It is important to note that P_{cr} is inversely proportional to pressure, while the clamped intensity I is pressure independent. This means that as the pressure is lowered, the critical power and the filament area increase. The filament length depends more weakly on air pressure, and Equations 4.11 and 4.13 predict that the filament becomes shorter at low pressure, such that $L_{fil} \sim \sqrt{p}$. Equations 4.8,4.11, and 4.13

predict that the volume of the filamentation region should scale with pressure like $V_{fil} = A_{fil}L_{fil} \propto \sqrt{p}/p = 1/\sqrt{p}$. However, these scaling relationships assume that the laser propagates in the single filament regime. Measurements of the filament length that include the multi-filament to single filament transition do not agree with this prediction [138]. However the assumptions are sufficient for this simple derivation, which is only meant to illustrate the essential pressure dependence of the plasma conductance.

Figure 4.11 shows the conductance as a function of pressure based on Equations 4.18-4.20 using known constants and a laser power of $P_L = 0.27$ TW, and $\tau_p = 50$ fs, which correspond to the data in Figure 4.9. The values used to calculate G are given in Table 4.1.

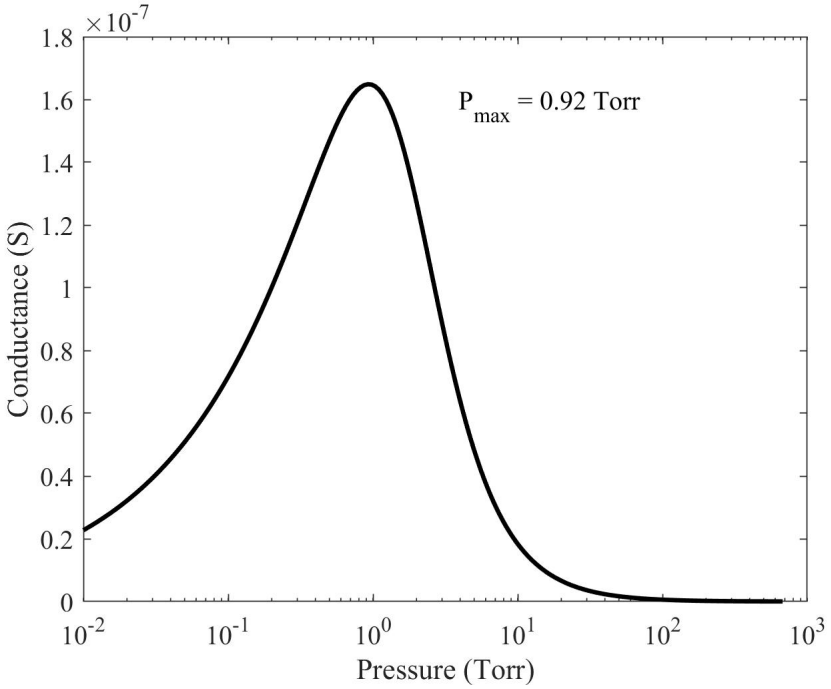

Figure 4.11: Conductance of the filament plasma as a function of air pressure using Equations 4.18-4.20 with the values listed in Table 4.1.

The calculated conductance reproduces all the important features of the microwave pressure dependence shown in Figure 4.9. The peak conductance occurs at nearly

Table 4.1: Values Used to Calculate the Filament Plasma Conductance in Figure 4.11

Microwave frequency, ω	2.00 GHz
Electron-neutral collision rate, $\nu_{en,0}$	5.24 THz
Plasma frequency, $\omega_{pe,0}$	0.898 THz
Laser wavelength, λ	800 nm
Rayleigh length, z_R	0.370 cm
Nonlinear refractive index, $n_{2,0}$	3.20×10^{-19} cm^2/W
Focal length, f	300 cm
Laser power, P_L	0.268 TW
Critical density, N_c	1.74×10^{21} cm^{-3}
Multiphoton ionization cross section, σ_K	3.70×10^{-96} cm^{16}W^{-8}s^{-1}
Laser pulse duration, τ_p	50 fs
Atmospheric number density, N_0	2.50×10^{19} cm^{-3}

the same pressure as the maximum microwave yield (0.92 Torr versus 0.5 Torr) and the latter is measured in coarse pressure increments. The shape of the conductance plot agrees with the experiment and shows that the ability of the filament plasma to radiate is determined by two competing effects: the size of the filament and its conductivity. As the pressure decreases, the conductivity is relatively constant while the filament area goes like $A \sim 1/p$, and $A/L \sim p^{-3/2}$. The plasma conductivity in the low frequency limit, $\omega \ll \nu_{en}$, is

$$\sigma_p = \frac{e^2 n_e}{m_e \nu_{en}}. \tag{4.21}$$

Near atmospheric pressure ν_{en} is on the order of 1 THz, while the microwave frequencies are on the order of 1 GHz. Since both N_e and ν_{en} are proportional to the neutral density, the low frequency conductivity is independent of air pressure. Figure 4.12 estimates the filament plasma conductivity at several microwave frequencies as a function of pressure using the real part of the conductivity from Equation 4.4, and compares with the low frequency limit of Equation 4.21. The low frequency limit is valid when the neutral collision rate is high relative to the microwave frequency of interest, but decreases significantly when the neutral and microwave frequencies

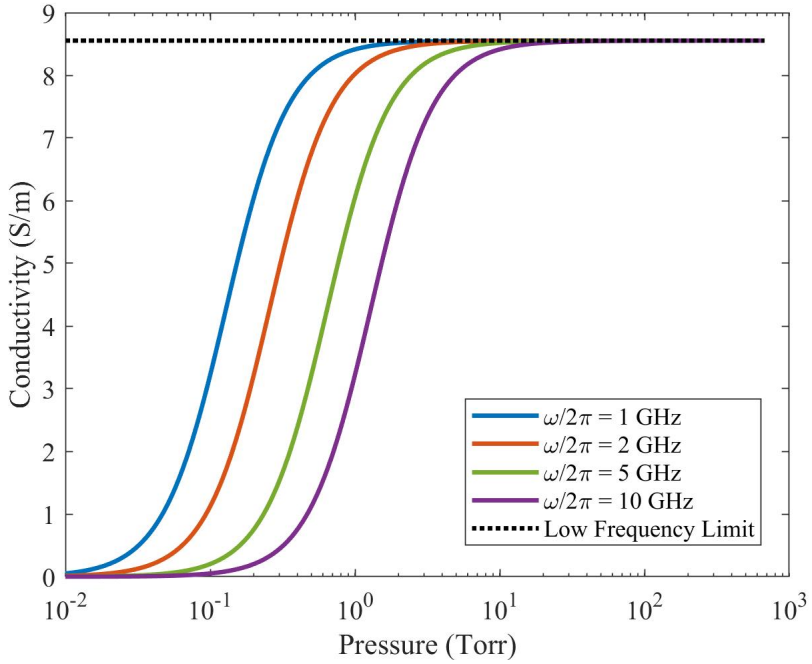

Figure 4.12: The conductivity of the filament plasma based on Equations 4.4 and 4.21. The conductivity at several frequencies is compared with the low frequency limit. The latter holds at high values of air pressure where ν_{en} is large.

approach each other. The higher the microwave frequency, the higher the pressure at which it approaches the collision rate. The conductivity of higher frequencies will diminish at higher values of air pressure. This behavior is the cause for the microwave yield and conductance peaks in Figures 4.9 and 4.11, respectively. The conductance increases until the plasma's conductivity transitions out of the low frequency limit. The rapid decrease in conductivity after the transition dominates the inverse pressure dependence of the plasma's physical dimensions. According to Figure 4.12 the pressure at which the peak occurs depends on the microwave frequency, with higher frequencies peaking at higher values of pressure.

The scaling analysis of the filament area and length predicts that $V_{fil} \propto 1/\sqrt{p}$, and that $A_{fil}/L_{fil} \propto p^{-3/2}$. Clearly these relationships cannot be valid in the limit $p \to 0$. Furthermore, as the pressure decreases and the critical power increases, the contribution of the nonlinearity of the air to the pulse propagation will become very

small, and the scaling will no longer hold. The similar pressure dependence exhibited between the experimental measurement in Figure 4.9 and the result of the calculation shown in Figure 4.12 implies that the rapid decrease in the plasma conductivity at low pressure when $\omega > \nu_{en}$ dominates the pressure dependence of the plasma conductance in the regime when the pressure dependence of A_{fil} and L_{fil} should be no longer related to the nonlinearity of the air.

The results presented in Section 4.3 do not reach a sufficiently low pressure to observe a defined peak in the microwave emission. In those experiments, the pressure dependence of the plasma's diameter and length dominate the microwave yield, and the plasma conductivity remains in the low frequency regime.

4.4.2 Review of Filamentation and Terahertz Generation at Low Pressure

The pressure dependence of the microwave radiation is a new result that builds upon prior studies of filamentation at reduced pressure. Zhou *et al.* measured an increase in current in a filament over a similar frequency range ($>$ 1 GHz) with decreasing pressure in both nitrogen and argon [139] that appears to have the same functional dependence on pressure as the time domain measurements of the microwave amplitude in Figure 4.2(a). Their explanation for the increase is that the electron mean free path increases at low pressure, allowing larger transient charge imbalances to build up in the wake of the laser pulse since there is less impediment to the electron motion due to neutral collisions. This may be true since $\lambda_{mfp} = (N\sigma_N)^{-1}$, but their explanation does not seem to account for the simultaneous decrease in neutral collisions and electron density. For their measurements the current density in the filament plasma should be constant subject to given driving fields, per Equation 4.21 and Figure 4.12. It is important to note that measuring current using an inductive probe as Zhou *et al.* have done is not the same as measuring far field radiation. Antenna theory relates the two quantities by a frequency-dependent radiation efficiency

[90]. For the filament plasma, developing a concept of radiation efficiency relies on finding the radiation generation mechanism. Therefore it is not proper to compare too deeply the details of their results and those presented in this Chapter.

While the mechanism that allows the plasma to radiate at microwave frequencies is unclear, there are prior simulations and measurements that support the idea that the plasma conductance varies inversely with air pressure. Simulations and experiments predict that the on-axis electron density decreases with gas pressure [140], but also that the filament diameter is larger, so that the total number of plasma electrons per unit length is invariant with gas pressure [120]. An increase in the diameter of the filament at low pressure has been observed experimentally using the fluorescence of collisionally excited nitrogen molecules [121], and in the beam mode itself [122]. The angular distribution of the microwaves observed in Figures 4.5 and 4.8 is similar to the prediction of theories of radiation due to single color filaments that describe THz and sub-THz generation initiated by the laser pulse's ponderomotive force [73, 80]. On the other hand, both models predict that emission decreases as the plasma density is lowered, and they neglect the decrease in the electron collision rate with air pressure and its effect on the plasma current.

Terahertz generation as a function of gas pressure has been investigated, however there do not seem to be simulations or experiments which specifically study the case of single color filamentation. There are results for two color filaments, single color plasma sparks made with a hard focused beam, and two color sparks as a function of gas pressure. In general, the THz and microwave generation do not seem to have the same dependence on pressure. For single and two color hard focused laser pulses, the THz yield generally scales with the gas pressure [119, 141, 142, 143]. This is the expected result, where the radiation yield varies with the electron density. In a hard focusing setup, even if the pulse power is above P_{cr}, the short focal distance does not allow self-focusing to develop. Without the action of the Kerr nonlinearity, intensity

clamping of the pulse that ultimately causes the inverse pressure dependence of the microwave yield cannot contribute to the pulse propagation.

In two color filaments, the main feature of the pressure dependence is due to the changing refractive indices for the harmonics and their resulting relative phase. In a long filament there is sufficient walk-off of the fundamental and second harmonic that several cycles of their constructive and destructive interference can be observed, causing a sinusoidal modulation of the THz yield with pressure [144, 145]. Depending on the gas species [145], there can be an increase in the THz yield at reduced pressure, but it is much smaller than the order of magnitude or greater increase we have measured for the microwave electric field. Also, Manceau *et al.* found that the relative index change can be used to control the polarization state of the radiated THz field [146]. The oscillations in the THz yield and the polarization control can be explained by the photocurrent mechanism [119]. In a single color filament where the laser field is not asymmetric in time, the photocurrent mechanism will not be a dominant source of radiation.

There are two discrepancies between the THz and microwave pressure dependence that suggest that they may arise from different mechanisms. The first is the difference in the field enhancement at reduced pressure. Accounting for previous studies, the THz enhancement is much less than an order of magnitude, while for the microwaves the increase is at least an order of magnitude. The second is that for the microwaves, most of the enhancement is seen at the lower frequencies that we measured relative to the high frequency spectral content. These findings are inconsistent with the idea that the microwaves are simply a low frequency spectral tail of the THz radiation, however additional experiments are needed to confirm such a conclusion. Comparison of the microwave and THz spectra as a function of plasma length, and an additional comparative study of the microwave and THz polarization properties may confirm that hypothesis.

4.5 Conclusion

The air pressure dependence of the microwave radiation from the filament plasma gives a strange and interesting result that has not been observed before. The experiments and results presented in this Chapter give detailed quantitative data about the pressure dependence of the microwave frequency spectrum that are enabled by the calibrated receiver that was developed in Chatper III. However since the experiments are the first performed in this frequency range, the findings capture only a limited picture of the behavior of secondary radiation from the filament plasma at reduced pressure. Additional experiments are required to confirm the conclusions made in Section 4.4. The optimization experiments discussed in Chapter VI provide some support to the assertions made here since they are carried out as a function of air pressure. The claims would be strengthened by additional systematic studies, especially of the combined dependence of the microwave yield and spectrum on gas pressure and plasma length.

The non-uniform increase in the low versus high frequency components of the microwave spectra is opposite of what one would expect if the microwaves were a low-frequency tail of the THz radiation. In light of previous work, the rapid growth in the amplitude of low-frequency microwaves suggests that the filament plasma may contain multiple sources of radiation. Also, the studies of THz radiation from two color filaments found much smaller increases in the radiation yield than the order of magnitude enhancement we have measured. It is harder to make a direct comparison to THz studies on the latter point because the literature exclusively treats two color filaments. A comparison of the microwaves and THz pressure dependence with a single color filament would be a helpful next step.

The microwaves may correspond to a late time interval in the filament plasma lifetime. The qualitative dependence of the microwave waveforms on the pressure, namely the slow relaxation observed in Figure 4.3(a), implies that the microwaves

arise due to dynamics of the plasma on slower, nanosecond timescales. This is in contrast to the THz radiation which comes from the picosecond-scale (near the plasma frequency) response of the plasma to ponderomotive or photocurrent drivers. The different frequency regimes of radiation may ultimately serve as probes of the initial and final phases of the filament plasma evolution.

CHAPTER V

Microwave Generation from Two-Color Mid-Infrared Laser Pulses

5.1 Introduction

Presently there is considerable interest across the field of laser plasma physics in measuring how high intensity interactions scale to longer laser wavelengths. The vast majority of experiments to date have used lasers that operate in the near infrared (NIR) which encompasses wavelengths of 0.7 – 1.3 μm. Nonlinear crystals allow for relatively easy access to wavelengths of 0.27 – 0.7 μm (near ultraviolet through visible) through second or third harmonic generation. Efforts to extend high intensity laser technology to the short-wavelength infrared (SWIR) between 1.3 – 3 μm, mid-infrared (MIR) – 3 to 8 μm, and long-wavelength infrared at 8 – 15 μm are beginning to mature. Long pulses of long wavelength laser light sufficient for material spectroscopy have been possible for some time using difference frequency generation [147, 148], including optical parametric oscillators (OPOs) [149, 150]. Short pulse laser systems using optical parametric amplifiers (OPAs) [151] and optical parametric chirped pulse amplification (OPCPA) [152, 153] that are capable of producing long wavelength, 100 GW-class pulses are more recent technological developments [154, 155].

This Chapter compares the microwave radiation measured from plasmas produced

in air by focused NIR pulses from a Ti:sapphire laser at $\lambda = 0.8$ μm, with that generated by MIR pulses at $\lambda = 3.9$ μm. A short focal length off-axis parabola (OAP) focuses the pulses, strongly suppressing nonlinear propagation. The laser pulses do not experience partial filamentation such as in Chapters IV and VI. Longer wavelengths are desirable for laser plasma interactions whose goal is to impart the greatest energy to the plasma electrons [156, 157], since the electron quiver velocity scales with λ, and the ponderomotive potential with λ^2. The critical density at which the laser field becomes evanescent in the plasma also scales like λ^{-2}. If the intensity is high enough to create an overdense plasma, it can resonantly absorb energy from the laser field at the surface where the laser and plasma frequencies are equal [158]. However, our experiments do not use sufficiently high intensities to generate the overdense plasma required for resonant absorption to occur even though the critical density at 3.9 μm ($N_e \sim 7.3 \times 10^{19}$ cm^{-3}) is ~ 24 times smaller than that at 0.8 μm ($N_e \sim 1.7 \times 10^{21}$ cm^{-3}). We expect the average electron energy after the passage of the laser pulse to be greater at long wavelengths because of the relatively more energetic motions of the electrons in the laser field. Therefore the yield of secondary radiation from the plasma should increase at long laser wavelengths. The results of the experiments show an order of magnitude increase in the radiated microwave field amplitude with the 3.9 μm laser pulses.

The Chapter further compares the microwave radiation from plasmas produced with single and two-color laser pulses from both fundamental wavelengths. While the increase in the yield of THz radiation from two-color pulses is well known [119], the effect has never been investigated in the microwave frequency range for any laser wavelength. This Chapter represents the first experiments reporting radiation in the microwave frequency range due to MIR laser pulses, and two-color laser pulses. If the relative phase between laser field harmonics is optimized, we see an additional factor of ~ 3 in the microwave field at $\lambda = 3.9$ μm, and a more modest increase when

$\lambda = 0.8$ μm.

Section 5.2 describes the laser system at the University of Maryland that was used to generate the MIR pulses, the generation of the two-color laser plasmas, and the protocol for making this set of microwave measurements. Section 5.3 compares the microwave radiation in the time and frequency domains for single and two-color laser pulses from the NIR and MIR lasers. The presentation of the measurements is split between two sets of comparisons. The first shows the differences between the radiation due to single color and two color pulses from both lasers. In this case the laser energy is fixed. The second compares only single color pulses from both lasers, and the pulse energy varies. The plasmas radiate microwaves up to and beyond 70 GHz, which is the highest frequency we can measure. The frequency content observed in this experiment is higher than that measured from the experiments in Chapters IV and VI, which may be due to the relatively smaller plasma size. Section 5.4 presents images of the plasma fluorescence which indicate that the dominant wavelength of the microwave radiation may be related to the length of the plasma.

5.2 Experimental Methods

5.2.1 Optical Parametric Amplification for Long Wavelength Ultrashort Pulses

The MIR laser used in the experiments relies on parametric amplification of long wavelength light in nonlinear crystals. Figure 5.1 shows an energy level diagram indicating how parametric amplification works. The presence of photons at the seed pulse frequency, which is called the signal ω_s in this context, stimulates second order difference frequency generation in the nonlinear crystal between ω_s and the photons at the pump pulse frequency, ω_p. The remaining energy generates a photon at a frequency $\omega_i = \omega_p - \omega_s$, which is called the idler. The generation of the idler and

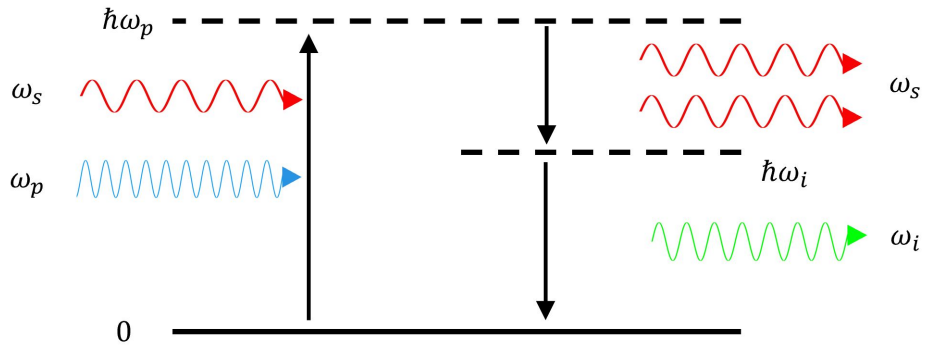

Figure 5.1: Parametric amplification energy level diagram. Difference frequency generation stimulated at ω_s splits the energy of the pump photon into an additional photon at $\hbar\omega_s$ and an idler pulse at $\hbar\omega_i$, such that $\omega_p = \omega_s + \omega_i$.

amplification of the signal are coupled as the waves propagate in the crystal. If the pump, signal, and idler are phase matched ($k_p = k_s + k_i$) the coupling reinforces the amplification at ω_s [66]. OPCPA is the implementation of parametric amplification with a stretched and chirped seed pulse.

In traditional CPA, a laser gain crystal (such as Ti:sapphire) stores the energy of the pump beam in an excited atomic state for a long time relative to the delay between the pump and seed pulses, so their relative timing is not as critical. A stretched seed pulse extracts energy that was deposited in the gain medium by the pump pulse before its arrival. In both CPA and OPCPA, the maximum stretching ratio of the broadband seed is limited by the acceptable amount of higher order dispersion in the gain or nonlinear crystal [159]. The compressor gratings are only meant to reverse the initial chirp (second order dispersion). This imposes a practical limit on the seed pulse duration of $\sim$ 100 ps [160]. When the pump energy is stored for a long time it is effective to pump with a high energy long pulse from a nanosecond laser. Parametric amplification instantaneously transfers energy from the pump to the seed without energy storage in the nonlinear crystal. In OPCPA, transferring large amounts of energy to the stretched seed means matching its duration with that of the pump pulse. Furthermore, the relative timing jitter between the pump and the seed must be very

small. This presents two challenges for generating high peak power pulses. First, high energy picosecond pump lasers with low jitter were not available until recently [161, 162] and are still uncommon. Second, large area nonlinear crystals are needed to transversely spread out the higher intensity of the short duration pump pulse and the amplified seed. High peak power, long wavelength OPAs are an emerging technology at present because of ongoing developments in pump laser technology and preparation of large area nonlinear crystals that transmit in the MIR.

The MIR laser used in the experiments combines an OPA initial amplifier stage with a final amplifier that relies on three OPCPA stages [163]. The synchronization of the seed and the pump beams in the nonlinear crystals of the final amplifier comes from splitting the pump pulse into three, and managing the relative delays using the optical path length differences between the OPCPA stages. The laser generates pulses at $\lambda = 3.9$ μm with energy up to 25 mJ in a 100 fs pulse duration (the maximum peak power is 250 GW) at a repetition rate of 20 Hz.

5.2.2 Plasma Generation with a Two-Color Laser Pulse

The most common method for generating a two-color pulse is to transmit laser light at the fundamental frequency through a second harmonic crystal, which partially converts the field from frequency ω to 2ω. The significance of two-color laser pulses for generating THz radiation from filament plasmas and hard focused plasma sparks has been established in Chapters I and IV as most of the ongoing research in THz generation from laser plasmas relies on the two color scheme. Two color THz generation with laser field components other than the fundamental and second harmonic has been studied [164], but superposition of the fundamental and second harmonic is by far the most common technique.

Second harmonic generation is a second order nonlinear process where the electric field of the second harmonic is proportional to the nonlinear polarization induced at

2ω in the medium by the fundamental

$$E(2\omega) \propto P^{(2)}(2\omega) = \epsilon_0 \chi^{(2)} E^2(\omega), \tag{5.1}$$

where $\chi^{(2)}$ is the second order nonlinear susceptibility. While there are many good explanations of second harmonic generation in crystals elsewhere (see for example [165]) it is briefly addressed here because the experiments use different crystals to frequency double the NIR and MIR laser light, and the output polarization of the harmonics can differ between them. This polarization difference ultimately affects the motion of the plasma electrons in the two-color laser field.

The conversion efficiency depends on matching the phase of the fundamental and second harmonic waves in the crystal. A wavevector mismatch of Δk in a crystal of length L (L is much less than the coherence length) scales the second harmonic generation intensity by

$$I(2\omega) = I_0(2\omega) \left(\frac{\sin(\Delta k L/2)}{\Delta k L/2} \right)^2, \tag{5.2}$$

where $\Delta k = 2k_\omega - k_{2\omega}$ [66]. In order to meet the phase matching condition $\Delta k \sim 0$ in a positively dispersive medium (linear refractive index increases with ω) it is necessary to use the crystal birefringence to delay the fundamental relative to the second harmonic. There is a popular scheme for NIR second harmonic generation using a β-barium borate (BBO) crystal. Two photons of the fundamental polarized along the ordinary axis of the BBO crystal generate one photon at the second harmonic whose field is polarized along the extraordinary axis. This situation is called type-I phase matching and results in fundamental and second harmonic waves that are cross-polarized.

BBO becomes opaque to wavelengths above 3.5 μm [166], so it cannot be used to frequency double the MIR pulses used in the experiment. Gallium selenide (GaSe) is

used instead. However GaSe may exhibit type-0 phase matching in addition to type-I. Type-0 phase matching is also called quasi-phase matching as it results from a change in the direction of the ordinary and extraordinary crystal axes throughout its depth [167]. The hexagonal crystal structure of GaSe forms layers that can cause such a change in the orientation of the axes [168]. In quasi-phase matching, the fundamental and second harmonic waves are co-polarized.

A MIR polarizer was not available to examine the relative polarization of the 3.9 μm fundamental and 1.95 μm second harmonic, but there was a spectrometer with range out to ~ 2.5 μm. The MIR microwave measurements are performed using the crystal orientation that maximizes the second harmonic yield, but we do not know if this is due primarily to type-I or type-0 phase matching in the GaSe crystal. Therefore we do not know the relative polarization of the harmonics in the MIR.

The comparison experiment performed in the NIR instead uses the orientation of the BBO crystal that maximizes the microwave yield in the 18-40 GHz frequency range. The main reason for changing the conditions between the NIR and MIR experiments is the small microwave yield observed at laser energies that match the MIR experiment. The 18-40 GHz frequency range is chosen because that antenna has the largest gain of the available antennas, and therefore shows the clearest indication of the conditions that produce the largest microwave yield. The crystal orientation is far detuned from that which produces the most second harmonic, 0.4 μm light. In fact the azimuthal rotation of the BBO that produces the greatest microwave yield is only about 5° off from that which minimizes the second harmonic generation. This is because the fundamental and second harmonic are not co-polarized in a type-I crystal. The relative polarization between the fundamental and second harmonic can be varied because the second harmonic is always polarized along the extraordinary axis. The portion of the fundamental that can be converted to second harmonic is given by the projection of its polarization vector on to the ordinary axis, which

reduces the conversion efficiency according to Equation 5.2. The result is that the angle between the polarization of the harmonics is smaller than the cross-polarization that results from ideal type-I phase matching. However, the birefringence of the BBO causes the fundamental to become elliptically polarized when it leaves the crystal. We can estimate what the exit polarization state is by calculating the phase retardation, Γ, for 0.8 μm waves in a 100 μm thick BBO crystal.

$$\Gamma = \frac{2\pi(n_0 - n_e)L}{\lambda} = \frac{2\pi(1.6605 - 1.5455) \times 10^{-4}\ \mathrm{m}}{8 \times 10^{-7}\ \mathrm{m}} \sim \frac{3\pi}{2} \tag{5.3}$$

This value of phase retardation does not result in significant ellipticity of the polarization state at a 5° rotation of the crystal axes relative to the laser polarization, but it is important to acknowledge the birefringence of the BBO crystal since the polarization state of the laser field after the crystal determines the electron trajectories in the plasma. There is an optimum crystal orientation for the microwave generation that results from a trade-off between the degree of co-polarization of the harmonics and the second harmonic conversion efficiency. Similar behavior has been observed in THz generation measurements [169].

It would be trivial to avoid this complication by using a half waveplate to rotate the second harmonic polarization and co-polarize it with the fundamental after generating it in the BBO crystal. This was attempted, but ultimately rejected because the group velocity walk-off of the harmonics in the waveplate prevented control of their relative phase, which is critical to demonstrating the two-color effect for the microwaves. Because the relative polarization is not known for the MIR experiment, we decided it was more important to prioritize control of the relative phase, and matching the pulse intensity and focal geometry between the experiments. Proper polarization control of the harmonics is left for a future experiment.

Plasma generation due to two color pulses unfolds differently than the single color

case. The strong field ionization rate depends the instantaneous value of the electric field, so it will change with the relative phase of the harmonics assuming they are co-polarized. Once electrons have been ionized from the air, their motion in a two-color field is aperiodic. The electrons do not experience a net transverse displacement in a plane wave monochromatic laser field. However in a two color laser field, the distance by which an electron moves off-axis in a half-cycle of the field is not canceled by the next half-cycle. The electrons drift along the polarization direction of the combined ω and 2ω fields, which constitutes a macroscopic current when the drift motion is integrated over the laser pulse duration. This is the photocurrent mechanism, and it is the current source for THz radiation due to a two color laser pulse [170].

5.2.3 Experimental Setup for NIR and MIR Two-Color Measurements

Figure 5.2 shows the setup for both the NIR and MIR two-color microwave generation experiments. The MIR laser system is located at the University of Maryland, while the NIR laser system is that used in the experiments described in Chapter IV. A diaphragm iris at the laser output limits the aperture to a 10 mm diameter. The energy of the input pulses at either $\lambda = 0.8$ μm or 3.9 μm is attenuated before transmission through the second harmonic crystal. The relative phase of the fundamental and second harmonic waves is controlled by the path length difference of the waves in a glass microscope coverslip placed after the second harmonic crystal. An OAP with a 15 cm reflected focal length focuses the pulses at $f/15$. The focused pulses make a plasma spark that is ≤ 1 cm in length. Four broadband horn antennas are used over many different laser shots to receive the microwaves radiated from the plasma. The antennas collectively cover the frequency range of 2-70 GHz, and their characteristics are described in Chapter III. The distance from the plasma to the antenna aperture in all cases is 55 cm. A Tektronix DPO77002SX with 70 GHz real time bandwidth, and a maximum sampling rate of 200 GS/s digitizes the microwave waveforms. The

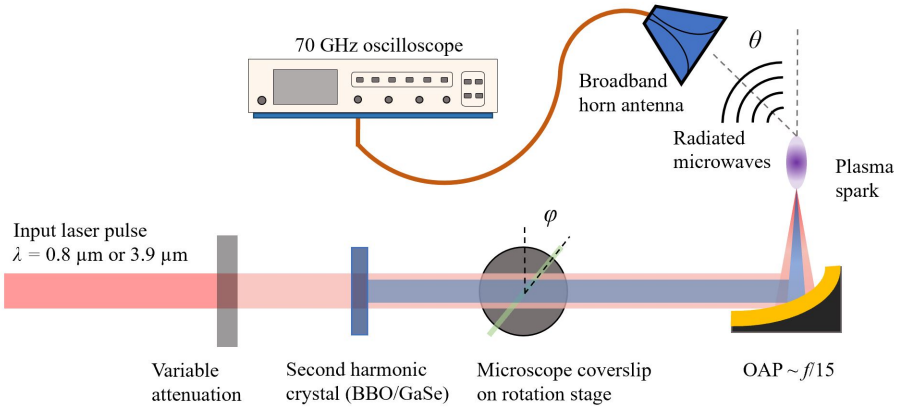

Figure 5.2: Experimental setup for the NIR and MIR measurements. Four horn antennas receive the microwave radiation, whose waveform is digitized using a Tektronix DPO77002SX. The distance between the plasma and antenna aperture is 55 cm. The beam diameter is 10 mm at the aperture of both laser systems. For the two color experiments, the beam energy after the microscope coverslip is 2 ± 0.3 mJ. The coverslip and second harmonic crystal are removed to conduct single color experiments.

spectrum of the microwaves calculated from the Fourier transform of the time domain waveform is absolutely calibrated using the procedure given in Chapter III.

Spectral-angular maps are recorded with both the NIR and MIR laser systems in 10° increments from $\theta \simeq 0°$ to 90°, and frequencies of 2-70 GHz for the base pulse energy at 2 mJ with single and two color pulses. Because of the large signal, we are able to compare spectral-angular maps of the microwaves from the MIR pulses at the relative phase that optimizes the emissions with maps that correspond to detuned values of the relative phase. With the NIR pulses, the only two color case that produces sufficient signal is when the relative phase is optimized. Finally, the energy dependence of the NIR and MIR single color pulses is compared from 2-70 GHz in larger angular increments.

The pulse energy in the base test case for the two color experiments, and the single color experiments they are compared to, is limited by a desire to stay far below the damage tolerance of the GaSe crystal. Since it is unknown for short pulses of MIR light, the energy incident on the GaSe crystal is a maximum of about 4 mJ.

Fresnel reflections from the crystal and the glass coverslip cause about 50% energy loss at $\lambda = 3.9$ μm, and about 30% at $\lambda = 0.8$ μm. For the NIR pulses and BBO crystal, the input energy is adjusted so that in both the NIR and MIR cases, the laser energy after the coverslip is 2.0 ± 0.3 mJ. The second harmonic crystal and coverslip are removed for the single color comparison measurements, and the pulse energy is attenuated to match the two color experiments. The pulse duration for the MIR laser is estimated to be ~ 100 fs.

In the configuration described here, the single and two color MIR laser pulses produce easily measurable microwave fields. For the NIR laser, a ~ 20 GW pulse (2 mJ in 100 fs) focused at $f/15$ does not produce microwave fields with amplitudes that are reliably above the microwave receiver's noise floor. Figure 5.3 compares microwave waveforms due to single color NIR pulses with 12 mJ energy that have durations of $\tau_p \sim 50$ fs versus $\tau_p \sim 100$ fs. The shortest pulse duration generates the brightest supercontinuum from an air plasma, which is used to find $\tau_p \sim 50$ fs. A single shot autocorrelator verified that the brightest supercontinuum occurs at a pulse duration of 46 fs, which is about the same as 50 fs given the autocorrelator's 10% uncertainty at best. It was also used to estimate a pulse duration that is approximately the same as that of the MIR laser ($\tau_p = 93$ fs). At 12 mJ the waveforms due to the longer

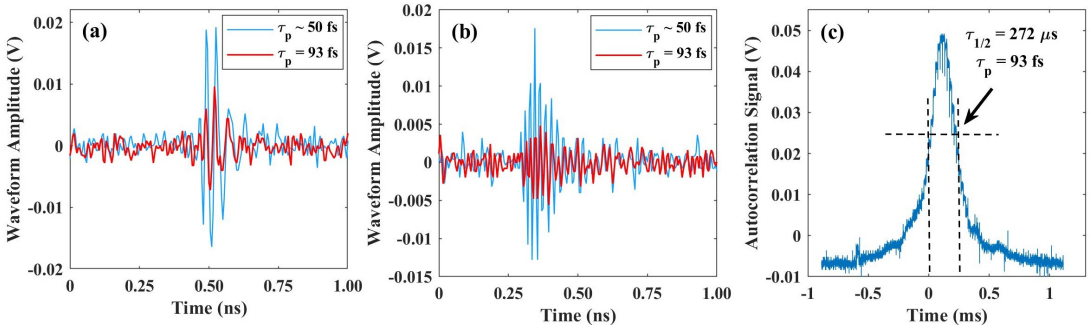

Figure 5.3: Waveforms recorded with (a) 18-40 GHz, and (b) 50-70 GHz antennas at a position of $\theta = 30°$ due to NIR laser pulses ($\lambda = 0.8$ μm) with 12 mJ energy at $\tau_p \sim 50$ fs and $\tau_p = 93$ fs. (c) An example trace from a single shot autocorrelator which allows estimation of the laser pulse duration.

laser pulses are barely above the receiver noise floor. Using the 100 fs pulses but reducing the energy to 2 mJ will not give enough signal for a useful comparison with the MIR laser. Moving the antenna closer to the plasma to increase the signal is undesirable because the near field effects will become significant and invalidate the receiver calibration. Therefore, we decided to shorten the pulse duration of the NIR laser system to $\tau_p \sim 50$ fs. The results presented in Section 5.3 for the NIR laser produced microwave radiation all use $\tau_p \sim 50$ fs. The peak pulse intensity with the NIR laser is about twice that with the MIR laser (assuming comparable focal spot sizes). In spite of using higher intensity pulses, the microwave yield due to the NIR laser is much smaller than that due to the MIR laser.

The glass microscope coverslip can control the relative phase between the fundamental and second harmonic of both the NIR and MIR pulses by slightly changing their respective path lengths through the glass. The path lengths depend on the thickness of the glass traversed, and the angle of incidence, φ, where $\varphi = 0$ means that the two color pulse is normal on the air-glass interface. Figure 5.4 gives a diagram of how the different wavelengths of the pulse refract in the coverslip. The angles

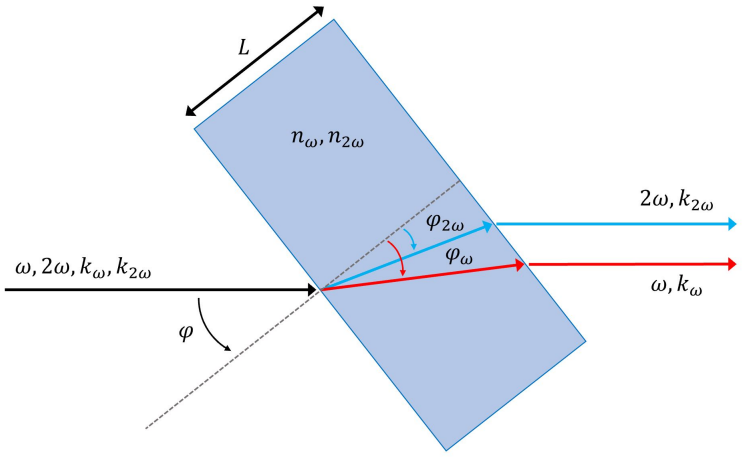

Figure 5.4: The fundamental and second harmonic propagate in a microscope coverslip of thickness L with an angle of incidence φ. Due to refraction and the wavelength dependence of the phase velocity, propagation through the glass imposes a phase delay between the fundamental and second harmonic.

by which the fundamental and second harmonic refract are given by Snell's law

$$\varphi_\omega = \sin^{-1}\left(\frac{\sin\varphi}{n_\omega}\right) \tag{5.4}$$

$$\varphi_{2\omega} = \sin^{-1}\left(\frac{\sin\varphi}{n_{2\omega}}\right), \tag{5.5}$$

where φ_ω and $\varphi_{2\omega}$ are the angles at which the fundamental and second harmonic propagate in the glass relative to normal incidence, respectively. Equations 5.4 and 5.5 assumed that in the air $n_\omega = n_{2\omega} = 1$. Considering that the change in phase of a wave over a distance x is $\Delta\psi = 2\pi n x/\lambda$, we can use the geometry of Figure 5.4 and the angles φ_ω and $\varphi_{2\omega}$ to find the total path length difference and therefore the phase difference for a coverslip thickness L

$$\Delta\psi = 2\pi L\left[\frac{n_\omega}{\lambda_\omega\cos\varphi_\omega} - \frac{n_{2\omega}}{\lambda_{2\omega}\cos\varphi_{2\omega}} + \frac{\sin\varphi}{\lambda_{2\omega}}\left(\tan\varphi_\omega - \tan\varphi_{2\omega}\right)\right]. \tag{5.6}$$

The coverslip is made of borosilicate glass, and its refractive index is well characterized over a large wavelength range [171]. For the purposes of the experiments, it is sufficient to observe the dependence of the microwave yield on the angle φ. While Equation 5.6 indicates that propagating through the glass provides a means of changing the relative phase, it does not account for difference in phase and group velocities of the fundamental and second harmonic after leaving the glass in the air up to the position where plasma generation starts. Even though Equation 5.6 is based on the assumption that the linear refractive index in air is unity regardless of wavelength, this is not strictly true and will become significant over long propagation distances. The length of the beam path between the GaSe crystal and the plasma is 190 cm, so we cannot expect that the absolute phase difference at the output of the glass is the same as that when ionization occurs. It is not necessary to know the absolute value of $\Delta\psi$ to prove that the two color pulse affects the microwaves. We need only

observe a change in the microwave radiation that is periodic in the total thickness of the glass through with the pulses propagate.

5.3 Results

The measurements compare two related situations. The first examines single and two color pulses with 2 mJ energy in the MIR and NIR including the relative phase of the fundamental and second harmonic. The second examines the laser energy dependence of the microwaves with single color MIR and NIR pulses. Both demonstrate that the MIR pulses result in significantly greater microwave yields. The comparison of the single and two color cases demonstrates that the relative phase of the fundamental and second harmonic can be tuned to further enhance the microwave yield relative to the single color cases. On the other hand, the single color pulse energy dependence measurements of the microwaves give an unexpected result: the center frequencies of the microwave spectra vary inversely with the laser energy. This is observed using both laser systems, and therefore is a repeatable effect.

5.3.1 Single Versus Two Color Laser Pulses and the Two Color Relative Phase

Time Domain Analysis

The large microwave yield produced by the MIR laser pulses relative to the NIR pulses is evident from the peak-to-peak voltage amplitude, V_{pp}, of the microwave waveforms across the frequency range of three of the antennas (18-40 GHz, 40-60 GHz, and 50-70 GHz) that receive the radiation. The signal in the 2-18 GHz frequency range is quite small, and therefore does not illustrate the qualitative aspects of the microwave radiation as clearly as the other antennas. Figure 5.5 compares the angular distributions of the voltage amplitudes measured with each of the antennas due to

single and two color pulses with both laser systems. All test cases represented in Figure 5.5 use a pulse energy of 2 mJ.

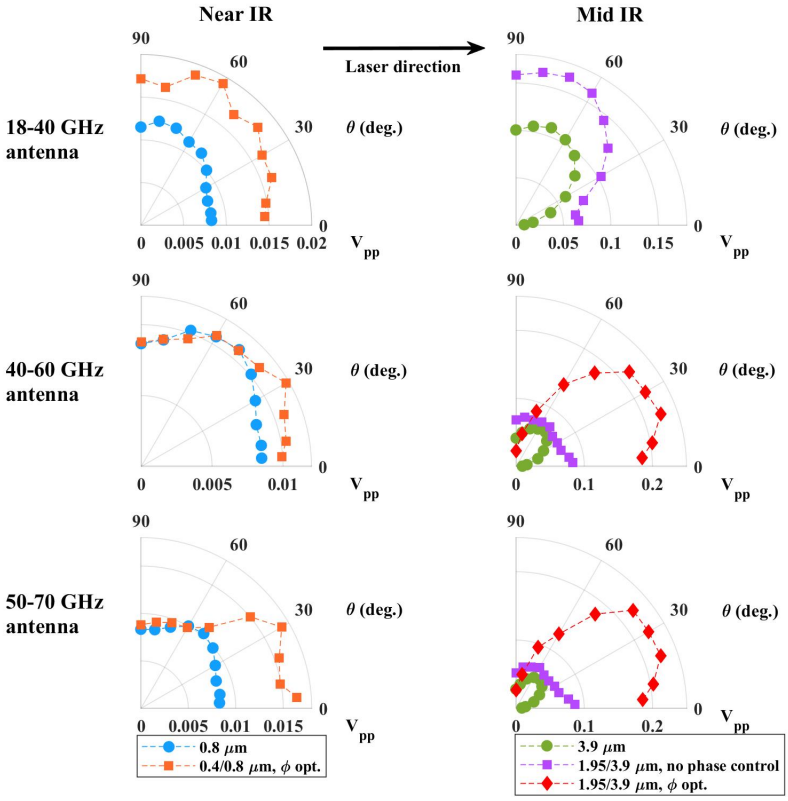

Figure 5.5: The left column of polar plots compares the single color NIR peak to peak voltages (blue circles) with the two color NIR case (orange squares). The relative phase is optimized in the latter case. The right column also compares the fundamental (green circles) with a pair of two color cases: when the glass coverslip is removed (purple squares) and when the angle of the coverslip is tuned to maximize the microwave yield (red diamonds). Each row of polar plots corresponds to the different antenna frequency ranges.

The microwaves due to the single color MIR pulses result in a V_{pp} that is as much as an order of magnitude larger than the single color NIR pulses. V_{pp} for the two color NIR pulses is about 150% of the single color case at 18-40 GHz, and in the forward direction for 50-70 GHz but only if the relative phase of the harmonics is optimized to give the largest microwave signals. This is modest compared to the order of magnitude increase that is typically observed at THz frequencies [169]. However the relatively small enhancement is likely due in part to the polarization mismatch of the harmonics that we did not correct. A similar 150% increase in V_{pp} for the two

color relative to single color MIR pulses is also found. However this is accomplished without inserting the glass coverslip into the beam to control the relative phase. If the coverslip is used to optimize the relative phase, we observe an additional factor of $\sim$ 3 increase in V_{pp} over the un-optimized two color case from 40-70 GHz. The phase-optimized two color MIR pulses have a V_{pp} that is about 25 times greater than the single color NIR pulses at the same laser pulse energy.

Figure 5.5 demonstrates that a two color laser pulse can significantly alter the microwave emission. To further explore the two color effect on the microwave radiation, Figure 5.6 examines V_{pp} for the same horn antennas but as a function of the relative phase between the fundamental and second harmonic. Figures 5.6(a) and (c) correspond to two color MIR laser pulses, while Figures 5.6(b) and (d) correspond to two color NIR pulses. A general feature of the measurements are peaks in the dependence of V_{pp} on the relative phase. The periodicity confirms that the microwave radiation is changing with the relative phase of the fundamental and second harmonic of both

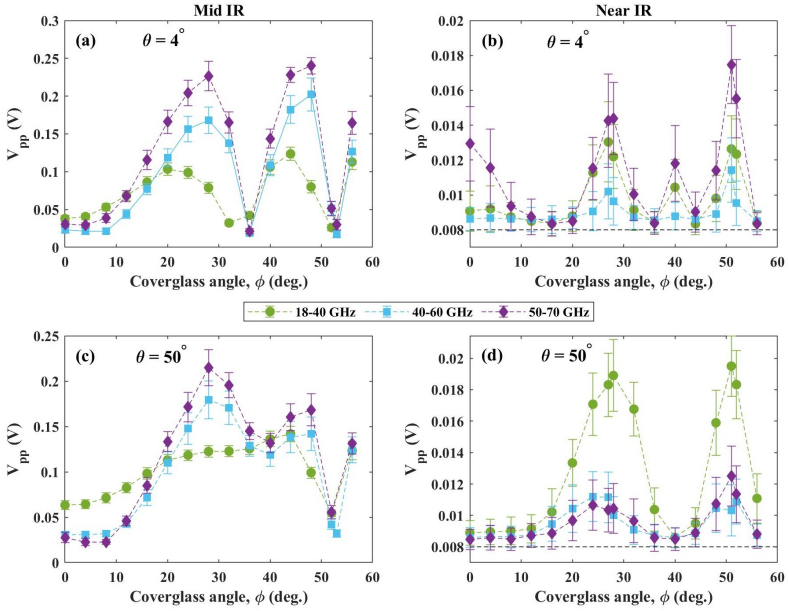

Figure 5.6: Waveform peak-to-peak voltage as a function of the glass coverslip angle φ with the 18-40 GHz, 40-60 GHz, and 50-70 GHz antennas positioned at $\theta = 4°$ for (a) MIR and (b) NIR two color laser pulses. The measurements are repeated in (c) and (d) but with the antennas at $\theta = 50°$.

the MIR and NIR laser pulses. The effect is very pronounced with the MIR pulses, as certain values of the relative phase can strongly suppress the microwave emission in the forward direction ($\theta = 4^{\circ}$), although this suppression does not also occur as strongly at more oblique angles ($\theta = 50^{\circ}$). For the MIR case in the 18-40 GHz frequency range, the relative phase dependence is somewhat different than for the 40-70 GHz frequency range. In Figure 5.6(a), the peak emission for 18-40 GHz occurs at values of the relative phase that are noticeably offset from the higher frequencies. Figure 5.6(c) shows that there is a single maximum for 18-40 GHz, while there are two for the higher frequency antennas. This indicates that the two color effect for the microwaves is frequency dependent. We did not perform a study to investigate if the emission of specific microwave frequencies is optimized at different angular positions for different values of relative phase. While it is possible that such dependence exists, and would require finely resolved spectral-angular maps at each value of the relative phase, its observation is left for future experiments.

While Figures 5.5 and 5.6 show that there is a two color effect for the microwaves, it is unclear whether or not it is due to the photocurrent mechanism that is believed to be responsible for the enhancement of THz radiation from two color laser plasmas [119, 170, 172]. While two color pulses can increase the THz energy generation efficiency by more than an order of magnitude [173], the increase more modest relatively speaking for the microwaves in each of the NIR and MIR cases. Further, our data show that the relative phase not only affects the yield of microwave radiation, but also its angular emission pattern.

The microwave waveforms themselves are somewhat different than those observed with the longitudinally extended filament plasmas from the gas pressure dependence experiments of Chapter IV. While the pulse duration was on the order of 1 ns in the latter case, Figure 5.7 shows that it is ≤ 0.5 ns with the hard focused MIR and NIR plasma sparks. However the waveform shape appears to change among the single

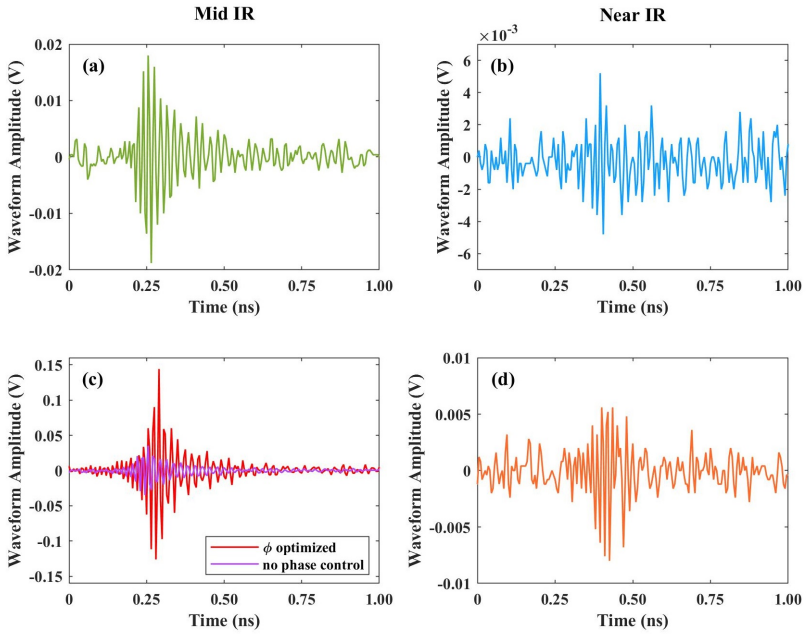

Figure 5.7: Waveforms recorded with the 50-70 GHz antenna at $\theta = 30°$ for (a) single color pulses at $\lambda = 3.9$ μm, (b) single color pulses at $\lambda = 0.8$ μm, (c) two color MIR pulses without phase control (purple trace) and with the relative phase optimized (red trace), and (d) two color NIR pulses with the relative phase optimized.

color, two color, NIR and MIR cases. Not much can be said about the single color NIR waveform in Figure 5.7(b) because its peak is very near to the receiver noise floor. However, the single color MIR pulse does not have the one large amplitude cycle seen for the opitimzed two color MIR pulse. The envelopes of the two color MIR pulses are different from the optimized two color NIR pulse as well.

Figure 5.8 shows how the waveforms in the two color MIR case change in amplitude and shape for the 50-70 GHz antenna as a function of the relative phase. The values of φ chosen correspond to the maxima and minima of V_{pp} for the 50-70 GHz and 40-60 GHz antennas shown in Figure 5.6(a). The waveforms shift along the time axes of the plots due to trigger jitter. Figures 5.6(a) and (c) show that the amplitude fluctuations of the waveforms are on the order of 10%, so we can consider the differences in waveform shapes in Figure 5.8 likely to be due to the relative phase of the harmonics, and not shot-to-shot fluctuations of the microwave signals. The raw waveforms are

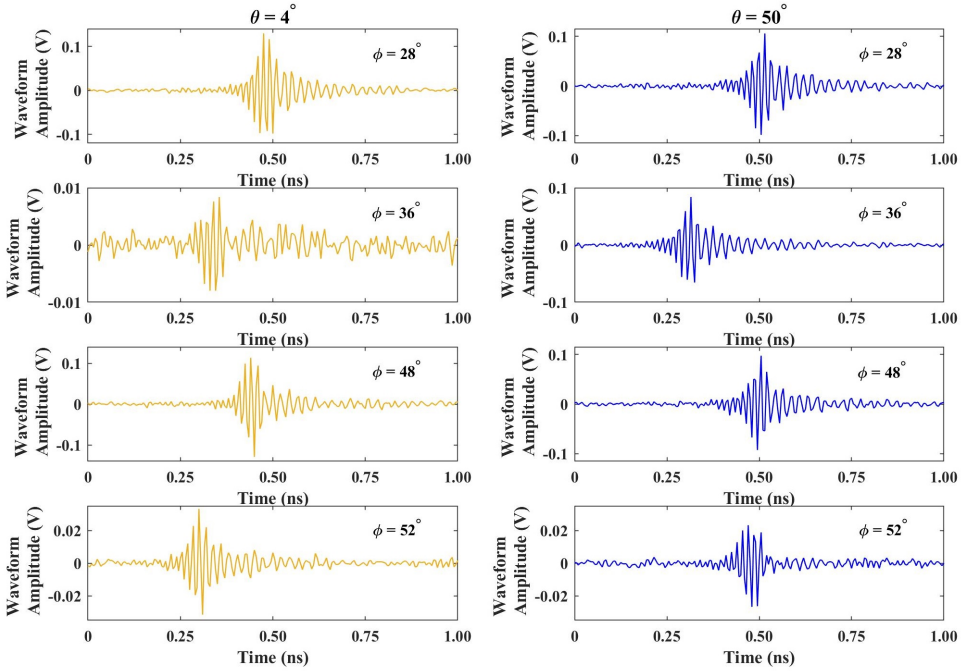

Figure 5.8: Waveforms recorded with the 50-70 GHz horn antenna due to two color MIR laser pulses at values of the relative phase that produce extrema of the microwave emission. In the left column of plots, the antenna position is $\theta = 4°$, while in the right column it is $\theta = 50°$.

presented because they better represent the microwave radiation as it occurs in the experiment than frequency domain data. While it is clear that the waveforms for the values of φ have different shapes in addition to different amplitudes, the differences are properly quantified in the frequency domain.

Frequency Domain Analysis

Using the calibration procedure from Chapter III, we can combine the frequency spectra of the waveforms measured with the four horn antennas. The spectra presented in this Section do not always cover the whole 2-70 GHz frequency range, but in all cases they contain sufficient bandwidth to demonstrate the spectral dependence of the radiation on the laser wavelength and relative phase of the laser harmonics.

Figure 5.9 shows examples of the frequency spectra from 2-70 GHz comparing the microwave emission in the single and two color MIR and NIR cases. Figure 5.5 clearly

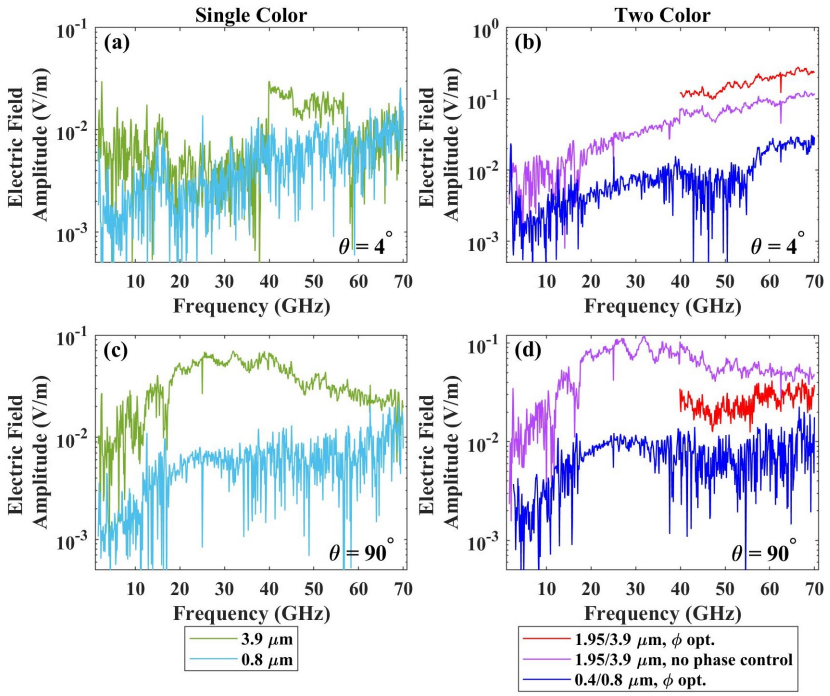

Figure 5.9: Calibrated electric field spectra due to (a) single color and (b) two color laser pulses having 2 mJ energy. The antenna position is in the forward direction at $\theta = 4°$. Panels (c) and (d) correspond to (a) and (b), respectively but with the antenna at $\theta = 50°$.

shows that the MIR and NIR single color laser pulses generate plasmas that do not radiate strongly in the forward direction. Therefore the spectra in Figure 5.9(a) which compares the microwaves from the single color pulses at $\theta = 4°$ consist mostly of noise. They are shown because with the MIR and NIR two color pulses, the microwaves become much more strongly forward directed as evidenced by Figure 5.9(b). This is notable because Chapters IV and VI circumstantially indicate that the microwaves become more forward directed with longer plasmas and higher frequencies. However, none of the radiation patterns in those cases where the plasma was many centimeters in length showed strong radiation at comparable frequencies only a few degrees off the laser propagation axis.

The microwave field radiated from the plasma appears to be almost uniformly an order of magnitude larger for the MIR laser pulses relative to the NIR pulses. Figure 5.9(b) indicates that the frequency content for the two color MIR and NIR cases is

similar at $\theta = 4°$, even though the field in the latter case is 10 times smaller. However the NIR produced spectrum has a significant dip in the frequency content in the 40-60 GHz range that is not present in the MIR case. If the relative phase is optimized, the high frequency radiation (40-70 GHz) in the forward direction increases further above that found without manipulating the relative phase of the harmonics. If the microwaves are measured along the direction perpendicular to the laser propagation ($\theta = 90°$) the frequency content in the single and two color cases shifts lower, similar to the angular dependence of the spectrum presented in Chapter IV. The increase in the spectra above 40 GHz for the single and two color NIR produced microwaves is likely dominated by uncompensated noise. The electric field calibration (Equation 3.48) is proportional to frequency, so the noise floor of low SNR signals can look like a linear function of frequency. In spite of the noisy spectra, it appears as though the peak frequency of the single and two color NIR produced microwaves is lower than the MIR cases in both of Figures 5.9(c) and (d). At $\theta = 90°$, the electric field amplitude of the optimized two color MIR produced microwaves is smaller than the un-optimized field. This is further indication of how changing the relative phase of the laser harmonics changes the emission pattern of the microwaves.

Spectral-angular maps of the microwave electric field spectra further demonstrate the two color effect for the MIR pulses. Figure 5.10(a) shows the map for single color MIR pulses from 2-70 GHz. Most of the frequency content radiates in the transverse direction, similar to a dipole. A two color pulse without phase control, shown in Figure 5.10(b) produces a similar emission pattern to the single color case, but there is also a strong forward-directed high frequency component to the radiation. A longitudinal current oscillation creates a dipole radiation pattern [87]. The appearance of a spectral feature in the forward direction in addition to the dipole-like pattern implies that the two color laser pulse drives a higher order multipole current distribution in the plasma. Figures 5.10(c) and (d) show that the relative phase of the

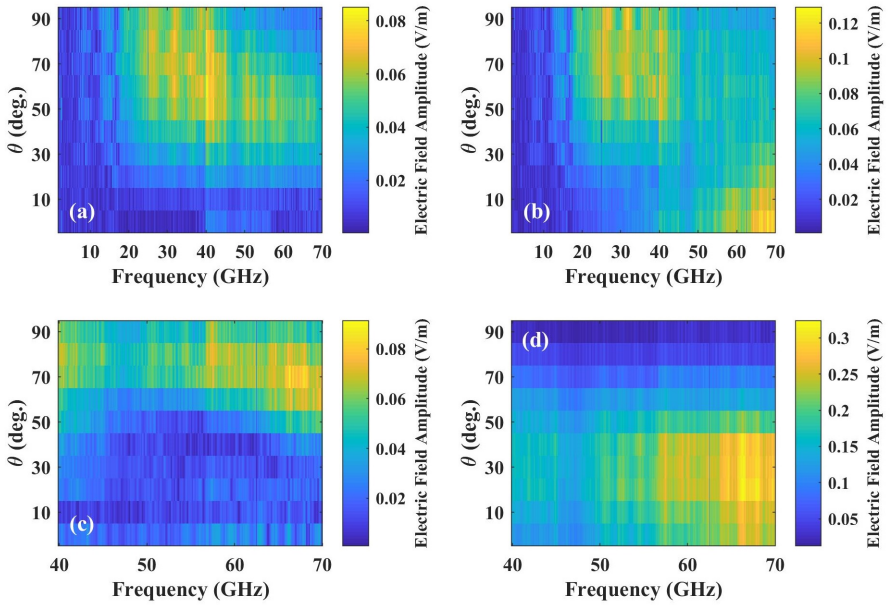

Figure 5.10: Spectral angular maps of the microwave electric field amplitude due to laser pulses at $\lambda = 3.9$ μm: (a) single color pulses (b) two color pulses without phase control, (c) two color pulses with the microwave yield minimized ($\varphi = 0°$), and (d) two color pulses with the microwave yield maximized ($\varphi = 28°$). The frequency range in (a) and (b) is 2-70 GHz, while in (c) and (d) it is 40-70 GHz.

fundamental and second harmonic steers the emission angle of the high frequency microwaves. The microwave emission is minimized in Figure 5.10(c) with the coverslip at $\varphi = 0°$. In this case the emission pattern above 40 GHz is very close to a dipole as the radiation is directed close to $\theta = 90°$. Whereas in Figure 5.10(d), when the microwave field strength is maximized ($\varphi = 28°$) the emission is forward directed similar to Figure 5.10(b).

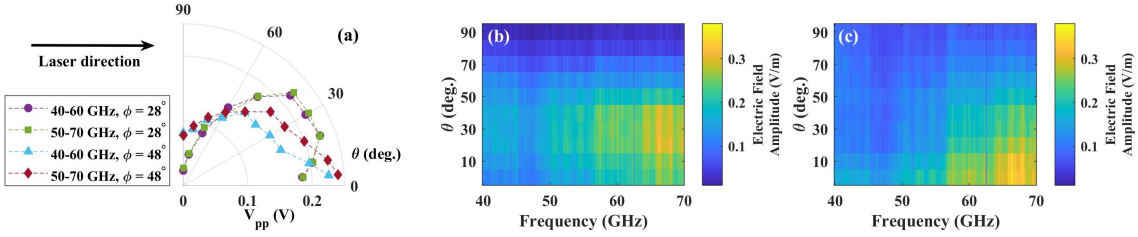

Figure 5.11: (a) Angular emission pattern based on V_{pp} measured with the 40-60 GHz and 50-70 GHz antennas for the values of φ that give maximum microwave emission. Calibrated spectral-angular maps from 40-70 GHz at (b) $\varphi = 28°$, and (c) $\varphi = 48°$.

Figure 5.6 shows that we find two emission maxima in the angular range of the glass coverslip at $\varphi = 28°$ and $\varphi = 48°$. Since the relative phase of the fundamental and second harmonic can only take on values between 0 and 2π, one would expect that the characteristics of the microwave emission should repeat from cycle to cycle of the relative phase. However we find this is not true in this experiment. Figure 5.11 compares the emission pattern based on V_{pp} for the 40-60 GHz, and 50-70 GHz antennas along with calibrated spectral-angular maps from 40-70 GHz at the two emission maxima. While the peak electric field amplitudes are comparable, the shapes of the emission patterns are noticeably different. While both are forward directed, the case of $\varphi = 48°$ peaks along $\theta = 4°$ or less, considering the finite antenna beamwidth (that is, solid angle of reception). When $\varphi = 28°$ the angle of peak emission is clearly resolved at about $\theta \sim 30°$.

The cause for the difference in emission may ultimately not be very interesting. For example it may result from transverse separation of the fundamental and second harmonic due to refraction in the glass coverslip, which will increase with φ. However the glass is only about 160 μm thick at normal incidence. The beam diameter should be large relative to the separation, and it would be surprising if the transverse displacement caused such a significant change in the relative positions of the fundamental and second harmonic fields on the focusing parabola. Whether the difference in the radiation in instances where there should be none indicates an experimental flaw or an interesting new effect is unclear. However it is important to report this observation so that it can be revisited in future experiments. The long laser wavelength makes it difficult to know the beam position since it is invisible to conventional visual aides. Understanding the cause of the different radiation patterns would be best approached with a NIR laser at higher pulse energies than we are able to employ in these experiments. If the change in the microwave emission angle is not caused by transverse separation of the fundamental and second harmonic, then

it might be a means for measuring the absolute phase, that is the number of electric field cycles by which the coverslip displaces the fundamental and second harmonic laser field components.

5.3.2 Energy Dependence of the Microwaves due to Single Color Pulses

Time Domain Analysis

The energy dependence of the microwave emission is studied only with single color pulses out of concern for the damage tolerance of the second harmonic crystals. In the time domain, the difference between the single color MIR and NIR produced microwave radiation is summarized by Figure 5.12. It shows the angular emission pattern of the microwaves based on V_{pp} measured with the 18-40 GHz antenna when energy of the laser pulses is 12 mJ. Figure 5.5 shows a similar increase in the microwave yield at 2 mJ laser energy. Figure 5.12 indicates that the radiation due to the MIR

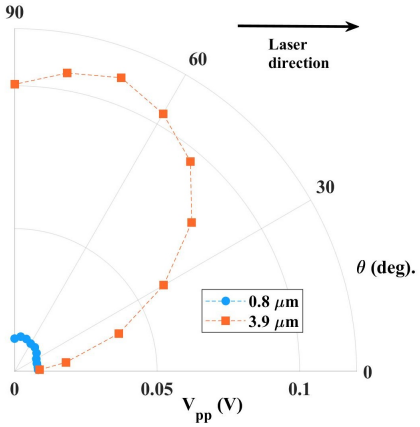

Figure 5.12: Comparison of the angular emission patterns of microwaves in the 18-40 GHz frequency range due to single color NIR (blue circles) and MIR (orange squares) laser pulses having 2 mJ energy. The average uncertainty for the NIR amplitude data is 11%, while for the MIR amplitude data it is 6%.

laser pulses is slightly more forward-directed than that due to the NIR pulses. The latter appears to peak around $\theta = 80°$, while the former peaks at $\theta = 70°$. This may be due to the difference in the plasma size resulting from the NIR versus MIR laser

pulses, which is shown in Section 5.4.

Frequency Domain Analysis

The microwave spectra generated by the single color pulses depend on input laser pulse energy. Figure 5.13 how the frequency spectrum of the radiation from 2-70 GHz changes with energy of the MIR laser pulses. The measurement is repeated at three angular positions of the antennas to prove that the dependence is real, and not a function of the antennas' observation angle. It is unexpected that the frequency

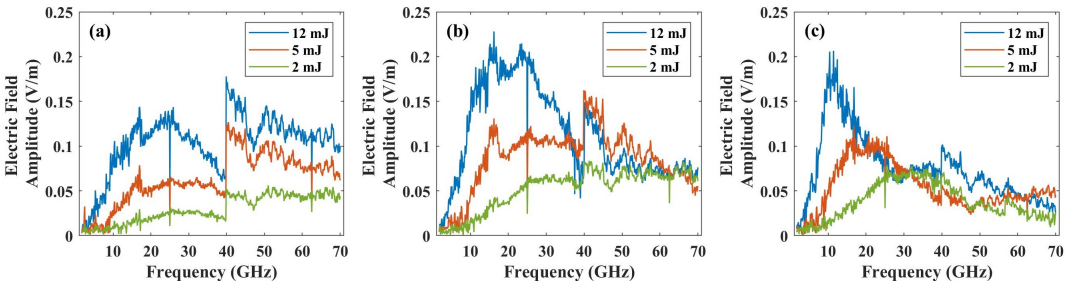

Figure 5.13: Microwave frequency spectra due to single color MIR at 12 mJ (blue), 5 mJ (orange), and 2 mJ (green) measured at antenna angular positions of (a) $\theta = 30°$, (b) $\theta = 60°$, and (c) $\theta = 90°$.

content shifts higher as the laser energy decreases. This energy dependence is apparent in each of the plots in Figure 5.13. The discontinuous jumps in the spectra, which are most pronounced at 40 GHz in Figure 5.13, are likely due to slight relative misalignment of the pointing of the antenna apertures. While the antenna mounts are fairly mechanically stable, it is difficult to keep the exact angular alignment of the apertures over many repetitive angular position scans with the antennas. In spite of the artifacts, it is clear that the lower energy laser pulses result in higher frequency microwave radiation from the plasma.

The inverse energy dependence of the frequency content on the laser energy can also be observed with the plasma produced by the NIR laser. Figure 5.14 compares the energy dependence of the spectra due to the MIR and NIR lasers measured with

the antennas at $\theta = 90°$. The microwaves produced by the NIR pulses do not have

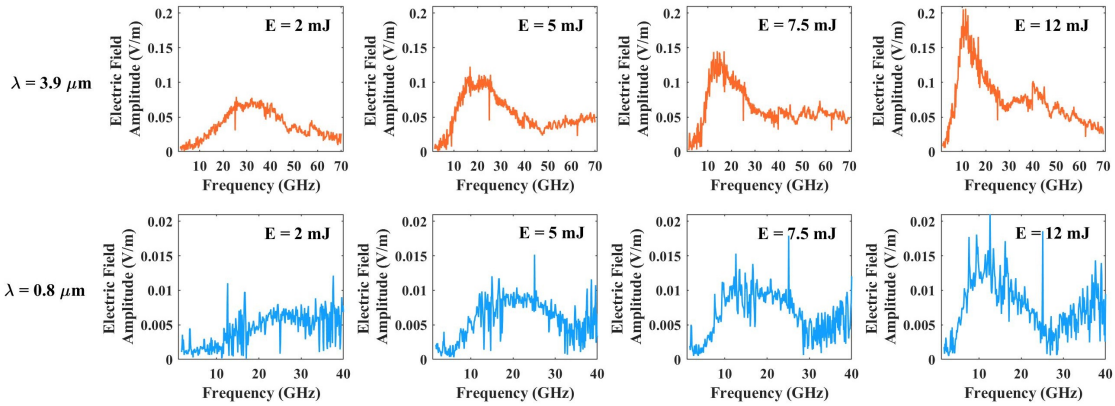

Figure 5.14: Energy dependence of the single color MIR and NIR produced microwave spectra measured at an angular position of $\theta = 90°$. The top row of plots shows spectra from 2-70 GHz produced by $\lambda = 3.9$ μm laser pulses. The spectra in the bottom row correspond to $\lambda = 0.8$ μm pulses, and are truncated at 40 GHz because of low SNR from 40-70 GHz. The spectra are measured at laser pulse energies of 2 mJ, 3 mJ, 5 mJ, 7.5 mJ, and 12 mJ.

sufficient signal strength above 40 GHz to demonstrate the shift in the frequency content, so the corresponding spectra range from 2-40 GHz in Figure 5.9. The MIR produced microwaves on the other hand are shown from 2-70 GHz. In both cases, the spectral peak appears to shift from $\sim$ 30 GHz at 2 mJ pulse energy to $\sim$ 15 GHz at 12 mJ. This effect has not been documented before, but must be a general feature of the plasma evolution because it is observed on two different laser systems operating at very different wavelengths. We believe the energy dependence of the frequency content is related to the plasma size. This is discussed further in Section 5.4.

While measuring V_{pp} from the time domain waveforms can give qualitative indications of the relative microwave yields, it is quantitatively more accurate to estimate the total received power over the frequency band of the measurements. Figure 5.15 shows a quantity that is proportional to the total power due to the single color MIR and NIR pulses as a function of laser energy and antenna position. Each data point results from squaring and summing the electric field spectrum at each value of laser energy from 2-70 GHz. The data in each plot are normalized to the total power of

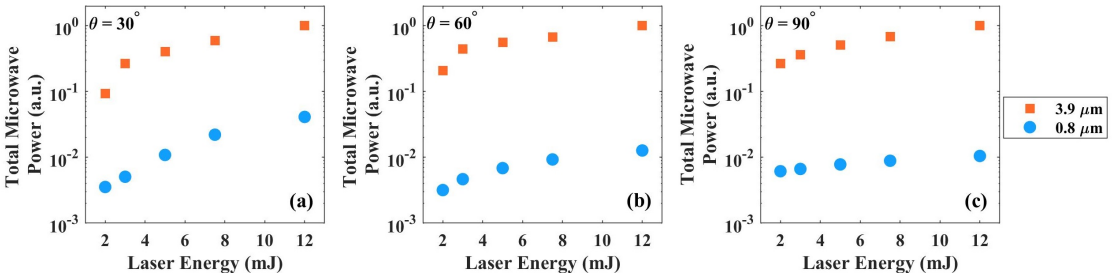

Figure 5.15: Normalized total power integrated from 2-70 GHz at each value of energy due to the MIR and NIR single color laser pulses. The position of the antennas in each set of measurements is (a) $\theta = 30°$, (b) $\theta = 60°$, and (c) $\theta = 90°$.

the MIR produced microwaves at 12 mJ. The microwave power appears to depend linearly on the input pulse energy, with the MIR pulses consistently producing about two orders of magnitude more power than the NIR pulses.

5.4 Discussion

The first experiment described in Section 5.3.1 demonstrates that the relative phase of the laser harmonics can strongly influence the microwave radiation from plasmas produced by two color laser pulses. Section 5.3.2 presents the second experiment, which shows that the frequency content of the microwaves due to single color laser pulses depends on the laser pulse energy, and that the center microwave frequency decreases with increasing laser energy. We provide some possible explanations for these findings by analyzing images of the plasma fluorescence.

It is important to note that the images of the fluorescence may not accurately represent the actual size of the plasma, and that the intensity and spectrum of the emitted light depends simultaneously on the electron density and energy distribution. Especially in a chemical system as complex as air, it is not possible to determine if it is the electron energy or the density that is changing just by taking a picture of the fluorescence. However relative changes in the fluorescence can be used as a benchmark for the behavior of the microwave radiation. Each set of images of the plasmas

in Figures 5.16(a), 5.18(a), and 5.18(b) are captured with different CCD or CMOS camera. While they all have silicon-based sensors and therefore are primarily sensitive to visible wavelengths of light, the gain and exposure settings differ, so the brightness of the fluorescence in one set of images cannot be accurately compared against another set. The images are useful for relative inferences, not absolute measurements.

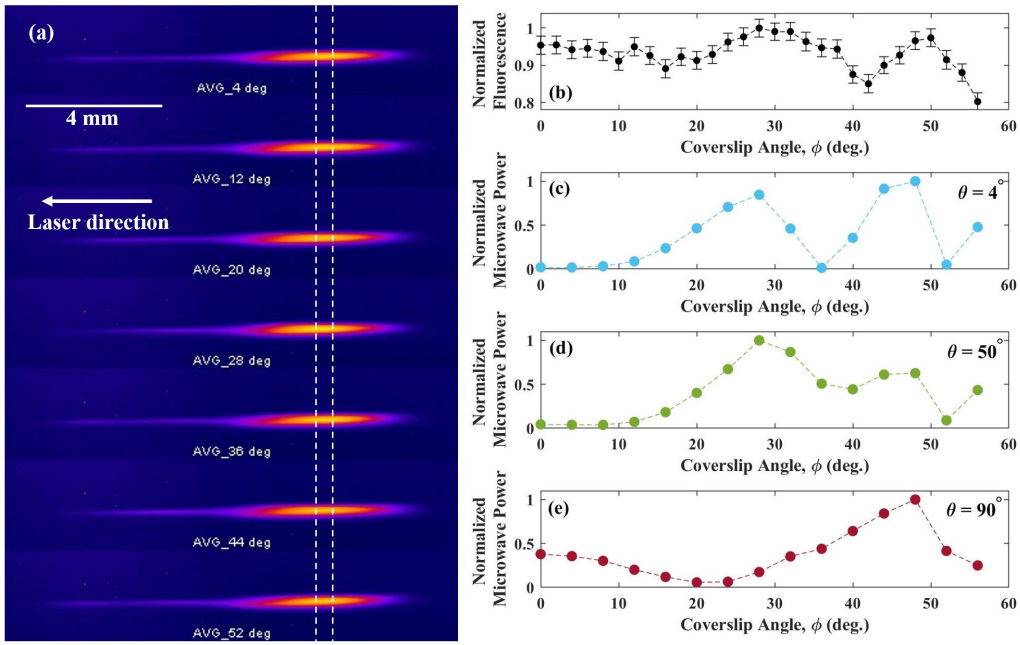

Figure 5.16: (a) False color images of the two color MIR produced plasma fluorescence indicating the locations in the images that are used to calculate the fluorescence. The laser pulses propagate from right to left, and the plasmas are about 8 mm long. (b) Normalized fluorescence of the plasma versus the coverslip angle φ is compared to the total normalized microwave power calculated from microwave frequency spectra integrated over 18-70 GHz at antenna positions of (c) $\theta = 4°$, (d) $\theta = 50°$, and (e) $\theta = 90°$.

Figure 5.16 compares the total radiated microwave power to spatially averaged plasma fluorescence captured by a CCD camera as a function of the relative phase of the fundamental and second harmonic of the MIR pulses. False color images of the two color MIR laser plasma fluorescence are shown in Figure 5.16(a). 100 sample images at each value of φ are averaged together. The averaged images are integrated in the transverse dimension (up to down in the pictures) to produce longitudinal profiles. The profiles are fit with the sum of three Gaussian functions in order to

find the longitudinal location of the peak. The pixels values adjacent to the peak (denoted approximately by the vertical dashed white lines) are averaged to give an integrated value of the fluorescence. The result is normalized and plotted as a function of φ in Figure 5.16(b). The total power of the calibrated microwave spectra at each value of φ is calculated and normalized in the same manner as the data in Figure 5.15. Figures 5.16(c)-(e) show the result for different antenna positions. In general the microwave power correlates with the plasma fluorescence. We do not know the detailed collisional kinetics between the electrons and heavy species in the air plasma that cause the fluorescence, as it in general depends simultaneously on the electron temperature and density. However, these observations indicate that the microwave field strength correlates with energy deposition in the air plasma.

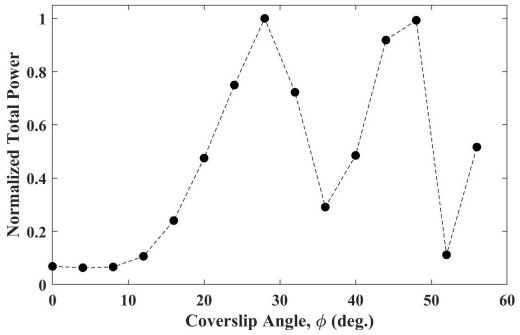

Figure 5.17: Total power as a function of coverslip angle. The data above are calculated from the sum of the un-normalized values of the total power at $\theta = 4°$, $50°$, and $90°$, i.e. Figures 5.16(c)-(e).

The minimum in the radiated microwave power shown in Figure 5.16(e) at $\theta = 90°$ and $\varphi \sim 24°$ would seem to disagree with our argument. However, it was shown in Figure 5.10 that the relative phase of the laser harmonics significantly changes the emission pattern of the microwaves. The microwave yield integrated in space finds a maximum at $\varphi = 28°$ and $\varphi = 48°$ as shown in Figure 5.17. We highlight the minimum observed in Figure 5.16(e) in contrast to the maxima observed in Figures 5.16(c) and (d) to reinforce the fact that one must consider that the angular dependence of the microwave radiation when discussing the total radiated power.

One factor that may contribute to the differences observed in the microwave emission between the single color MIR and NIR experiments is the size of the air plasmas generated by the lasers in each case. Figure 5.18 shows side images of the plasma fluorescence due to the single color MIR and NIR laser pulses at each of the pulse energies presented in Section 5.3.2. The size of the fluorescing regions increases with

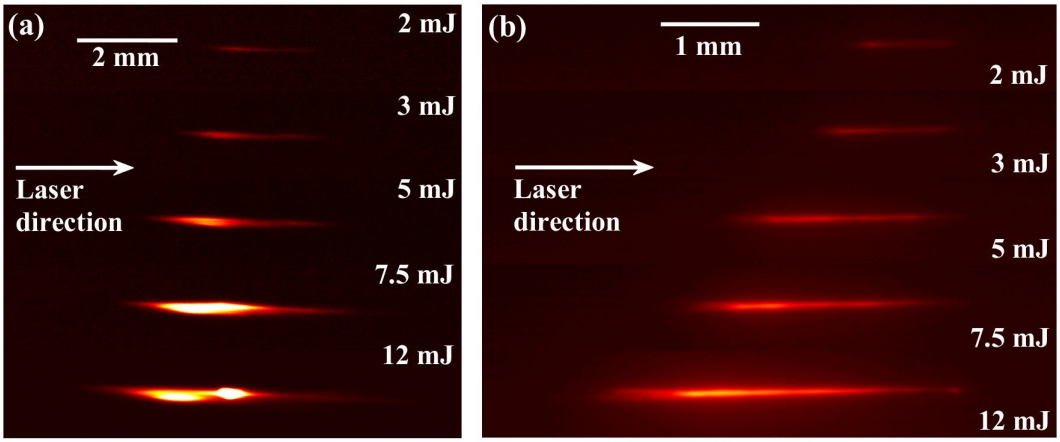

Figure 5.18: False color images of the plasma fluorescence due to the single color (a) MIR, and (b) NIR laser pulses as a function of pulse energy. In both sets of images the laser pulses propagate from left to right. Note the difference in the length scale between the images.

laser pulse energy, but the images indicate that the NIR produced plasmas are much smaller than the MIR produced plasmas at each value of energy. The two-spot structure seen in the fluorescence due to the MIR pulses at 12 mJ is caused by imperfections in the transverse profile of the beam. Even though higher order contributions to the beam modes play a role in the differences in the focal properties of the MIR and NIR laser pulses, there are three other facts to consider that will affect the plasma generation. First, the diffraction limited spot size of the MIR pulses is much larger than that of the NIR pulses. If the experiments were using perfect Gaussian beams,

then the Airy disk diameters would be

$$d = \frac{4\lambda L_f}{\pi D} = 15.3\ \mu\text{m at } \lambda = 0.8\ \mu\text{m}$$
$$= 74.5\ \mu\text{m at } \lambda = 3.9\ \mu\text{m}.$$

The discussion of the microwave generation from filament plasmas as a function gas pressure in Section 4.4 argues that the increasing diameter of the filament plasma at low air pressure drives the observed increase in the microwave yield. Therefore we must also consider that the same effect occurs in these experiments due to the difference in laser wavelength the focused spot size.

On the other hand, we are not propagating ideal beams in vacuum, so the they will not focus to Airy disks. Plasma defocusing should also play a role in the diameter of the beam and the plasma itself. This is the second difference: the spatial phase imposed on the beam due to the plasma scales like $-N_e/N_{crit}$ [172]. Plasma defocusing in the MIR versus NIR cases must be considered carefully. If one makes the naive assumption that N_e is similar at both laser wavelengths, then the plasma defocusing is ~ 24 times stronger for the NIR laser pulses, which would mean that the focused NIR pulses would depart farther from the diffraction limited spot size than the MIR pulses. This could result in plasma diameters that are closer than expected. However, the third difference is the untenable assumption that N_e is similar at the different wavelengths.

Theories for strong field ionization predict N_e to be smaller for a given pulse intensity in the MIR versus NIR due to the lower ionization rate that follows from the lower photon energy [74]. However, if the laser pulse spectrum overlaps an absorption line of an air constituent species, then the theories no longer hold. For example, carbon dioxide has a very strong absorption line at 4.3 μm [174]. Furthermore, the

ponderomotive potential for the MIR laser pulses in the experiment is

$$U_p \text{ [eV]} = 9.38 \times 10^{-5} I \text{ [PW/cm}^2\text{]} \ \lambda^2 \text{ [nm]} = 142 \text{ eV}, \tag{5.7}$$

where $I \sim 10^{14}$ W/cm^2, and $\lambda = 3900$ nm [69]. This means that a significant population of the electrons could gain sufficient energy from the laser field to cause secondary ionization events by impact ionization after the passage of the laser pulse. The ionization potential of nitrogen, for example, is 15.6 eV [75]. This is usually not considered at NIR laser wavelengths either because the ponderomotive potential is much smaller, or because the laser intensity is so high that all the electrons are stripped from the gas atoms in the laser field. The short pulse ionization dynamics at long laser wavelengths are not well understood, and have yet to be studied in detail because there have been no such laser sources capable generating plasmas until recently. These experiments represent an interesting preliminary test of a situation in which understanding of long wavelength, strong field ionization dynamics is critical to the explaining the relevant plasma physics.

We can use the microwave spectral data from the single color MIR pulse energy scan in Figure 5.14 to infer that there may be a correspondence between the frequency content of the microwaves and the length of the plasma. Figure 5.19(a) shows the wavelength corresponding to the peak frequency of the microwave radiation generated by the single color MIR plasma. The peak frequency is found by fitting Fourier series consisting of 6, 7, and 8 terms to each spectrum, and taking the frequency that corresponds to the maximum of each fit. The data reported in Figure 5.19(a) are the average of the peak frequencies for each fit, and the error bars denote their standard deviation. The spectra recorded from 2-70 GHz at $\theta = 90°$ are shown in Figure 5.14. Using images of the plasma fluorescence, such as those in Figure 5.18(a), we can estimate the physical length and width with ticks on a ruler for size calibration.

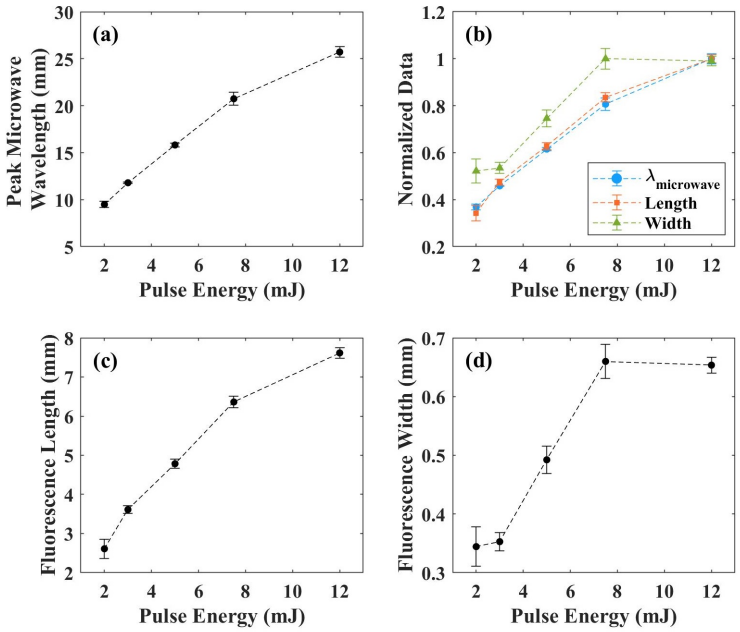

Figure 5.19: (a) Peak microwave frequency extracted from the top row of plots in Figure 5.14 due to single color MIR laser pulses as a function of laser energy. (b) Comparison of the normalized length and width of the plasma fluorescence to the normalized peak microwave wavelength. (c) Length and (d) width of the plasma fluorescence as a function of MIR laser energy.

Figures 5.19(c) and (d) show the length and width calculated from measurements performed on 20 images at each laser energy. The microwave wavelength is given by $\lambda_{peak} = c/f_{peak}$, and is compared to the length and width in Figure 5.18(b). Each set of data is normalized to its maximum value to clarify the relative trends of the different quantities with laser energy. We observe that the peak wavelength and length of the plasma fluorescence in Figure 5.18(b) lie within each others' error bars. The width increases with laser energy, but does not as closely match the wavelength dependence. Together with the low frequencies observed in Chapter IV for long filament plasmas, and the slightly higher frequencies observed in Chapter VI for filament plasmas made with a shorter focal length lens, Figure 5.19(b) suggests that the frequency content of the microwave radiation depends at least in part on the length of the laser plasma. This means that the radiation is due to a longitudinal change in the current density whose scale length is determined by the plasma extent.

5.5 Conclusion

These experiments are the first to compare microwave radiation from single and two color laser plasmas. They are also the first study of microwaves generated by a plasma from a MIR laser system. The primary finding is that for similar input pulse intensities, the plasma generated by the MIR laser radiates microwaves with an order of magnitude greater field strength than that due to the NIR laser. The increase in conversion efficiency may result from a greater transfer of energy from the laser field to the plasma electrons because the ponderomotive force scales with λ^2. However other causes to be considered are the increase in the plasma volume at long laser wavelengths, and the difference in the ionization dynamics for the MIR and NIR cases that result in laser plasmas of different densities. The latter likely involves a series of interesting questions that are beyond the scope of the present study.

The experiments also demonstrate an increase in the yield of microwaves with two color MIR and NIR laser pulses when the relative phase between the laser harmonics is optimized. This is the first time that a two color effect has been observed with microwave radiation from a laser plasma. While the microwave signal due to the two color NIR pulses was too small for a comprehensive study of the effects of the relative phase, a complicated dependence was observed with two color MIR pulses. Figure 5.10 shows that the amplitude, emission pattern, and frequency content of the microwave field changes with the relative phase. Even though the total radiated microwave power is periodic in the thickness of glass traversed by the two color pulse, the angular emission patterns for the two maxima we measured have different shapes, as shown in Figure 5.11.

A simulation of the plasma generation and radiation due to the two color pulse is likely the best avenue for determining the relationship between the relative phase and the microwaves. The multifaceted changes we have observed are likely not immediately amenable to analytic theory. The challenge, however is running the simulation

long enough to capture all of the relevant physics. The sensitivity of the radiation to the relative phase means that a useful simulation would have to resolve the laser fields. Simulation of the pulse envelopes would be insufficient. This necessitates using a particle-in-cell (PIC) code. However, the simulation volume would need to be at least one microwave wavelength across (a few centimeters at minimum) to capture the radiation near field. Furthermore, the simulation would have to run long enough to calculate both the ionization events, and also the formation of the plasma currents and the fields emitted from the plasma. This would take a few nanoseconds of simulation time. At a time step sufficient to resolve the MIR laser field (a few fs) and spatial increment that resolves the wavelength ($\sim$ 100 nm) this means an axisymmetric, that is 2D, simulation would have on the order of $(10^5)^2$ uniform grid points, and run for $\sim 10^6$ time steps. While an adaptive mesh that increases the grid size away from the plasma could reduce some of the required computational power, the large number of time steps time restricts a proper simulation of the experiment to a high performance computer.

In addition to the two color measurements, we have examined the single color laser pulse energy dependence of the microwave emission spectrum. Figures 5.13, 5.14, and 5.19 indicate that the frequency content of the microwaves shifts lower as the laser pulse energy increases because the plasma increases in longitudinal extent. An early hypothesis of the dissertation research was that the microwave frequency reflects the timescale of cold plasma oscillations that become coherent during the relaxation of the plasma due to the passage of the laser pulse. The inverse dependence we have observed shows that this is incorrect – the microwave frequency is not related to the plasma frequency. If it were, the frequency content of the radiation would shift higher with increasing energy as the plasma becomes more dense, and therefore quicker to respond to electrostatic perturbations. Instead the measurements imply that the microwave frequency content has some dependence on the inverse scale length of the

longitudinal variations in the plasma properties.

CHAPTER VI

Adaptive Control of Filamentation

6.1 Introduction

Nonlinear phenomena can be difficult to work with because a small change in the initial conditions will produce a large change in the outcome. In laser filamentation, the sensitivity to small changes in the initial conditions of the laser pulse may be leveraged to drastically alter the filament propagation. With sufficient study it is possible that correct manipulation of the initial laser pulse can produce user-designed filaments or arrays of multiple filaments that can be controlled in real time.

This Chapter presents two experiments that make progress toward that goal. They use a deformable mirror (DM) to impose iteratively refined distortions to the spatial phase of the laser pulses that optimize a desired aspect of the laser-plasma interaction. The spatial phase describes the transverse shape of its wavefronts. For example, plane waves have uniform spatial phase. The first experiment builds upon the pressure dependence experiments Chapter IV and uses the wavefront distortion to maximize the microwave yield. The optimization is performed as a function of air pressure. The second experiment is the only experiment in the dissertation that does not involve microwave generation. It uses the deformable mirror to control the transverse distribution of filaments in the multi-filament regime.

The intention of the experiments is not primarily to determine how particular

wavefront distortions affect the filamentation propagation and plasma generation, but rather to determine if wavefront control in general is capable of producing a desired outcome. In this sense, the purpose of these preliminary experiments is to observe what degree of optimization is possible, rather than connecting the wavefront changes to the microwave generation mechanism, or seeding of the filament configuration. The experiments are quite successful on these grounds. However, the fine control that the DM exerts on the wavefront would be useful in future studies of the physical processes that govern filamentation.

The experiments run on a closed loop that is controlled by a genetic algorithm (GA). It is a type of evolutionary algorithm that executes many repetitive semi-random searches that converge to a solution using biologically inspired operators. Section 6.1.1 describes how the algorithm functions. GAs can be useful tools when searching a large parameter space in which the correspondence between the attributes of the input and their effect on the output is difficult to predict. The DM may only impart a small phase distortion to the initial laser pulse, but that may result in a much larger, non-proportional phase distortion due to amplification by the Kerr effect at the beginning of the filamentation region. Manipulating the spatial phase may also influence filament propagation through the low intensity energy reservoir that co-propagates with the filaments. Experiments have shown that the behavior of the core of a filamenting laser pulse depends on the non-filamenting energy reservoir of laser light at the pulse periphery [28, 175]. Not only is the propagation nonlinear in the longitudinal direction, but it is also transversely correlated. In principle, phase distortions made at the periphery can change the behavior of the core even if no phase is imparted at the core.

Our experiments are not capable of discriminating whether the optimizations of the microwaves or filament configurations are primarily due to manipulations of the spatial phase that map directly to the cores of the filaments, or indirectly to the

energy reservoirs. However it is important to keep in mind that the results possibly arise from two effects of the spatial phase on the filament propagation.

The reason we cannot directly state the correspondence between the wavefront at the DM and the experimental outcome is a consequence of the nonlinear propagation of the laser pulses. The intensity profile of a laser pulse at a given position along its trajectory is determined by the wavefront it had throughout its propagation prior to reaching that position. This follows from Huygens' principle [176], and means that modulation of the spatial phase precipitates intensity modulations. Huygens' principle applies in the nonlinear regime, but one has to consider that the laser pulse continuously modifies its own wavefront. The wavefront measured at a given position cannot be traced backward an arbitrary distance. This concept is called non-reciprocity [177], and it complicates the interpretation of the experiments. The nonlinearity means that correspondence between the shape of the mirror and the resulting intensity profile is inherently more complex than what is observed in the linear regime.

In the experiments, the pulses propagate through several meters of air before reaching the filamentation region. The evolution of the wavefronts will depend on nonlinear contributions over that distance in addition to natural diffraction of the pulses. Absent from our measurements are phase profiles recorded in close proximity to the DM or the filamentation region with, for example, a Shack-Hartmann sensor. The pulses would need to be attenuated in order to experimentally measure the wavefront, eliminating the nonlinear contribution to the wavefronts. When the experiment is performed at the operating laser power, the wavefront measured for the attenuated beam cannot be expected to correspond to that which exists in the experiment. This is the reason that the experiments described in this Chapter do not make direct attempts to explain how the shape of the DM corresponds to the optimizations we observe.

The presentation of the two experiments with the DM are organized as follows. Section 6.2 describes the optimization of the microwave yield, where the waveform peak-to-peak voltage is provided as feedback to the GA. The optimization increases the microwave field strength by about a factor of 2 over the unoptimized case. The results in Section 6.2.2 follow the format of the previous Chapters, giving the time domain measurements first, before looking more closely at the calibrated electric field frequency spectra. Section 6.2.3 discusses the measurements, and uses images of the plasma fluorescence to establish a qualitative connection between the plasma generation observed with the optimized wavefronts and the increase in the microwave yield. The second experiment, contained in Section 6.3 controls the transverse configuration of the filaments by rapidly processing images of the beam profile. Section 6.3.2 discusses three related results which use the same input laser beam to accomplish: i) optimization of the overlapping between filaments in the center of the beam profile, ii) moving the overlapped filaments in controlled radial increments away from the center, and iii) separating the filaments repeatably in to two and four-filament configurations. Section 6.3.3 analyzes the repeatability of the method. The Chapter concludes in Section 6.4 by evaluating the performance of the DM and the GA in controlling filamentation based on the findings of the experiments.

6.1.1 Genetic Algorithm for Manipulating the Laser Spatial Phase

Modifications of the spatial phase can be imposed either by refractive index perturbations (transmission), or path length differences (reflection). Spatial light modulators are used in the former case, while deformable mirrors accomplish the latter. Spatial light modulators are undesirable for use with ultrashort pulses because they have low damage thresholds due to self-focusing in transmissive elements.

The aperture of a deformable mirror is divided into independent movable sections each of which is driven by a precise actuation mechanism. There are many different

actuator technologies, each of which is specialized to different applications in adaptive optics [178]. The mirror used in the experiments is a Xinetics DM37PMNS4, which uses low-hysteresis piezoelectric stacks that are covered by a continuous metallic face sheet. The aperture of the mirror is 47 mm, and each actuator has a maximum stroke of 5λ ($4\ \mu$m at $\lambda = 800$ nm) with resolution better than $\lambda/100$. The deflection of

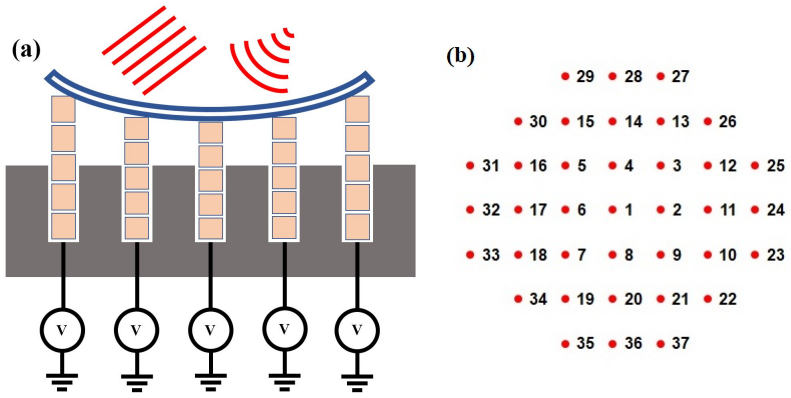

Figure 6.1: (a) The voltage applied to the piezoelectric stacks controls the shape of the mirror surface. (b) The 37 actuators that drive the mirror are laid out to approximate a circular aperture. The spacing between neighboring actuators is 7 mm.

its 37 actuators is proportional to the voltage applied to each. Figure 6.1 sketches the push-pull action of the actuators. To a good approximation the deflection of each actuator is independent of the others. Therefore the parameter space that the GA searches has 37 dimensions. Each dimension is approximately continuous in the applied voltage, but in reality consists of increments that are equal to the voltage resolution of the power supply driving the mirror. The span of each dimension starts at zero deflection, and is limited by the maximum stroke of a single actuator, which is imposed to prevent damage to the mirror's surface. If there are K voltage increments between zero and maximum actuator deflection, then the GA searches a parameter space that consists of K^{37} possibilities for the mirror shape.

One motivation for using an advanced search algorithm is the vast size of the parameter space. The other is the fact that not all of the laser-plasma interactions of interest require a perfect vacuum focus to achieve the desired result. For example, an

experiment that optimized the THz yield from single and two color filament plasmas in air found that aberrations applied by the mirror extended the plasma length and increased the THz yield above what could be achieved with a beam corrected to be aberration-free [179]. Additionally, when the GA was used to optimize the total charge and angular divergence of a laser wakefield-accelerated electron beam, the laser wavefront that optimized the accelerating fields did not correspond to the best focus [180]. In both cases, it was not clear beforehand that optimum laser-plasma interaction would arise from aberrated wavefronts. It is likely, although unproven, that a different wavefront shape optimizes a given laser-plasma interaction for a given input laser pulse. On the other hand, the uniqueness of the wavefront solution within a single problem is a deeper question beyond the scope of the dissertation.

The experiments in Sections 6.2 and 6.3 implement a basic GA, which is described conceptually in the flowchart in Figure 6.2. It gives the example of a population of two individuals that are each 8-bit binary numbers. The attributes of each individual are described by its bits. In the jargon of GAs each bit would constitute a gene. The first step is to create an initial population of individuals by randomly sampling the total parameter space. The individuals in Figure 6.2 are not chosen randomly in order to illustrate the GA's operations.

The most consequential step in the algorithm is to evaluate each individual in a iteration against a fitness function, which should be designed to give a relative indication of how well an individual achieves the desired optimization. There is not a systematic way to choose a fitness function for a particular problem. This is a source of complication because the fitness function influences whether or not the algorithm converges, the rate of convergence, and whether it finds the global optimum or a local one within the parameter space [181]. The most straightforward implementation of the fitness function produces a single value, called a figure of merit (FOM) although multi-valued fitness functions can be used [182].

The experiments described here use FOMs where a larger value indicates better fitness. Say that the goal is to find the number 100 in the example in Figure 6.2. A reasonable choice for the fitness function may be $\mathcal{F} = 1/|M - 100.1|$ (where M is the base-10 value) so that the FOM, $\mathcal{F}$, increases as the value assigned to an individual approaches 100, but cannot give a divide-by-zero error because of the extra added 0.1. The individuals that score the largest FOMs in an iteration become the parents

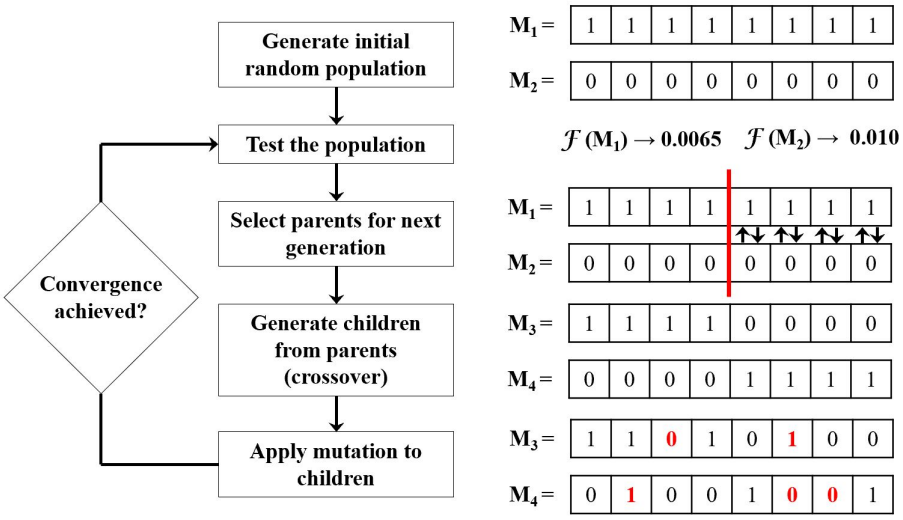

Figure 6.2: A flowchart indicating the steps of a generic GA. As an example, the operations of the algorithm on individuals in a population of two 8-bit numbers represented in binary are shown alongside the flowchart.

for the next iteration. Crossover and mutation operations are applied to the parents' genes to populate the individuals for the next iteration.

For the purposes of the GA, each different mirror figure is an individual. It is defined by the voltages applied to the piezoelectric actuators. The position of each actuator (or equivalently each voltage) is a gene. Both experiments are initialized with a population of 100 random mirror figures, and each subsequent iteration tests 100 different figures. At the end of each iteration, the 10 individuals with the largest FOMs become the parents for the next iteration. The population evolves due to the inheritance of optimal actuator positions between iterations. However, if the

algorithm happens to be initialized with no figures that improve the FOM, or if the inherited actuator positions between iterations decrease the FOM, failure of the algorithm may be avoided by allowing mutation. Each of the actuator positions in each of the 100 individuals has a user-defined probability of being reset to a random value. If a mutation increases the FOM enough it is retained in the next iteration, otherwise it is discarded. Determining the optimal mutation probability is not an exact process - too much mutation dominates inheritance and keeps the mirror figure from converging on a solution, but too little can lock the feedback loop to a local maximum instead of the global maximum. The results presented in Sections 6.2.2 and 6.3.2 use a mutation probability of 20%. This determines both the likelihood of a mutation occurring, and the amplitude of the maximum possible change in deflection that can be applied to the mutated actuator.

The definition of convergence for a GA is usually not rigorous unless the solution is known beforehand. It is common practice to allow the algorithm to run for a set maximum number of iterations, or to monitor the FOMs as the iterations advance, and declare convergence when the change between iterations becomes small [183]. In both experiments, the latter approach is used to determine convergence. The algorithm stops after the values of the FOMs of the ten best individuals become relatively steady for several iterations.

6.2 Pressure Dependent Optimization of the Microwave Yield from Filament Plasmas

It is not guaranteed that the shape of the wavefront can significantly influence all aspects of the plasma generation due to the laser pulses. While small wavefront changes applied by the mirror may be amplified by the nonlinear propagation, there are several sequential physical processes (nonlinear propagation, ionization of the air,

and formation of plasma currents) that must occur for the wavefront manipulation to translate to changes in the yield of secondary radiation. Previous experiments that used the DM to optimize the THz yield [179] indicate that there is such a connection. However the results presented so far in the dissertation imply that the THz and microwave radiation arise from different mechanisms in the filament plasma. The purpose of these experiments is to establish if a correspondence exists that is sensitive to the spatial phase that the DM is able to apply to the pulses.

There is good reason to expect that the DM can influence the microwave radiation. The intensity profile of the laser pulse when it starts filamenting has some dependence on the wavefront acquired from the DM. The underlying question, which the experiments do not address, is the strength of the intensity profile dependence during filamentation due to the spatial phase that the DM applied at a distance. Strong field ionization depends on the instantaneous value of the laser electric field, so reshaping the wavefront can effect a degree of change in the size and properties of the plasma. This is how we expect the deformable mirror can optimize the microwave yield. We observe that the GA is able to find DM configurations that enhance the electric field strength of the microwave radiation by about a factor of 2 over the frequency range of the measurements.

6.2.1 Experimental Methods

The experimental setup, shown in Figure 6.3 similar to that of the air pressure experiments described in Chapter IV. The λ^3 laser [184] in the Center for Ultrafast Optical Science at the University of Michigan was used in the experiments. It is a high repetition rate Ti:sapphire system that delivers pulses at $\lambda = 800$ nm with a full-width-at-half-maximum pulse duration of about 35 fs. The maximum repetition rate of 500 Hz is used, and the pulse energy is held constant at 3.6 ± 0.5 mJ. This corresponds to a laser power of about $20P_{cr}$ at atmospheric pressure. After reflecting

from the deformable mirror, a concave mirror that has a focal length of 2 meters ($f/40$) focuses the pulses. The region where the plasma forms is contained inside a quartz gas cell. A diaphragm pump connected to the cell allows the pressure to vary from atmosphere to 1 Torr.

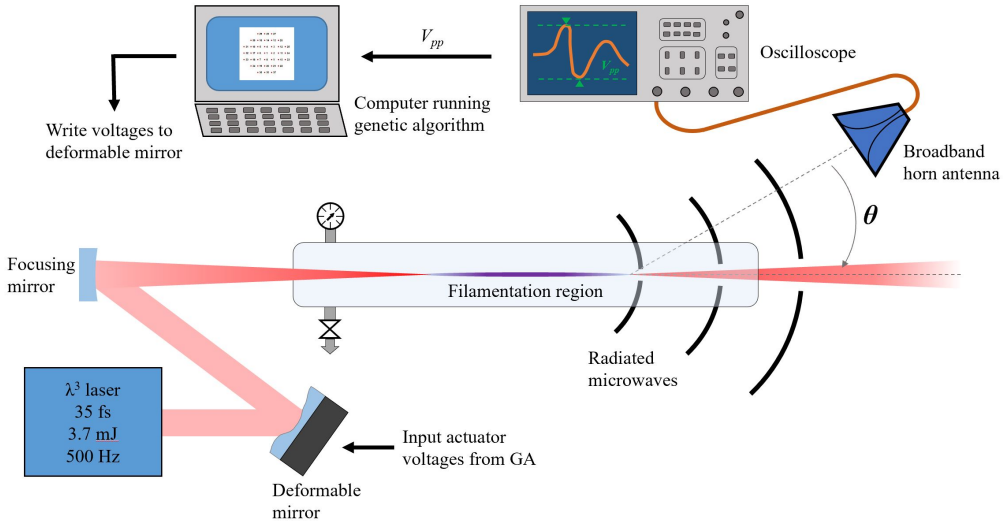

Figure 6.3: The experimental setup for the microwave optimization is similar to the air pressure dependence experiments of Chapter IV. The pulse wavefront is modified by the deformable mirror before reflecting from the surface of the focusing mirror. The microwaves generated by the filament plasma are collected by a 2-18 GHz horn antenna and the waveforms are recorded using a 13 GHz oscilloscope.

A broadband horn antenna that has 2-18 GHz bandwidth (AEL H-1498) receives the microwave radiation, and a 13 GHz oscilloscope (Agilent DSOX91304A) records the waveforms. The total bandwidth of the microwave spectra is limited by that of the oscilloscope. The aperture of the antenna is about 1.1 meters from the termination of the plasma. The beam is elevated about 0.5 meters above the surface of the optical table to provide distance between the plasma and any surfaces that could reflect the radiation. Microwave absorbing foam is placed on the optical breadboard to damp reflections from its surface.

The oscilloscope provides the waveform peak-to-peak voltage, V_{pp}, as the input to the GA which enables the optimization of the microwave yield. The GA runs in

LabVIEW, so it is not difficult to incorporate the waveform data into the optimization routine. Because of the high repetition rate of the laser and the large number of iterations required to achieve convergence, one needs to be mindful of the time it takes to perform a single mirror correction and measure the result. The fastest way to do this is to use the waveform measurement utilities on the oscilloscope and transfer the smallest and simplest data possible between it and the GA. LabVIEW's entry level functions steer a user toward reading the whole waveform into LabVIEW and using it to make the measurements. This is a mistake to be avoided as it will drastically slow down the GA's iterations.

The oscilloscope makes a fast measurement of V_{pp} of every waveform it records, and sends it to the GA. For these experiments, optimizing the microwave yield is the same as maximizing V_{pp}. However it is possible to use other waveform measurements (for example duration, rise time, etc.) or even spectral measurements of the microwaves to perform the optimization. V_{pp} is an intuitive choice for these preliminary experiments and can be quickly processed by the GA.

An angular map of the microwave radiation is measured for the optimized and unoptimized cases at each value of air pressure. The purpose of this is to determine if the wavefront that gives the optimal microwave yield alters the laser pulses in the same way at each pressure, or if the optimization is also pressure dependent. The similarities between the optimized wavefront shapes for different test cases are discussed in Section 6.2.3. The angle between the horn and the laser propagation axis is denoted in Figure 6.3 as θ, where $\theta = 0^\circ$ is along the laser propagation direction. The microwaves are measured in increments of 5° over an angular range of $\theta = 5^\circ - 55^\circ$. As Figure 6.5 shows, V_{pp} peaks at an angular position of about $\theta \sim 25^\circ - 30^\circ$. Therefore the base test case is to run the GA with the horn at $\theta = 25^\circ$. This is somewhat of an arbitrary choice, so optimizations at additional angles ($\theta = 5^\circ$ and $\theta = 50^\circ$) are tested when the pressure is 1 Torr, 10 Torr, and

100 Torr in addition to the base case at $\theta = 25°$. The consistency of the results is evaluated in Section 6.2.3.

A Stanford Computer Optics 4 Quik E intensified charged coupled device (ICCD) camera records images of the plasma fluorescence. The sensor that forms the images has 16-bit dynamic range. The camera views the plasma in the direction normal to the laser propagation so that its length and width can be inferred. A ruler placed in the camera's field of view is used as a fiducial to obtain a size calibration for the images. Additionally, we attempted to image the beam mode at the exit of the filamentation region to infer how the mirror reconfigured the beam's intensity profile. Unfortunately, the general shape of the beam is the only information that might be usable, and only in the most topical and qualitative sense. The laser energy deposition in the filament plasma is at most 10% [185, 186] so plenty of power remains in the pulse after filamentation for it to propagate nonlinearly in the air and especially the thin exit window of the gas cell. The consequence, as described in the introduction to Section 6.1, is that the intensity profile has is non-reciprocal with propagation. The issue is resolved in Section 6.3 by taking a weak surface reflection from a glass wedge placed near the termination of the filamentation region. This cannot be practically implemented inside the gas cell. However, a re-designed gas cell that incorporates a wedge and a thin vacuum window to transmit reflections that capture the intensity profile will be used in future experiments.

6.2.2 Results

The effects of the mirror optimization are understood by examining the microwaves in the time domain with measurements of the voltage waveforms, and their peak-to-peak amplitude V_{pp}. The calibration procedure of Chapter III is applied to enable absolute analysis of the microwaves in the frequency domain. Figure 6.4 shows measurements of V_{pp} that are characteristic of the microwave yield increase observed

with an optimized mirror shape. Figure 6.4(a) shows that the microwave yield varies

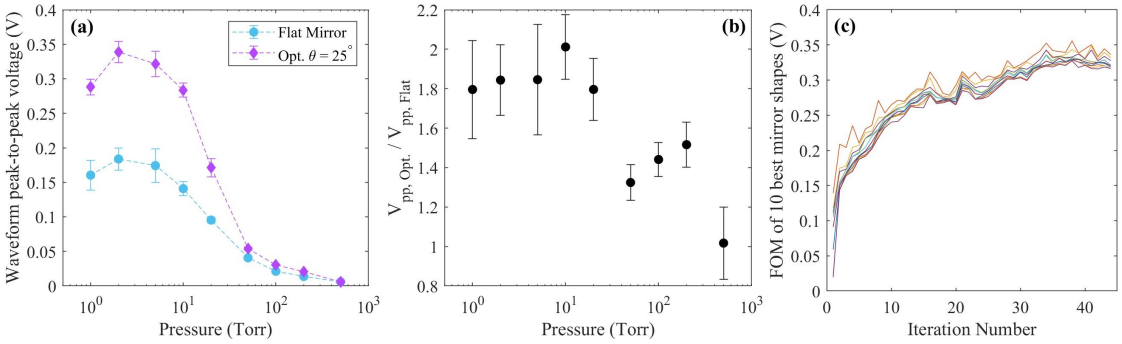

Figure 6.4: (a) Waveform peak-to-peak voltage, V_{pp}, versus air pressure when the mirror is flat (blue circles), and when it is optimized (purple diamonds) based on an antenna position of $\theta = 25°$. (b) The increase in the signal amplitude due to the optimization as a function of pressure using the data in panel (a). (c) Evolution of the FOM (that is, V_{pp}) read by the GA for the ten best individuals in each iteration. It corresponds to the optimization at 2 Torr that is shown in panel (a), but is representative of all the GA runs.

inversely with air pressure, and that the maximum yield occurs at pressure of 2 Torr both when the mirror shape is optimized and when it is flat. The increase in radiation due to the optimization depends on pressure, and is at most about a factor of 2, as Figure 6.4(b) shows. Figure 6.4(c) shows the evolution of V_{pp}, which is the FOM in the experiments, for the 10 best individuals in each iteration of the GA for the case where the pressure is 2 Torr (maximum microwave yield) and the antenna is positioned at $\theta = 25°$. The FOMs for the best individuals exhibit a well-behaved logarithmic rise. We stop the GA once the FOMs remain roughly constant for about 10 iterations, as shown after iteration 30 in Figure 6.4(c). The data presented in Figure 6.4 are representative of the complete set of pressures, emission angles, and optimization cases. The subsequent results more deeply explore the details of the measurements.

Figure 6.5 shows the angular emission pattern based on the waveform peak-to-peak voltage. The microwaves are forward directed, and in general the angular maximum for the 13 GHz bandwidth of the measurements occurs at about $\theta = 25°$. Figures 6.5(a)-(c) show that the factor of ~ 2 increase in the microwave yield demon-

strated in Figure 6.4 for $\theta = 25°$ is typical across the angular emission pattern. The optimization therefore constitutes an increase in the total conversion efficiency of laser energy to microwave radiation. One might expect that the optimization would increase the yield along the angular position of the antenna at the expense of radiation emitted in other directions. Figure 6.5 shows that this does not happen when V_{pp} is optimized. Similar increases in the microwave yield appear to occur regardless

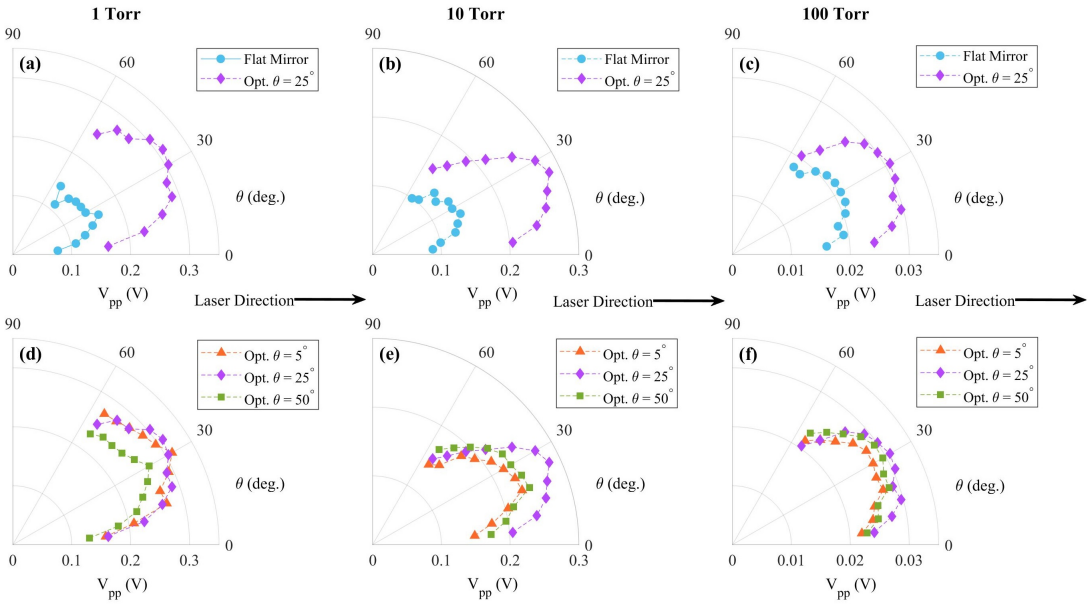

Figure 6.5: Angular emission pattern of the microwaves given by V_{pp}. Panels (a)-(c) compare the patterns found at 1 Torr, 10 Torr, and 100 Torr when the mirror is flat, versus when the microwaves are optimized with the antenna at $\theta = 25°$. Comparison of the same pressure range is shown in panels (d)-(f) for different optimization cases: when the antenna is at $\theta = 5°$ (orange triangles), $\theta = 25°$ (purple diamonds), and $\theta = 50°$ (green squares). The arrows in between the first and second row of panels indicates the laser propagation direction.

of the angular position of the antenna during the optimization. Figures 6.5(d)-(f) compare emission patterns measured when the GA has been run with the antenna at $\theta = 5°$, $\theta = 25°$, and $\theta = 50°$. It is possible that the optimizations at $\theta = 25°$ slightly outperform the others, but not beyond the $\sim 15\%$ uncertainty in V_{pp} due to shot-to-shot fluctuations of the laser. Along with Figure 6.4(b), the comparison of the optimizations at different values of θ seems to indicate that the quality of the GA

optimization may be improved in cases with greater initial SNR. There is more signal at low pressure relative to atmosphere, and at $\theta = 25°$ relative to $\theta = 5°$ or $50°$, so the GA may perform better when it starts in one of these cases.

The effect of the optimization on the microwave waveforms is shown in Figure 6.6. The amplitude increases in the optimized case. The waveforms have been shifted in time to align their features so that the shape comparison is clear. The shape of the main part of the pulse is almost exactly repeated between the optimized and flat mirror shapes for each case of angle and pressure. There may be some deviation between the waveforms in the low frequency, low amplitude portion that follows the main pulse after $t = 1.0$ ns in the plots. Frequency domain analysis is a clearer indicator of differences between low and high frequency components of the pulses.

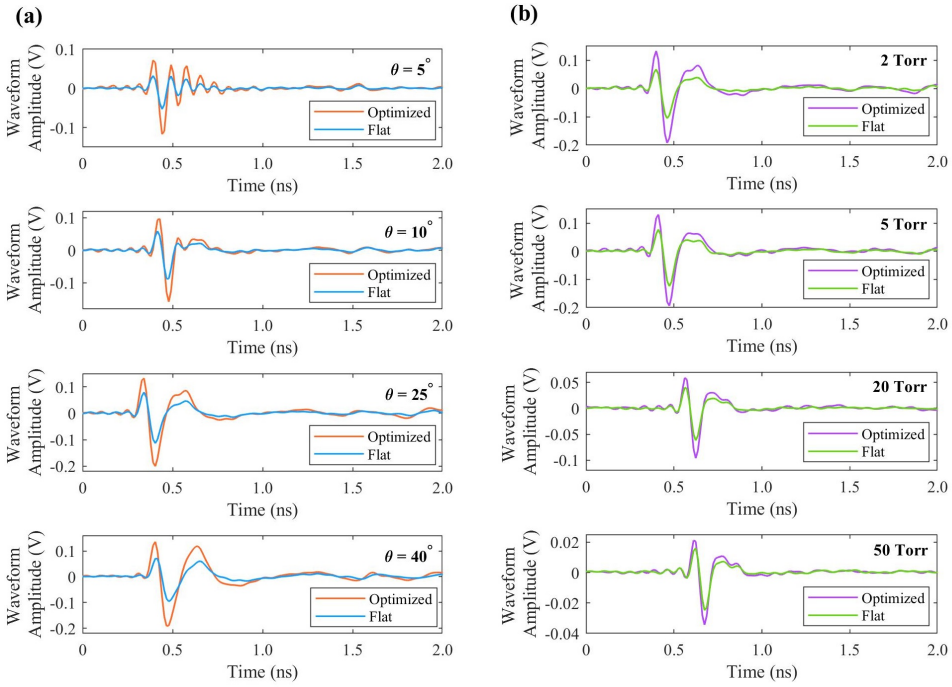

Figure 6.6: (a) The first column of waveforms compares the optimized and flat cases as a function of emission angle at a fixed pressure of 2 Torr. (b) The second column also compares the optimized and flat cases, but as a function of air pressure. The waveforms in (b) are recorded at a fixed angular position of $\theta = 25°$.

Together with the waveforms shown in Chapter IV (Figures 4.3 and 4.4) Figure 6.6 demonstrates that the microwave radiation from the filament plasma is a repeatable

effect. The dependence of the waveforms on pressure and emission angle is the same between two different experiments performed on two different laser systems. In both experiments the waveforms have the same polarity, and single or few-cycle shape. One notable difference, however, is that the duration of the microwave pulses appears to be shorter in Figure 6.6 (≤ 0.5 ns for the main portion of the pulse) than in Figures 4.3 and 4.4 (~ 1 ns), even though the lower frequency bound of both measurements is the same. Chapter VII provides some speculation on the cause of this difference. Still, the similarities between the waveforms mean that the radiation we have measured is likely not caused by some peculiarity of any one laser system. Rather it is a general consequence of the dynamics of filament plasmas.

Calibrated electric field spectra for the optimized and flat mirror shapes calculated from the waveforms in Figure 6.6 are shown in Figure 6.7. Figure 6.7(a) shows the angular dependence of the spectrum at fixed pressure (2 Torr), while Figure 6.7(b) shows its pressure dependence at $\theta = 25°$. There is a clear spectral peak in Figure 6.7(a) that shifts to lower frequencies as θ increases for both the optimized and flat cases. Figure 6.7(b) confirms the non-uniform increase that was observed in Chapter IV in low frequency components relative to high frequencies with decreasing air pressure.

The non-uniform increase in the low frequency components also appears in cases where the optimization is performed with the antenna at $\theta = 5°$ and $50°$. Figure 6.8 shows spectral-angular maps of the radiation at 1 Torr, 10 Torr, and 100 Torr, where the GA is run with the horn at different angular positions. The spectral maps show some slight differences. For example, at 1 Torr, the optimization with $\theta = 5°$ produces the strongest low frequency content. However, the spectral amplitudes for the different optimization cases at each pressure have essentially the same spatial distribution.

The electric field spectra in Figures 6.7 and 6.8 show that even though the optimization is performed with the antenna in a single angular position, the increase in

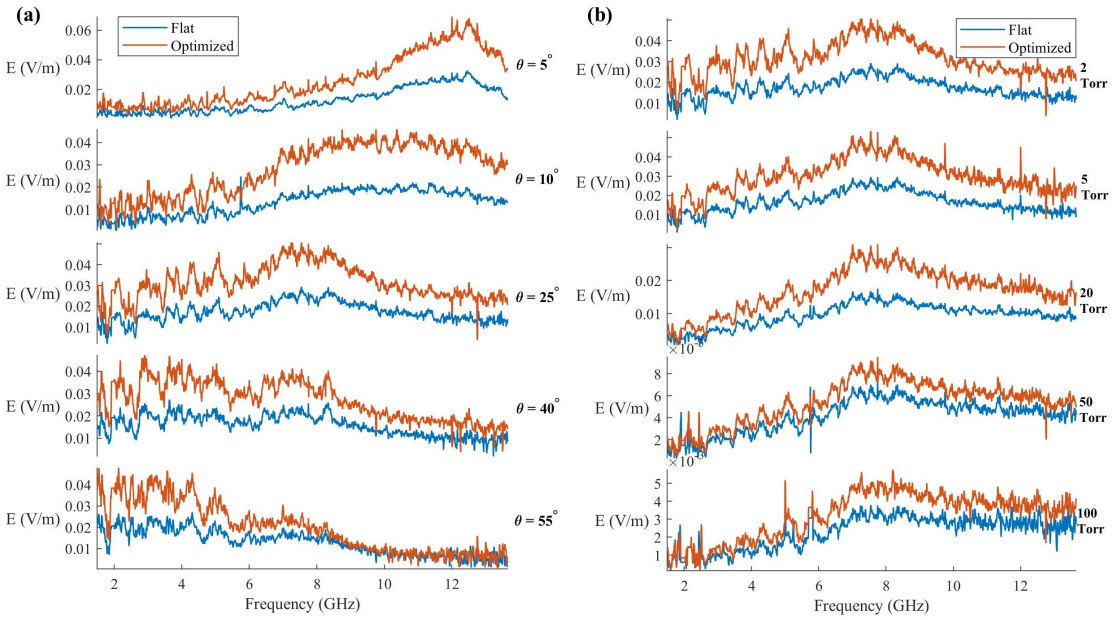

Figure 6.7: Calibrated spectra corresponding to the waveforms in Figure 6.6. (a) Flat versus optimized as a function of emission angle at a fixed pressure of 2 Torr. (b) Flat versus optimized as a function of pressure at a fixed angle of $\theta = 25°$. In order to better demonstrate the trends in the spectral measurements, additional spectra at $\theta = 55°$ and a pressure of 100 Torr are shown in (a) and (b), respectively.

the amplitude of the field is almost perfectly uniform across the receiver bandwidth regardless of what the antenna angular position is during the optimization. While this might seem unusual, consider that the short microwave pulses are broadband, and the waveform envelope forms due to the coherent superposition of many frequency components. In this sense by optimizing V_{pp} we require the GA to find the wavefront that simultaneously maximizes as many frequency components as possible. If the GA can so reliably enhance all the frequency components simultaneously, it is possible that it could flexibly handle optimizations that target more nuanced features of the waveforms and their spectra. For example, the oscilloscope can measure pulse duration and rise time. It may be interesting to use the GA to try to compress or stretch the pulse envelope or oscillations of the microwave field within the envelope in time. In the frequency domain, this would be equivalent to increasing or decreasing the total microwave bandwidth, or optimizing specific frequency components, respectively.

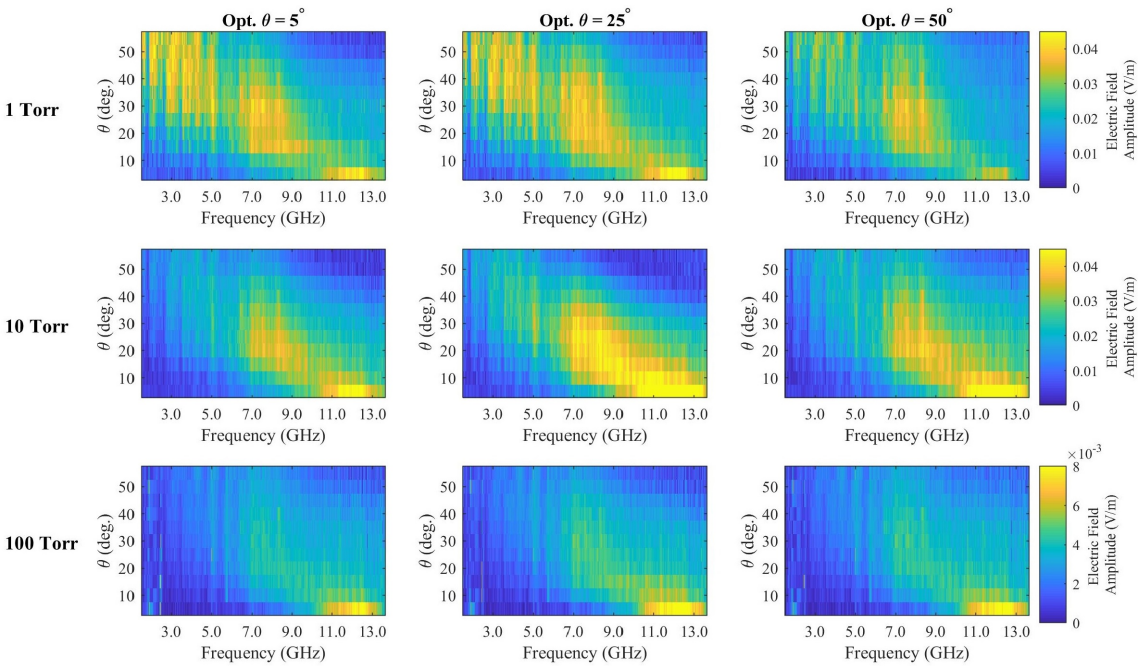

Figure 6.8: The panels are arranged in a matrix to compare the optimizations performed with the antenna at different angular positions as a function of pressure. Each panel contains a calibrated spectral-angular map of the microwave electric field. The color scales are the same in each row of the matrix, and are given on the righthand side of each row.

6.2.3 Discussion

Comparison of Images of the Beam Mode and Plasma for Optimized and Unoptimized Mirror Configuration

We have observed a change in the intensity profile due to the microwave optimization with the GA. Figure 6.9 shows examples of the beam mode of the laser before and after optimizing the microwave yield from the filament plasma. Due to the nonreciprocity of nonlinear propagation described in Section 6.1, these images can give no indication other than that the GA's optimization of the microwave yield changes the beam profile. The images demonstrate that the microwave yield is sensitive to the transverse shape of the laser pulses, but the nature of the dependence must be left to future investigations.

It is difficult to measure what modification the optimized wavefront applied to the

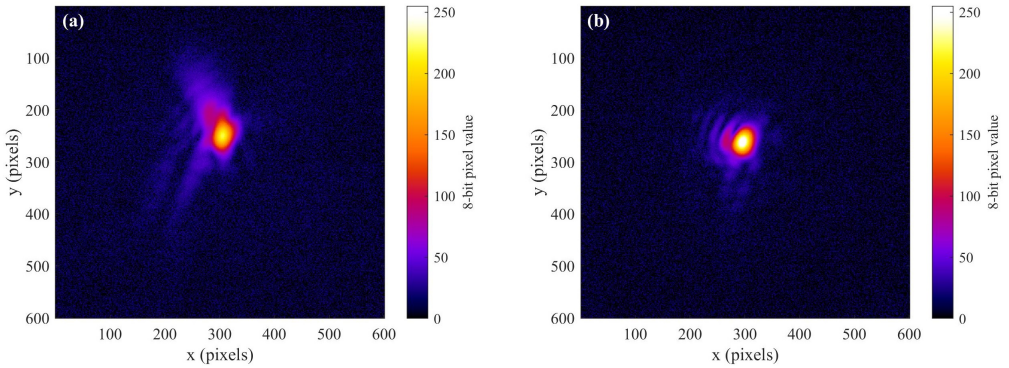

Figure 6.9: Images of the beam mode at the filament termination when the air pressure is 2 Torr (a) before optimization and (b) after optimization. For this particular case, images of the plasma fluorescence from the side show that the filament termination does not shift longitudinal position significantly between (a) and (b).

plasma in order to increase the microwave yield. However, pictures of the plasma fluorescence indicate that the modification is repeatable. Figure 6.10 shows the plasma fluorescence observed with a 16-bit ICCD camera at each pressure, and compares the plasma produced by a flat mirror with the optimized mirror shape. In the images, the laser propagates from right to left. Qualitatively, it is clear from the pictures that the plasmas produced by the optimized mirror have generally longer and brighter regions of fluorescence. The plasma also appears to be wider in the direction transverse to the laser propagation at the lowest values of air pressure. This is in contrast to the results of the THz optimization for which the plasma was also elongated, but whose fluorescence in the visible wavelength range was significantly dimmer than when the DM was flat [187]. This is another indirect, yet significant indication that the THz and microwave radiation are not due to the same behavior of the filament plasma.

Semi-quantitative data about the size of the plasma can be extracted from the images in Figure 6.10. It is not accurate to say that the size of the plasma is the same as the size of the region that produces fluorescence [138]. However, we make the assumption that the size of the fluorescence correlates to the true size of the plasma. Figure 6.11 shows intensity profiles of the fluorescence calculated by integrating over

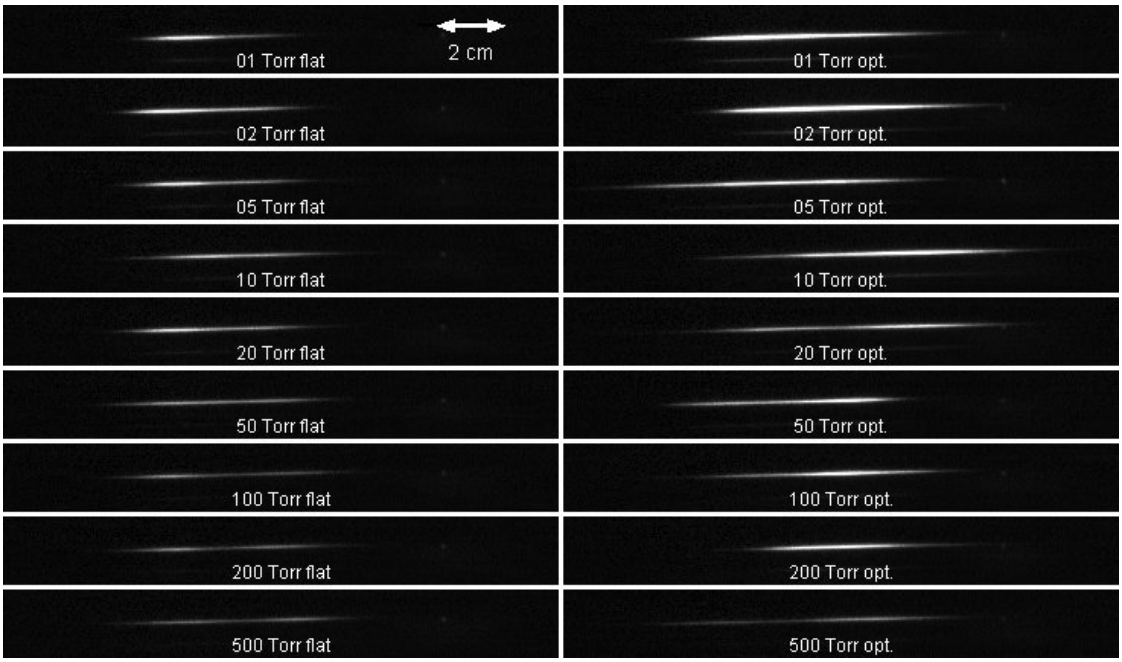

Figure 6.10: Comparison of images of the filament plasma fluorescence when the mirror is flat (left column) versus optimized with the antenna at $\theta = 25°$ (right column). The direction of laser propagation is right to left.

the length and width of the the images. Each profile shown in the plots is the average of 10 profiles calculated from repetitive images of the plasma. The camera was mounted at a slight angle to the direction normal to propagation. This rotation is removed using image processing before integrating the images so that the longer plasmas do not appear to be fictitiously wider in the integrated profiles.

Figures 6.11(a) and (b) give an indication of how the plasma changes due to the optimized wavefront. When the mirror is flat, the plasma appears to have two longitudinally separated regions of brightness, with the brighter of the two toward the termination of the filament region. The effect of the mirror optimization is either to eliminate the separation between the high brightness regions in the plasma, or to shift the brighter one closer to the beginning of the filament region. The examples shown at 2 Torr, 20 Torr, and 200 Torr are representative of the length profiles at all the cases shown in Figure 6.10. The two longitudinally distinct regions of fluorescence imply that the laser focus is astigmatic if the DM is flat. Some astigmatism in the

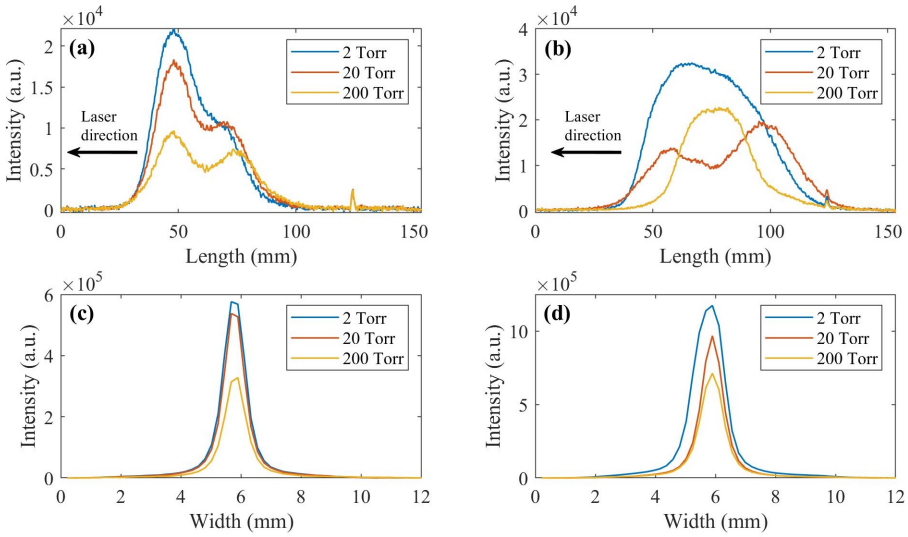

Figure 6.11: Intensity profile of the plasma fluorescence in the longitudinal direction found by integrating in the transverse dimension when the DM is (a) flat versus (b) optimized. The arrows indicate the direction of laser propagation. The transverse intensity profiles for the (c) flat and (d) optimized mirror shapes are calculated by integrating along the longitudinal dimension.

focus is expected as a limitation of the experimental setup we have used. Figure 6.3 shows that the laser reflects from the surface of the DM and is incident on the focusing mirror at an angle. This aspect of the diagram exists in the real experimental setup – there is a slight angle in the beam path. Reflections from a concave surface due to off-normal incidence exhibit astigmatism at the focus. The longitudinal profiles of the plasma fluorescence for the optimized wavefront indicate the possibility that the DM corrects the aberration. The intensity of an astigmatic beam is lower at the focus than that of an ideal beam. Perhaps the increase in the microwave yield is in part due to greater intensity achieved when the wavefront aberrations are compensated.

The profiles of the plasma width in Figures 6.11(c) and (d) are not quite as useful as the length for three reasons. The first is that the images are composed to fit the whole plasma at once, so the resolution in the transverse direction is low. The second is that the curvature of the quartz tube is in the direction of the transverse dimension which gives the plasma images a small cylindrical distortion. Third, the

plasma expands over its lifetime. A simple calculation shows that over the 100 ns integration time used to record the images in Figure 6.10, the final image includes smearing of the transverse profile due to radial plasma expansion.

The continuity equation for species k in the filament plasma is given by

$$\frac{\partial N_k}{\partial t} + \nabla \cdot \mathbf{\Gamma}_k = 0, \tag{6.1}$$

where $\mathbf{\Gamma}_k = N_k \mathbf{v}_k$ is the flux of species k. The filament plasma is unmagnetized and has no wall interactions. It therefore decays by simple ambipolar diffusion, which is explained by the following scenario. The high mobility electrons try to escape down the plasma's radial pressure gradient, and the inertia of the ions initially prevents them from moving with the electrons. The negative space charge that results has an electric field that accelerates the ions, and the energy in this field comes from the kinetic energy of the electrons. In ambipolar diffusion, the electrons diffuse more slowly than what would be found by solving the momentum equation with ∇p_e. Similarly, the ions diffuse more quickly than only accounting for ∇p_i. In fact they diffuse at the same rate, which can be found by equating the fluxes of each species. The result is $\mathbf{\Gamma}_e = \mathbf{\Gamma}_i = \mathbf{\Gamma}$, and

$$\mathbf{\Gamma} = -\frac{\mu_i D_e + \mu_e D_i}{\mu_i + \mu_e} \nabla N = -D_A \nabla N, \tag{6.2}$$

where $\mu_k = |q|/m_k\nu$ is the mobility, and $D_k = k_B T_k / m_k \nu$ is the diffusion coefficient. Equation 6.2 assumes $N_i = N_e$, and that each species is isothermal so that $\nabla p_k = k_B T_k \nabla N_k$. Electrons in the filament plasma have much higher mobility than the ions, so in the limit $\mu_e \gg \mu_i$, D_A can be approximated as

$$D_A \simeq D_i \left(1 + \frac{T_e}{T_i}\right). \tag{6.3}$$

We can use Equations 6.2 and 6.3 to make an order of magnitude estimate of how far the plasma expands over the 100 ns gate time of the ICCD images.

$$\Gamma = N \times v \rightarrow v = \frac{dr}{dt} = -D_A \frac{\nabla N}{N}, \tag{6.4}$$

$$\frac{dr}{dt} \sim \frac{\Delta r}{\Delta t} \rightarrow \Delta r \sim D_A \frac{\nabla N}{N} \Delta t \sim 1 \text{ mm}. \tag{6.5}$$

Equation 6.5 calculates Δr at a pressure of 2 Torr where the maximum microwave yield occurs, and assumes the ion-neutral collision rate occurs between singly ionized nitrogen and neutral nitrogen. The ions are assumed to be at room temperature, and $T_e = 1$ eV. The density gradient scale length $(\nabla N/N)^{-1}$ is approximated to be 50 μm (the radius of a typical filament), and $\Delta t = 100$ ns.

A plasma diameter of about 1 mm is what we observe in the images of the fluorescence in Figure 6.10, especially at low pressure. At atmospheric pressure, the recombination time for the filament plasma is about 5 ns [91, 188], so the plasma will recombine before expanding nearly as much it would at lower pressures. Equation 6.5 is likely an overestimate of how much the plasma expands, because the rate at which its boundary extends will decrease as the plasma becomes more diffuse. However, it indicates that the apparent width of the plasma fluorescence in the images is a combination of the size of the plasma initially produced by the laser pulse, and plasma expansion long after the pulse has propagated away. Nonetheless, we can use the width measurements from the images as a relative indication of the plasma size at individual values of air pressure. If the filament plasma made by the optimized wavefront shape at a given pressure is initially larger than that due to a flat DM, then after 100 ns of evolution we assume that it will appear larger than a filament plasma that initially had a smaller radius.

A fitting routine extracts the length and width of the fluorescing region of the plasma from the longitudinal and transverse profiles shown in Figure 6.11. The

routine finds each dimension at the $1/e^2$ folding of each profile referenced to its maximum value. Figure 6.12 shows the length and width of the fluorescence as a

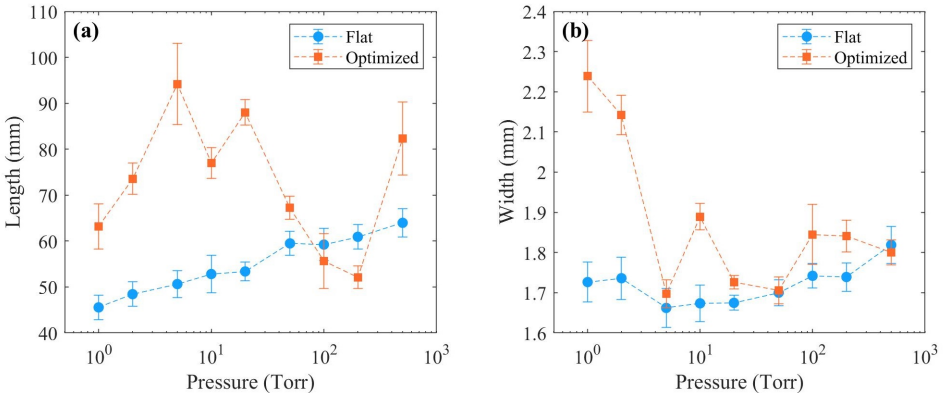

Figure 6.12: (a) Length of the plasma fluorescence as a function of pressure for the optimized and flat cases. (b) Apparent width of the plasma fluorescence calculated from the same images.

function of pressure. In general, it appears that the plasma becomes shorter at low pressure if the DM is flat. The width may also decrease, but given the uncertainties in the data it may be more conservative to say that the data imply a roughly constant width with pressure. Figures 6.12(a) and (b) show that the optimization generally increases the length and width of the plasma, but not by the factor of ~ 2 that we observe in the microwave yield.

The images of the plasma fluorescence are useful in that they allow us to draw two conclusions about the wavefront optimization that maximizes the microwave yield. First, the optimization causes the plasma to increase in size. The length increase is quite stark, while the relative width increase is measurable but subject to the caveat that the plasma shape evolves in the transverse direction over the camera integration time. The second conclusion is that the optimization increases the brightness of the plasma fluorescence. It appears to change the structure of the plasma from two longitudinally displaced high brightness regions when the DM is flat, to one that does not have a dip in the middle. This may indicate that the microwave optimization causes the DM to correct astigmatism present in the initial beam focus. Finally, comparison

of the fluorescence intensity profiles with a previous and similar experiment on THz optimization provides additional indication that the microwaves and THz are due to different mechanisms. Optimizing the THz signal causes the plasma to elongate but to fluoresce less brightly, indicating that the length of the plasma is more important for THz generation than the focal intensity of the laser. Other experiments have shown that longer filament plasmas are more efficient sources of THz radiation [189, 190]. Optimizing the microwave yield also increases the filament plasma length, but instead increases its fluorescence. This implies that the focal intensity of the laser is significant for maximizing the microwave yield.

Repeatability of the Optimized Mirror Configuration

The converged mirror configurations found at different pressures and antenna positions indicate that the wavefronts the mirror applies to optimize the microwave radiation are similar. Figure 6.13 shows the actuator displacements as they are arranged in the DM aperture for the optimizations with the antenna at $\theta = 25°$ and compares them to the mirror configurations found with the antenna at $\theta = 5°$ and $50°$. There seem to be common patterns to the actuator displacements in between the antenna positions in each of Figures 6.13(d)-(f). Furthermore, the optimizations at the different pressures share some of these patterns. For example, the dip in displacement at actuator #5 repeats in several instances. However, this feature is not always as pronounced in the optimizations performed at $\theta = 5°$ so the commonality is not simply due to a broken voltage supply on that actuator. The common features in optimized mirror configurations indicate that the GA converges to similar solutions for each test case.

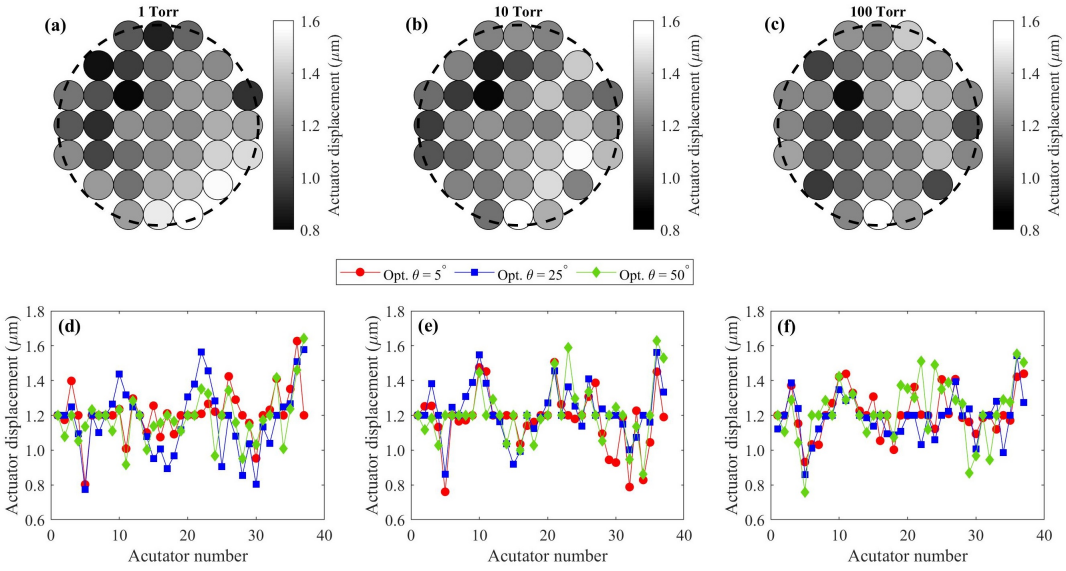

Figure 6.13: Actuator configuration and displacement for optimizations with the antenna at $\theta = 25°$ at (a) 1 Torr, (b) 10 Torr, and (c) 100 Torr. Plots (d)-(f) compare the displacements of the actuators for the different antenna positions ($\theta = 5°$, $25°$, and $\theta = 50°$) at 1, 10, and 100 Torr, respectively.

6.3 Adaptive Control of the Configuration of Multiple Filaments

Many envisioned applications of filamentation require manipulating filaments in air at some great distance from the laser that produces the pulses. Examples include white light LIDAR [191], guiding high voltage discharges [192], remote sensing [115], and remote generation of terahertz radiation [170]. These depend on controlling the location, extent, and configuration of the filaments. Manipulation of the spatial phase with the DM should allow for fast control of the number and position of the filaments if the mechanisms governing the break up of the beam in the multifilamentation regime are well understood. This includes the interplay between the energy reservoir with the filament at its core, and the mutual interactions of the energy reservoirs of neighboring filaments.

Other efforts to control multiple filamentation have succeeded in creating station-

ary configurations of multiple filaments. The ability to tune the onset and extent of single and multiple filaments has also been demonstrated. Beam ellipticity [193] and imposed astigmatism [194] can provide one dimensional control over the filament configuration. A circularly polarized input beam has been shown to create a pair of co-propagating filaments with high spatial stability [195]. Amplitude masks have been employed to create two-dimensional filament arrays [196, 197], as have phase plates [198], although these approaches incur significant loss of pulse energy and cannot be easily reconfigured on demand. Some researchers have indeed used deformable mirrors to fix the onset of filamentation [199, 200], and also to impose transverse phase profiles that seed multiple filaments the beam [201, 202] albeit without the ability to precisely choose the locations within the energy reservoir where the filaments appear.

Since filamentation is sensitive to so many aspects of a laser pulse in addition to atmospheric fluctuations, some researchers investigating remote applications of filamentation have turned to evolutionary algorithms similar to that discussed here in order to optimize the signal derived from their experiments. These include maximizing target fluorescence at a distance for remote sensing applications [203], maximizing the supercontinuum emissions from the filaments [204], and constraining their onset and termination [205]. The work presented here focuses particularly upon showing the feasibility of using the GA to configure the filaments within the energy reservoir.

These experiments are a proof-of-principle demonstration that the DM can be used to configure filaments at a distance of several meters. The description of the experiment and its results are based on a journal article publication written by the author [49]. We believe that the ability of the DM to place the filaments within the beam profile is due to seeding of the transverse modulational instability, which is commonly given as the cause of beam breakup and multi-filamentation when the laser pulse is far above the critical power for self-focusing [206, 207, 40]. Modulational instabilities arise in optical physics in contexts other than filamentation [66], but they

can be explained in the same manner. In filamentation, infinitesimal perturbations of the laser spatial phase grow unstably due to the Kerr nonlinearity. Linear stability analysis predicts that only certain transverse wavenumbers, that is modulations of the spatial phase, are unstable. The growth rate, γ, is given by [208]

$$\gamma = k_r \sqrt{\frac{2P_L}{P_{cr}} - \frac{k_r^2}{4}}, \tag{6.6}$$

where k_r is the radial wavenumber, P_L is the pulse power, and P_{cr} is the critical power. If solutions to the linearized wave equation for a pulse propagating in the z direction have $\exp(\gamma z)$ dependence, then Equation 6.6 shows that values of the radial wavenumber $0 < k_r < 2\sqrt{2P_L/P_{cr}}$ will grow unbounded with increasing z. In reality, the instability saturates when the pulse breaks up into multiple filaments and each begins ionizing the air. In order for the DM to configure the filaments in a repeatable configuration, it must apply spatial phase changes in the unstable wavenumber range that are larger than that due to random noise or systematic aberrations.

This capability may be useful for studying interactions between filaments in the multifilament regime. Mutual interactions of two filaments have been examined theoretically [209] and experimentally [210, 211], and can be carefully controlled by splitting a beam and focusing the two beam paths. Self organization without external manipulation of hundreds of filaments into unit cells defined by the energy reservoirs has also been observed [32, 33]. However controlled filament interactions have not been fully generalized to arrays of an arbitrary number of filaments. The ability to perform such studies will be useful for the applications suggested above, and better understanding the role of the energy reservoir in single and multiple filamentation.

6.3.1 Experimental Methods

The λ^3 laser is also used in these experiments at its maximum pulse repetition rate of 500 Hz. In order to generate multiple filaments in atmosphere, the pulse energy is maintained within 12.5-15 mJ for all filament configuration tests. If $P_{cr} \sim 5$ GW, then each laser pulse achieves approximately $86P_{cr}$. If we use a value of about $10P_{cr}$ per filament needed to form a multifilamenting pulse [212] as a heuristic, there should be less than 10 filaments visible in the exit mode.

The image of the exit mode from the filament region is formed with minimal astigmatism by reflecting the beam off of a wedge placed beyond the end of the filaments, and then a concave $f/7.5$ mirror, which nearly retro-reflects the attenuated beam back off the wedge and on to a turning mirror. The first wedge reflection reduces the laser power to about $3P_{cr}$, and only propagates a short distance before the second reflection, which reduces the power to $\sim 0.1P_{cr}$. This assumes a 4% reflection from the front surface of the wedge. The exit mode images formed on the camera reliably represent the mode at the filament termination because of the power reduction and short propagation distance. The light remaining after both wedge reflections is neutrally filtered, and then bandpass filtered at 800 ± 5 nm before illuminating a CCD camera (DMK21BU04 by Imaging Source). Even with self-phase modulation of the laser light, the filament spectrum peaks at 800 nm, so filaments appear as bright spots in the images. The CCD sensor has a resolution of 640 by 480 with 5.6 μm pixels and 8-bit depth. The camera is triggered by the laser, and integrates for a single shot, recording once every 33 shots.

Figure 6.14 shows the experimental setup. The beam fills the deformable mirror and is subsequently transported about 7 meters in air, where it is focused through a $f/20$ lens, for a total of 8 meters of propagation between the deformable mirror and the filamentation region. The LabVIEW program which runs the GA takes the camera settings and user-defined filament locations as inputs, interfaces with the

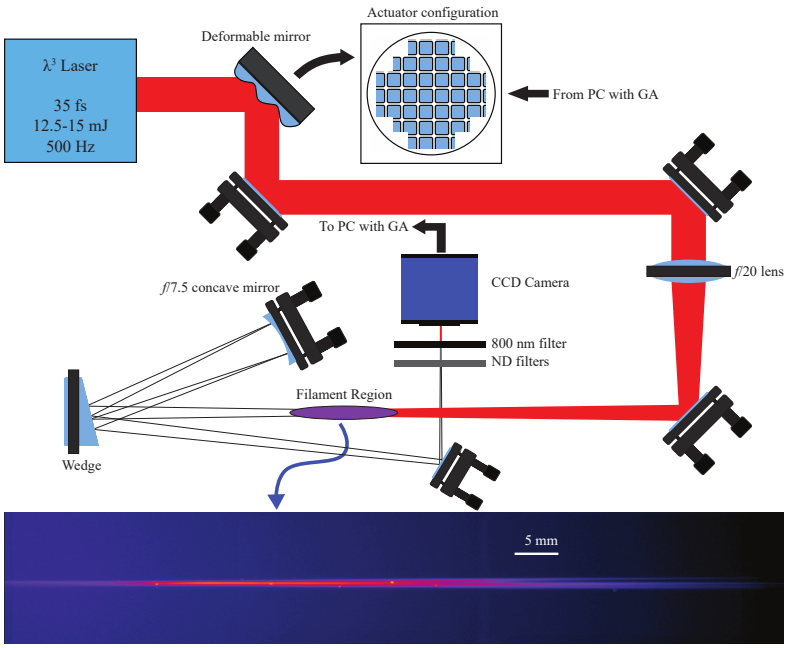

Figure 6.14: Diagram of the experiment. The image of the filament region is a composite of several false-color images captured with a CMOS camera (DMK23UX174 by Imaging Source). The confocal parameter of a non-filamenting beam in this setup is about 1 mm.

mirror to set the actuator voltages, and calculates the FOM corresponding to each tested mirror figure.

The fitness function used to determine the FOM of each individual from the exit mode image is given by

$$\mathcal{F} = \prod_{k=1}^{N} \sum_{\substack{i,j \\ x_i \neq x_k, y_j \neq y_k}} \frac{I_{ij}}{[(x_i - x_k)^2 + (y_j - y_k)^2]^4}, \tag{6.7}$$

where I_{ij} indicates each pixel value, i and j are indices which increment the pixels, x_i and y_j indicate pixel coordinates in the camera image, x_k and y_k are the desired coordinates of the filaments, and N is the desired number of filaments. Written as an image moment [180, 213], Equation 6.7 encourages filaments to occur simultaneously at all coordinate pairs (x_k, y_k). If the pixel values at or near (x_k, y_k) are low, then the whole FOM is multiplied by a small number, even if there are filaments at the other desired coordinates. The image moment formulation – multiplying several times by

the inverse of the distance in the image between each pixel and (x_k, y_k) – tends to draw regions of high pixel values toward (x_k, y_k). Since the filaments are typically the brightest features in the exit mode images, their locations in the energy reservoir are expected to settle on each (x_k, y_k) given enough iterations of the GA. Clearly, if N is greater than the number of filaments that can be produced with the available pulse energy, the algorithm will fail.

Figure 6.14 also shows an example of a false color image [214] of the air plasma left in the wake of the filaments viewed in the sagittal plane. For this particular test case, a few filaments appear to converge and fuse near the geometrical focus of the $f/20$ lens. This image is included because it is representative of the appearance of the filaments when the deformable mirror is not flat. The aberrations introduced by the deformable mirror lengthen the filaments relative to those observed when the mirror is flat, and create the branching filament structure. The focusing lens constrains the pulse's energy deposition in space and forces the filaments to come together.

6.3.2 Results

Single Filament Control

The results demonstrate filament control through three related experiments. The first involves using the GA to create an apparent intensification of a single filament by setting $N = 1$ and (x_k, y_k) to the center of the pulse in Equation 6.7. The second demonstrates that the GA can be used to reposition a single filament arbitrarily within the energy reservoir reliably and with reasonable shot-to-shot repetition. The third experiment shows the ability of the GA to create patterns of filaments where $N \neq 1$. For all three experiments the laser power and external focusing at $f/20$ are constant as described in Section 6.3.1.

Intensity clamping prevents greater intensity in a filament to be achieved simply by tighter focusing of the pulse. Figure 6.15 compares the exit mode observed when

the mirror is flat with one observed after the GA has optimized the exit mode for a single filament ($N = 1$) with the target filament location set to the initial filament location, that is, the center of the pulse.

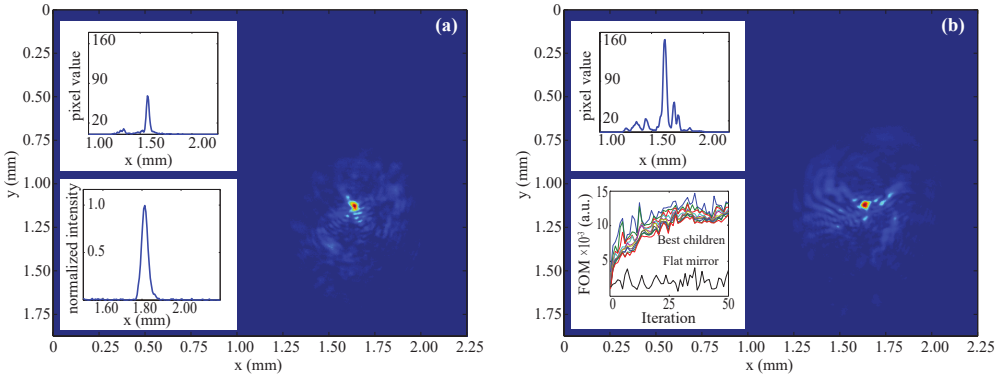

Figure 6.15: Comparison of the exit mode when the deformable mirror is (a) flat versus when it is (b) optimized to place the filament at the existing location in (a). The top insets in (a) and (b) show lineouts of the beam profile taken horizontally through the center of the beam spot for both cases. The bottom inset in (a) shows a lineout of the beam profile near the geometrical focus of the $f/20$ lens with the laser power attenuated to the linear propagation regime, and the deformable mirror flattened. The bottom inset in (b) shows the evolution of the FOM for the ten best mirror figures in each iteration compared to the FOM calculated for a flat mirror. The raw exit mode image pixel values have been mapped to 8-bit RGB color.

Break-up of the beam caused by multiple filamentation is responsible for the poor beam quality shown in Figures 6.15(a) and 6.15(b). The bottom inset in Figure 6.15(a), whose intensity values do not correspond to the top insets and are therefore normalized, shows that the beam quality of the laser is quite good in the absence of filamentation. The structure of the energy reservoir for a filamenting pulse evolves randomly as it propagates. In comparing Figures 6.15(a) and 6.15(b), it seems that not only is the brightness of the filament is increased, but also that of the energy reservoir. The lineouts in each of the top insets include the maxima in both images, and indicate a nearly three-fold increase in the apparent brightness for the optimized case. With respect to the energy reservoir, we can only speculate that the deformable mirror may shape the wavefront so as to redistribute energy in the tails of the pulse toward the center. Confirmation of such an effect will need further study.

The increased brightness in the single observed filament is likely due to overlapping of multiple filaments at the pulse center such that the overlapping filaments are more tightly arranged than when the mirror is flat. Another effect possibly contributing to the increase in brightness observed in Figure 6.15(b) is that the filament may be closer to the optimal object plane of the concave mirror imaging the exit mode. The image in Figure 6.15(a) was recorded with the imaging plane manually optimized such that the pulse diameter seen on the camera was minimized. We have observed that running the GA continuously while moving the imaging plane causes the downrange end of the filament to move in lockstep with the camera in order to keep the end of the filament in focus. While the layout of the imaging optics is unchanged between Figures 6.15(a) and 6.15(b), some part of the brightness increase in Figure 6.15(b) may be due to the GA performing a minor adjustment to the length of the filament in order to optimize its longitudinal termination at the object plane. However, this does not explain necessarily the increased brightness of the reservoir.

The bottom inset in Figure 6.15(b) shows the typical evolution of the FOM as the GA iterations advance. In most cases, the envelope traced by the 10 best children in each iteration exhibits a logarithmic rise, making it clear when the algorithm has converged, and it is acceptable to stop its function.

In order to demonstrate that our approach permits arbitrary positioning of a filament within the energy reservoir, we ran successive cases in which the target filament location was moved in increments of about 50 μm along each of the four cardinal directions ($\theta = 0, \pi/2, \pi, 3\pi/2$) defined in the sense of a unit circle. Figure 6.16 shows one case in which the filament is positioned along $\theta = 3\pi/2$. It is clear that the location of the filament moves within the energy reservoir, and that the trivial solution to Equation 6.7 with $N = 1$– steering the whole beam so that its center coincides with (x_k, y_k) – is not observed.

In order to distinguish filaments in the exit mode, the raw image files starting with

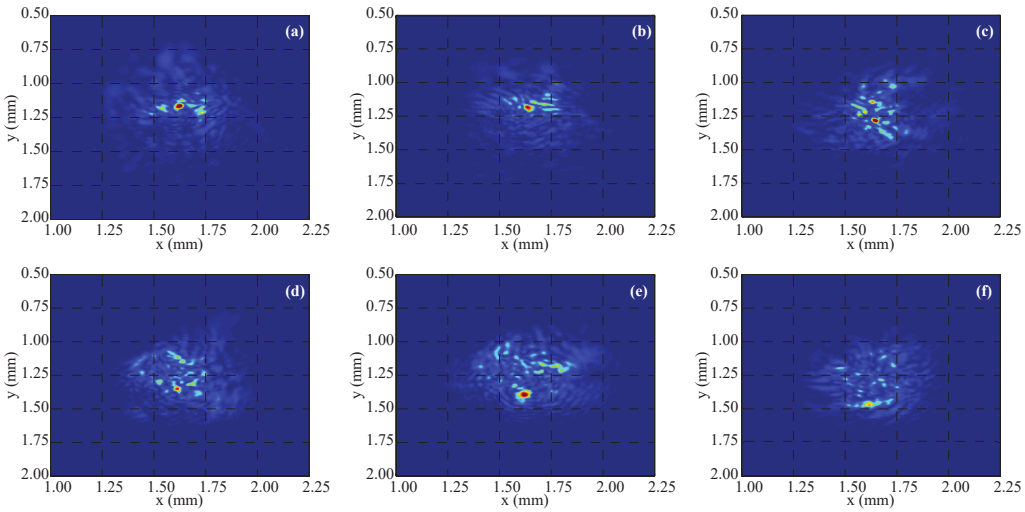

Figure 6.16: Each of (a)-(f) show the exit mode profiles of a single filament moving in increments of 50 μm along $\theta = 3\pi/2$, starting from the center (a) and ending at a displacement of 250 μm (f) along the periphery of the pulse.

the cases such as that in Figure 6.16(a) are thresholded so that the filament optimized in the center of the reservoir appears on a dark background. The characteristic size and brightness of this center filament is used to determine which features in all other images, once thresholded, are filaments. The typical observed diameter for the filaments in our experiments is about 40 μm. The pulse energy is not attenuated to the single filament regime in these tests, so it is likely that at least in some of the test cases, multiple filaments have been made to overlap. Figure 6.16(e) shows a filament which has an apparent size approximately double that of the other cases, which based on repetitive images of this test case indicate possibly two filaments in close proximity at the target filament location.

Overlapping of filaments when the target location is off-center is rare. What is much more likely to happen is that a single filament is optimally imaged at the target location so that it appears very bright in the exit mode. If the filament is within about its characteristic size of the user-specified (x_k, y_k) then it is considered to be on target. Additional filaments commonly appear elsewhere in the reservoir. The phase profile imposed by the mirror tends to create these satellite filaments which are

usually not quite as bright as the filament being controlled. They appear at other places within the reservoir which are clearly distinct from the target location. Many of the satellite filaments repeat shot-to-shot with moderate probability along with the controlled filament. This implies that they are unintended artifacts of the mirror shape, as opposed to the result of random fluctuations in the pulse profile.

Figure 6.17 quantifies the shot-to-shot reliability of the GA-optimized mirror figures, including the likelihood of creating satellite filaments along with the controlled filament. Twenty exit mode images are recorded for each target filament location with the deformable mirror fixed in its optimized shape. The position of the controlled filament is fairly stationary, however Figure 6.17 demonstrates a few cases in which the GA fails (twice in Figure 6.17(b) and twice in Figure 6.17(e)) near the periphery of the energy reservoir. Averaging over each of the twenty four test cases shown in Figures 6.17(a), 6.17(b), 6.17(d), and 6.17(e), the average difference between the target locations (x_k, y_k) and the mean location of the on-target filaments is less than two pixels (with an uncertainty of one pixel) or about a quarter of the nominal filament size. During experiments, the beam location tended to drift downward as viewed on the camera. This is a result of the heating of the air by the filament plasma. Because of the high pulse repetition rate (500 Hz) the air in the filamentation region cannot dissipate the heat the plasma generates between shots, creating a density depression that is subject to hydrodynamic forces from the surrounding air [111]. In Figure 6.17 the target filament location is adjusted to compensate for steering of the beam over time but maintain the 50 μm interval between targets, which is reflected in the downward drift of the diamond target location markers as the distance from the beam center increases.

As the target location is moved further away from the center of the reservoir, the shot-to-shot scatter of the filaments tends to increase, as Figure 6.17(c) shows. Further, in Figure 6.17(f) the aggregated data from Figures 6.17(a), 6.17(b), 6.17(d),

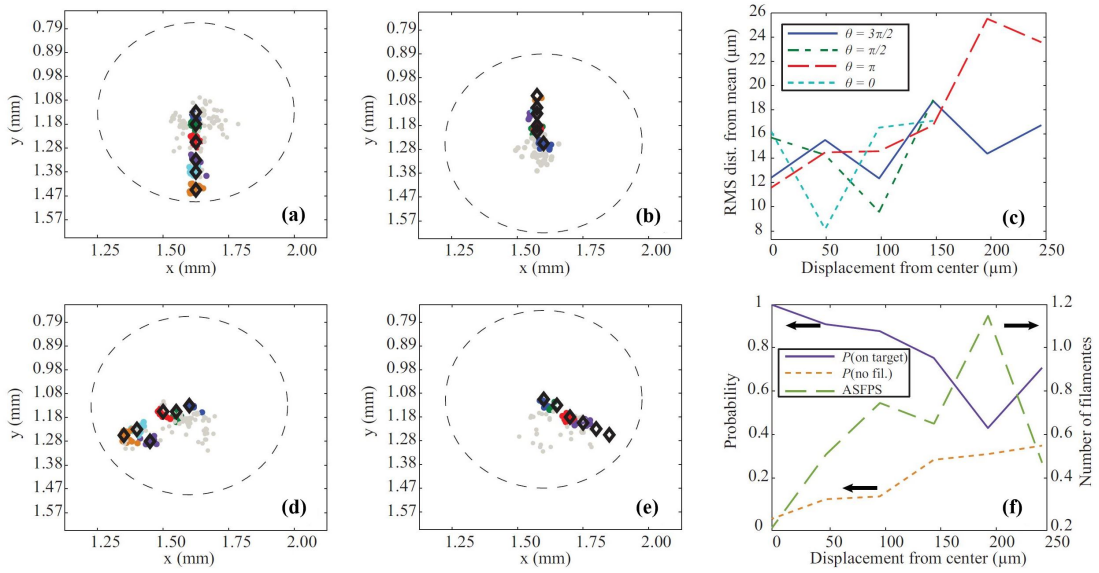

Figure 6.17: The centroids of all filaments marked for each of the different test cases when (a) $\theta = 3\pi/2$, (b) $\theta = \pi/2$, (d) $\theta = \pi$, and (e) $\theta = 0$. The target filament locations are marked with diamonds, and the different test cases are colored so that they may be distinguished. The nominal reservoir size is indicated by the dashed circle based on targeting the filament in the center of pulse. The aggregate of all satellite filament centroids for each direction are marked in each figure in gray. The sample size for each target filament location is 20 shots.The RMS scatter of the samples shown in (a),(b),(d), and (e) are plotted as a function of distance from the drift-compensated pulse center in (c). (f) shows the probability of having the filament on target, the probability that no filaments are visible in the exit mode, and the average number of satellite filaments per shot (ASFPS) as a function of distance from the pulse center.

and 6.17(e) indicate the probability that the brightest (i.e. most in focus) filament is on target tends to decrease with distance. The likelihood that the mirror figure seeds one or more satellite filaments increases, as does the probability that no filaments are visible in the exit mode. Taken as a whole, the statistics of the test case samples lead us to conclude that the efficacy of the GA and the deformable mirror in controlling the filament is diminished with distance from the center of the energy reservoir. Two factors contributing to the decrease in the quality of the optimization may be: i) simply that there is less available laser energy around the periphery of the reservoir to ensure that the filament propagates into the optimal object plane, and ii) that the phase profile is subject to the action of fewer actuators at the edge of the mirror, so that the changes to the wavefront there are limited.

Multiple Filament Control

The GA can also manipulate the deformable mirror to place multiple filaments at different target locations using the same laser power and focusing conditions as the experiments which controlled a single filament. In Equation 6.7, this corresponds to $N > 1$ and multiple target coordinate pairs (x_k, y_k). Figure 6.18 shows examples of two test cases where multiple filaments are configured within the energy reservoir. The fitness function does not converge nicely for multi-filament control, unlike the

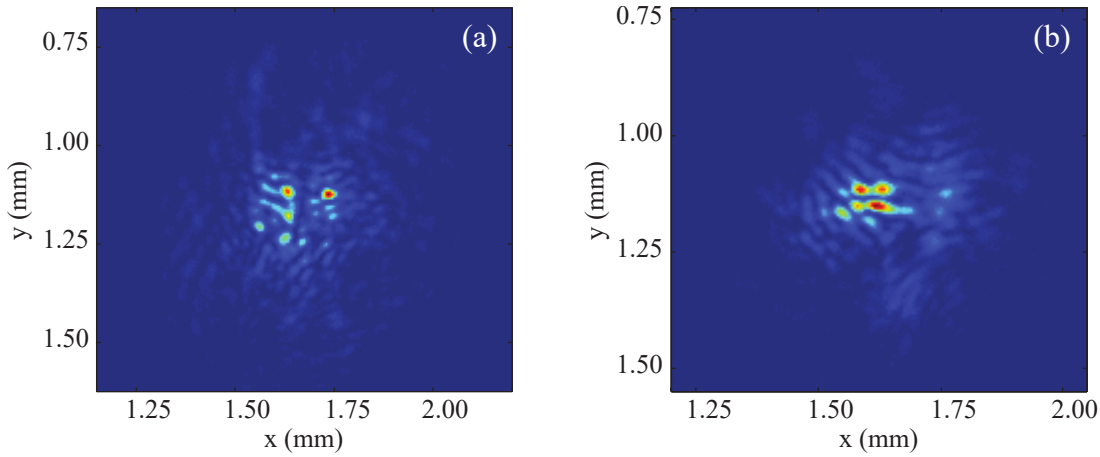

Figure 6.18: User-defined placement of (a) 2 and (b) 4 filaments.

asymptotic behavior observed for the single filament control experiments. The stop condition for the GA when controlling multiple filaments is to observe the exit mode corresponding to the best child from an iteration, and stop after the exit mode appears to not change significantly for about ten iterations. The shot-to-shot variations taken together become more severe with the control of more filaments.

Table 6.1 quantifies the repeatability of the filament configurations shown in Figure 6.18. The probability that one, two, three, or four, $P(1-4)$, filaments are visible and at the target location are given in percentages. Samples where only satellite filaments are observed account for 10% of the samples in the two-filament test, which is why $P(1) + P(2) = 90\%$. In the four-filament test, all samples showed at least

Table 6.1: Shot-to-Shot Statistics for Multiple Filament Configurations

Target # fil.	$P(1)$	$P(2)$	$P(3)$	$P(4)$	ASFPS	RMS dist. from mean (μm) f_1	f_2	f_3	f_4
2	44.0%	46.0%	–	–	0.70	24.5	19.2	–	–
4	11.8%	39.2%	39.2%	9.80%	0.098	16.0	14.0	16.2	21.5

one filament on target. The average scatter of the filaments from shot-to-shot are calculated for each filament f_{1-4}, and are approximately a factor of 2 larger than that observed for single filament control. For the two-filament case, the sample size is $n = 61$, while for the four-filament case, it is $n = 56$. The two-filament case is successful 46% of the time, while all filaments in the four-filament case are on target in only about one of ten shots. However, the four filaments use up the available energy in the pulse, so there are few satellite filaments.

Filaments on the corners of a square, as presented in Figure 6.18(b), can also be produced by other means of multiple filament control, such as a periodic mesh [196]. A similar method is to drill holes in a sheet of opaque material and transmit the beam through the holes so that the filaments form in a regular pattern [215, 216, 217, 218]. These methods produce repeatable filament configurations, but significantly diminish the pulse energy that can be delivered at a distance since the pulse is partially blocked by the mesh or regularizing screen.

6.3.3 Discussion

Repeatability of the Mirror Shape

It is unclear from our experiments whether or not inputting the same number and target locations for the filaments into the GA cause it to always converge to the same (or even to a similar) mirror figure. Figure 6.19 shows results from two sets of three trials for two different input values of the mutation probability applied to the actuators. In all the trials, the target filament location is set to the center of the

energy reservoir. Yet each set of trials produces mirror figures that have arguably

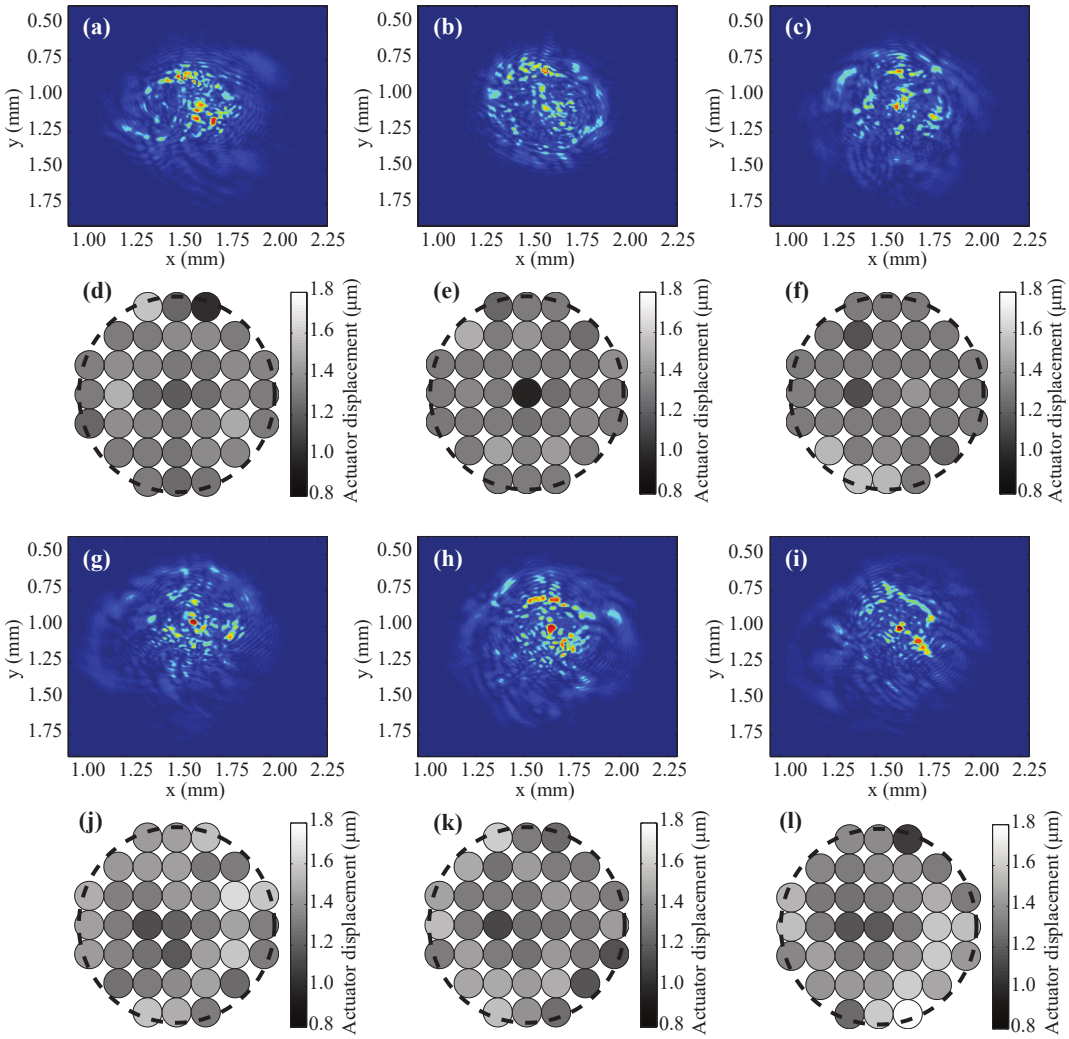

Figure 6.19: (a)-(c) show three separate trials where the target filament location is set to the center of the pulse, with the mutation probability and amplitude set to 2%. (d)-(f) show the corresponding displacements of the mirror actuators that the GA converges to in each trial. (g)-(i) and (k)-(l) show trials of the same test case, except with the mutation probability set to 20%.

no common features, as shown by comparing each of Figures 6.19(d)-6.19(f) to each other, and also to each of Figures 6.19(j)-6.19(l). The dominating effect leading to this observation is the noisy nature of the experiment. The fluctuations in the pulses and the atmosphere ensure that optimized mirror figures will always exhibit differences, even if all else remains unaltered.

In Figures 6.19(a)-6.19(f) the mutation amplitude and probability is set to 2%,

while it is set to 20% in Figures 6.19(g)-6.19(l). It is clear that the latter gives better results, even though the positions of the center actuators in Figures 6.19(j)-6.19(l) are not obviously much different from those actuators closer to the edge. Whereas in Figure 6.19(e), the center actuator is significantly displaced from the others, and yet there is no filament on target in Figure 6.19(b). When the mutation probability is small, it is likely that the small subset of the solution space to which the GA is initialized does not contain any significant maxima. Increasing the mutation probability allows the GA to access a larger portion of the solution space without having to test every mirror figure within it. However, too much mutation precludes convergence of the GA. Advanced versions of GAs such as ours can dynamically adjust the mutation probability based on the FOM history over the iterations.

Prospects for Multifilamentation Control with a Deformable Mirror

By reshaping the wavefront to manipulate the energy reservoir of a filamenting laser pulse, it is possible to precisely control the locations where filaments appear. The approach we have described demonstrates the feasibility of controlling a single filament within the energy reservoir, and can be extended to the simultaneous, independent control of multiple filaments, albeit with diminished reliability. The phase profiles which give the target filament configurations can be found quickly and accurately by exploiting a genetic algorithm to optimize the wavefront.

There are many competing factors that influence the ability of the GA and deformable mirror to control multiple filaments. Some have to do with the parameters of the mirror, such as actuator size and spacing. Others, such as interference among filaments [219] are physical features of multi-filamentation itself. Our setup was not deliberately optimized to control multiple filaments at a distance. It is likely that improvement in the reliability of the control of multiple filaments could be accomplished by obtaining detailed understanding of how the wavefront as altered by the

mirror changes as the pulse propagates, and modifying the layout of the experiment accordingly.

Our results demonstrate the principle of controlling filaments in this manner, but are far from indicating a mature approach for application. Possible improvements may be sought by using a different form for the FOM – perhaps one that actively discourages the formation of satellite filaments. More rapid, higher quality mirror optimizations might be achieved by a different, more natural basis set for the genes that the GA operates upon. For example, instead of each actuator position being its own completely independent gene, the set of genes may instead be coefficients of several superimposed Zernike polynomials. Also, it should be noted that the deformable mirror used in these experiments was relatively coarse, having only 37 actuators. Significantly improved control of the filaments could likely be achieved with a larger mirror having more actuators.

6.4 Conclusion

The experiments demonstrate that wavefront manipulations controlled by a GA are an extremely versatile method for optimizing filament propagation and plasma generation. It seems that the sensitivity of filamentation to the initial conditions of the wavefront, and the resulting changes to the intensity profile of the laser mean that one could probably expect a result from almost any implementation of the optimization routine. Of course, it is possible to prevent convergence of an optimization by choosing a measurement for finding the FOM that exhibits large shot-to-shot fluctuations. The cost of the GA's versatility is the ambiguity of how a particular wavefront configuration maps to the optimized results we have observed.

Section 6.1 pointed out that even if we had experimentally measured the wavefront, the non-reciprocity of the nonlinear propagation and intensity dependence of the wavefronts means that measurements performed using available techniques would

be useless. If knowing the wavefront in the filamentation region becomes critical to understanding the experiments or building upon their results, then there are two options. The first is development of a means for measuring the wavefront during filamentation, which is unlikely. The proper approach would be to take the wavefront applied at the mirror, account for additional systematic aberrations accrued during propagation (for example, the astigmatism due to off-normal incidence on a concave mirror) and use a propagation simulation to predict the wavefront when filamentation starts. Both paraxial and non-paraxial codes could find the spatial phase. The latter will be able to achieve more detailed description of the wavefront as the governing equations remain correct during the collapse phase that initiates filamentation, although they are computationally expensive. A paraxial solver could be expected to accurately represent the nonlinear contribution to the wavefront evolution up to the point of collapse.

Section 6.2 found that an optimized wavefront can increase the microwave yield from the filament plasma by about a factor of 2 uniformly across the receiver bandwidth. The spectral uniformity of the microwave yield increase is repeatable at many values of air pressure, and also when the optimization is performed with the microwave antenna at different angular positions around the plasma. This may be due to the choice of the value of the waveform peak-to-peak voltage for the FOM. Because many frequency components are superimposed at the peak of the waveform, the GA may find a wavefront shape that increases all of them instead of only increasing the strongest frequency components that make up the waveform. Images of the plasma fluorescence show that the optimized wavefront may be one that reduces astigmatism that was initially present in the focus of the laser. The optimized wavefronts increase the length and the brightness of the plasma. This is different from the outcome of similar experiments that optimized THz emission from filaments. In that case the optimized wavefront also increased the plasma length, but decreased its brightness.

This implies that the largest microwave field strength may be achieved with the highest laser intensity, whereas the largest THz field strength is achieved with the plasma of greatest longitudinal extent.

The DM and GA are also able to arbitrarily configure the transverse locations of multiple filaments that co-propagate in the beam when the laser pulse power is high enough for multi-filamentation. The FOM needed to accomplish the desired filament configuration is calculated from an image moment that heavily weights the appearance of filaments in the beam profile that coincide with user-defined locations. Using the same input pulse power and focusing conditions, the GA can find wavefront shapes that optimally overlap the filaments, move the overlapped filaments in precise increments arbitrarily within the energy reservoir of the pulse, and create arrays of two and four filaments. The shot-to-shot repeatability of the filament configurations diminishes as the filaments approach the edge of the energy reservoir. Also, the repeatability decreases with the control of more filaments. For the pulse power we used, which is capable of generating a maximum of 4 to 5 filaments, the two-filament configuration was on target in 46% of the laser shots, while for the four-filament configuration the on target probability dropped to 10%. However, the repeatability might be improved with a larger density of actuators on the DM.

The experiments represent a small sampling of the possible ways to optimize the filaments. In fact, experiments such as these where the stimulus, in this case being the actuator displacements, and the optimized outcome are not related in a predictable manner may call for a different approach than the normal procedure of experimental design. The traditional method of forming a hypothesis that predicts a relationship between the input and outcome (i.e. the wavefront and the filaments, respectively) and systematically performing an experiment that probes the hypothesis may not be the best way to understand the underlying physics. Instead, understanding the physical mechanisms might be more efficiently accomplished by performing a series

of different optimizations that operate on different aspects of the laser plasma interaction, and using the aggregate of the results to infer an answer. Instead of starting with a hypothesis, the notion is to reverse the thought process and start with a series of results in order to retrodict an explanation.

Another potential avenue for future investigation is the use of different optimization algorithms other than a GA. Some examples of these include stochastic parallel gradient descent, stimulated annealing, hill climbing (and related hybrid methods), and pattern extraction [220, 221]. The GA can reliably find an optimum, but in general it converges slowly in time. Certain problems may benefit from faster convergence that may result from using a different kind of algorithm. The best algorithm for a given application remains an open research topic in the field of adaptive optics. Finding the highest performing algorithms for manipulating nonlinear propagation in a given context could be the basis of a research program of a few years in duration.

The experiments have several potential uses going forward. They may provide opportunities to carefully characterize interactions between arbitrary numbers of filaments, and the effects of general beam aberrations on the propagation of the filaments and the plasmas they generate. With further development, such as the ability to learn from stored mirror shapes for many target configurations, it is a potential technique for fast, even real-time control of filament position and structure.

CHAPTER VII

Conclusion

7.1 Summary

The dissertation is the first detailed investigation of broadband microwave radiation generated by ultrashort laser produced plasmas in air. The laser conditions that lead to the plasma generation and microwave emission center on nonlinear filamentation, but the measurements across the different experiments show that the microwave radiation is a general feature of the plasma evolution whether or not the laser propagation is strictly in the pure filamentation regime.

The starting point for the research was initial observation of an effect that had not received serious attention. The dissertation definitively proves that this effect is not only interesting as a question of physical principle, but goes on to repeatedly demonstrate that the microwave radiation is useful as a means for building an understanding of the charge dynamics in the laser plasma after the laser pulse has passed. It adds to these results by showing the utility and versatility of adaptive optics in the optimization of the microwave radiation from filament plasmas, and highly reconfigurable control of nonlinear propagation in the multi-filament regime. While the contributions of the individual experiments are notable on their own, together they constitute a substantial body of work that advances the understanding of laser-plasma interactions and nonlinear laser propagation on multiple fronts.

The specific contributions that the dissertation research makes to the scientific understanding of laser plasmas, filamentation, and microwave instrumentation include:

1. The creation of a technique based on time domain spectroscopy for measuring short pulses of extremely broadband microwaves whose bandwidth far exceeds that of any of the frequency bands established by microwave circuit technology.

2. The first measurement of the pressure dependence of the microwave radiation due to filamentation, and the explanation of the dramatic increase in the microwave fields at low air pressure indicating the role of electron-neutral collisions in determining the filament plasma conductivity. The competition of the pressure dependence of the conductivity with that of the area of the plasma channel is reflected in the microwave measurements, which establishes their utility as a probe of the nature of the plasma.

3. The first comparison of the microwave radiation from plasma sparks made by laser pulses with wavelengths centered in the mid-infrared with that due to sparks made by near-infrared laser pulses. The experiments are the best example that laser produced plasmas in air are the broadest bandwidth microwave sources in existence, as the observed frequency spectrum is continuous from < 5 GHz to > 70 GHz. The radiated microwave field strength caused by the mid-infrared laser is an order of magnitude stronger than that caused by the near-infrared laser. The large difference may be due to multiple factors, but it is likely that the increase in the energy imparted to the plasma electrons by the long wavelength laser field is in part due to the λ^2 scaling of the ponderomotive force. These experiments also show fairly definitively that the frequency content of the microwaves depends on the longitudinal variation of the currents along the length of the plasma.

4. The first measurement of a two color relative phase effect on the generation of

the microwaves. The experiment tests if the microwave generation mechanism is similar to that responsible for THz radiation from two color ultrashort laser produced plasmas in air. For the THz, superposition of the fundamental and second harmonic of the laser frequency and optimizing the relative phase delay between them results in an enormous yield increase. A significant increase in the microwave yield is measured with optimized relative phase of the laser harmonics, but it is not as drastic as that observed at THz frequencies. Relative to the single color pulses, optimization of the relative phase increases the microwave field amplitude by about a factor of 3 with NIR pulses, and a factor of almost 10 for MIR pulses. The experiment is performed on two laser systems using pulses having wavelengths in the mid-infrared and near-infrared. The dependence of the microwave emission on the relative phase of the laser harmonics is very complicated, as it alters the amplitude, frequency content, and emission pattern of the microwaves. It is unknown if a similar effect has been observed before at in the THz regime.

5. The demonstration that it is possible to optimize the microwave generation by reshaping the laser wavefront using a deformable mirror run by a genetic algorithm. The optimization routine is performed several times as a function of air pressure, and results in a doubling of the microwave field strength at low pressure.

6. The use of the same deformable mirror and genetic algorithm to control the transverse configuration of multiple filaments simultaneously within the energy reservoir of the laser pulse. Unlike prior approaches to driving multi-filamentation in a deterministic manner, the deformable mirror can be reconfigured to arbitrarily arrange the filaments, which may enable generalized studies of their mutual interactions that were not possible before.

The detailed experimental measurements of the short microwave pulses generated by the laser plasmas in air are evidence of the sensitivity of the currents in the plasmas to nonlinear propagation of the laser field and the field's spatial phase, as well as energy exchange between the laser field, electrons, and heavy species through collisions. By decreasing the air pressure, increasing the laser wavelength, and optimizing the laser wavefront, the experiments demonstrate multiple independent possibilities for increasing the microwave field strength, and better understanding the nature of the laser plasma interaction in the filamentation regime. Each of the experimental Chapters presents multiple opportunities for further investigation that could lead to significant insight into the nature of laser produced plasmas in gases. Some of these possibilities are discussed in Section 7.3.

A highlight of the findings of the dissertation is the apparent correspondence between the microwave yield and the plasma conductance and conductivity. The pressure dependence of the conductivity at microwave frequencies is the rationale for a potentially novel electron temperature diagnostic for the filament plasma. If additional measurements can confirm that the peak of the microwave yield occurs at a pressure where the electron neutral collision rate is equal to the microwave frequency, then the proposed diagnostic will constitute a significant discovery for the filamentation field. At present there are no reliable temperature diagnostics for the filament plasma. Finding one would enable important predictions of the plasma evolution, such as long-lived flows in the plasma due to pressure gradients. The next Section introduces the potential temperature diagnostic, and presents preliminary experimental results.

7.2 Proposed Electron Temperature Diagnostic for the Filament Plasma

It is possible that the pressure dependence of the microwave yield that was described in Chapter IV can be used as a new plasma diagnostic that may be a solution to a long standing problem in the field of laser filamentation. There have been many measurements of the electron density in a filament plasma, and the body of literature agrees that for 800 nm filaments at atmospheric pressure the nominal electron density is $N_e \sim 10^{16}$ cm^{-3} [135, 136]. However few attempts have been made to measure or infer the electron temperature. As a result, the literature concerning filament plasmas generally avoids making any conclusions that rely on knowing T_e. While this is a generalization, it is not controversial to say that the understanding of filament plasmas is stunted by a lack of electron temperature measurements. The filament plasma is small, tenuous, short-lived, and predicted to be cold [136] relative to other laser produced plasmas. Its properties are such that no straightforward implementation of an established diagnostic technique (physical probes, optical emission spectroscopy, Thomson scattering, etc.) can find T_e reliably. A pump-probe experiment [222] and optical emission spectroscopy [223] have been performed, but the measurements are difficult.

We propose a new technique that relies on the pressure dependence of the filament plasma conductivity. Figure 4.9 shows the dependence of the microwave yield on a larger range of pressure than what was reported in Section 4.3, and that the yield peaks at 0.5 Torr. Figure 4.11 demonstrates that the microwave yield depends on the size of the plasma and its conductivity. Figure 4.12 shows that the conductivity of the plasma transitions between the low frequency and high frequency limits as the electron neutral collision rate decreases with air pressure. The pressure at which the transition occurs scales with the measured microwave frequency. The basis of the

diagnostic is that the transition occurs when the microwave frequency is equal to the electron-neutral collision rate.

Figure 7.1 demonstrates how the diagnostic works. The spectrum of the microwaves at 0.5 Torr is shown in Figure 7.1(a) for the waveform data in Figure 4.9. The centroid, $f_{centroid}$, of the frequency spectrum is taken to be the microwave frequency that corresponds to the collision rate. It is calculated from the first moment

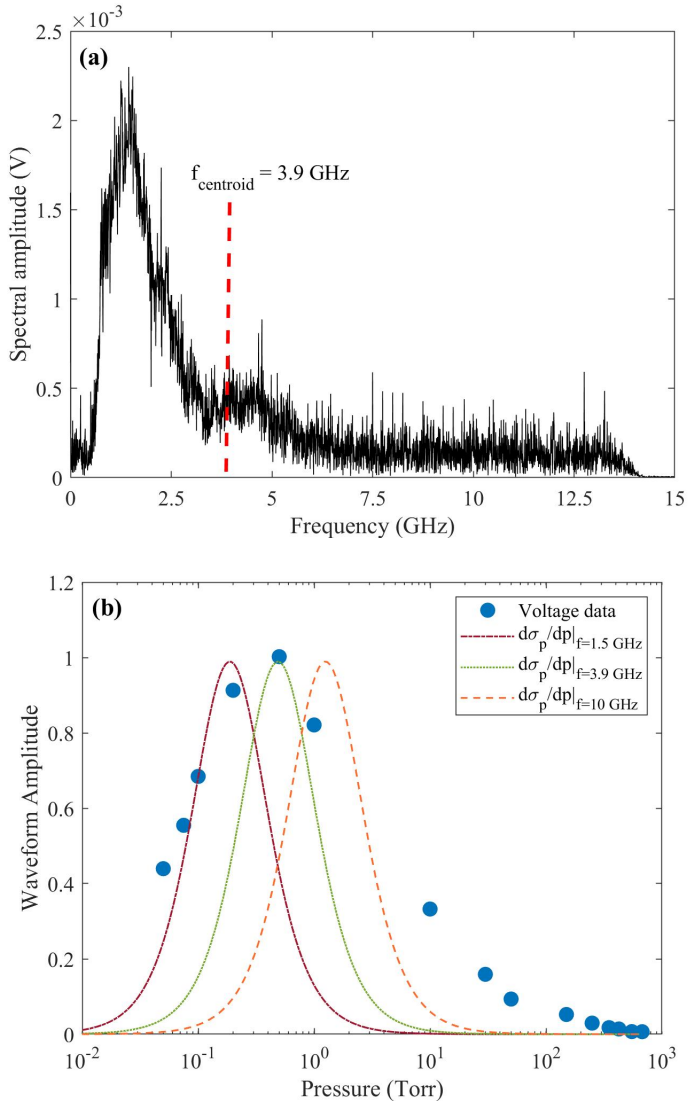

Figure 7.1: (a) Uncalibrated voltage spectrum of the microwave waveform recorded at the maximum microwave yield at 0.5 Torr. (b) The peak-to-peak voltage data from Figure 4.9 plotted against $d\sigma_p/dp$ evaluated at 1.5 GHz, which corresponds to the spectral peak in (a), $f_{centroid}$ = 3.9 GHz, and 10 GHz.

of the voltage spectrum

$$f_{centroid} = \frac{\int_0^{f_{max}} f V_m(f)\ df}{\int_0^{f_{max}} V_m(f)\ df} = 3.9 \text{ GHz}, \tag{7.1}$$

where f_{max} is the maximum frequency of the oscilloscope in Figure 7.1(a). For the Agilent oscilloscope, $f_{max} = 13$ GHz. There is enough low amplitude noise out to the Nyquist frequency (40 GHz for this oscilloscope) to skew the centroid calculation. Figure 7.1(b) shows the agreement between $f_{centroid}$ and the experimental data. The peak-to-peak voltages from Figure 4.9 are plotted against $\mathrm{d}\sigma_p/\mathrm{d}p$. The latter has been evaluated by differentiating the real part of the conductivity in Equation 4.4 with respect to pressure. The transition in the conductivity occurs somewhat slowly as a function of pressure looking at Figure 4.12 by eye. Evaluating the pressure at which the conductivity is changing the most rapidly establishes the correspondence between the microwave frequency and the neutral collision rate. Figure 7.1(b) demonstrates that when $f = 3.9$ GHz in Equation 4.4, the pressure where $\mathrm{d}\sigma_p/\mathrm{d}p$ is maximized occurs at the same pressure where the microwave yield is maximized.

The electron temperature is calculated by setting $f_{centroid} = \nu_{en}$, and solving Equation 4.5 for T_e

$$T_e = \frac{m_e}{k_B}\left(\frac{f_{centroid}}{N\sigma_N}\right)^2. \tag{7.2}$$

For $f_{centroid} = 3.9$ GHz, $N = 2.5 \times 10^{25}\ \mathrm{m}^{-3} \times \frac{0.5\ \mathrm{Torr}}{760\ \mathrm{Torr}} = 1.6 \times 10^{22}\ \mathrm{m}^{-3}$, and $\sigma_N = 5.0 \times 10^{-19}\ \mathrm{m}^2$,

$$\boxed{T_e = 1.5 \times 10^4\ \mathrm{K} = 1.3 \pm 0.9\ \mathrm{eV}} \tag{7.3}$$

The uncertainty in T_e is about 70%, which is estimated based on the variance in $f_{centroid}$ from three waveforms. In contrast, the spectral data in the rest of the dissertation report the average and variance of at least 100 waveforms for a single mea-

surement. Still, an electron temperature of 1.3 eV agrees with existing measurements [222, 223]. The value of T_e in Equation 7.3 is based on limited data, which is reflected in the large uncertainty. Further experiments and analysis with a large number of waveform samples would mitigate this issue. However, further experiments and analysis are needed to confirm the correspondence between the frequencies of the microwave radiation and T_e. This will determine the usefulness of the pressure dependence of the conductivity as a temperature diagnostic for the filament plasma.

One potential issue with the measurement is that the Doppler shift of the microwaves due to the motion of the radiation source will give different answers for T_e if a calculation like Equation 7.1 is used to find the frequency that corresponds to the neutral collision rate. The dependence of the frequency content on the angular position of the horn relative to the laser propagation direction is clear in Figure 4.7 even though the microwaves come from the same plasma. Radiation due to a source moving at a velocity v_s at an angle θ relative to an observer has a frequency

$$f_{obs} = \left(\frac{c}{c - v_s \cos\theta} \right) f_s, \tag{7.4}$$

where f_s is the frequency in the proper frame of the source. If the radiation is observed along a direction perpendicular to that of the current density, then the frequency content will not be Doppler shifted. However Figure 4.2(c)-(d) shows that the filament plasma in this experiment radiates very little in the perpendicular direction. The solution to this problem is left for future work.

Another more easily solved problem is that the temperature scales unfavorably with the microwave frequency ($T_e \propto f_{center}^2$) if the diagnostic is to be precise. The calculations achieve good agreement between the conductivity at $f_{centroid} = 3.9$ GHz and the pressure of maximum microwave yield, but in reality the choice of frequency is somewhat arbitrary when using the broadband spectrum in Figure 7.1(a). For ex-

ample a natural choice for the frequency could be the spectral peak at $f \sim 1.5$ GHz. Figure 7.1(b) includes a plot of $\mathrm{d}\sigma_p/\mathrm{d}p|_{f=1.5\ \mathrm{GHz}}$ to show that this does not agree with the waveform data. Since the temperature scales with frequency squared in Equation 7.2, a small variance in the measured frequency could result in a large variance in T_e. The solution is to make repetitive measurements at different frequencies to reduce the uncertainty. If the pressure increments are small and carefully controlled, it in principle should be possible to track the pressure dependence of small sections of the frequency spectrum. The pressure dependence of each section should be self consistent with Equation 7.2, and each should give the same answer for T_e. The uncertainty in T_e would be reduced by the square root of the number of T_e measurements. The data in Figure 4.9 is measured in increments of pressure too coarse to permit repetitive calculations of T_e.

Using a high performance oscilloscope with a large real time bandwidth is not a requirement for the temperature measurement, since it is easier to calculate the plasma conductivity in the limit of a single frequency. Figure 7.2 shows a modified receiver that could be used as an alternative to one that includes a fast oscilloscope. A single broadband horn could be used, and a narrow bandpass filter would limit

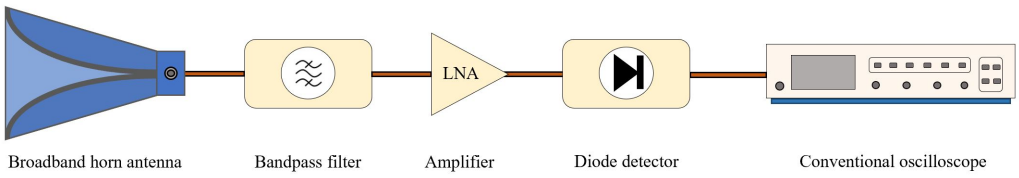

Figure 7.2: Concept microwave receiver for measuring T_e. A series of bandpass filters having different center frequencies can select narrow frequency bands from the plasma radiation. The reduction in signal is compensated by an LNA, and a broadband rectifier diode allows the signal to be measured without a high performance oscilloscope.

the spectral content that the receiver measures. Reducing the signal bandwidth also significantly reduces its power, so a broadband LNA may be needed to boost the filtered signal to measurable levels. The output of the LNA would be at the carrier

frequency selected by the bandpass filter, which could only be resolved by a fast oscilloscope. However, broadband diode detectors exist that function from nearly DC to the millimeter wave range, and could measure the total power at the output of the LNA. A conventional oscilloscope would measure a voltage that is proportional to the power coming out of the bandpass filter. The pressure dependence of a narrow frequency range could be measured. A more precise electron temperature is found by using several bandpass filters with different center frequencies and repeating the pressure dependence measurement.

Since the collisionality of the plasma changes with pressure, the temperature measurement as proposed likely only holds at the pressure where the maximum microwave yield occurs. Extrapolation of the measured temperature to other values of pressure is desirable. Such an extrapolation needs to consider how the electron energy distribution due to multiphoton ionization changes in the presence of a large neutral collision rate. Also, the temperature corresponds to the electron energy distribution integrated over a finite time interval of the filament plasma's evolution. When this interval starts and stops relative to the instantaneous position of the propagating laser pulse is unclear. The microwave measurements seem to agree well with the notion of conductance, which is a concept that relies on the fluid description of a plasma, meaning that its electrons have achieved approximate thermal equilibrium. This implies that the relevant time interval begins some time after the ionization event that generates the plasma. Its non-equilibrium nature upon generation would only be captured by a fully kinetic treatment [139, 224]. The question of when the microwave radiation arises in the filament plasma evolution is important to generalizing the proposed electron temperature diagnostic.

Even though the temperature measurement as proposed requires further development to have broad utility, the fact that there is a predictable correspondence between the microwave radiation and T_e is an advancement. At present it is a partial solu-

tion to an important problem in the field, and it is possible that it could become a robust diagnostic requiring the fewest assumptions about the plasma in temperature measurements for filament plasmas.

7.3 Future Work

Verification of the relationship between the pressure dependence and the filament plasma electron temperature suggested in Section 7.2 represents a possible direction for additional investigation whose significance is tangible. However the results of the experiments raise other questions about the microwave generation mechanism and the plasma evolution in addition to the proposed temperature diagnostic.

Measurements presented throughout the dissertation suggest directly and indirectly that the frequency content of the microwave radiation depends on the large scale longitudinal variations of the plasma current. However, the dissertation contains no systematic investigation of the relationship between the plasma length and microwave frequency explores the length dependence in isolation from the electron temperature and density. Since the current density assuming cold ions is given by $\mathbf{J}_e = -eN_e\mathbf{v}_e$, and the electron velocity may arise in response to pressure gradients, it is probable that the microwave field depends simultaneously on the electron density, temperature, and their longitudinal variations. The task would be to design an experiment, perhaps supported by modeling, that could deconvolve the components of the combined dependence. Using focusing optics with different focal lengths is a start, but with a fixed beam diameter, the different numerical apertures of the focusing geometries will lead to plasmas of highly variable densities [36]. If different plasma lengths result from different focal lengths but with fixed numerical aperture (i.e. the input beam diameter changes with the focal length), then such an experiment may correctly isolate the plasma length dependence of the microwaves. This would be one manner to approach experimental identification of the microwave generation

mechanism.

Experiments whose intention is direct comparison with the THz radiation from filaments and laser plasmas in air is another possibility that may lead to uncovering the generation mechanism. This is somewhat difficult as the techniques for detecting microwaves and THz are quite different at present, and may not be amenable to direct comparison. One possibility is to use different detection schemes, but benchmark each against other behavior of the plasma, as was attempted in Chapters V and VI by correlating the microwave yield with the plasma fluorescence, and invoking similar experiments performed by others for THz fields. However, this approach is muddied by the fact that the laser conditions are not necessarily comparable among all the experiments.

Instead, it might be possible to develop a technique that can simultaneously resolve the GHz and THz frequency components of the radiation in a single measurement. The development effort would be substantial, but the idea is to employ what is called a time lens [225], or a similar technique called photonic time stretch analog to digital conversion [226, 227] to measure a waveform that directly corresponds to the THz and microwave fields, but has been stretched uniformly in time so that it can be directly digitized on an oscilloscope. The author attributes the suggestion that such techniques could be good candidates for measuring the radiation from the plasma to the dissertation of Nicholas Barbieri [228].

The measurement is a pump-probe type experiment in which the pump pulse drives the microwave and THz emission, and the probe is split from the pump and stretched by GVD in a long optical fiber to a duration that is slightly longer than that of the combined microwave and THz pulse. This means that the probe would need to be stretched to a few nanoseconds. The probe is then transmitted through an electro-optic crystal and polarizer so that the Pockels effect [165] turns modulation of the probe laser polarization into intensity modulations in time. Up to this step the

technique is similar to spectral encoding in which the modulated probe is dispersed in a spectrometer, so that the time modulations appear as spatial modulations of a camera image [229]. The time stretch technique takes a different approach. The probe that now carries an intensity modulation that corresponds to the waveform of the radiation from the plasma would then be stretched again in a longer section of optical fiber. The second stretching step slows down the time variation of the intensity modulation such that it can be measured by a high bandwidth photodiode.

There are many potential issues with the technique, such as higher order dispersion in the optical fiber that would skew the linear relationship between the initial modulation and the stretched output. Also self modulation of the probe will occur in the fiber if it is initially too intense. A fairly large initial probe intensity might be required in order for the photodiode to register any signal after the probe is stretched twice. However, this technique is relatively well established, and some compensation of non-ideal probe behavior is possible [230]. Stretching ratios on the order of 100 are possible using this technique [227], and high bandwidth silicon photodiodes exist that could correctly respond to a ~ 40 GHz (25 ps) modulation in time [231]. Using the 70 GHz oscilloscope to digitize the photodiode signal, a stretching ratio of 100 with a maximum stretch frequency of 40 GHz would correspond to a true bandwidth of 4 THz in the experiment. A sampling rate of 200 GS/s with a 100 ns stretched photodiode signal would require a memory depth of only 20,000 samples.

The main difficulties would arise from collecting the combined radiation field, and finding an electro-optic crystal that could respond to it in a predictable way. The emission angle of the radiation from the plasma depends on its frequency, so one can think of the field as having negative radial spatial chirp. Collecting the microwaves and THz simultaneously might require very large metallic mirrors. Also, the radiation is radially polarized, so aligning it to the crystal axes would not be possible. Using a linear polarizer on the combined radiation field would also not be possible because

of the huge differences in wavelength across its bandwidth. There may be solutions to these issues, and if they can be solved the photonic time stretch technique could be a powerful tool for measuring the waveform of the radiation from the plasma from GHz to THz in a single shot.

Finally, the dissertation research is entirely experimental in nature. This is largely because first principles simulation tools capable of simultaneously accounting for all the necessary physics of the laser propagation, filamentation, plasma generation, and microwave radiation do not yet exist. If the propagation of the laser pulse is to occur in the same simulation as the microwave radiation, then the required number of grid points and time steps is prohibitively large unless it is performed on a high performance computer with enormous memory capacity. Such a code would have to be purpose built in order to be optimized for memory allocation and speed, an endeavor which is beyond the scope of a the dissertation. A computational tool capable of a first principles simulation of the microwave generation is an interesting and worthy scientific challenge in its own right. It is also possible that the microwave radiation generation can be described by an analytic theory given an assumed radiation mechanism.

There are many possibilities for continuing the research presented in the dissertation. Those described above represent significant, medium to long term research efforts. Simpler options, such as measuring the microwave radiation when the plasma forms in a gas other than air, are also possible. Microwave radiation from ultrashort laser produced plasmas in gases, as the dissertation shows, is a common phenomenon. Basic measurements in a large range of laser conditions can be accomplished with relative ease. The more advanced measurement techniques developed during this research effort can also be improved upon for example, to extend the frequency range, increase the sensitivity, and deconvolve the receiving antenna pattern from the measurements.

APPENDICES

APPENDIX A

Microwave Circuit Technology

The experimental chapters of the thesis draw the conventions of microwave engineering to streamline the presentation of the results. An overview of the relevant terms and their context is given here for reference. The internal dimensions of a microwave circuit component are determined by a range of wavelengths for which the component properly functions (see Section 3.4.2). The microwave technology community has standardized these frequency bands, and common components are manufactured to operate over the extent of one or sometimes a few of the bands. The most common designation scheme assigns a letter to each frequency band. Table A.1 lists the frequency bands from 1-330 GHz. The frequency bands covered in the execution of the experiments are listed in boldface. The four antennas operate over 2-18 GHz (S-K_u band), 18-40 GHz (K-K_a band), 40-60 GHz (U band), and 50-70 GHz (V band), respectively. The rated maximum frequencies of the coaxial cables used in the experiments are 18 GHz, 40 GHz, and 70 GHz.

As Section 3.4 shows, the lossy nature of the receiver is dominated by the cable used to connect the horn and oscilloscope. The frequency limits of coaxial transmission line connectors are in Table A.2. The connectors are a seemingly insignificant experimental detail, but they must be chosen judiciously or else the receiver will not

Table A.1: Microwave Frequency Bands

Letter Designation	Frequency Range (GHz)	Waveguide Band Name
L	**1-2**	WR-650
S	**2-4**	WR-284
C	**4-8**	WR-159
X	**8-12**	WR-90
$\mathbf{K_u}$	**12-18**	WR-62
K	**18-26.5**	WR-42
$\mathbf{K_a}$	**26.5-40**	WR-28
Q	33-50	WR-22
U	**40-60**	WR-19
V	**50-75**	WR-15
E	60-90	WR-12
W	75-110	WR-10
F	90-140	WR-8
D	110-170	WR-7
G	140-220	WR-5
Y	170-260	WR-4
H	220-330	WR-3

function correctly.

The nominal impedance of the cables, connectors, and the oscilloscope is 50 Ω over their rated frequency range. The impedance is a common design choice that optimizes the trade-off between power handling and low dielectric losses [97]. The cables and connectors can usually operate slightly above their rated frequencies, albeit with increased signal absorption. Far above the rated maximum frequency, the impedance of the coaxial transmission line will start to deviate significantly from 50 Ω. Physically, this means that the wavelength of the guided transverse electromagnetic mode (TEM) becomes smaller than the space between the center conductor and outer conductor, and the dominant mode will no longer be the fundamental. Instead it will be a higher order mode that has an uncharacterized impedance. This is called overmoding and it determines the frequency beyond which the cable does not transmit usable signals, unless the impedance of the higher order modes can be predicted or measured for

Table A.2: Connectors for Microwave Coaxial Cables

Connector Name	Dielectric Material	Maximum Frequency (GHz)
BNC	PTFE	2
SMA	PTFE	18
N	Air	18
3.5 mm	Air	33
2.92 mm/K-connector	Air	40
2.4 mm	Air	50
1.85 mm/V-connector	Air	67
1.0 mm/W-connector	Air	110

that particular cable.

APPENDIX B

Heterodyne Receivers

The initial approach for measuring the spectrum of the microwaves involved the construction of a heterodyne receiver. This Appendix briefly explains how heterodyne receivers function, and gives the details of the design choices involved in building one that was used to measure the microwave radiation. The construction of the heterodyne receiver was mentioned in Chapter III. Ultimately it was rejected in favor of directly digitizing the microwave waveforms. Without phase locking the CW signal of the frequency synthesizer to the timing of the laser pulses, the heterodyne signal amplitude varies randomly as the phase of the microwaves and the phase of the synthesizer drift past each other. This cannot be fixed with a simple microwave delay line. The design process for the heterodyne receiver is included nonetheless because it is one of a very small number of methods for measuring microwaves and sub-THz frequency electromagnetic fields at frequencies in excess of 100 GHz.

Figure B.1 shows the parts of a conceptual heterodyne receiver, in addition to the behavior of the signal in the frequency domain. Consider a perfect impulse entering the receiver antenna. Its frequency spectrum has uniform amplitude with infinite bandwidth. The front end of the receiver has a non-uniform frequency response over a finite range, which truncates the spectrum of the incident field. The process

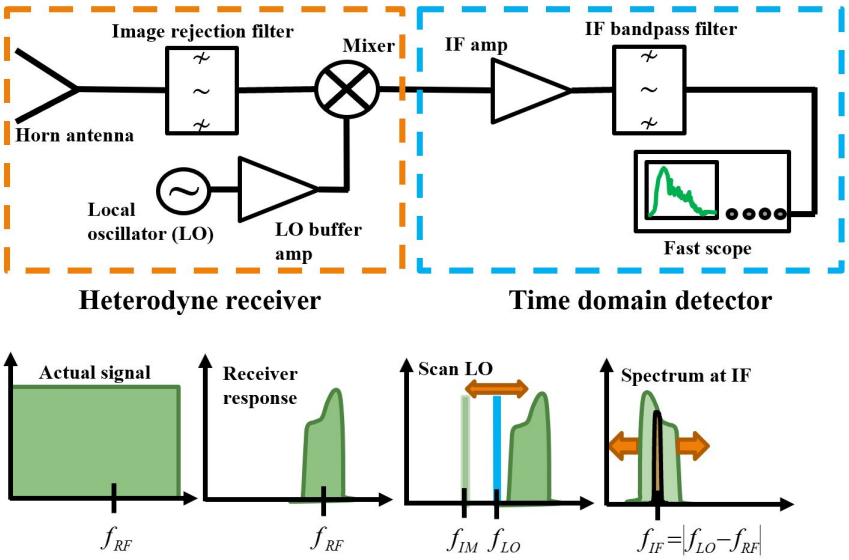

Figure B.1: A diagram describing the process of heterodyne detection as implemented earlier in the dissertation research. In typical heterodyne receivers, the detector back end includes a video amplifier (also called an envelope detector) that rectifies the IF signal so that only the quasi-DC envelope of the microwave pulse is recorded.

of heterodyning the microwave signal begins with an initial bandpass filter on the output of the receiving antenna.

The design of the heterodyne receiver for measuring the frequency spectrum of the microwave pulses is based on the superheterodyne total power radiometer [232]. The purpose of the heterodyne receiver is to down-convert the pulsed, high-frequency emission of interest into a signal at a lower, measurable frequency. Detecting the down-converted signal with a fast oscilloscope is necessary for correctly measuring pulses because its large instantaneous bandwidth is able to resolve the carrier after the frequency down-conversion. A spectrum analyzer, for example, would not be able to correctly reproduce the amplitude spectrum of the radiated microwaves because of their short duration relative to the analyzer's sweep time.

Down-conversion is accomplished by mixing (i.e. multiplying) the high-frequency, pulsed signal with a CW signal of known frequency, called the local oscillator (LO) and measuring at the beat frequency corresponding to their difference, as shown in

Figure B.1. The purpose of the mixer is to generate the difference frequency, called the intermediate frequency (IF), whose amplitude is proportional to that of the high-frequency emission, assuming linearity of the microwave circuit performing the down-conversion. To first order, the frequency down-conversion follows the relationship,

$$f_{IF} = |f_{LO} - f_{pulse}| \tag{B.1}$$

where the IF frequency is f_{IF}, f_{LO} is the known LO frequency, and f_{pulse} is the frequency component whose amplitude is measured. The beat frequency corresponding to $f_{LO} + f_{pulse}$ in this case is well outside the operating frequency range of the microwave circuit. For a given f_{LO} and f_{IF} there are two values of f_{pulse} that satisfy Equation B.1. These are the sidebands of f_{IF}: one is at the frequency of interest, f_{pulse}, and the other is called the image frequency (IM). For the receiver to function as a spectrometer, f_{IF} must either be centered at zero, so that both sidebands are contiguous in frequency space, or the f_{IM} component must be completely attenuated before it enters the mixer. After the mixer, the signal amplitude measured due to f_{pulse} cannot be discriminated from that due to f_{IM} because both convert to f_{IF}.

The amplitude spectrum of the microwaves is measured over many laser shots by tuning f_{LO} at fixed f_{IF}, thereby sampling different values of f_{pulse}. Figure B.2 shows the circuit diagram for the heterodyne receivers. While there are three receivers that each function over adjacent frequency bands: 12-18 GHz (K_u), 18-26.5 GHz (K), and 26.5-40 GHz (K_a) the circuit layout is the same as are the individual microwave components in most cases. The single most important component is the broadband mixer (Marki Microwave T3-1040) which operates at frequencies from 10-40 GHz at its RF and LO ports, and can output IF frequencies from 1-18 GHz. A bandpass filter placed before the RF port of the mixer enforces single-sideband operation of the receiver, and rejects image frequency contributions to the measured signal amplitude.

This image rejection filter, along with the horn antenna, and the cable between them are the only components that are different among the three heterodyne receivers. A second bandpass filter at the IF stage of the receiver determines the frequency resolution as well as the throughput. This filter is centered at 8 GHz, with a bandwidth of 1 GHz. It provides adequate signal strength for measuring the filament emissions, with spectral resolution of 1 GHz. The center frequency of the filter is chosen so that the image frequency is outside the passband of the image rejection filter for the K_u, K, and K_a bands. Two amplifiers are included in the IF stage to compensate conversion losses, and provide net gain on the signal amplitude. A third bandpass filter after the second amplifier blocks noise from the second amplifier at frequencies outside of the desired IF passband.

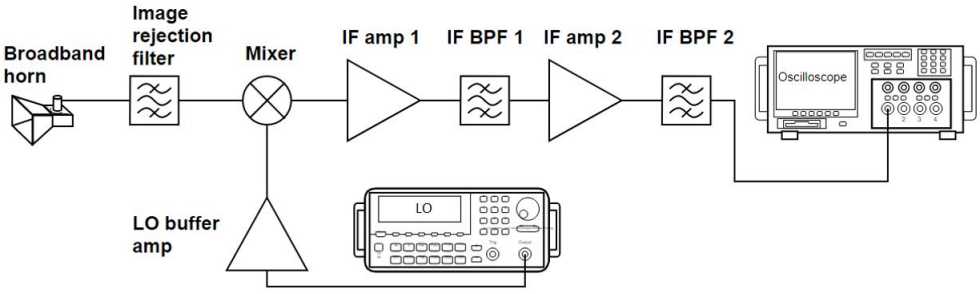

Figure B.2: Heterodyne receiver circuit diagram.

Table B.1 shows the test matrix for the heterodyne radiometers, with values of f_{LO}, f_{pulse}, and f_{IM} for f_{IF} fixed at 8 GHz. A Hewlett-Packard 83640A synthesized sweeper signal generator provides the CW f_{LO} at a known power level. In order to access values of f_{pulse} up to 40 GHz, the sideband that is used in the measurement changes for the K_a band from below to above fLO, which is valid under Equation B.1 as long as the other sideband is rejected. In the jargon of microwave engineering, the K_u and K band measurements are performed with high-side LO, while the K_a band is low-side LO. While this may seem arbitrary, it is necessary in order for f_{LO} and f_{pulse} to remain within the operating frequency range of the mixer, while maintaining

Table B.1: Heterodyne Receiver RF/LO Test Matrix

Ku Band			K Band			Ka Band		
RF (GHz)	LO (GHz)	IM (GHz)	RF (GHz)	LO (GHz)	IM (GHz)	RF (GHz)	LO (GHz)	IM (GHz)
12	20	28	18	26	34	26	18	10
13	21	29	19	27	35	27	19	11
14	22	30	20	28	36	28	20	12
15	23	31	21	29	37	29	21	13
16	24	32	22	30	38	30	22	14
17	25	33	23	31	39	31	23	15
18	26	34	24	32	40	32	24	16
			25	33	41	33	25	17
			26	34	42	34	26	18
			27	35	43	35	27	19
						36	28	20
						37	29	21
						38	30	22
						39	31	23
						40	32	24

reliable image frequency rejection from 12-40 GHz.

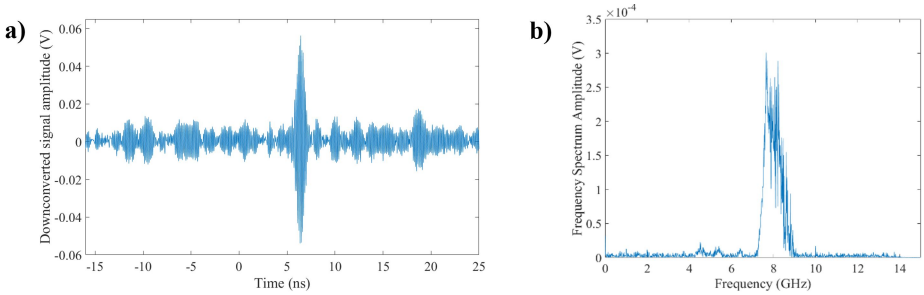

Figure B.3: (a) Example waveform from the heterodyne receiver, and (b) its uncalibrated, background-compensated frequency spectrum. The difference in frequency between the RF and LO inputs to the mixer produce components at the IF (which is 8 GHz) that are directly digitized on the oscilloscope. The signal corresponds to experimental conditions of f_{pulse} = 40 GHz, with air pressure of 5 Torr, and the horn positioned 5 degrees from the laser propagation axis.

An example IF waveform and its Fourier transform are shown in Figure B.3 for a single set of experimental conditions. The Fourier transform can be integrated over the IF passband to give the total electric field received at the value of f_{pulse} determined by the setting of f_{LO}.

APPENDIX C

List of Publications

JOURNAL ARTICLES

1. **A. Englesbe**, J. Elle, R. Reid, A. Lucero, H. Pohle, M. Domonkos, S. Kalmykov, K. Krushelnick, and A. Schmitt-Sody, "Gas pressure dependence of microwave pulses generated by laser-produced filament plasmas," Optics Letters **43**, 4953-4956 (2018).

2. **A. Englesbe**, Z.-H. He, J. A. Nees, A. G. R. Thomas, A. Schmitt-Sody, and K. Krushelnick, "Control of the configuration of multiple femtosecond filaments in air by adaptive wavefront manipulation," Optics Express **24**, 6071–6082 (2016).

CONFERENCE PAPERS

1. **A. Englesbe**, R. Schwartz, A. Korolov, D. Jang, D. Woodbury, K. Kim, H. Milchberg, R. Reid, A. Lucero, H. Pohle, S. Kalmykov, K. Krushelnick, A. Schmitt-Sody, and J. Elle, "Microwave Radiation from Single and Two Color Mid-Infrared Laser Produced Plasmas in Air," in Conference on Lasers and Electro-Optics (Optical Society of America, 2019) paper FTh1M.3.

2. A. Lucero, **A. Englesbe**, J. Elle, A. Schmitt-Sody, J. Lin, J. Nees, and K. Krushelnick, "Optimization of RF Emission from Ultrashort Pulse Laser Filament via Genetic Algorithm and Deformable Mirror," in Conference on Lasers and Electro-Optics, (Optical Society of America, 2019), paper JTh2A.6.

3. S. Kalmykov, **A. Englesbe**, J. Elle and A. Schmitt-Sody, "Generation of Broadband THz Pulses by Laser Wakefield at Radial Boundary of Plasma Column," IEEE Advanced Accelerator Concepts Workshop, (2018), pp. 1-5.

BIBLIOGRAPHY

BIBLIOGRAPHY

[1] A. Braun, G. Korn, X. Liu, D. Du, J. Squier, and G. Mourou, "Self-channeling of high-peak-power femtosecond laser pulses in air," Optics Letters **20**, 73–75 (1995).

[2] J. Benford, J. Swegle, and E. Schamiloglu, *High Power Microwaves* (CRC Press, 2015).

[3] J. E. Rowe, *Nonlinear electron-wave interaction phenomena* (Academic Press, 2013).

[4] Y. Hidaka, E. M. Choi, I. Mastovsky, M. A. Shapiro, J. R. Sirigiri, and R. J. Temkin, "Observation of large arrays of plasma filaments in air breakdown by 1.5-MW 110-GHz gyrotron pulses," Physical Review Letters **100**, 035003 (2008).

[5] B. Shim, S. E. Schrauth, C. J. Hensley, L. T. Vuong, P. Hui, A. A. Ishaaya, and A. L. Gaeta, "Controlled interactions of femtosecond light filaments in air," Physical Review A **81**, 061803 (2010).

[6] X. Yang, J. Wu, Y. Tong, L. Ding, Z. Xu, and H. Zeng, "Femtosecond laser pulse energy transfer induced by plasma grating due to filament interaction in air," Applied Physics Letters **97**, 071108 (2010).

[7] V. A. Andreeva, O. G. Kosareva, N. A. Panov, D. E. Shipilo, P. M. Solyankin, M. N. Esaulkov, P. González de Alaiza Martínez, A. P. Shkurinov, V. A. Makarov, L. Bergé, and S. L. Chin, "Ultrabroad terahertz spectrum generation from an air-based filament plasma," Physical Review Letters **116**, 063902 (2016).

[8] D. Strickland and G. Mourou, "Compression of amplified chirped optical pulses," Optics Communications **56**, 219 – 221 (1985).

[9] A. Irbäck and M. Larsson, "The Nobel Prize in Physics 2018," https://www.nobelprize.org/uploads/2018/10/press-physics2018.pdf (2018).

[10] E. Brookner, "Phased-array radars," Scientific American **252**, 94–103 (1985).

[11] C. V. Shank and E. P. Ippen, "Subpicosecond kilowatt pulses from a mode-locked CW dye laser," Applied Physics Letters **24**, 373–375 (1974).

[12] J. A. Valdmanis, R. L. Fork, and J. P. Gordon, "Generation of optical pulses as short as 27 femtoseconds directly from a laser balancing self-phase modulation, group-velocity dispersion, saturable absorption, and saturable gain," Optics Letters **10**, 131–133 (1985).

[13] A. N. Fletcher, "Laser dye stability," Applied Physics B **31**, 19–26 (1983).

[14] J. Diels, W. Rudolph, P. Liao, and P. Kelley, *Ultrashort Laser Pulse Phenomena* (Elsevier Science, 2006).

[15] H. W. Mocker and R. J. Collins, "Mode competition and self-locking effects in a Q-switched ruby laser," Applied Physics Letters **7**, 270–273 (1965).

[16] K. Sala, M. Richardson, and N. Isenor, "Passive mode locking of lasers with the optical kerr effect modulator," IEEE Journal of Quantum Electronics **13**, 915–924 (1977).

[17] E. P. Ippen, "Principles of passive mode locking," Applied Physics B **58**, 159–170 (1994).

[18] F. Batysta, R. Antipenkov, T. Borger, A. Kissinger, J. T. Green, R. Kananavičius, G. Chériaux, D. Hidinger, J. Kolenda, E. Gaul, B. Rus, and T. Ditmire, "Spectral pulse shaping of a 5 Hz, multi-joule, broadband optical parametric chirped pulse amplification frontend for a 10 PW laser system," Optics Letters **43**, 3866–3869 (2018).

[19] C. L. Haefner, A. Bayramian, S. Betts, R. Bopp, S. Buck, J. Cupal, M. Drouin, A. Erlandson, J. Horáček, J. Horner, J. Jarboe, K. Kasl, D. Kim, E. Koh, L. Koubíková, W. Maranville, C. Marshall, D. Mason, J. Menapace, P. Miller, P. Mazurek, A. Naylon, J. Novák, D. Peceli, P. Rosso, K. Schaffers, E. Sistrunk, D. Smith, T. Spinka, J. Stanley, R. Steele, C. Stolz, T. Suratwala, S. Telford, J. Thoma, D. VanBlarcom, J. Weiss, and P. Wegner, "High average power, diode pumped petawatt laser systems: a new generation of lasers enabling precision science and commercial applications," (Vol. 10241 SPIE Optics & Optoelectronics: Research Using Extreme Light, Entering New Frontiers with Petawatt-Class Laser III, 2017).

[20] C. R. Giuliano, "Laser-induced damage to transparent dielectric materials," Applied Physics Letters **5**, 137–139 (1964).

[21] P. Lallemand and N. Bloembergen, "Self-Focusing of Laser Beams and Stimulated Raman Gain in Liquids," Physical Review Letters **15**, 1010–1012 (1965).

[22] U. Kogelschatz, "Filamentary, patterned, and diffuse barrier discharges," IEEE Transactions on Plasma Science **30**, 1400–1408 (2002).

[23] A. L. Peratt, *Physics of the plasma universe* (Springer, 1992).

[24] C. M. Huntington, A. G. R. Thomas, C. McGuffey, T. Matsuoka, V. Chvykov, G. Kalintchenko, S. Kneip, Z. Najmudin, C. Palmer, V. Yanovsky, A. Maksimchuk, R. P. Drake, T. Katsouleas, and K. Krushelnick, "Current Filamentation Instability in Laser Wakefield Accelerators," Physical Review Letters **106**, 105001 (2011).

[25] P. Gibbon and E. Förster, "Short-pulse laser-plasma interactions," Plasma Physics and Controlled Fusion **38**, 769 (1996).

[26] M. Mlejnek, E. M. Wright, and J. V. Moloney, "Dynamic spatial replenishment of femtosecond pulses propagating in air," Optics Letters **23**, 382–384 (1998).

[27] W. Liu, F. Théberge, E. Arévalo, J.-F. Gravel, A. Becker, and S. L. Chin, "Experiment and simulations on the energy reservoir effect in femtosecond light filaments," Optics Letters **30**, 2602–2604 (2005).

[28] S. Eisenmann, J. Peñano, P. Sprangle, and A. Zigler, "Effect of an energy reservoir on the atmospheric propagation of laser-plasma filaments," Physical Review Letters **100**, 155003 (2008).

[29] A. Dubietis, E. Kučinskas, G. Tamošauskas, E. Gaižauskas, M. A. Porras, and P. D. Trapani, "Self-reconstruction of light filaments," Optics Letters **29**, 2893–2895 (2004).

[30] J. Zhang, Z. Hao, T. Xi, X. Lu, Z. Zhang, H. Yang, Z. Jin, Z. Wang, and Z. Wei, *Self-focusing: Past and Present* (Springer, 2009), chap. Self-organized Propagation of Femtosecond Laser Filamentation in Air.

[31] L. Bergé, S. Skupin, F. Lederer, G. Méjean, J. Yu, J. Kasparian, E. Salmon, J. P. Wolf, M. Rodriguez, L. Wöste, R. Bourayou, and R. Sauerbrey, "Multiple filamentation of terawatt laser pulses in air," Physical Review Letters **92**, 225002 (2004).

[32] W. Ettoumi, J. Kasparian, and J.-P. Wolf, "Laser filamentation as a new phase transition universality class," Physical Review Letters **114**, 063903 (2015).

[33] W. Ettoumi, J. Kasparian, and J.-P. Wolf, "Spin-glass model governs laser multiple filamentation," Physical Review Letters **115**, 033902 (2015).

[34] A. Becker, N. Aközbek, K. Vijayalakshmi, E. Oral, C. M. Bowden, and S. Chin, "Intensity clamping and re-focusing of intense femtosecond laser pulses in nitrogen molecular gas," Applied Physics B **73**, 287–290 (2001).

[35] W. Liu, Q. Luo, and S. L. Chin, "Competition between multiphoton/tunnel ionization and filamentation induced by powerful femtosecond laser pulses in air," Chinese Optics Letters **1**, 56–59 (2003).

[36] F. Théberge, W. Liu, P. T. Simard, A. Becker, and S. L. Chin, "Plasma density inside a femtosecond laser filament in air: Strong dependence on external focusing," Physical Review E **74**, 036406 (2006).

[37] K. Lim, M. Durand, M. Baudelet, and M. Richardson, "Transition from linear- to nonlinear-focusing regime in filamentation," Scientific Reports **4**, 7217 EP – (2014). Article.

[38] J. Kasparian, R. Sauerbrey, and S. Chin, "The critical laser intensity of self-guided light filaments in air," Applied Physics B **71**, 877–879 (2000).

[39] W. Liu and S. L. Chin, "Direct measurement of the critical power of femtosecond ti:sapphire laser pulse in air," Optics Express **13**, 5750–5755 (2005).

[40] A. J. Campillo, S. L. Shapiro, and B. R. Suydam, "Relationship of self-focusing to spatial instability modes," Applied Physics Letters **24**, 178–180 (1974).

[41] M. Mlejnek, M. Kolesik, J. V. Moloney, and E. M. Wright, "Optically turbulent femtosecond light guide in air," Physical Review Letters **83**, 2938–2941 (1999).

[42] Y. Petit, S. Henin, W. Nakaema, P. Béjot, A. Jochmann, S. Kraft, S. Bock, U. Schramm, K. Stelmaszczyk, P. Rohwetter, J. Kasparian, R. Sauerbrey, L. Wöste, and J. P. Wolf, "1-J white-light continuum from 100-TW laser pulses," Physical Review A **83**, 013805 (2011).

[43] S. Skupin, L. Bergé, U. Peschel, F. Lederer, G. Méjean, J. Yu, J. Kasparian, E. Salmon, J. P. Wolf, M. Rodriguez, L. Wöste, R. Bourayou, and R. Sauerbrey, "Filamentation of femtosecond light pulses in the air: Turbulent cells versus long-range clusters," Physical Review E **70**, 046602 (2004).

[44] J. Kasparian, P. Béjot, J. P. Wolf, and J. M. Dudley, "Optical rogue wave statistics in laser filamentation," Optics Express **17**, 12070–12075 (2009).

[45] P. M. Lushnikov and N. Vladimirova, "Non-gaussian statistics of multiple filamentation," Optics Letters **35**, 1965–1967 (2010).

[46] J. H. Marburger, "Self-focusing: Theory," Progress in Quantum Electronics **4**, 35 – 110 (1975).

[47] B. La Fontaine, F. Vidal, Z. Jiang, C. Chien, D. Comtois, A. Desparois, T. Johnston, J.-C. Kieffer, H. Pépin, and H. Mercure, "Filamentation of ultrashort pulse laser beams resulting from their propagation over long distances in air," Physics of Plasmas **6**, 1615–1621 (1999).

[48] S. Eisenmann, E. Louzon, Y. Katzir, T. Palchan, A. Zigler, Y. Sivan, and G. Fibich, "Control of the filamentation distance and pattern in long-range atmospheric propagation," Optics Express **15**, 2779–2784 (2007).

[49] A. C. Englesbe, Z.-H. He, J. A. Nees, A. G. R. Thomas, A. Schmitt-Sody, and K. Krushelnick, "Control of the configuration of multiple femtosecond filaments in air by adaptive wavefront manipulation," Optics Express **24**, 6071–6082 (2016).

[50] G. Point, Y. Brelet, A. Houard, V. Jukna, C. Milián, J. Carbonnel, Y. Liu, A. Couairon, and A. Mysyrowicz, "Superfilamentation in air," Physical Review Letters **112**, 223902 (2014).

[51] A. Proulx, A. Talebpour, S. Petit, and S. L. Chin, "Fast pulsed electric field created from the self-generated filament of a femtosecond ti:Sapphire laser pulse in air," Optics Communications **174**, 305 – 309 (2000).

[52] S. Tzortzakis, G. Méchain, G. Patalano, Y.-B. André, B. Prade, M. Franco, A. Mysyrowicz, J.-M. Munier, M. Gheudin, G. Beaudin, and P. Encrenaz, "Coherent subterahertz radiation from femtosecond infrared filaments in air," Optics Letters **27**, 1944–1946 (2002).

[53] E. H. Amstrong, "Method of receiving high-frequency oscillations," (1920). United States Patent US1342885A.

[54] G. Méchain, "Etude de la filamentation d'impulsions laser femtosecondes dans l'air," Ph.D. thesis, École Polytechnique (2005).

[55] B. Forestier, A. Houard, M. Durand, Y. André, B. Prade, J.-Y. Dauvignac, F. Perret, C. Pichot, M. Pellet, and A. Mysyrowicz, "Radiofrequency conical emission from femtosecond filaments in air," Applied Physics Letters **96**, 141111 (2010).

[56] C. D'Amico, A. Houard, M. Pellet, C. Pichot, and A. Mysyrowicz, "Dipolar-like antenna emission in the radiofrequency range by laser-produced plasma channels in air," Journal of Physics D: Applied Physics **41**, 245206 (2008).

[57] D. J. Cook and R. M. Hochstrasser, "Intense terahertz pulses by four-wave rectification in air," Optics Letters **25**, 1210–1212 (2000).

[58] G. Askaryan, "Effect of the field gradient of an intense electromagnetic beam on electrons and atoms," Zhurnal Eksperimentalnoy i Teoreticheskoy Fiziki (USSR) **42**, 1567–1570 (1962).

[59] G. Fibich and A. L. Gaeta, "Critical power for self-focusing in bulk media and in hollow waveguides," Optics Letters **25**, 335–337 (2000).

[60] G. G. Luther, J. V. Moloney, A. C. Newell, and E. M. Wright, "Self-focusing threshold in normally dispersive media," Optics Letters **19**, 862–864 (1994).

[61] X. D. Cao, G. P. Agrawal, and C. J. McKinstrie, "Self-focusing of chirped optical pulses in nonlinear dispersive media," Physical Review A **49**, 4085–4092 (1994).

[62] L. Bergé, J. J. Rasmussen, E. A. Kuznetsov, E. G. Shapiro, and S. K. Turitsyn, "Self-focusing of chirped optical pulses in media with normal dispersion," Journal of the Optical Society of America B **13**, 1879–1891 (1996).

[63] R. H. Stolen and W. J. Tomlinson, "Effect of the Raman part of the nonlinear refractive index on propagation of ultrashort optical pulses in fibers," Journal of the Optical Society of America B **9**, 565–573 (1992).

[64] S. Varma, Y.-H. Chen, and H. M. Milchberg, "Trapping and destruction of long-range high-intensity optical filaments by molecular quantum wakes in air," Physical Review Letters **101**, 205001 (2008).

[65] J. P. Palastro, T. M. Antonsen, S. Varma, Y.-H. Chen, and H. M. Milchberg, "Simulations of femtosecond atmospheric filaments enhanced by dual pulse molecular alignment," Physical Review A **85**, 043843 (2012).

[66] R. W. Boyd, *Nonlinear optics* (Elsevier, 2008).

[67] H. M. Milchberg, Y.-H. Chen, Y.-H. Cheng, N. Jhajj, J. P. Palastro, E. W. Rosenthal, S. Varma, J. K. Wahlstrand, and S. Zahedpour, "The extreme nonlinear optics of gases and femtosecond optical filamentation," Physics of Plasmas **21**, 100901 (2014).

[68] T. Tajima, K. Nakajima, and G. Mourou, "Laser acceleration," La Rivista Del Nuovo Cimento **40**, 33–133 (2017).

[69] A. Macchi, *A Superintense Laser-Plasma Interaction Theory Primer* (Springer, 2013).

[70] F. F. Chen, *Introduction to Plasma Physics and Controlled Fusion* (Springer, 2016).

[71] E. Esarey, P. Sprangle, and J. Krall, "Laser acceleration of electrons in vacuum," Physical Review E **52**, 5443–5453 (1995).

[72] N. E. Andreev, M. E. Veisman, S. P. Goreslavskii, and M. V. Chegotov, "Residual electron momentum and energy in a gas ionized by a short high-power laser pulse," Plasma Physics Reports **27**, 278–292 (2001).

[73] P. Sprangle, J. R. Peñano, B. Hafizi, and C. A. Kapetanakos, "Ultrashort laser pulses and electromagnetic pulse generation in air and on dielectric surfaces," Physical Review E **69**, 066415 (2004).

[74] V. S. Popov, "Tunnel and multiphoton ionization of atoms and ions in a strong laser field (keldysh theory)," Physics-Uspekhi **47**, 855–885 (2004).

[75] A. Kramida, Yu. Ralchenko, J. Reader, and and NIST ASD Team, NIST Atomic Spectra Database (ver. 5.6.1), [Online]. Available: `https://physics.nist.gov/asd` [2019, May 14]. National Institute of Standards and Technology, Gaithersburg, MD. (2018).

[76] M. Y. Ivanov, M. Spanner, and O. Smirnova, "Anatomy of strong field ionization," Journal of Modern Optics **52**, 165–184 (2005).

[77] L. V. Keldysh, "Ionization in the field of a strong electromagnetic wave," Soviet Journal of Experimental and Theoretical Physics (JETP) **20**, 1307–1314 (1965).

[78] S. V. Popruzhenko, V. D. Mur, V. S. Popov, and D. Bauer, "Strong field ionization rate for arbitrary laser frequencies," Physical Review Letters **101**, 193003 (2008).

[79] I. Frank and I. Tamm, "Coherent visible radiation of fast electrons passing through matter," Comptes Rendus of the Academy of Sciences of the USSR **24**, 109–114 (1937).

[80] C. D'Amico, A. Houard, S. Akturk, Y. Liu, J. L. Bloas, M. Franco, B. Prade, A. Couairon, V. T. Tikhonchuk, and A. Mysyrowicz, "Forward THz radiation emission by femtosecond filamentation in gases: theory and experiment," New Journal of Physics **10**, 013015 (2008).

[81] G. Manganaro and D. Robertson, "Interleaving ADCs: Unraveling the Mysteries," Analog Dialogue **49** (2015).

[82] X. Lin, "Spurs analysis in the RF sampling ADC," Application report slaa824, Texas Instruments (2018).

[83] W. Kester, "Converting oscillator phase noise to time jitter," Tutorial mt-008, Analog Devices (2009).

[84] S. W. Smith, *The Scientist and Engineer's Guide to Digital Signal Processing* (California Technical Publishing, 1997).

[85] H. Schantz, *Ultrawideband antennas* (Artech House, 2005).

[86] V. H. Rumsey, *Frequency independent antennas* (Academic Press, 2014).

[87] J. D. Jackson, *Classical Electrodynamics* (Wiley, 1998).

[88] C. H. Walter, *Traveling Wave Antennas* (Dover, 1970).

[89] A. Yaghjian, "An overview of near-field antenna measurements," IEEE Transactions on Antennas and Propagation **34**, 30–45 (1986).

[90] C. A. Balanis, *Antenna Theory: Analysis and Design* (Wiley, 2016).

[91] S. Tzortzakis, B. Prade, M. Franco, and A.Mysyrowicz, "Time-evolution of the plasma channel at the trail of a self-guided ir femtosecond laser pulse in air," Optics Communications **181**, 123 – 127 (2000).

[92] D. Abdollahpour, S. Suntsov, D. G. Papazoglou, and S. Tzortzakis, "Measuring easily electron plasma densities in gases produced by ultrashort lasers and filaments," Optics Express **19**, 16866–16871 (2011).

[93] D. Mongin, E. Schubert, L. de la Cruz, N. Berti, J. Kasparian, and J.-P. Wolf, "Linearity of charge measurement in laser filaments," Optics Express **25**, 16517–16526 (2017).

[94] J. Papeer, D. Gordon, P. Sprangle, M. Botton, and A. Zigler, "Temporal evolution of femtosecond laser induced plasma filament in air and N_2," Applied Physics Letters **103**, 244102 (2013).

[95] M. Alshershby, Y. Ren, J. Qin, Z. Hao, and J. Lin, "Diagnosis of femtosecond plasma filament by channeling microwaves along the filament," Applied Physics Letters **102**, 204101 (2013).

[96] J. Kerr, "Short axial length broad-band horns," IEEE Transactions on Antennas and Propagation **21**, 710–714 (1973).

[97] D. M. Pozar, *Microwave engineering* (Wiley, 2009).

[98] R. Ginley, "IEEE Standard for Precision Coaxial Connectors (DC to 110 GHz)," Ieee std 287-2007, IEEE Instrumentation and Measurement Society (2007).

[99] H.-J. Kunze, *Introduction to plasma spectroscopy* (Springer, 2009).

[100] A. Brablec, D. Trunec, and F. Stastný, "Deconvolution of spectral line profiles: solution of the inversion problem," Journal of Physics D: Applied Physics **32**, 1870–1875 (1999).

[101] G. Petrov, "A simple algorithm for spectral line deconvolution," Journal of Quantitative Spectroscopy and Radiative Transfer **72**, 281 – 287 (2002).

[102] A. Hati, C. Nelson, N. Ashby, and D. Howe, "Calibration uncertainty for the NIST PM/AM noise standards," NIST Special Publication **250**, 90 (2012).

[103] C. E. Baum and E. G. Farr, "Extending the Definitions of Antenna Gain and Radiation Pattern into the Time Domain," Sensor and simulation note 350, Air Force Research Laboratory (1992).

[104] C. E. Baum, E. G. Farr, and C. A. Frost, "Transient gain of antennas related to the traditional continuous-wave (CW) definition of gain," in *Ultra- Wideband Short-Pulse Electromagnetics 4 (IEEE Cat. No.98EX112),* (1998), pp. 109–118.

[105] W. Wiesbeck, G. Adamiuk, and C. Sturm, "Basic properties and design principles of UWB antennas," Proceedings of the IEEE **97**, 372–385 (2009).

[106] "Cables, Radio Frequency, Flexible and Semirigid, General Specification," MIL-DTL-17, Defense Logistics Agency (2019).

[107] "Interface Dimensions Series RPC-1.85 (code 08)," Tech. rep., Rosenberger Group GmbH (2019).

[108] H. Nyquist, "Thermal agitation of electric charge in conductors," Physical Review **32**, 110–113 (1928).

[109] G. Heinzel, A. Rüdiger, and R. Schilling, "Spectrum and spectral density estimation by the Discrete Fourier transform (DFT), including a comprehensive list of window functions and some new at-top windows," Tech. rep., Max Planck Institute for Gravitational Physics (2002).

[110] MegaPhase, "MegaPhase UltraPhase Cable Data Sheet," (2017). Https://www.megaphase.com/wp-content/uploads/2017/05/MegaPhase-UltraPhase-Cable-Data-Sheet-v5.pdf.

[111] N. Jhajj, Y.-H. Cheng, J. K. Wahlstrand, and H. M. Milchberg, "Optical beam dynamics in a gas repetitively heated by femtosecond filaments," Optics Express **21**, 28980–28986 (2013).

[112] G. Stibenz, N. Zhavoronkov, and G. Steinmeyer, "Self-compression of millijoule pulses to 7.8 fs duration in a white-light filament," Optics Letters **31**, 274–276 (2006).

[113] A. Mysyrowicz, A. Couairon, and U. Keller, "Self-compression of optical laser pulses by filamentation," New Journal of Physics **10**, 025023 (2008).

[114] D. Kartashov, S. Ališauskas, A. Pugžlys, A. Voronin, A. Zheltikov, M. Petrarca, P. Béjot, J. Kasparian, J.-P. Wolf, and A. Baltuška, "White light generation over three octaves by femtosecond filament at 3.9 microns in argon," Optics Letters **37**, 3456–3458 (2012).

[115] P. R. Hemmer, R. B. Miles, P. Polynkin, T. Siebert, A. V. Sokolov, P. Sprangle, and M. O. Scully, "Standoff spectroscopy via remote generation of a backward-propagating laser beam," Proceedings of the National Academy of Sciences **108**, 3130–3134 (2011).

[116] H. Xie, G. Li, W. Chu, B. Zeng, J. Yao, C. Jing, Z. Li, and Y. Cheng, "Backward nitrogen lasing actions induced by femtosecond laser filamentation: influence of duration of gain," New Journal of Physics **17**, 073009 (2015).

[117] P. Polynkin and Y. Cheng, *Air Lasing* (Springer, 2018).

[118] A. Englesbe, J. Elle, R. Reid, A. Lucero, H. Pohle, M. Domonkos, S. Kalmykov, K. Krushelnick, and A. Schmitt-Sody, "Gas pressure dependence of microwave pulses generated by laser-produced filament plasmas," Optics Letters **43**, 4953–4956 (2018).

[119] K. Y. Kim, A. J. Taylor, J. H. Glownia, and G. Rodriguez, "Coherent control of terahertz supercontinuum generation in ultrafast laser-gas interactions," Nature Photonics **2**, 605–609 (2008).

[120] A. Couairon, M. Franco, G. Méchain, T. Olivier, B. Prade, and A. Mysyrowicz, "Femtosecond filamentation in air at low pressures: Part I: Theory and numerical simulations," Optics Commununications **259**, 265–273 (2006).

[121] S. Hosseini, O. Kosareva, N. Panov, V. Kandidov, A. Azarm, J. Daigle, A. Savel'ev, T. Wang, and S. L. Chin, "Femtosecond laser filament in different air pressures simulating vertical propagation up to 10 km," Laser Physics Letters **9**, 868 (2012).

[122] S. Champeaux and L. Bergé, "Long-range multifilamentation of femtosecond laser pulses versus air pressure," Optics Letters **31**, 1301–1303 (2006).

[123] D. Reyes, M. Baudelet, M. Richardson, and S. Rostami Fairchild, "Transition from linear- to nonlinear-focusing regime of laser filament plasma dynamics," Journal of Applied Physics **124**, 053103 (2018).

[124] M. C. Wanke, M. A. Mangan, and R. J. Foltynowicz, "Atmospheric propagation of THz radiation," Sand2005-6389, Sandia National Laboratories (2005).

[125] Y. Yang, A. Shutler, and D. Grischkowsky, "Measurement of the transmission of the atmosphere from 0.2 to 2 thz," Optics Express **19**, 8830–8838 (2011).

[126] L. Rothman, I. Gordon, A. Barbe, D. Benner, P. Bernath, M. Birk, V. Boudon, L. Brown, A. Campargue, J.-P. Champion, K. Chance, L. Coudert, V. Dana, V. Devi, S. Fally, J.-M. Flaud, R. Gamache, A. Goldman, D. Jacquemart, I. Kleiner, N. Lacome, W. Lafferty, J.-Y. Mandin, S. Massie, S. Mikhailenko, C. Miller, N. Moazzen-Ahmadi, O. Naumenko, A. Nikitin, J. Orphal, V. Perevalov, A. Perrin, A. Predoi-Cross, C. Rinsland, M. Rotger, M. imekov, M. Smith, K. Sung, S. Tashkun, J. Tennyson, R. Toth, A. Vandaele, and J. V. Auwera, "The HITRAN 2008 molecular spectroscopic database," Journal of Quantitative Spectroscopy and Radiative Transfer **110**, 533 – 572 (2009). HITRAN.

[127] "Attenuation by atmospheric gases," Recommendation ITU-R P.676-11, International Telecommunications Union (2016).

[128] R. H. Church, W. E. Webb, and J. B. Salsman, "Dielectric Properties of Low-Loss Minerals," Report of investigation 9194, Bureau of Mines, United States Department of the Interior (1988).

[129] S. Chen, K. N. Nguyen, and M. N. Afsar, "Complex dielectric permittivity measurements of glasses at millimeter waves and terahertz frequencies," in *2006 European Microwave Conference,* (2006), pp. 384–387.

[130] "Loss tangent," Tech. rep., Keysight Technologies (2019).

[131] R. N. Clarke, "Dielectric properties of materials," Tech. rep., National Physical Laboratory (2017).

[132] J. D. Huba, "NRL Plasma Formulary," Tech. rep., Plasma Phyisics Division, Naval Research Laboratory (2006).

[133] S. Tzortzakis, M. A. Franco, Y.-B. André, A. Chiron, B. Lamouroux, B. S. Prade, and A. Mysyrowicz, "Formation of a conducting channel in air by self-guided femtosecond laser pulses," Physical Review E **60**, R3505–R3507 (1999).

[134] A. Ting, I. Alexeev, D. Gordon, R. Fischer, D. Kaganovich, T. Jones, E. Briscoe, J. Peano, R. Hubbard, and P. Sprangle, "Measurements of intense femtosecond laser pulse propagation in air," Physics of Plasmas **12**, 056705 (2005).

[135] Y.-H. Chen, S. Varma, T. M. Antonsen, and H. M. Milchberg, "Direct measurement of the electron density of extended femtosecond laser pulse-induced filaments," Physical Review Letters **105**, 215005 (2010).

[136] A. Couairon and A. Mysyrowicz, "Femtosecond filamentation in transparent media," Physics Reports **441**, 47 – 189 (2007).

[137] Y. E. Geints, S. S. Golik, A. A. Zemlyanov, A. M. Kabanov, and G. G. Matvienko, "Influence of the laser beam size on the length of a filament formed by high-power femtosecond laser radiation in air," Quantum Electronics **44**, 489–497 (2014).

[138] J. Wymer, J. Elle, E. Ruden, A. Englesbe, and A. Lucero, "Characterization of femtosecond laser filament conductivity with varying pressure," in *60th Annual Meeting of the APS Division of Plasma Physics,* (2018).

[139] B. Zhou, A. Houard, Y. Liu, B. Prade, A. Mysyrowicz, A. Couairon, P. Mora, C. Smeenk, L. Arissian, and P. Corkum, "Measurement and control of plasma oscillations in femtosecond filaments," Physical Review Letters **106**, 255002 (2011).

[140] N. L. Aleksandrov, S. B. Bodrov, M. V. Tsarev, A. A. Murzanev, Y. A. Sergeev, Y. A. Malkov, and A. N. Stepanov, "Decay of femtosecond laser-induced plasma filaments in air, nitrogen, and argon for atmospheric and subatmospheric pressures," Physical Review E **94**, 013204 (2016).

[141] H. Hamster, A. Sullivan, S. Gordon, W. White, and R. W. Falcone, "Subpicosecond, electromagnetic pulses from intense laser-plasma interaction," Physical Review Letters **71**, 2725–2728 (1993).

[142] H. Hamster, A. Sullivan, S. Gordon, and R. W. Falcone, "Short-pulse terahertz radiation from high-intensity-laser-produced plasmas," Physical Review E **49**, 671–677 (1994).

[143] H. Roskos, M. Thomson, M. Kreß, and T. Löffler, "Broadband THz emission from gas plasmas induced by femtosecond optical pulses: From fundamentals to applications," Laser & Photonics Reviews **1**, 349–368 (2007).

[144] G. Rodriguez and G. L. Dakovski, "Scaling behavior of ultrafast two-color terahertz generation in plasma gas targets: energy and pressure dependence," Optics Express **18**, 15130–15143 (2010).

[145] Y. J. Yoo, D. Kuk, Z. Zhong, and K. Y. Kim, "High-power THz generation from two-color laser filamentation in various types of gases," in *Conference on Lasers and Electro-Optics,* (OSA, 2017), p. STu3J.7.

[146] J.-M. Manceau, M. Massaouti, and S. Tzortzakis, "Coherent control of THz pulses polarization from femtosecond laser filaments in gases," Optics Express **18**, 18894–18899 (2010).

[147] A. W. Smith and N. Braslau, "Observation of an optical difference frequency," Journal of Applied Physics **34**, 2105–2106 (1963).

[148] F. K. Tittel, D. Richter, and A. Fried, *Mid-Infrared Laser Applications in Spectroscopy* (Springer Berlin Heidelberg, Berlin, Heidelberg, 2003).

[149] J. A. Giordmaine and R. C. Miller, "Tunable coherent parametric oscillation in $LiNbO_3$ at optical frequencies," Physical Review Letters **14**, 973–976 (1965).

[150] R. Fischer and L. A. Kulevskiĭ, "Optical parametric oscillators (review)," Soviet Journal of Quantum Electronics **7**, 135–159 (1977).

[151] G. Cerullo and S. De Silvestri, "Ultrafast optical parametric amplifiers," Review of Scientific Instruments **74**, 1–18 (2003).

[152] A. Dubietis, G. Jonušauskas, and A. Piskarskas, "Powerful femtosecond pulse generation by chirped and stretched pulse parametric amplification in BBO crystal," Optics Communications **88**, 437 – 440 (1992).

[153] A. Dubietis, R. Butkus, and A. P. Piskarskas, "Trends in chirped pulse optical parametric amplification," IEEE Journal of Selected Topics in Quantum Electronics **12**, 163–172 (2006).

[154] A. V. Mitrofanov, A. A. Voronin, D. A. Sidorov-Biryukov, A. Pugžlys, E. A. Stepanov, G. Andriukaitis, T. Fl ory, S. Ališauskas, A. B. Fedotov, A. Baltuška, and A. M. Zheltikov, "Mid-infrared laser filaments in the atmosphere," Scientific Reports **5**, 8368 (2015).

[155] H. Liang, D. L. Weerawarne, P. Krogen, R. I. Grynko, C.-J. Lai, B. Shim, F. X. Kärtner, and K.-H. Hong, "Mid-infrared laser filaments in air at a kilohertz repetition rate," Optica **3**, 678–681 (2016).

[156] I. V. Pogorelsky, M. N. Polyanskiy, and W. D. Kimura, "Mid-infrared lasers for energy frontier plasma accelerators," Physical Review Accelerators & Beams **19**, 091001 (2016).

[157] J. Lin, Y. Ma, R. Schwartz, D. Woodbury, J. A. Nees, M. Mathis, A. G. R. Thomas, K. Krushelnick, and H. Milchberg, "Adaptive control of laser-wakefield accelerators driven by mid-ir laser pulses," Optics Express **27**, 10912–10923 (2019).

[158] W. Kruer, *The physics of laser plasma interactions* (CRC Press, 2018).

[159] S. Witte and K. S. E. Eikema, "Ultrafast optical parametric chirped-pulse amplification," IEEE Journal of Selected Topics in Quantum Electronics **18**, 296–307 (2012).

[160] S. Backus, C. G. Durfee, M. M. Murnane, and H. C. Kapteyn, "High power ultrafast lasers," Review of Scientific Instruments **69**, 1207–1223 (1998).

[161] A. H. Curtis, B. A. Reagan, K. A. Wernsing, F. J. Furch, B. M. Luther, and J. J. Rocca, "Demonstration of a compact 100 Hz, 0.1 J, diode-pumped picosecond laser," Optics Letters **36**, 2164–2166 (2011).

[162] T. Metzger, M. Gorjan, M. Ueffing, C. Y. Teisset, M. Schultze, R. Bessing, M. H afner, S. Prinz, D. Sutter, K. Michel, H. G. Barros, Z. Major, and F. Krausz, "Picosecond thin-disk lasers," in *Conference on Lasers and Electro-Optics,* (2014), p. JTh4L.1.

[163] G. Andriukaitis, T. Balčiūnas, S. Ališauskas, A. Pugžlys, A. Baltuška, T. Popmintchev, M.-C. Chen, M. M. Murnane, and H. C. Kapteyn, "90 GW peak power few-cycle mid-infrared pulses from an optical parametric amplifier," Optics Letters **36**, 2755–2757 (2011).

[164] L.-L. Zhang, W.-M. Wang, T. Wu, R. Zhang, S.-J. Zhang, C.-L. Zhang, Y. Zhang, Z.-M. Sheng, and X.-C. Zhang, "Observation of terahertz radiation via the two-color laser scheme with uncommon frequency ratios," Physical Review Letters **119**, 235001 (2017).

[165] A. Yariv and P. Yeh, *Optical waves in crystals* (Wiley, 2003).

[166] D. N. Nikogosyan, "Beta barium borate (BBO)," Applied Physics A **52**, 359–368 (1991).

[167] D. S. Hum and M. M. Fejer, "Quasi-phasematching," Comptes Rendus Physique **8**, 180 – 198 (2007). Recent advances in crystal optics.

[168] K. Y. Kim, "Strong THz generation from air plasma using a long wavelength laser," (2018). ONR Long Wave Multidisciplinary University Reaserch Initiative Annual Program Review.

[169] T. I. Oh, Y. S. You, and K. Y. Kim, "Two-dimensional plasma current and optimized terahertz generation in two-color photoionization," Optics Express **20**, 19778–19786 (2012).

[170] K. Y. Kim, J. H. Glownia, A. J. Taylor, and G. Rodriguez, "Terahertz emission from ultrafast ionizing air in symmetry-broken laser fields," Optics Express **15**, 4577–4584 (2007).

[171] "Optical Glass Data Sheets," Tech. rep., Schott A.G. (2013).

[172] T. I. Oh, Y. S. You, N. Jhajj, E. W. Rosenthal, H. M. Milchberg, and K. Y. Kim, "Intense terahertz generation in two-color laser filamentation: energy scaling with terawatt laser systems," New Journal of Physics **15**, 075002 (2013).

[173] X. Xie, J. Dai, and X.-C. Zhang, "Coherent control of THz wave generation in ambient air," Physical Review Letters **96**, 075005 (2006).

[174] P. E. Martin and E. F. Barker, "The infrared absorption spectrum of carbon dioxide," Physical Review **41**, 291–303 (1932).

[175] Z. Hao, J. Zhang, X. Lu, T. Xi, Z. Zhang, and Z. Wang, "Energy interchange between large-scale free propagating filaments and its background reservoir," Journal of the Optical Society of America B **26**, 499–502 (2009).

[176] E. Hecht, *Optics* (Pearson, 2016).

[177] J. P. Palastro, J. Peñano, W. Nelson, G. DiComo, M. Helle, L. A. Johnson, and B. Hafizi, "Reciprocity breaking during nonlinear propagation of adapted beams through random media," Optics Express **24**, 18817–18827 (2016).

[178] J. W. Hardy, *Adaptive optics for astronomical telescopes* (Oxford University Press, 1998).

[179] J. Hah, W. Jiang, Z.-H. He, J. A. Nees, B. Hou, A. G. R. Thomas, and K. Krushelnick, "Enhancement of thz generation by feedback-optimized wavefront manipulation," Optics Express **25**, 17271–17279 (2017).

[180] Z.-H. He, B. Hou, V. Lebailly, J. A. Nees, K. Krushelnick, and A. G. R. Thomas, "Coherent control of plasma dynamics," Nature Communications **6**, 7156 (2015). Article.

[181] K. E. Kinnear, W. B. Langdon, L. Spector, P. J. Angeline, and U.-M. O'Reilly, *Advances in genetic programming*, vol. 3 (MIT Press, 1999).

[182] T. Murata and H. Ishibuchi, "MOGA: multi-objective genetic algorithms," in *Proceedings of the 1995 IEEE International Conference on Evolutionary Computation,* (1995).

[183] D. Greenhalgh and S. Marshall, "Convergence Criteria for Genetic Algorithms," SIAM Journal on Computing **30**, 269–282 (2000).

[184] B. Hou, J. Easter, A. Mordovanakis, K. Krushelnick, and J. A. Nees, "Vacuum-free x-ray source based on ultrashort laser irradiation of solids," Optics Express **16**, 17695–17705 (2008).

[185] E. W. Rosenthal, N. Jhajj, I. Larkin, S. Zahedpour, J. K. Wahlstrand, and H. M. Milchberg, "Energy deposition of single femtosecond filaments in the atmosphere," Optics Letters **41**, 3908–3911 (2016).

[186] D. Pushkarev, E. Mitina, D. Shipilo, N. Panov, D. Uryupina, A. Ushakov, R. Volkov, A. Karabutov, I. Babushkin, A. Demircan, U. Morgner, O. Kosareva, and A. Savel'ev, "Transverse structure and energy deposition by a subTW femtosecond laser in air: from single filament to superfilament," New Journal of Physics **21**, 033027 (2019).

[187] J. Hah, "High power laser - plasma interactions for homeland security applications," Ph.D. thesis, University of Michigan (2018).

[188] L. A. Finney, P. J. Skrodzki, M. Burger, X. Xiao, J. Nees, and I. Jovanovic, "Optical emission from ultrafast laser filament-produced air plasmas in the multiple filament regime," Optics Express **26**, 29110–29122 (2018).

[189] T. I. Oh, Y. S. You, N. Jhajj, E. W. Rosenthal, H. M. Milchberg, and K. Y. Kim, "Scaling and saturation of high-power terahertz radiation generation in two-color laser filamentation," Applied Physics Letters **102**, 201113 (2013).

[190] J. Xie, W.-H. Fan, and X. Chen, "Systematic experimental study on a highly efficient terahertz source based on two-color laser-induced air plasma," Laser Physics **26**, 055002 (2016).

[191] J. Kasparian, M. Rodriguez, G. Méjean, J. Yu, E. Salmon, H. Wille, R. Bourayou, S. Frey, Y.-B. André, A. Mysyrowicz, R. Sauerbrey, J.-P. Wolf, and L. Wöste, "White-light filaments for atmospheric analysis," Science **301**, 61–64 (2003).

[192] Y. Brelet, A. Houard, L. Arantchouk, B. Forestier, Y. Liu, B. Prade, J. Carbonnel, Y.-B. André, and A. Mysyrowicz, "Tesla coil discharges guided by femtosecond laser filaments in air," Applied Physics Letters **100**, 181112 (2012).

[193] T. D. Grow and A. L. Gaeta, "Dependence of multiple filamentation on beam ellipticity," Optics Express **13**, 4594–4599 (2005).

[194] G. Fibich, S. Eisenmann, B. Ilan, and A. Zigler, "Control of multiple filamentation in air," Optics Letters **29**, 1772–1774 (2004).

[195] A. Trisorio and C. P. Hauri, "Control and characterization of multiple circularly polarized femtosecond filaments in argon," Optics Letters **32**, 1650–1652 (2007).

[196] V. Kandidov, N. Akozbek, M. Scalora, O. Kosareva, A. Nyakk, Q. Luo, S. Hosseini, and S. Chin, "Towards a control of multiple filamentation by spatial regularization of a high-power femtosecond laser pulse," Applied Physics B **80**, 267–275 (2005).

[197] G. Méchain, A. Couairon, M. Franco, B. Prade, and A. Mysyrowicz, "Organizing multiple femtosecond filaments in air," Physical Review Letters **93**, 035003 (2004).

[198] H. Gao, W. Chu, G. Yu, B. Zeng, J. Zhao, Z. Wang, W. Liu, Y. Cheng, and Z. Xu, "Femtosecond laser filament array generated with step phase plate in air," Optics Express **21**, 4612–4622 (2013).

[199] A. A. Ionin, N. G. Iroshnikov, O. G. Kosareva, A. V. Larichev, D. V. Mokrousova, N. A. Panov, L. V. Seleznev, D. V. Sinitsyn, and E. S. Sunchugasheva, "Filamentation of femtosecond laser pulses governed by variable wavefront distortions via a deformable mirror," Journal of the Optical Society of America B **30**, 2257–2262 (2013).

[200] Z. Jin, J. Zhang, M. Xu, X. Lu, Y. Li, Z. Wang, Z. Wei, X. Yuan, and W. Yu, "Control of filamentation induced by femtosecond laser pulses propagating in air," Optics Express **13**, 10424–10430 (2005).

[201] P. Rohwetter, M. Queißer, K. Stelmaszczyk, M. Fechner, and L. Wöste, "Laser multiple filamentation control in air using a smooth phase mask," Physical Review A **77**, 013812 (2008).

[202] C. Hauri, J. Gautier, A. Trisorio, E. Papalazarou, and P. Zeitoun, "Two-dimensional organization of a large number of stationary optical filaments by adaptive wave front control," Applied Physics B **90**, 391–394 (2008).

[203] J.-F. Daigle, Y. Kamali, M. Châteauneuf, G. Tremblay, F. Théberge, J. Dubois, G. Roy, and S. L. Chin, "Remote sensing with intense filaments enhanced by adaptive optics," Applied Physics B **97**, 701 (2009).

[204] R. Ackermann, E. Salmon, N. Lascoux, J. Kasparian, P. Rohwetter, K. Stelmaszczyk, S. Li, A. Lindinger, L. Wöste, P. Béjot, L. Bonacina, and J.-P. Wolf, "Optimal control of filamentation in air," Applied Physics Letters **89**, 171117 (2006).

[205] G. Heck, J. Sloss, and R. J. Levis, "Adaptive control of the spatial position of white light filaments in an aqueous solution," Optics Communications **259**, 216 – 222 (2006).

[206] V. I. Bespalov and V. I. Talanov, "Filamentary structure of light beams in nonlinear liquids," Soviet Journal of Experimental and Theoretical Physics Letters **3**, 307 (1966).

[207] A. J. Campillo, S. L. Shapiro, and B. R. Suydam, "Periodic breakup of optical beams due to self-focusing," Applied Physics Letters **23**, 628–630 (1973).

[208] S. Cháves-Cerda, M. D. Iturbe-Castillo, and J. M. Hickman, *Self-focusing: Past and Present* (Springer, 2009), chap. Diffraction-Induced High-Order Modes of the (2 + 1)D Nonparaxial Nonlinear Schrödinger Equation.

[209] T.-T. Xi, X. Lu, and J. Zhang, "Interaction of light filaments generated by femtosecond laser pulses in air," Physical Review Letters **96**, 025003 (2006).

[210] H. Cai, J. Wu, P. Lu, X. Bai, L. Ding, and H. Zeng, "Attraction and repulsion of parallel femtosecond filaments in air," Physical Review A **80**, 051802 (2009).

[211] B. Shim, S. E. Schrauth, C. J. Hensley, L. T. Vuong, P. Hui, A. A. Ishaaya, and A. L. Gaeta, "Controlled interactions of femtosecond light filaments in air," Physical Review A **81**, 061803 (2010).

[212] S. Henin, Y. Petit, J. Kasparian, J.-P. Wolf, A. Jochmann, S. D. Kraft, S. Bock, U. Schramm, R. Sauerbrey, W. M. Nakaema, K. Stelmaszczyk, P. Rohwetter, L. Wöste, C.-L. Soulez, S. Mauger, L. Bergé, and S. Skupin, "Saturation of the filament density of ultrashort intense laser pulses in air," Applied Physics B **100**, 77–84 (2010).

[213] Z.-H. He, B. Hou, G. Gao, V. Lebailly, J. A. Nees, R. Clarke, K. Krushelnick, and A. G. R. Thomas, "Coherent control of plasma dynamics by feedback-optimized wavefront manipulation," Physics of Plasmas **22**, 056704 (2015).

[214] S. Preibisch, S. Saalfeld, and P. Tomancak, "Globally optimal stitching of tiled 3D microscopic image acquisitions," Bioinformatics **25**, 1463–1465 (2009).

[215] V. P. Kandidov, N. Akozbek, M. Scalora, O. G. Kosareva, A. V. Nyakk, Q. Luo, S. A. Hosseini, and S. L. Chin, "A method for spatial regularisation of a bunch of filaments in a femtosecond laser pulse," Quantum Electronics **34**, 879–880 (2004).

[216] D. E. Shipilo, N. A. Panov, E. S. Sunchugasheva, D. V. Mokrousova, V. A. Andreeva, O. G. Kosareva, L. V. Seleznev, A. B. Savel'ev, A. A. Ionin, and S. L. Chin, "Fusion of regularized femtosecond filaments in air: far field on-axis emission," Laser Physics Letters **13**, 116005 (2016).

[217] D. V. Pushkarev, E. V. Mitina, D. S. Uryupina, R. V. Volkov, N. A. Panov, A. A. Karabutov, O. G. Kosareva, and A. B. Savel'ev, "Nonlinear increase in the energy input into a medium at the fusion of regularized femtosecond filaments," Journal of Experimental and Theoretical Physics Letters **106**, 561–564 (2017).

[218] D. Pushkarev, D. Shipilo, A. Lar'kin, E. Mitina, N. Panov, D. Uryupina, A. Ushakov, R. Volkov, S. Karpeev, S. Khonina, O. Kosareva, and A. Savel'ev, "Effect of phase front modulation on the merging of multiple regularized femtosecond filaments," Laser Physics Letters **15**, 045402 (2018).

[219] S. A. Hosseini, Q. Luo, B. Ferland, W. Liu, S. L. Chin, O. G. Kosareva, N. A. Panov, N. Aközbek, and V. P. Kandidov, "Competition of multiple filaments during the propagation of intense femtosecond laser pulses," Physical Review A **70**, 033802 (2004).

[220] H. Yang and X. Li, "Comparison of several stochastic parallel optimization algorithms for adaptive optics system without a wavefront sensor," Optics & Laser Technology **43**, 630–635 (2011).

[221] Y. Liu, J. Ma, B. Li, Y. Hu, and J. Chu, "Comparison of optimization algorithms for adaptive optics system without a wavefront sensor," (Vol. 841504 SPIE 6th International Symposium on Advanced Optical Manufacturing and Testing Technologies: Large Mirrors and Telescopes, 2012).

[222] Z. Sun, J. Chen, and W. Rudolph, "Determination of the transient electron temperature in a femtosecond-laser-induced air plasma filament," Physical Review E **83**, 046408 (2011).

[223] J. Bernhardt, W. Liu, F. Théberge, H. L. Xu, J. F. Daigle, M. Châteauneuf, J. Dubois, and S. L. Chin, "Spectroscopic analysis of femtosecond laser plasma filament in air," Optics Communications **281**, 1268 – 1274 (2008).

[224] P. B. Corkum, "Plasma perspective on strong field multiphoton ionization," Physical Review Letters **71**, 1994–1997 (1993).

[225] M. A. Foster, R. Salem, D. F. Geraghty, A. C. Turner-Foster, M. Lipson, and A. L. Gaeta, "Silicon-chip-based ultrafast optical oscilloscope," Nature **456**, 81 (2008).

[226] J. Chou, O. Boyraz, D. Solli, and B. Jalali, "Femtosecond real-time single-shot digitizer," Applied Physics Letters **91**, 161105 (2007).

[227] S. Gupta and B. Jalali, "Time stretch enhanced recording oscilloscope," Applied Physics Letters **94**, 041105 (2009).

[228] N. Barbieri, "Engineering and application of ultrafast laser pulses and filamentation in air," Ph.D. thesis, University of Central Florida (2013).

[229] J. van Tilborg, C. Tóth, N. H. Matlis, G. R. Plateau, and W. P. Leemans, "Single-shot measurement of the spectral envelope of broad-bandwidth terahertz pulses from femtosecond electron bunches," Optics Letters **33**, 1186–1188 (2008).

[230] Y. Han and B. Jalali, "Photonic time-stretched analog-to-digital converter: fundamental concepts and practical considerations," Journal of Lightwave Technology **21**, 3085–3103 (2003).

[231] "Insights into high-speed detectors and high-frequency techniques," Tech. rep., Newport Corporation (2019).

[232] F. T. Ulaby, R. K. Moore, and A. K. Fung, *Microwave Remote Sensing: Active and Passive. Volume 1-Microwave Remote Sensing Fundamentals and Radiometry* (Artech House, 1986).